Fall 2021

Catalytic and Non-catalytic Methods for Hydrocarbon Upgrading, Valorization, and Pollutant Control

Michael Morgan Royko

CATALYTIC AND NON-CATALYTIC METHODS FOR HYDROCARBON UPGRADING, VALORIZATION, AND POLLUTANT CONTROL

by

Michael Morgan Royko

Bachelors of Science
University of Alabama, 2017

Submitted in Partial Fulfillment of the Requirements

For the Degree of Doctor in Philosophy in

Chemical Engineering

College of Engineering and Computing

University of South Carolina

2022

Accepted by:

Jochen Lauterbach, Major Professor

Donna Chen, Committee Member

Chang Liu, Committee Member

Christopher Williams, Committee Member

Melissa Moss, Committee Member

Tracey L. Weldon, Vice Provost and Dean of the Graduate School

DEDICATION

My thesis is dedicated to my family who always believed in me and pushed me to do my best no matter what.

ACKNOWLEDGEMENTS

I would like to thank John Kile and Christopher Langer for their assistance, expertise, and supplies for two of my projects. Without their time and knowledge two of my projects would not have advanced as far as they have. I would also like to thank Savannah Howell, who worked with me on my ever-changing products for close to two years. I am forever indebted to the members of SAGE and Dr. Lauterbach for their input and feedback on my thesis and all my other work. I would specifically like to thank Dr. Blake MacQueen, Dr. Travis Williams, Dr. Calvin Thomas, Dr. Benjamin Ruiz-Yi, Dr. Katherine McCullough, Dr. Sunkyu Kim, Jennifer Naglic, Kaveh Shariati, Jennifer Naglic, Samuel Drummond, and Andrew Jaeschke. Finally, I would like to thank my family for always believing in me and their support; financially, emotionally, and everything else.

Chemix.org was utilized to create several of the diagrams used in this work.

ABSTRACT

This work investigates catalytic and non-catalytic oxidative chemical upgrading and pollutant remediation techniques to responsibly utilize hydrocarbon feedstocks with existing infrastructure as the transition to more renewable and cleaner feedstocks for energy generation are developed. These technologies include oxidative dehydrogenation of ethane, development of magnetically separable catalysts to reduce carbon monoxide emissions during biomass upgrading as well as the subsequent use of the upgraded biomass for partial coal replacement, and electrochemical treatment of a washcoat free wire mesh supported catalyst to reduce carbon monoxide emissions in combustion exhaust.

First, doping of secondary metals in M1/M2 catalysts for oxidative dehydrogenation of ethane was investigated to determine how these dopants influence catalytic activity via in-situ and ex-situ characterization. Next, a copper and zinc catalyst with novel magnetic separability and mechanical stability were studied to reduce carbon monoxide emissions during biomass upgrading and valorization. The biomass upgraded via this methodology can be burned in conventional coal power plants at a 30-40% co-firing rate with no capital changes to existing infrastructure and carbon monoxide emissions from the upgrading process were reduced by up to 95%. Lastly, an electrochemically treated wire mesh support was utilized with a platinum and palladium catalyst to reduce carbon monoxide emissions in combustion exhaust from natural gas furnaces or small engines such as portable generators, mopeds, and lawnmowers. This

treatment methodology increased the activity of the catalyst by a factor of 5.5 times with no increase in nominal precious metal loading.

PREFACE

Overall, the focus of this work is to develop methodologies to produce energy and chemicals sustainably and economically. Investigation and characterization of M1/M2 catalyst doping allows a better understanding of how these elements influence the chemical nature and performance of the catalyst and enable further studies on promotion utilizing the same or similar experimental framework.

The bulk of this work focuses on the development of two technologies to enable the utilization of hydrocarbon feedstocks for heating and energy generation while infrastructure for longer-term renewable energy sources is being developed and installed. The development of robust catalysts for natural gas furnace exhaust can also be extended for use in small applications such as household gasoline generators which when used improperly in residential applications can cost lives due to CO poisoning. Additional utilization of biomass provides a use case for forestry, logging, and agricultural waste within the state while providing a carbonaceous fuel source that is lower in heavy metals than coal and offsets fossil fuel consumption. I hope that this work can make a positive influence on the greater world in at least some small way.

TABLE OF CONTENTS

LIST OF TABLES

LIST OF FIGURES

LIST OF SYMBOLS

ΔH^0	Reaction enthalpy
γ	Gamma phase of a crystalline material

LIST OF ABBREVIATIONS

ALD ..... Atomic Layer Deposition

CO ..... Carbon Monoxide

CO_2 ..... Carbon Dioxide

EDX ..... Energy Dispersive X-Ray Spectroscopy

FWHM ..... Full Width at Half Maximum

GC ..... Gas Chromatography

HHV ..... Higher Heating Value

LDPE ..... Low-Density Polyethylene

N_2 ..... Nitrogen

ODH ..... Oxidative Dehydrogenation

pKa_1 ..... Acid Dissociation Constant for the First Acidic Hydrogen

PP ..... Polypropylene

PPM ..... Parts per Million

PTFE ..... Polytetrafluoroethylene

SEM ..... Scanning Electron Microscopy

SSWM ..... Stainless Steel Wire Mesh

TCD ..... Thermal Conductivity Detector

TGA ..... Thermogravimetric Analysis

TOF-SIMS ..... Trimethyl Aluminum

TOF-SIMS ..... Time of Flight Secondary Ion Mass Spectrometry

TPR ..... Temperature Programmed Reduction

VOC ..... Volatile Organic Compound

WGS ..... Water Gas Shift

XPS ..... X-Ray Photoelectron Spectroscopy

XRD ..... X-Ray Diffraction

CHAPTER 1

INTRODUCTION

1.1 Ethane Partial Oxidation

Despite being the second most abundant component found in natural gas deposits [1], ethane has relatively few industrial uses. While liquefied ethane possesses some niche uses as a cryogenic coolant [2], the vast majority of ethane is used as a feedstock for the production of ethylene. Unfortunately, the main industrial process to produce ethylene from ethane requires high temperatures, ~850°C, and is an incredibly energy-intensive endothermic reaction, constituting approximately 8% of the energy usage of the entire chemical processing industry [3]. Therefore, the development of a process that can produce high purity ethylene from ethane with a lower energy requirement could greatly reduce the costs of ethylene-derived goods such as plastics, anti-freeze, and ethylene oxide as well as being significantly more environmentally friendly.

One potential process through which this can be achieved is the oxidative dehydrogenation (ODH) of ethane. In this reaction, ethane is mixed with oxygen (or air) and passed over a catalyst to produce ethylene and further oxygenates at much milder conditions (less than 600°C). The ODH reaction is presented below as Reaction 1.

$$C_2H_6 + \tfrac{1}{2}O_2 \rightarrow C_2H_4 + H_2O \quad \Delta H^0 = -106 \text{ kJ/mol [4]} \qquad (1.1)$$

As this reaction is exothermic, it avoids the large energy penalty of steam cracking while only producing CO_2 and CO in the case of undesirable over-oxidation of ethane.

In pursuit of this goal, researchers at Union Carbide developed a mixed metal oxide composed of molybdenum, vanadium, and niobium [4] in the 1970s. Interestingly, the individual component metal oxides form almost entirely complete combustion products

[5]. Despite being more selective than previously studied materials, this catalyst lacked the desired industrial ethylene selectivity and conversion targets of 90% and 60-80% [6], [7], respectively. In order to further improve this catalyst, numerous researchers have looked into the addition of promoters [8]–[14], structural stabilizing agents [6], [10], [12], [15]–[17], crystal structure [6], [18]–[23], synthesis techniques [13], [24], [25], and post-synthesis treatments [24], [26], [27]. Fortunately, it has been shown that the incorporation of various dopants could greatly change the performance of the catalyst and is a common area of current work. However, studies, in particular *in-situ* studies, on how these promoters impact catalytic activity are lacking. The addition of this knowledge to the current literature would help guide researchers to promising dopants while eliminating lost time due to Edisonian experimental methodologies.

Despite the simplified reaction scheme depicted previously in Reaction 1, these catalysts produce a variety of additional products resulting from the overoxidation of ethylene to CO, CO_2, and acetic acid. This product distribution is dependent on several factors including catalysts surface structure, temperature, space velocity, and gas composition [27], [28]. As the formation of side products is due to sequential overoxidation of ethylene, decreasing space velocity increases the formation of more highly oxygenated products [29]. Further, there are a variety of active sites on this catalyst, with some studies suggesting that the bridging oxygen atom in M-O-V bonds may be the primary active site for the C-H scission of ethane, the first step of the ODH reaction [30]–[32], however, many studies have also focused on the terminal V^{5+}=O site [17], [32]–[35] and Te=O [31], [32], [34]. Regardless of the site of ethane activation, mobility of lattice oxygen is important for catalytic activity as lattice oxygen participates via the Mars-Van-Krevelen mechanism

[36]. For example, the presence of two highly oxidized species near the site of ethane activation can cause overoxidation of ethylene [37]. In the case of mild over-oxidation, this results in the formation of acetic acid, especially at lower space velocities [14] where the sequential oxidation of ethylene to acetic acid is given sufficient time to occur. However, complete oxidation produces CO and CO_2.

This work seeks to address the nature of the active phase on the M1/M2 catalysts using a composition of $Mo_8V_2Nb_1R_{0.005}Te_{0.995}$, where R = Ti or Pd, to probe the effect of redox dopant on catalytic performance. The structure was resolved via a comprehensive *in-situ* Raman spectroscopy study and supplemented with *ex-situ* X-Ray Diffraction (XRD) to monitor the vibrational and crystallographic structure of the catalysts under operating conditions. The results of this show that the M-O-V bond with a Raman shift located at ~944 cm^{-1} was most influenced under operating conditions, suggesting this is the active vibrational phase. Furthermore, the catalytic performance of these materials shows the incorporation of Pd into the catalysts promotes the over-oxidation of ethane and Ti influences oxygen coordination, while the inclusion of Te results in phase segregation and increases selectivity to ethylene.

1.2 CO Oxidation over Stainless Steel Mesh

Due to the prevalence of health and environmental regulations, carbon monoxide (CO) emissions are commonly limited from stationary or mobile combustion sources [38] to improve air quality. The oxidation of CO from combustion exhaust can present some issues due to harsh process conditions, specifically high temperatures (greater than 500°C) in the presence of steam [39]. To reduce CO levels in combustion exhaust gas, catalytic oxidation over platinum and palladium-based washcoated catalysts are frequently

implemented [39]–[44]. Generally, these washcoats are composed of primarily γ-Al_2O_3 or similar metal oxides coated on a ceramic cordierite monolith to improve metal dispersion and catalyst adherence [39], [40], [44], [45].

Despite their ubiquitous nature in automotive catalytic converters, a substantial amount of engineering must be done to ensure washcoat adherence to the underlying monolith. Washcoats are commonly exposed to regular, rapid temperature increases and decreases observed during startup and shutdown of exhaust generating equipment, thus accelerating the rate of degradation in typical washcoat applications [46], [47]. For example, an approximate coefficient of thermal expansion for alumina is $1.3*10^{-5}$ 1/K, while cordierite is $0.44*10^{-6}$ 1/K [48], [49], representing a mismatch by a factor of nearly 30, which can lead to adhesion failure. The differences in expansion rates can result in the loss of the washcoat and the active precious metals used to treat CO emissions from poor adhesion to the monolith due to delamination and thermal shock [46], [50]–[55]. Additionally, washcoats can be susceptible to mechanical losses due to vibrations [46], [54], [56]. Due to the lack of a washcoat and pliability of stainless steel wire mesh, these monoliths can be easily knitted or formed into a variety of different shapes [57] such as pellets, sheets, tubes with tunable void fractions making these materials also useful for catalytically active filters [58] or mist eliminators and other applications [59]. Additionally, utilizing a metal mesh substrate has been shown to have better radial mixing, heat and mass transfer, reduced pressure drop, and higher mechanical strength than ceramic substrates [59]–[62]. Therefore, an attractive alternative to washcoating is to modify the surface of the monolith material to produce a surface capable of direct uptake of precious metals.

Anodic oxidation of a metallic monolith can produce a suitable monolith for exhaust applications due to increased surface roughness and surface structuring, such as pore development [63]. Platinum and/or palladium-based anodically oxidized stainless steel or alumina monolith-based catalysts have been studied previously. However, testing has mainly been confined to low-temperature volatile organic carbon oxidation [64]–[68], which does not examine the stability of these catalysts under harsher conditions, such as those seen in exhaust conditions [69]. To this end, this study examines these catalysts under simplified exhaust gas conditions, namely temperatures of 600°C and the presence of characteristic amounts of steam at 13.5 mole percent [70], [71] in addition to developing a more fundamental understanding of the effect of treatment parameters on the activity of the final produced catalyst. This work examines the roughening of stainless-steel wire mesh monoliths via anodic oxidation to form a suitable, washcoat free catalyst support. Ultrasonically assisted wet impregnation was selected as a synthesis methodology as it has been previously shown to produce bimetallic platinum/palladium catalysts [72]. To the best of the authors' knowledge, a systematic investigation of how various synthesis parameters influence the efficacy of anodically oxidized stainless-steel mesh-based catalysts has not been conducted.

The effects of how electrolyte acid weight loading, anodization voltage, and acid strength influence the anodic treatment and subsequent catalyst activity were systematically studied with an L9 Taguchi statistical design. This design was selected as it allows for rapid data collection while still enabling statistical analysis of each synthesis parameter's effect on the produced catalyst. A 3 level, 3 factor Taguchi L9 design was implemented with electrolytes of acetic (pKa_1=4.75), citric (pKa_1=3.13), and phosphoric

acid (pKa_1=2.16) [73] at voltages of 3, 5, and 7 V and electrolyte acid weight loadings of 5, 10, and 15 weight percent acid to determine the influence of each synthesis parameter on the catalytic CO oxidation activity of the platinum and palladium impregnated mesh. Acid identity was selected as a variable due to the complicated nature of its interactions with the stainless steel monolith. Due to increased ionization, increasing acid strength increases anodic current or voltage, which often leads to an increase in surface roughness [74], which reduces particle sintering and would increase activity at the conditions examined in this work [75]. However, previous work on anodically treated stainless steel monoliths has shown that increasing acid strength is not a direct predictor of activity as monoliths treated with weaker acids have previously been shown to form more active catalysts than those created with stronger acids [68], however, this has only been shown for low temperature volatile organic compound oxidation and warrants further study. In addition, electrolyte acid weight loading, which influences solution pH as well as anodic current, was selected as manipulating pH with the same acid in the electrolyte has been previously shown to affect anodic oxidation kinetics and surface composition [76]–[79]. Increasing applied voltage increases the anodization current and has also been shown to control volume expansion, pore diameter, and structure, as well as oxide layer thickness for alumina [80], [81]. However, an understanding of how these synthesis variables influence the performance of an anodically oxidized stainless steel mesh monolith is still lacking.

It should be noted here that this study only utilizes a simplified exhaust gas stream and only seeks to determine the effect of synthesis parameters on the hydrothermal stability and activity of the produced catalysts. In practice, combustion exhaust would contain a

variety of other components such as CO_2, NO_x, and unburnt hydrocarbons. These components would have a deleterious effect on CO oxidation activity [82]. This work seeks to establish basic relationships between synthesis parameters and catalyst activity, however knowledge of how these other gas components influence activity, as well as further optimization and sintering inhibition techniques, would be crucial for large-scale implementation of these types of catalysts.

1.3 Catalytic Biomass Torrefaction

With an ever-growing U.S. population, electricity demand continually increases [83]. Due to our reliance on fossil fuel energy sources, excess CO_2 has been released via combustion increasing atmospheric CO_2 concentration from 280 ppm at the start of the industrial revolution to over 400 ppm currently, surpassing the 300 ppm ceiling that has not been exceeded for the past approximately 800,000 years [84], [85]. As stated by The Intergovernmental Panel on Climate Change (IPCC), an organization endorsed by the U.N. in 1988, human influence has unequivocally led to climate change. To combat this change, renewable carbon-neutral energy sources must be rapidly developed to satisfy energy demand. Unfortunately, most of these sources are either location-dependent (geothermal, hydroelectric, wind, solar, tidal energy) or produce hazardous waste (nuclear). An attractive alternative is to utilize biomass-based energy sources as they reduce due to the rapid growth rate of conventionally utilized biomass [86] when compared to mined fossil fuels. Further, waste biomass such as farming residues, sawdust, fallen trees, and lawn waste is either openly burned, releasing CO_2 with no accompanying energy generation, or sent to landfills contributing to methane emissions. This results in not only overcrowding of landfills but as methane is a more powerful greenhouse gas than CO_2, this release also

directly contributes to climate change. Biomass based energy sources are a viable alternative but are difficult to transport due to high moisture content [87], poor processability due to tough cell walls and high molecular weight polymers [88], and have large differences in properties due to inhomogeneity [89]. To remedy these issues, biomass torrefaction can be carried out on fresh biomass to chemically alter it to impart better grindability, transportability, storage properties as well as increase the energy density and combustion properties. Biomass torrefaction is a mild pyrolysis process that is generally conducted between 200 - 300 °C [90]. This process results in a loss of volatile species and a decrease in the O/C ratio which results in materials with a higher energy density than the original biomass sample [91]. As an added benefit, the biomass becomes hydrophobic which results in better storage properties as the torrefied biomass does not uptake water to nearly the same extent as fresh biomass. This reduction in moisture content greatly slows the decomposition process [92]. Further, due to the nature of the long polymers in the cellular material of the biomass, grinding is an energy-intensive process. After torrefaction, the breakdown of a significant portion of these polymers results in a material much more amenable to grinding, driving down the cost of downstream cost and equipment wear and tear during pelletizing or powdering [93], [94].

Unfortunately, this process also produces large amounts of CO [95] as well as VOCs which create a toxic and polluting gas environment around torrefaction facilities unless the exhaust stream is treated. Fortunately, low-temperature WGS, typically catalyzed by a copper-based catalyst, is also active at these temperatures and serves as a way to both produce energy and to oxidize CO while producing H_2 which can be used either for heating, purified for other uses, or used for H_2 based selective catalytic reduction

of NO_x or SO_2 [96]–[98]. However, unlike traditional catalyst beds, it would be advantageous to mix the WGS catalyst with the biomass to eliminate the need for a heated catalyst section downstream of the torrefaction reactor and to ensure mild agitation of the bed to prevent condensation and accumulation of bio-oils in the bed. Mechanical mixing of the catalyst and biomass has been demonstrated previously [95], however, it is difficult to separate the biomass from the catalyst rapidly and inexpensively which limits its application on a larger than lab-scale implementation. One inexpensive and scalable way to implement this industrially is to utilize magnetic separation, but as Cu, Zn, and Al are essentially non-magnetic an additional magnetic metal must be added to the system to enable this form of separation. An inexpensive method to accomplish this, both for this catalyst system and essentially any other, is to embed a core of stainless steel mesh inside the catalyst pellet which enables magnetic separation without compromising catalytic activity and imparting extra mechanical strength to the pellet due to the presence of a reinforcing core. Therefore, embedding stainless steel in a Cu, Zn, Al catalyst can provide a robust, mechanically separable catalyst capable of reducing CO emissions while providing localized heating in the torrefaction reactor due to the exothermicity of the water gas shift reaction, and being easily retrievable/recyclable with an electromagnet.

Copper-based catalytic torrefaction catalysts were synthesized via two distinct methods, namely wet impregnation and co-precipitation depending on the desired properties for the final catalyst. Wet impregnation is useful for making catalysts with a relatively low loading of active metals (~20 wt%) while co-precipitation can produce catalysts with essentially any weight loading of active materials. However, in practice this method is generally used for high loadings of active metals materials with inert

dispersants/stabilizers tend to reduce the activity of the produced catalyst at high loadings. After impregnation on alumina, the wet impregnated pre-catalyst adopts a play-doh-like consistency that can be molded onto monolithic stainless steel supports and can form practically any shape of the finished product for niche applications. However, these catalysts are less active than co-precipitation-based catalysts, even when the activity is normalized for active metal content.

Currently, torrefaction utilizes burners to combust torrefaction off-gas, containing CO as well as VOCs, to provide energy to operate the drying unit, which is generally a very energy-intensive unit in a torrefaction facility. However, by operating a torrefaction facility in conjunction with a power plant, better heat integration can be utilized by using hot flue gas as a heating medium for both drying and torrefying the biomass. Therefore, this methodology utilizes an otherwise waste stream of low-value heat. This also has the advantage of producing and consuming the fuel on-site and avoiding transportation in between steps. Additionally, with locally sourced woody biomass, common in areas such as the southeastern United States, transportation costs can be greatly reduced for the entire process. Finally, biomass torrefaction is generally conducted in oxygen-free environments with nitrogen or another inert gas although torrefaction can also be conducted in low oxygen environments [95]. However, the separation of N_2 from air is a costly process and harms the economics of this process. Utilization of coal combustion flue gas provides a naturally low oxygen stream as oxygen is consumed during combustion of the fuel in the boiler and the flue gas is depleted in oxygen content. Therefore, utilization of coal combustion flue gas provides energy and a low oxygen gas stream from an otherwise waste

stream that would not be utilized. A summary of all catalytic processes, applications, and utilized catalysts is shown in Figure 1.1.

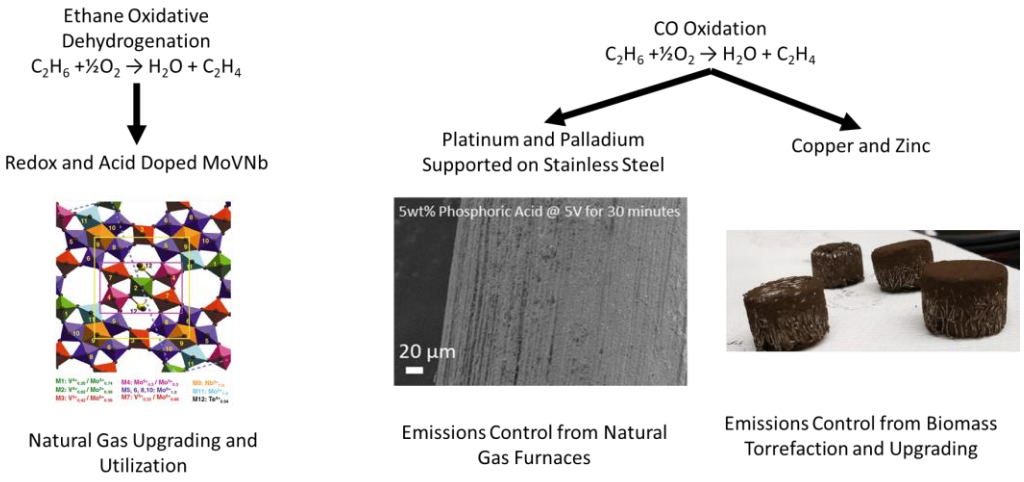

Figure 1.1 Summary of catalytic process discussed in this work (Utilizes a figure from [99]).

1.4 Atomic Layer Deposition

Atomic layer deposition (ALD) is a technique for growing conformal thin films in a highly controllable manner. However, to only have growth controlled via ALD-like behavior, care must be taken to ensure that proper experimental conditions are selected and that the reactor system work appropriately. One of the most important parameters is the substrate temperature utilized during coating. If too low of a temperature is selected, insufficient energy is available for the reaction and therefore the growth rate will be significantly inhibited. Further, at low temperatures precursors are capable of condensing either on the substrate or reactor walls which can greatly impact experimentally observed growth per cycle values. Conversely, too high of a substrate temperature can either increase or decrease growth rates by either transitioning to chemical vapor deposition (CVD) or by preventing adsorption of the precursor to the substrate surface respectively. Additionally,

proper dosing pressures and times are necessary to ensure that the sample is coated properly. This is especially important for samples with a high aspect ratio such as in the electronics industry. Care must also be taken to ensure that the first precursor has been sufficiently removed from the reactor system before introducing the second precursor. If the second precursor is not sufficiently removed, or non-ideal surface or gas-phase reactions will occur coating the substrate in a thicker than desired layer of film. Finally, reactor geometry and other equipment parameters can play a large role in regulating the performance of the ALD process so it is important to verify that a given reactor system will work properly with a verifiable process before extending to testing unknown chemistries and processes.

The primary aim of this work was to verify that the experimental system utilized at the Ludwigshafen BASF site was performing in a predictable and controllable way utilizing testing the system with a well-known and understood process, namely the trimethylaluminum (TMA)/water process. This process should display linear growth per cycle over a wide range of operating parameters, and it was desired to verify that samples coated in the reactor utilized here displayed linear growth rates comparable to previous literature. For ideal growth, film contamination levels should match that of literature and constant film stoichiometries should be observed once past initial growth. In addition, the work was extended to the titanium tetrachloride ($TiCl_4$)/water process after establishing that the trimethylaluminum/water process behaved ideally and that the reactor system was functioning as intended. However, the $TiCl_4$ process shows many non-ideal growth traits and some experimental observations do not agree with previous literature suggesting that changes to experimental conditions may need to be made to correct for this. Finally,

polymer substrates were utilized to determine how the second class of substrate behaved in the reactor system and to determine if chemical changes to the polymer were occurring.

CHAPTER 2

EXPERIMENTAL

2.1 Ethane Partial Oxidation

The catalysts utilized in this study were synthesized via a hydrothermal method described in further detail in a previous study conducted via this lab [14]. Dopants were added to the autoclaves before the addition of the base catalyst composition, in the form of stock solution of ammonium tetrachloropalladate (Sigma-Aldrich, St. Louis, MO, USA, 97%), titanium sulfate solution (Sigma-Aldrich, St. Louis, MO, USA, 99.9%), or telluric acid (Sigma-Aldrich, St. Louis, MO, USA, 98%).

Tellurium was selected as an acidic dopant due to its near-ubiquitous nature in most modern formulations of MoVNb type catalysts due to its ability to stabilize the catalyst, create new active sites [23], [31], [34], and increase oxygen mobility [34] which can influence the performance of Mars-Van-Krevelen mechanism-based reactions. Palladium was selected as a redox dopant due to its ability to control the reducibility of the catalyst [100], and further insight into this effect may shed light on how to design future generations of these catalysts. Finally, titanium was also selected as a redox dopant as it is a more novel dopant in this catalyst system and has been shown to affect the product distribution of this reaction, particularly at low space velocities [14].

Ethane partial oxidation experiments were conducted with a stoichiometric gas composition with an inert dilution of 2:1:3 (33.3% ethane, 16.6% oxygen, 50% helium). The product distribution was analyzed via the use of a Shimadzu Gas Chromatograph GC-2014 (Kyoto, Japan), equipped with a thermal conductivity detector (TCD). The reactor was constructed from a 316 stainless steel tube with a space velocity of 12,000 hr^{-1}. Catalyst bed temperature was measured using an OMEGA K-type thermocouple (Connecticut, USA).

Raman characterization was conducted with a Horiba X-Plora equipped with a 638 nm laser with a 0.3mW power output, a grating of 1200 gr/mm, and a thermoelectric-cooled CCD detector. In-situ experiments were conducted in a Linkham THMS600 stage (Epsom, England) with ethane partial oxidation experiments conducted using a gas feed of 2:1:3 ethane to oxygen to helium ratio (33.3% ethane, 16.6% oxygen, 50% helium) while inert and oxygen experiments were carried out under pure oxygen or helium. Analysis of the Raman spectra, including background subtraction and peak fitting were carried out on Fityk version 1.3.1.

Temperature programmed reduction (TPR) experiments were conducted on a Micromeritics AutoChem II 2920 (Georgia, USA) equipped with a TCD detector using a 10% H_2 in helium with a flow rate of 50 mL/min and a ramp rate of 5 °C/min. Quantification of hydrogen uptake was calculated via the use of an AgO calibration standard from Micromeritics (Georgia, USA).

X-Ray Diffraction (XRD) experiments were conducted via the use of a Rigaku Miniflex II (Tokyo, Japan) utilizing a Cu-Kα X-Ray source. Scans were conducted from 10-80° 2θ with a scan rate of 2° per minute and a step size of 0.02°.

2.2 Stainless Steel Based CO Oxidation Catalysts

Stainless steel CO oxidation catalysts were prepared by impregnating an etched metal mesh surface with catalytically active metals. This process began with degreasing the stainless steel mesh with acetone in an ultra-sonic cleaner until the acetone solution was no longer discolored with greases and oils contained on the mesh due to processing. An image of the oil removed during ultra-sonication is shown in Figure 2.1 where the beaker originally contained colorless acetone before sonication.

To form the wire mesh monoliths used in this study, 1 gram of a stainless steel alloy wire with ~0.2 mm diameter, CRAL 20-5 (Buck Enterprises, LLC), was formed into a pellet as shown in Figure 1a and degreased ultrasonically with acetone in four discrete steps to remove grease and oils present during material processing as shown in Figure 1b where the solution was originally colorless. After ultrasonic cleaning, the mesh disks were dried at 120°C for one hour before anodization. A Keithley 2231A-30-3 power supply was used to perform the anodic oxidations. Two-electrode electrochemical cells were constructed via a 150 mL beaker with a PTFE magnetic stir bar for convection, mesh disks as the working electrode, and a titanium metal sheet (McMaster Carr, 99% Purity) as the counter electrode. The electrolytes were 5, 10, and 15 wt % acetic acid, citric acid, or phosphoric acid in 18.2 MΩ*cm deionized water. The anodic oxidation treatments were conducted at constant voltage (3, 5, and 7 V) for 30 minutes. After anodization, the pellets were washed with deionized water (18.2 MΩ*cm) to remove excess acid and again dried at 120°C for one hour. The initial and final currents during anodic oxidation were recorded at each voltage for further analysis.

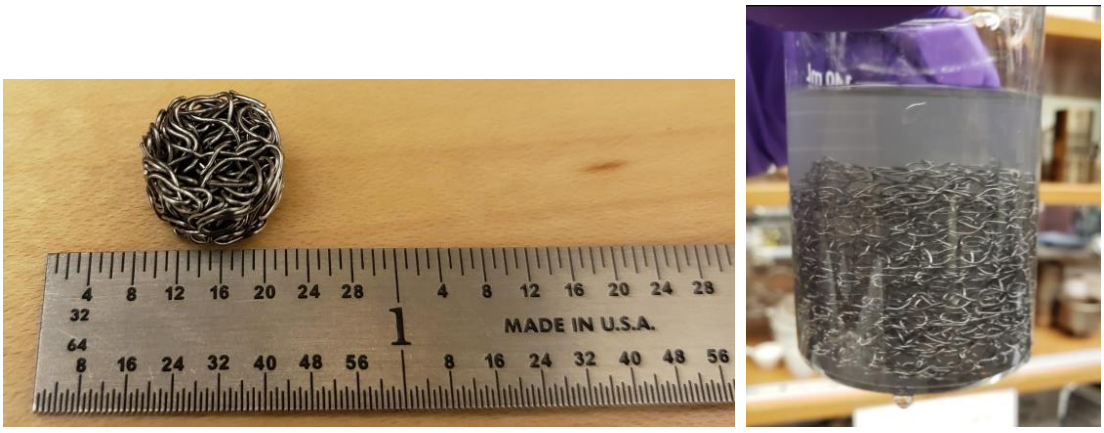

Figure 2.1. a) Stainless steel wire disk with a 1" ruler for scale and b) mesh during degreasing in acetone.

Ultrasonically assisted wet impregnation was used to synthesize Pt and Pd catalysts for CO oxidation. Tetraamine platinum (II) chloride hydrate (Sigma-Aldrich, 99.99%) and ammonium tetrachloropalladate (Sigma-Aldrich, 97%) were utilized as precious metal precursors and acetic acid (Sigma-Aldrich, ACS Reagent ≥99.7%), citric acid monohydrate (Fisher Scientific, Certified ACS Granular), and phosphoric acid (Alfa Aesar, 85% aqueous solution) were individually mixed with deionized water (18.2 MΩ*cm) and used as electrolytes. These precursors were used without further modification.

Catalysts with a total nominal precious metal weight loading of 0.15 wt% and a 1:1 Pt:Pd mass ratio were synthesized. Ultrasonically assisted wet impregnation was carried out for 3 hours using deionized water (18.2 MΩ*cm) as a solvent diluted to a total solution volume of 5 mL at a bath temperature of 50°C. After impregnation, catalysts were dried at 120°C for two hours and calcined at 800°C for 4 hours to produce the final catalyst. For comparison, a monolith that was not anodically treated was tested as control, denoted as "untreated catalyst." The untreated catalyst was handled and impregnated using the same procedure as the anodically treated catalysts.

Catalytic activity was analyzed with a Shimadzu Gas Chromatograph GC-2014, equipped with a thermal conductivity detector (TCD) using helium as a reference gas. The catalyst bed temperature was measured using a K-type thermocouple (OMEGA). For all experiments, 250 mg of catalytically active wire mesh was added to a 12.75 mm inner diameter quartz tube (Technical Glass Products) plug flow reactor with 3.5% CO, 4.5% O_2, 13.5% H_2O vapor, and balance Ar at temperatures between 250°C and 600°C and a space velocity of 24,000 mL/(g_{mesh}*hr). A schematic of the experimental setup is shown in Figure 2.2.

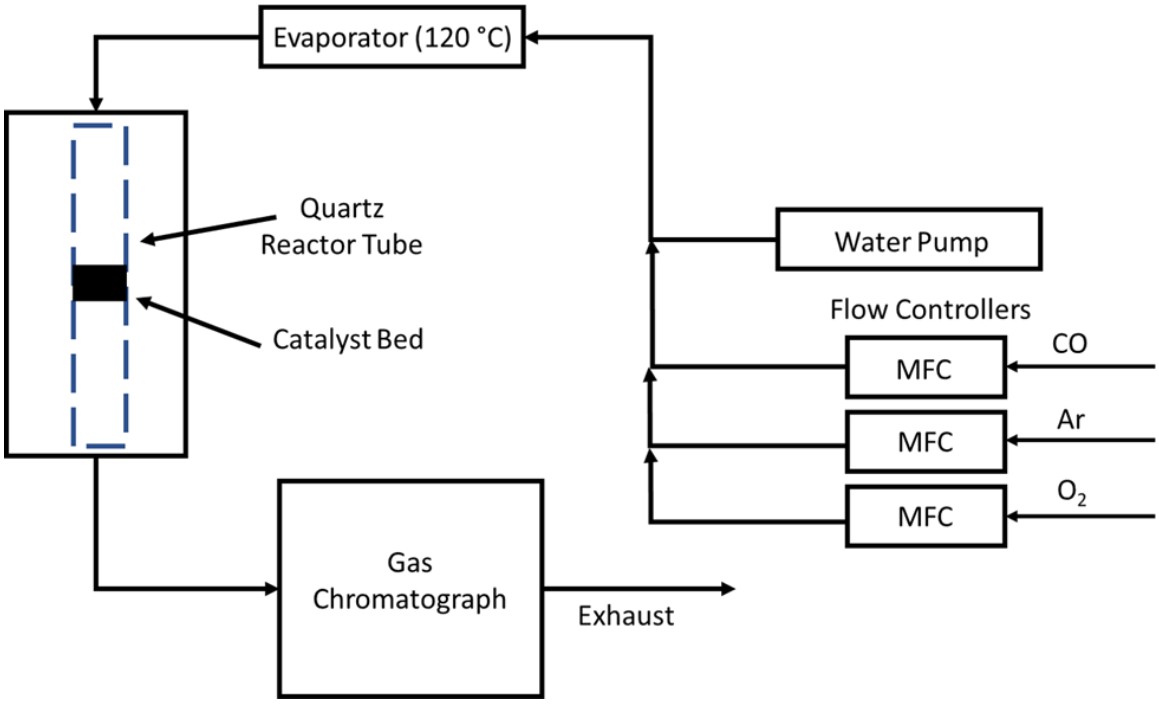

Figure 2.2. Experimental setup for catalytic evaluation of stainless steel wire mesh catalysts.

To rule out contributions from gas-phase reactions or reactions with the anodically oxidized metal meshes, baseline experiments on platinum and palladium-free meshes showed negligible activity below 700°C, as seen in Figure 2.3. To determine the experimental error, which is represented here as the standard error (standard deviation divided by the square root of the sample size of 3), the activity of the best performing catalyst was evaluated in triplicate. Carbon balances were closed within 5% and multiple data points were taken for each temperature to ensure consistency and reproducibility within the experiment.

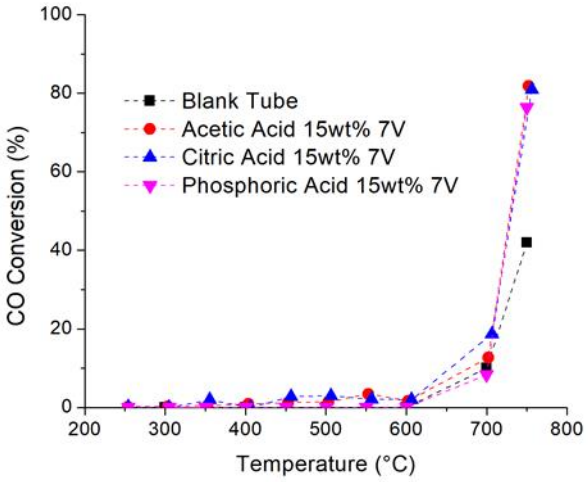

Figure 2.3. Catalytic activity of anodically treated catalyst-free wire meshes.

An L9 Taguchi design of experiments was created and analyzed via Minitab. The main effects plot was generated by Minitab by calculating the mean CO conversion of each variable and comparing it to the mean of the other variables as well as the mean of all variables (mean of means) This design has been previously been utilized to determine important factors influencing catalyst performance while requiring a small dataset [101]. Catalysts were tested in a random order as generated by Minitab during the creation of the design space. A visualization of the design space is shown in Figure 2.4.

The metal loading for each catalyst was determined via inductively coupled plasma – optical emission spectroscopy (ICP-OES) using an Avio 200 (Perkin Elmer) equipped with an S10 autosampler. Before analysis, analytes were digested in freshly prepared aqua regia overnight at 120°C before analysis for Pt (265.945 nm), Pd (340.458 nm), Cr (276.654 nm), and Fe (258.204 nm). Electron microscopy was conducted on a Gemini 500 Field Emission Scanning Electron Microscope (Zeiss) at 5 keV with a working distance of 7 mm.

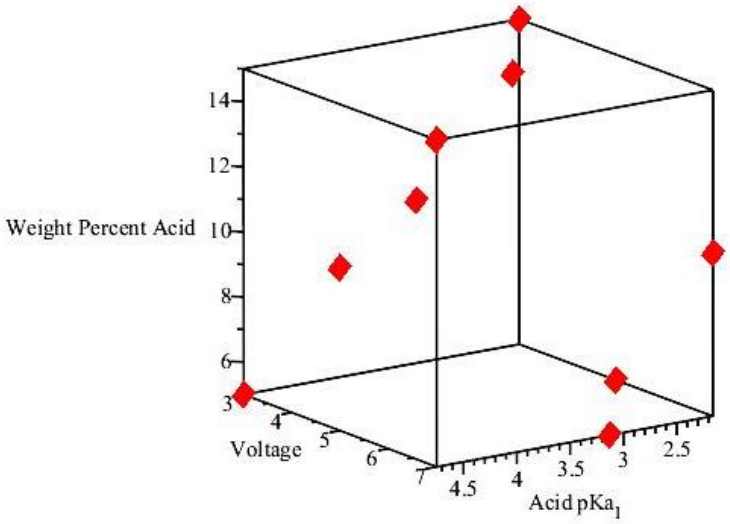

Figure 2.4. Experimental design space for the Taguchi Design of Experiments.

2.3 Catalytic Biomass Torrefaction

Depending on the desired final properties of the catalyst, there are two routes to synthesize suitable biomass torrefaction catalysts. The first class of catalysts is synthesized via a wet-impregnation route in which zinc nitrate hexahydrate (Sigma-Aldrich, St. Louis, MO, USA,) and copper nitrate trihydrate (Sigma-Aldrich, St. Louis, MO, USA,) and dissolved in deionized water until completely solvated and then added to dry gamma-alumina powder (Sasol Catalox SBA-150) which was previously calcined at 600°C for 3 hours as shown in Figure 2.5. This mixture is then stirred at 120°C until the copper impregnated alumina powder obtains a consistency similar to play-doh. At this point, the catalyst is formed around previously cut and shaped stainless steel meshes in the desired shape and size. Finally, the composite catalyst is dried at 120°C for 12 hours and then calcined at 450°C for 3 hours.

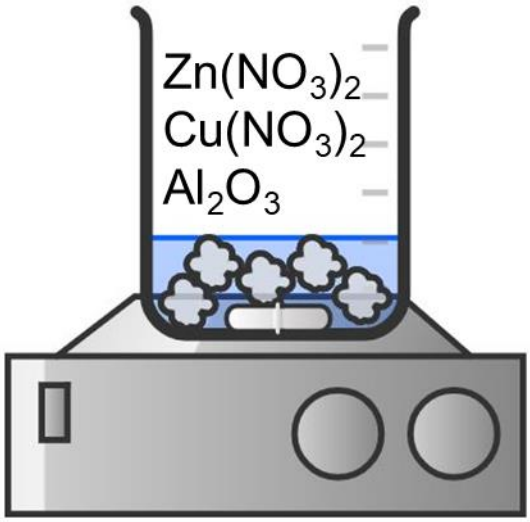

Figure 2.5. Preparation of wet impregnated catalysts.

To produce the second class of catalyst, two separate solutions are first prepared. The first solution contains copper, zinc, and aluminum in the forms of copper nitrate trihydrate (Sigma-Aldrich, St. Louis, MO, USA,), zinc nitrate hexahydrate (Sigma-Aldrich, St. Louis, MO, USA,), and aluminum nitrate nonahydrate (Sigma-Aldrich, St. Louis, MO, USA,) respectively dissolved in deionized water and is added to a 3-armed round bottom flask connected to a condenser column. The two other arms are capped with a septum and a nitrogen atmosphere is introduced via a constant flow of nitrogen through a needle. The flask is then placed in an oil bath to maintain a temperature of 80°C throughout the synthesis process with constant stirring. Alternatively, the catalyst can be produced under an air environment without heating which allows the synthesis to be conducted without the need for a condenser. After reaching the required temperature, the second solution, sodium carbonate (Sigma-Aldrich) dissolved in deionized water is added at a rate of 1 mL/min via a syringe pump as shown in Figure 2.6. After all of the precipitating solution has been added, the flask is removed from heat and stirring and

allowed to age for 2 hours. After aging, the catalyst is removed from the flask and filtered to isolate the solid and then dried and calcined at 120°C for 12 hours and then calcined at 450°C for 3 hours. After calcining, the produced powder is added to a hydraulic die press with or without a stainless steel mesh core and pressed with sufficient force to form a solid pellet.

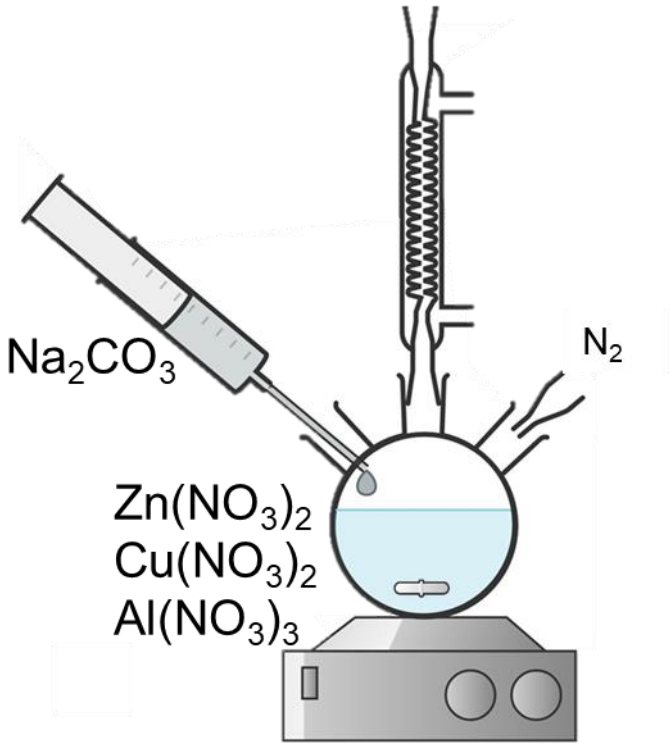

Figure 2.6. Preparation of co-precipitated catalysts.

All biomass-free catalytic testing was conducted with quartz tube reactors to minimize catalytic contributions from the reactor walls and thorough blank tube and blank stainless steel mesh testing were conducted before experiments were conducted to verify that the stainless steel itself was not catalytically active at the temperatures examined in this work. Except where otherwise noted, biomass-free catalytic testing was carried out

utilizing 100mg of catalyst with 100 mL/min of total gas flow with 13.5% H_2O, 3.5% CO, and 2%O_2 (when O_2 was used).

Physical stability of mesh free and mesh containing catalyst pellets was determined via adding 25 g of pellets (5, 5g pellets) to a rubber drum containing 100 ¼" stainless steel ball bearings and tumbled at approximately 37 rpm to simulate physical abrasion and would be encountered inside when biomass and catalysts pellets are mixed within a reactor system. Mesh was added to the core of the pellets as opposed to as a sheath in this case.

Analysis of torrefaction effluent gas was accomplished utilizing a home built mass spectrometer system, shown in Figure 2.7, consisting of a vacuum chamber equipped with an adjustable leak valve (top) capable of admitting a controllable amount of analyte gas from the process, an atmospheric to UHV pressure gauge (bottom), and a Stanford Research Systems 200 atomic mass unit residual gas analyzer (right). The residual gas analyzer was equipped with an electron multiplier to increase sensitivity and decrease signal noise. The system was pumped by a Varian or Leybold turbomolecular pump (left) backed by a Varian oil-sealed rotary vane pump and was generally maintained at $1x10^{-8}$ torr base pressure. A desk fan was utilized to cool the turbomolecular pump and heat tape was wrapped around the chamber to enable regular bakeouts of the system. Analysis of CO in a nitrogen environment was accomplished by quantifying all contributions to the peaks at m/z=28 and m/z=14 and calculating the concentration of CO by determining the amount of m/z=28 that corresponded to nitrogen by examining the ratio of m/z=28/(m/z=14) which was determined experimentally.

Before the leak valve, a stainless steel orifice plate (Lenox Laser) with a hole diameter of 50-150 μm was placed in a Swagelok VCR fitting to obtain a slip stream of analyte gas from the system exhaust. This portion of the gas line downstream of the VCR fitting and upstream of the leak valve was pumped via another oil-sealed rotary vane pump

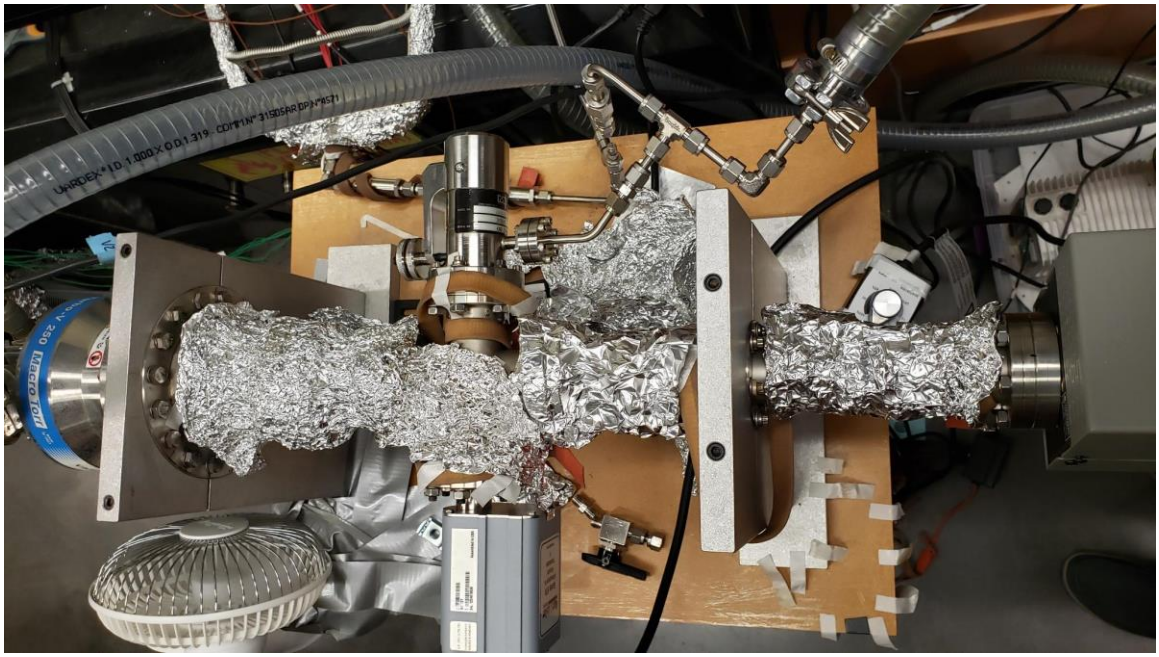

Figure 2.7. Homemade mass spectrometer system.

to continuously remove gas from the analytical lines to ensure a quick response time inside the mass spectrometer system. Further, the inlet line upstream of the orifice plate was 1/16" OD tubing fit through a bored-through fitting to enable the end of the 1/16" tubing to sample from the middle of the exhaust line to reduce the response time of the mass spectrometer to changing gas compositions. Without the differential pumping accomplished using the second rotary vane pump and bored-through fitting, the original response time of this system was substantially higher and would not be feasible for the time scales examined here for torrefaction. Additionally, small amounts of bio-oil passed

through the condenser system or organics in the gas phase polymerized within the heated exhaust system resulting in occasional plugging in particulate filters or the orifice upstream of the mass spectrometer. To alleviate this, the filter system was cleaned at least weekly. This was accomplished by one of two methods, first, the filter could be filled with acetone or another solvent and then blown out with compressed air. Secondly, the filter could be placed in a solvent like acetone in an ultrasonic bath with the solvent changed regularly until it stopped changing color upon sonication with the filter. The experimental setup occasionally developed plugs immediately downstream of the torrefaction reactor due to the presence of entrained pieces of biomass and heated bio-oils forming an extremely hard material that was not easily physically dislodged. It was, therefore, crucial to monitor the pressure at the inlet of the reactor system to ensure that plugs had not developed. If the pressure rose during experimentation, the experiments were halted for the day, and the system was allowed to cool before repairs took place.

Experiments concerning the injection of bio-oil without the presence of biomass were accomplished via pumping bio-oil into the reactor system alongside water before the vaporization section of the reactor system. Pumping was accomplished using a disposable 50 mL syringe on a New Era NE-4000 syringe pump. A Luer-lock to compression fitting adapter was utilized to allow the syringe to pump directly into the system utilizing 1/16” stainless steel tubing.

Future work involving testing on-site at Santee Cooper’s Cross Generating Station will utilize a pilot-scale unit built with collaborators at Buck Enterprises and shown in Figure 2.8. This unit consists of a custom-fabricated heated box containing two pipes, one with a by-pass section and one containing a reactor section. The reactor section has four

ports with custom fabricated biomass holders capable of holding over 100g of biomass each with K-type thermocouples mounted in the center of these baskets to monitor the temperature of the biomass during torrefaction. An additional thermocouple was mounted in the heated pipe before and after the biomass baskets to monitor upstream and downstream temperatures. The system was also equipped with a bio-oil draining section with an interlock to allow draining when operating without venting the entire reactor. The system also has a pressure relief valve to enable safe venting if pressures increase to unsafe levels. The majority of the piping in the setup is 2” NPT and high-temperature graphite or molybdenum threat sealants were used. All valves and other hardware were rated to at least 350°C to handle the process conditions with simulated flue gas.

Figure 2.8. Pilot biomass torrefaction unit to be tested on-site at Cross Generating Station.

X-Ray Diffraction (XRD) experiments were conducted via the use of a Rigaku Miniflex II (Tokyo, Japan) utilizing a Cu-Kα X-Ray source. Scans were conducted from 10-80° 2θ with a scan rate of 2° per minute and a step size of 0.02°.

Trace metal content of power plant flue gas exposed catalyst were determined via X-Ray Fluorescence spectroscopy utilizing a Fischerscope XDAL with a 0.3mm collimator using a 60 second acquisition time with samples in pellet form.

Gas Chromatography-Mass Spectrometry (CG-MS) experiments were conducted with a Shimadzu GC-2010 with a mass spectrometer detector (Kyoto, Japan). Analytes were separated with an RTX-1701 column and mass spectrometry cracking patterns were analyzed by comparison to the NIST database. The column had a thickness of 1μm, diameter of 0.32 mm, length of 30 m and the column was held isothermally at 40°C for 4 minutes before ramping at 5°C/min to 220°C and holding at 220°C for 5 minutes. The column oven was then cooled in preparation for an additional injection.

Nuclear magnetic resonance (NMR) experiments (examining ^{1}H) were conducted utilizing a Bruker Advance III-HD 300 MHz utilizing deuterated chloroform ($CDCl_3$) as a solvent to dilute the sample to 20 mg/mL of solvent for analysis.

Higher heating values (HHV) for biomass samples were determined via thermogravimetric analysis (TGA) [102] coupled with a fit equation determined in previous literature [103]. TGA was conducted utilizing Argon at a flow rate of 100 mL/min with a ramp of 10°C/min from room temperature to 105°C where the biomass was dried for 80 minutes. After drying, the temperature was ramped at 15°C/min to 700°C where it was held for 50 minutes to remove volatile species. After the first 30 minutes of the hold

at 700°C, the gas environment was changed to air to burn off fixed carbon and leave behind the remaining ash. Finally, heating stopped and was allowed to return to room temperature before loading an additional sample. HHVs were calculated using the fit equation determined in previous work [103] where the composition of biomass on a dry basis (after removal of moisture) was utilized to determine the HHV. An example of the TGA data is shown in Figure 2.9

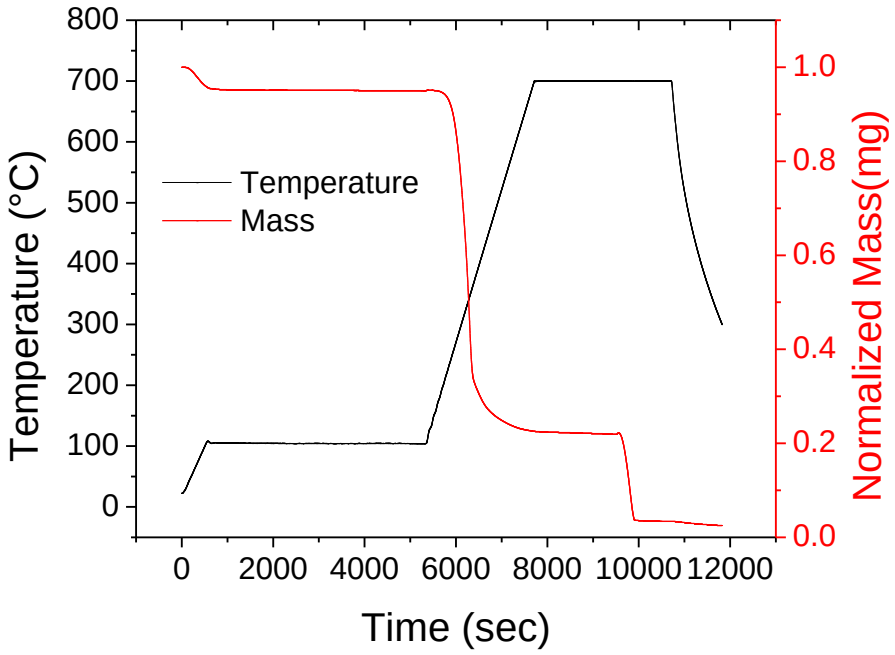

Figure 2.9. Example TGA data for raw biomass

Finally, polymers reinforced with torrefied biomass were produced by first grinding biomass pellets torrefied at 300°C for 30 minutes with 2% O_2, 12% CO_2, 13.5% H_2O, balance N_2 in a coffee grinder twice to produce a homogenous powder that can be mixed with the other components of the polymer material. For these experiments, corn starch was utilized as a model thermoplastic component, but any plant-derived polymer can be utilized such as potato starch, wood starch, or polylactic acid (PLA) from starch fermentation can

also be utilized. Alternatively recycled conventional plastics could also be utilized. At this point, the corn starch was physically mixed with the torrefied biomass and added to deionized water along with the plasticizer and acetic acid then heated at 120°C with stirring until enough water had evaporated to form a thick slurry that was poured into a mold and dried in an oven at 120°C or under direct sunlight until dry. At this point, the polymer was ready for usage. Plasticizers included polyethylene glycol (PEG) 8,000, polypropylene glycol (PPG) 425, ethylene glycol, and glycerin, and a high degree in variation of physical properties was noted for each of these plasticizers.

2.4 Atomic Layer Deposition

An in-house built atomic layer deposition reactor system shown in Figure 2.10 was utilized for depositing films of Al_2O_3 and TiO_2 on TiN, Cu, and SiO_2 wafers as well as polyamide (Nylon 6,6), polypropylene (PP), and low-density polyethylene (LDPE) sheets. These wafers were obtained by breaking off pieces from a single larger wafer, ensuring that the wafers were consistent from sample to sample. Before testing, these samples were cleaned utilizing a three-step process in which the wafers were sonicated first in acetone, then isopropanol, and finally deionized water in discrete 5-minute steps with a drying step utilizing a nitrogen gun in between each step. After ultrasonic cleaning, samples were loaded onto a 1” sample holder and introduced into the vacuum system and transferred into the ALD reactor by means of vacuum transfer manipulators. All polymers were cut from large sheets from Goodfellow. After coating, these samples were analyzed by a PHI Model 5000 XPS system attached to the ALD reactor without breaking vacuum, ensuring that the samples were not contaminated via exposure to air. For ALD experiments deionized water was obtained from an in-house Merck Milli-Q Advantage A10 system. All precursors were

degassed while attached to the system by means of seven freeze-pump-thaw cycles to ensure constant dosing of precursor and to prevent contamination during all experiments. After switching back to a previously freeze-pump-thawed precursor, only 3 cycles were utilized if the system rapidly pumped down indicating a lack of gas contamination in the container. All precursors were added into the dosing vessels and manipulated within a glovebox (<0.1 ppm oxygen and water) to prevent reactions with water or oxygen. The vessels were directly attached to the reactor system and all connections were thoroughly pumped before opening valves exposing the precursor to the system to prevent reactions with residual air or water in the fittings. Due to the vapor pressure of the precursors utilized in this work, external heating of the precursor vessels was not required, and the vessels were maintained at room temperature for all experiments. Ultrasonic cleaning in isopropanol was also utilized to clean the filament of the vacuum gauge used in these experiments.

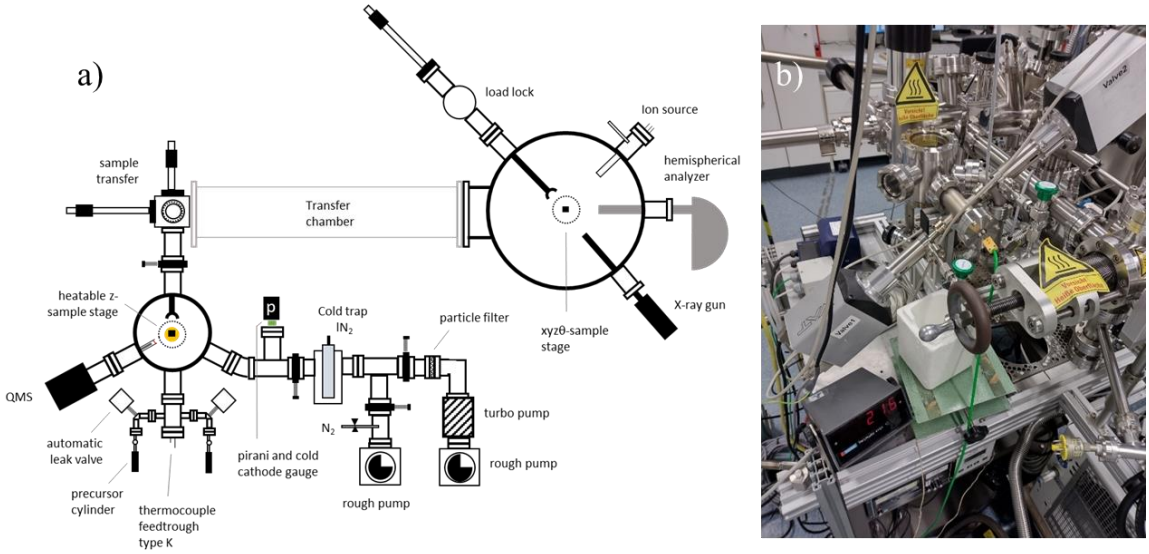

Figure 2.10. a) Schematic and b) photograph of the ALD reactor system.

The ALD reactor system in this work consisted of a cold-walled stainless-steel cylindrical reactor equipped with windows for observation of the sample loading and unloading process. The reactor also has a flange capable of accommodating a mass spectrometer to leak check the system, monitor dosing, and examine reaction products during the ALD process. However, this system was not present for this work and leak checks were accomplished by spraying flanges with acetone or isopropanol and monitoring pressure spikes within the system. If a large pressure spike was observed, liquid acetone or isopropanol was entering the system and vaporizing causing a large change in pressure. However, this method is only capable of finding large leaks and is not as sensitive as utilizing helium with a mass spectrometer. However, as the system readily pumped down below the base experimental pressure, this method was sufficient. The reactor system was pumped via two mechanical backing pumps and one turbomolecular pump. To prevent damage to the turbomolecular pump via precursor materials (particularly chlorides) a cold trap chilled by liquid nitrogen was utilized. This trap was then subsequently pumped via the second mechanical pump as it warmed and reached room temperature overnight allowing evacuation of un-reacted precursor or reaction byproducts while the turbomolecular pump was isolated to prevent damage. Sample heating was accomplished using a controllable heater capable of reaching ~200°C although all substrates were maintained at 120°C in this work (or 45°C for polymer substrates). Table 2.1 displays detailed experimental parameters for ALD experiments. For all experiments, dosing was accomplished by first dosing precursor from valve 1 to the desired pressure for 30 seconds followed by pumping the system down to base pressure before dosing the precursor from valve 2. After pumping the system down after dosing the second precursor, this process

was repeated for the desired number of dosing cycles. It is crucial to ensure that all unreacted precursor is removed before dosing the second reagent to ensure only ALD like growth is occurring. Additionally, the sample holder could accommodate multiple substrates, so in general SiO_2, Cu, and TiN substrates were coated at the same time for each experimental set. For polymer samples, polyamide, polypropylene, and low-density polyethylene were all coated simultaneously as well.

For experiments utilizing polymers as substrates, all experimental parameters were identical to those for wafer-based substrates except for substrate temperature. For polymer substrates, 45°C was used at higher temperatures, the pressure in the chamber exceeded the required experimental base pressure at temperatures as low as 60°C due to the higher volatility and therefore vapor pressure of the polymer substrates in comparison to the wafer-based substrates. XPS spectra for polymer samples were compared to reference spectra compiled by Briggs [104]. For all cases, the untreated polymer corresponded well with the reference spectra. Oxygen XPS for Nylon 6,6 were fitted according to parameters determined by Peng et.al [105].

Table 2.1. Experimental setpoints and parameters for the ALD Process.

ALD Process Parameter	**Experimental Setpoint**
Substrate Temperature	120°C or 45°C*
Dosing Pressure – Valve 1	$1*10^{-4}$ mbar
Dosing Time – Valve 1	30 seconds
Reactant 1	$TiCl_4$ or TMA
Dosing Pressure – Valve 2	$1*10^{-4}$ mbar
Dosing Time – Valve 2	30 seconds
Reactant 2	DI Water
Experimental Base Pressure	$5*10^{-6}$ mbar
Number of ALD Cycles	25, 50, 100, or 200

* for polymer substrates only

Deposited film thicknesses were determined via multiple routes to ensure accuracy. First, film thicknesses were estimated via XPS utilizing the thickogram method with spectra deconvoluted and fitted via CASA XPS. In addition to the obtained XPS spectra and relative sensitivity coefficients, this method also requires knowledge of the deposited film density to determine the photoelectron escape depth of the substrate material. As this information was not determined for these films, this method cannot determine the absolute thickness of the film but can provide useful information about the relative thickness of the film as a function of deposition cycles by assuming a constant film thickness. In this case, the value utilized was the escape depth of the film as a bulk material obtained from literature that was based on a NIST database. In this way, this method is useful for verifying that the growth per deposition cycle is linear and providing a check for the other methodologies. In addition, this method cannot estimate film thicknesses for films thicker than the sampling depth of XPS (~ 10nm) and therefore was only suitable for a subset of the films produced in this work. It is also important to note that this method determines film thickness graphically, so some error is introduced during the plotting and reading of data from a thickogram plot. Raw data used for the construction of the thickogram analysis are presented in Figures 2.11 (TMA/water) and 2.12 ($TiCl_4$/water) with a representative thickogram (for TMA/water) is shown in Figure 2.13.

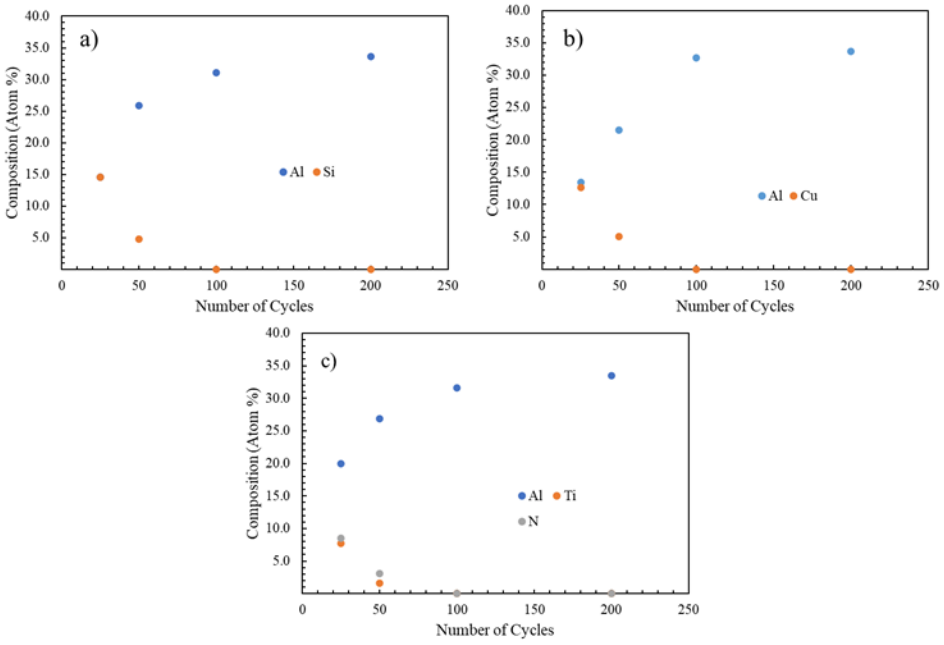

Figure 2.11. Atomic concentration of overlayer and substrate as a function of number of TMA/Water ALD cycles for a) SiO_2, b) Cu, and c) TiN.

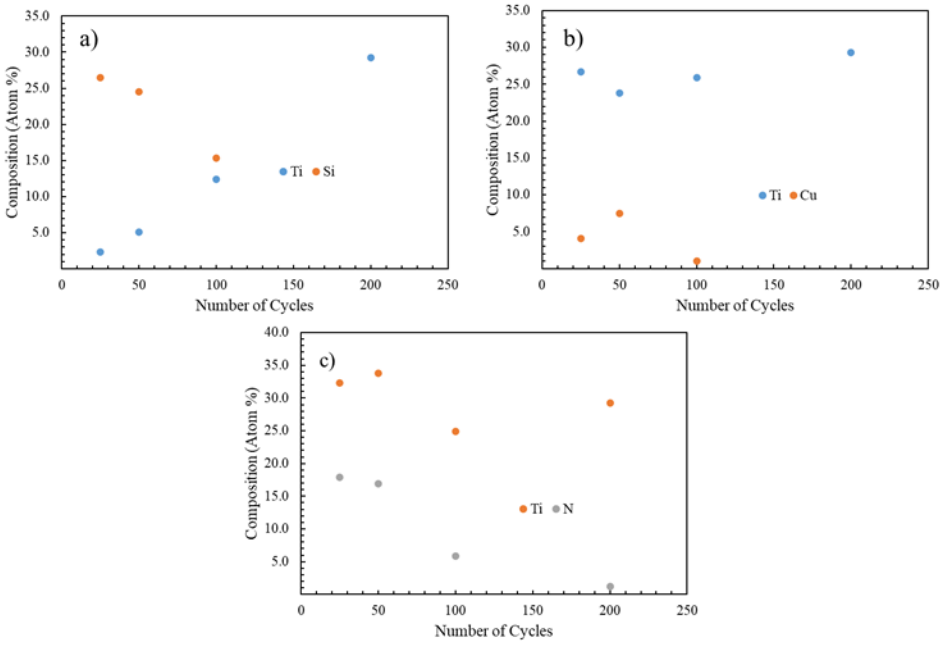

Figure 2.12. Atomic concentration of overlayer and substrate as a function of number of $TiCl_4$/Water ALD cycles for a) SiO_2, b) Cu, and c) TiN.

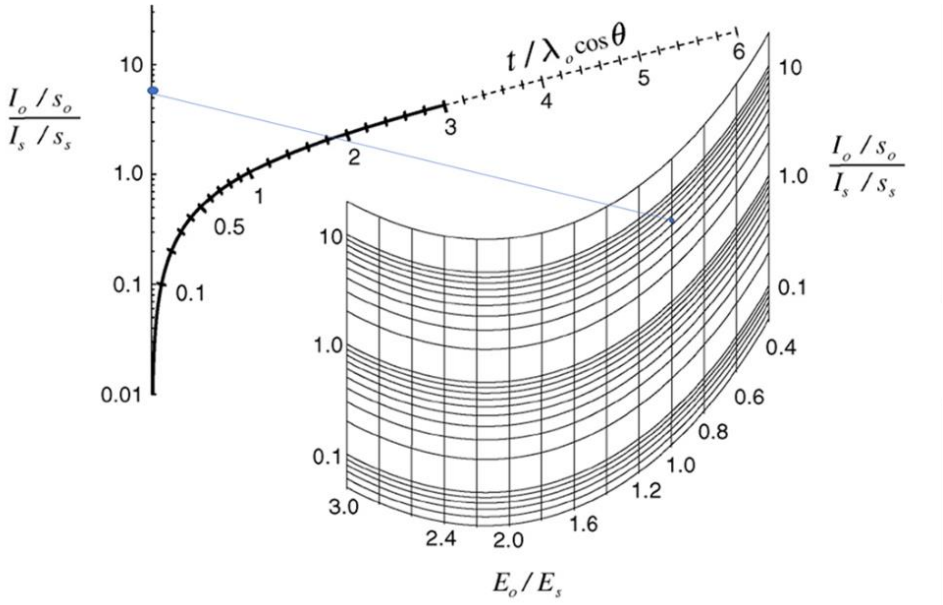

Figure 2.13. Representative thickogram plot for 25 cycles of TMA/Water deposited on a SiO_2 substrate.

Secondly, ellipsometry was utilized to determine film thickness. For the TMA/water process, screenshots of the fitting parameters and experimental fits are shown in Figure 2.14. In general, experimental data agreed well with fit equations.

Finally, a combination of time-of-flight secondary ion mass spectrometry (TOF-SIMS) and contact profilometry was utilized to sputter through the deposited film and then measure the depth of sputtered crater with multiple craters on each sample. Error for this method was determined by utilizing multiple sputtered craters as well as three separate measurements across both sides of the crater. Scanning electron microscopy (SEM) and Energy Dispersive X-Ray (EDX) images were obtained on a Phenom Pro X. It should be noted here that the films deposited in this work were homogenously deposited and were able to coat parts of the wafers that were covered with the 1-inch vacuum sample holder used in this work shown in Figure 2.15.

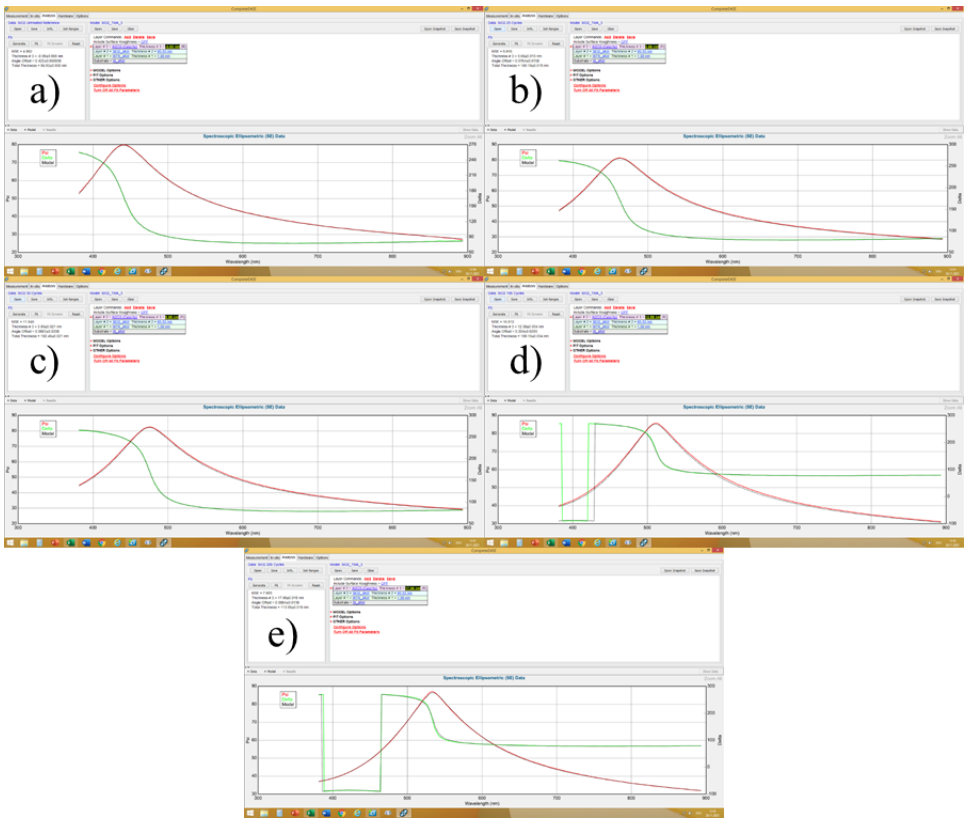

Figure 2.14. Screenshots of ellipsometer fitting for substrates coated using the TMA/water process, a) untreated reference, b) 25 cycles, c) 50 cycles, d) 100 cycles, and e) 200 cycles.

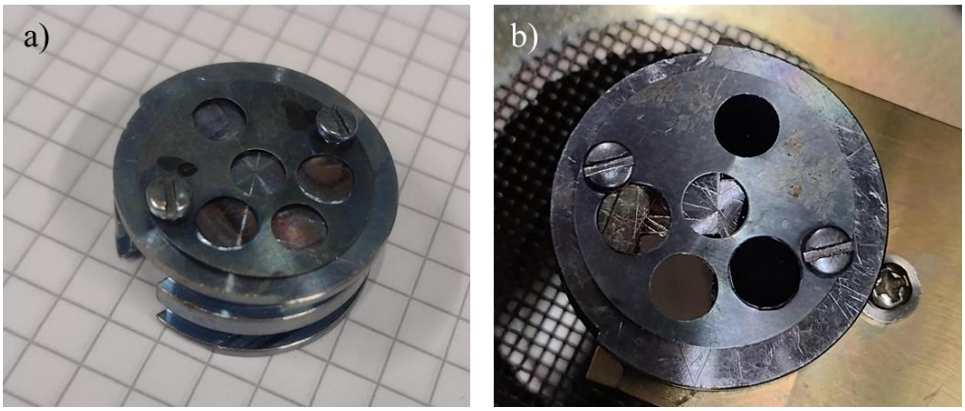

Figure 2.15. Photograph of the 1-inch sample holder utilized in this work with a) no samples loaded onto the holder and b) with Cu, SiO_2, and TiN substrates loaded onto the sample holder.

Examples of the good conformal coating are shown in Figures 2.16-2.18 for 100 TMA/water ALD cycles on SiO_2, Cu, and TiN respectively. For all images, similar results were obtained regardless of what portion of the sample was analyzed. It should also be noted here that Si is present as the largest component for all wafers, even for Cu and TiN. The reason for this is that all wafers are Si-based and Cu and TiN wafers have a coating of Cu and TiN respectively on top of Si. Due to the deeper sampling depth of EDX when compared to XPS, the underlying substrate can be detected.

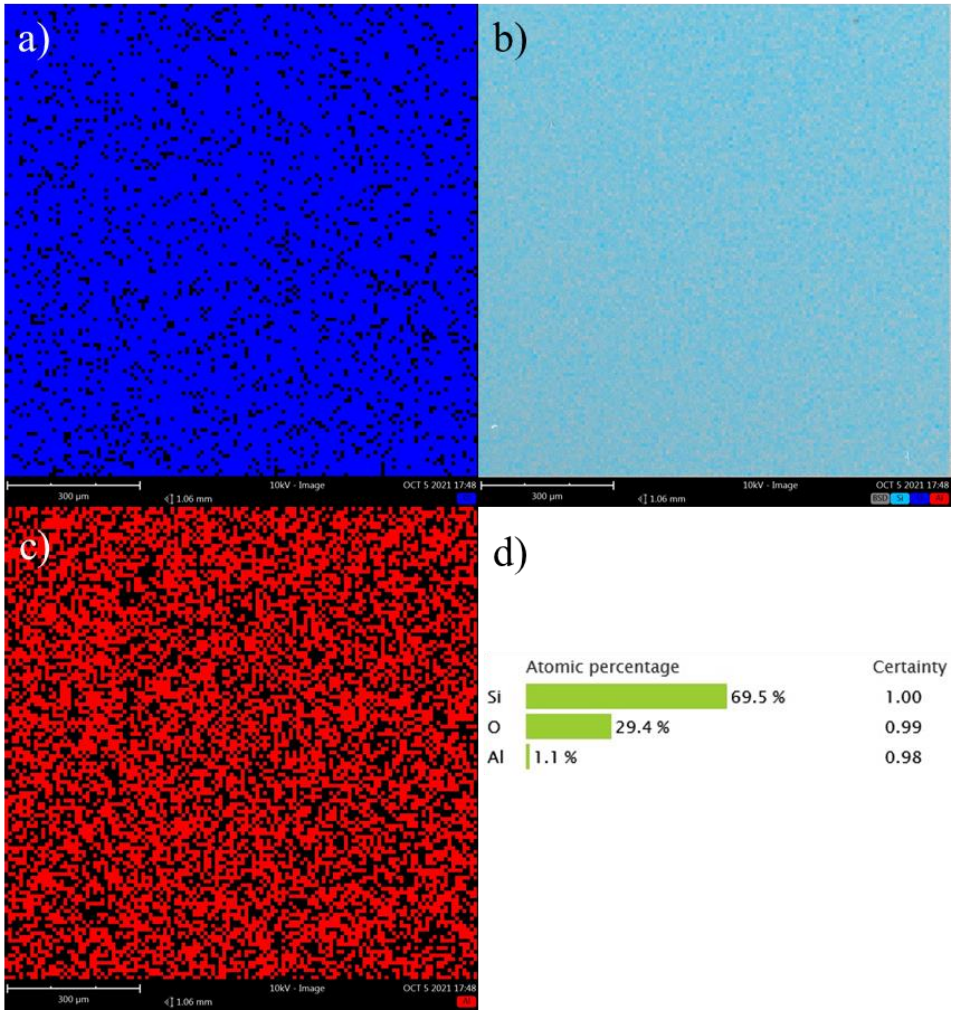

Figure 2.16. SEM/EDX mapping images for 100 TMA/Water ALD cycles on a SiO_2 substrate of a) O, b) all elements, c) Al, and d) overall composition of the material.

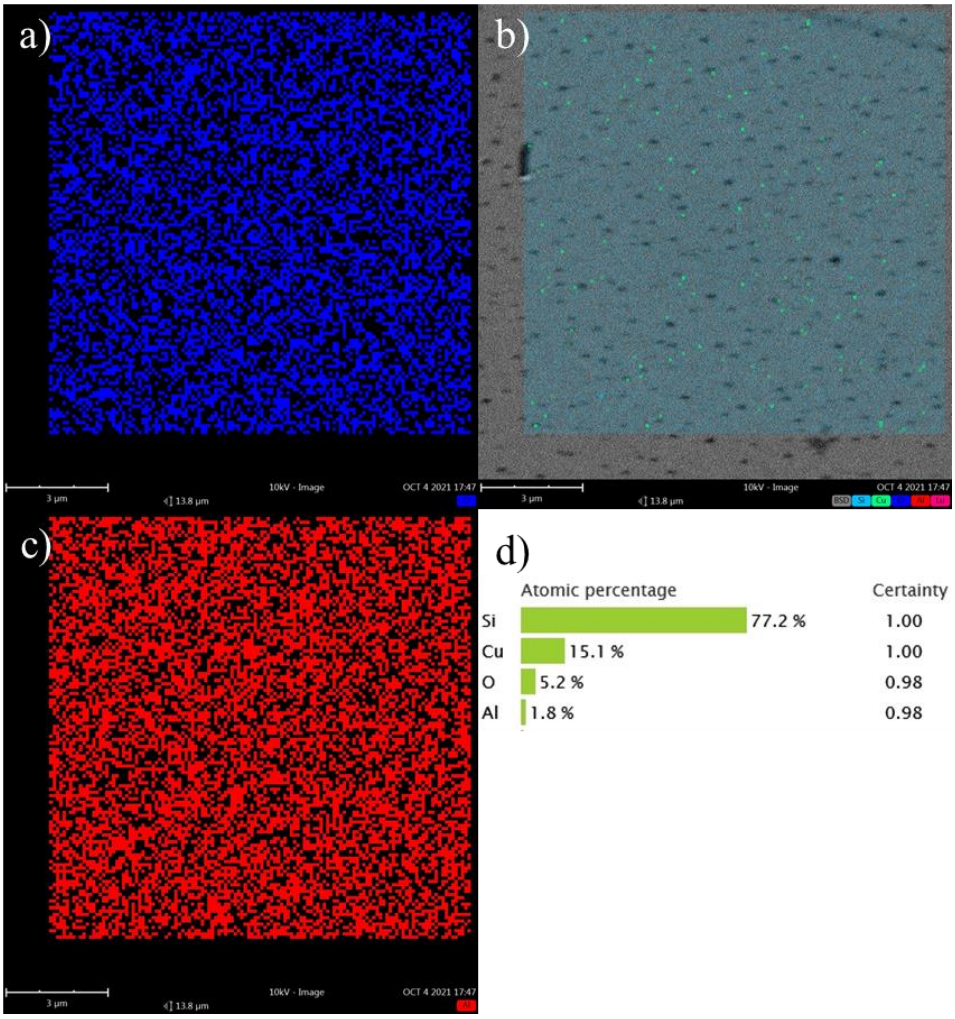

Figure 2.17. SEM/EDX mapping images for 100 TMA/Water ALD cycles on a Cu substrate of a) O, b) all elements, c) Al, and d) overall composition of the material.

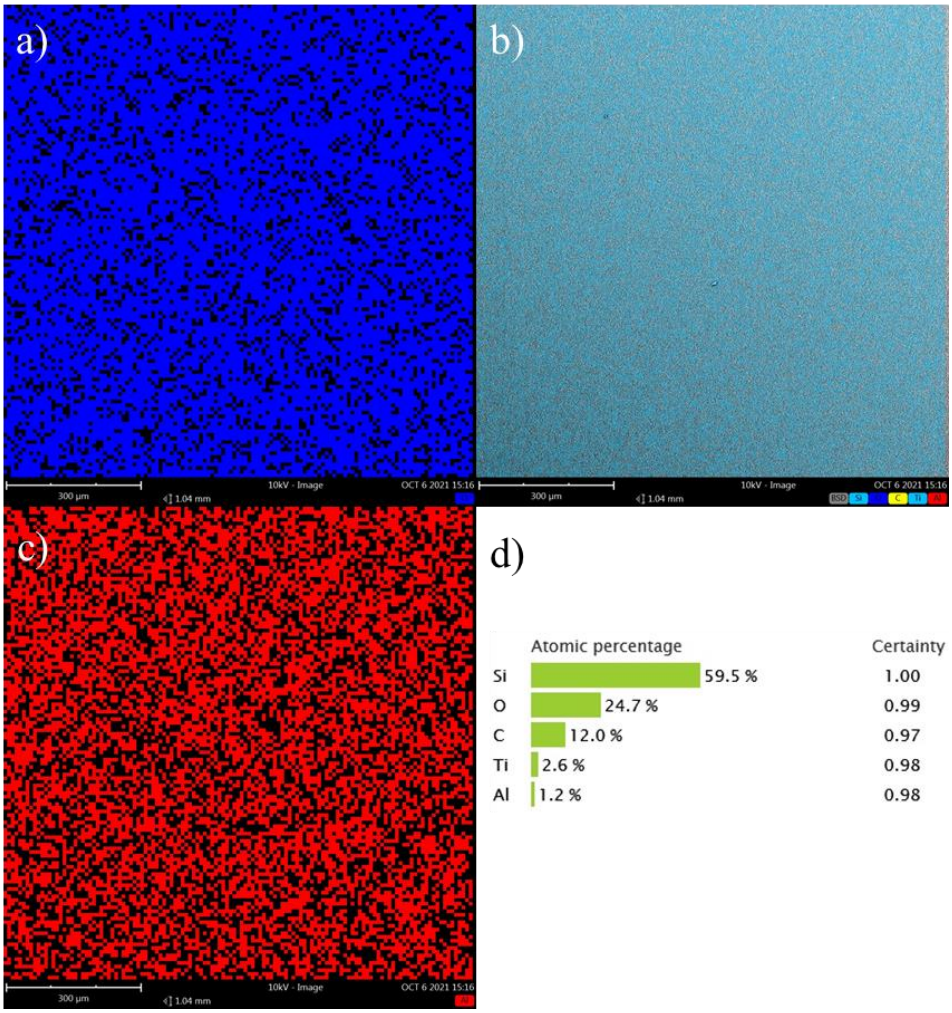

Figure 2.18. SEM/EDX mapping images for 100 TMA/water ALD cycles on a TiN substrate of a) O, b) all elements, c) Al, and d) overall composition of the material.

In general, composition of the deposited film and substrate (and therefore relative thickness from the thickogram method) was readily accomplished with simple peak quantification of the entire region of the film and substrate (Ti2p and Cu2p respectively for example). However, in two cases, detailed deconvolution and peak fitting was required for Al_2O_3 films on Cu due to overlap between Al 2p and Cu 2p and TiO_2 films on TiN due to both being Ti species. Examples of the fitted spectra for these two examples are shown below in Figures 2.19 and 2.20. Carbon spectra of polymer samples were fitted according

to Briggs [104] and are shown in detail with characteristic binding energies, area percent, and peak identifications based on previous literature assignments in Table 2.2. In all cases, the uncoated polymer corresponded well with literature.

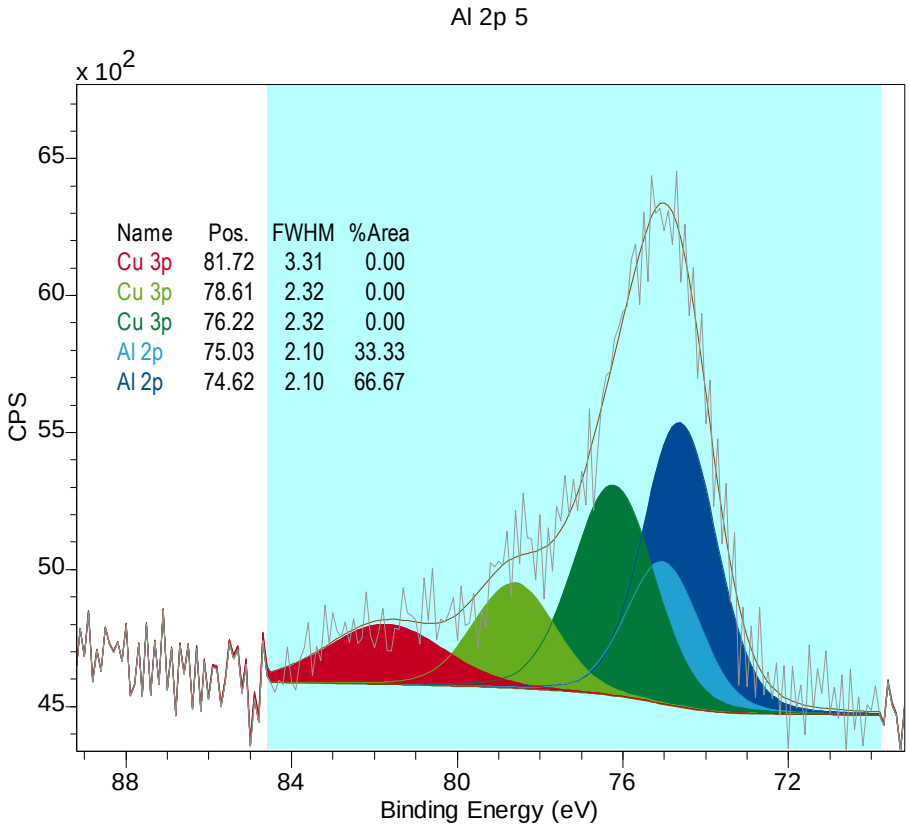

Figure 2.19. XPS fitting for 50 cycle TMA/water process on a Cu substrate. The adjusted area percent of Al was utilized for accurate quantification of the Cu and Al content for the survey scan.

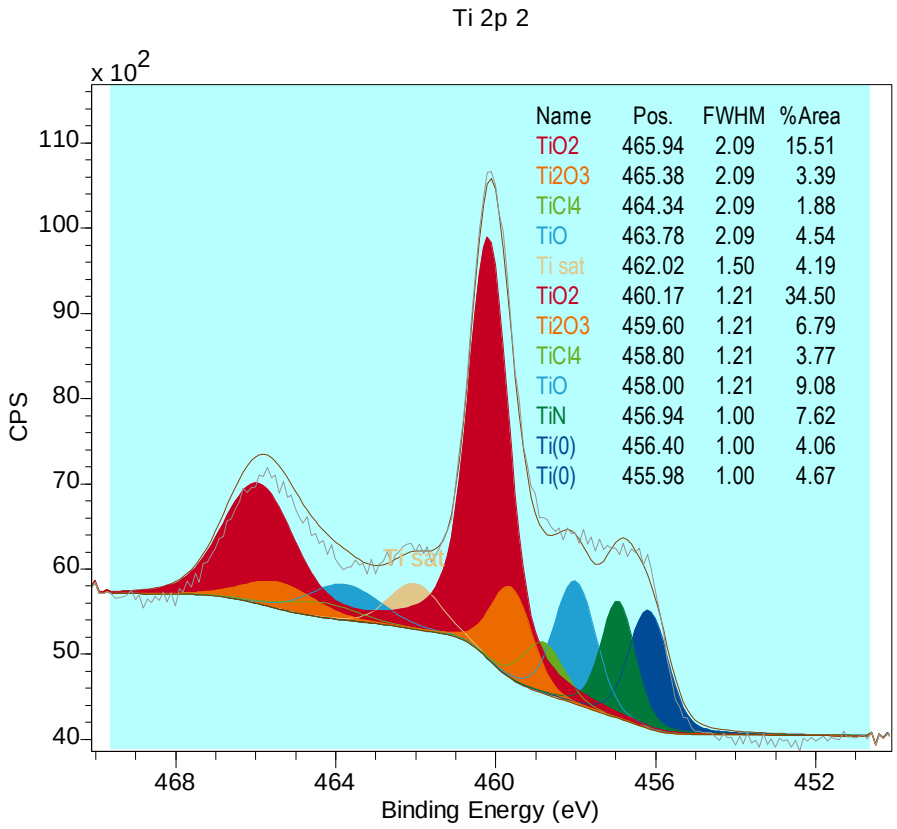

Figure 2.20. XPS fitting for 50 cycle $TiCl_4$/water process on a TiN substrate. The Ti $2p_{3/2}$ portion of the spectra was utilized for quantification.

An example plot of the reactor pressure as a function of time is shown below in Figure 2.21. This shows the capability of the system to reliably and accurately dose precursors to the desired pressure and ensure that the system is sufficiently evacuated before dosing the second precursor. When examining the slight spike in pressure before leveling out at 10^{-4} mbar it should be noted that this is a semi-log plot and any pressure overshoot is minimal.

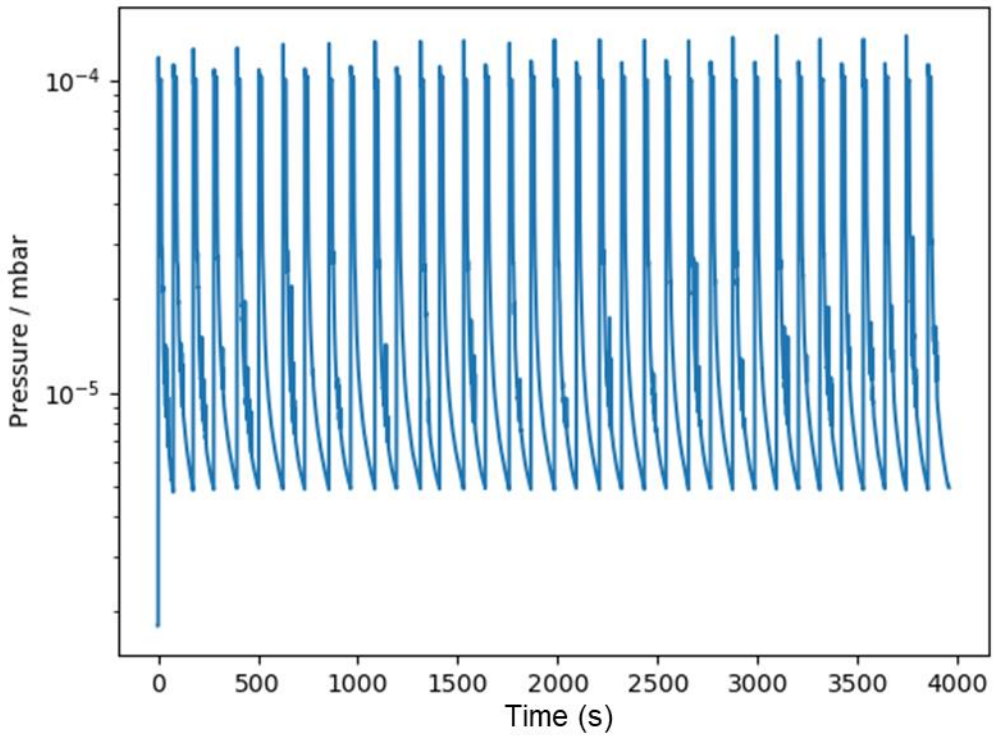

Figure 2.21. Pressure over time for a typical ALD process during precursor dosing.

Table 2.2. Carbon fitting of untreated polymer substrates compared to reference spectra

LDPE	Before ALD						After ALD					
	1	2	3	4	5	6	1	2	3	4	5	6
BE (eV)	284.99	285.38	285.77	286.16	286.28	287.57	285.00	285.39	285.78	286.17	287.21	289.75
Assignment	CH_x	CH_x	CH_x	CH_x	C-O	C=O	CH_x	CH_x	CH_x	CH_x	C-O	C=O
Area (%)	53.4	26.7	5.34	0.9	8.6	5.1	52.1	26.0	5.2	0.8	10.35	5.49

PP	Before ALD				After ALD			
	1	2	3	4	1	2	3	4
BE (eV)	284.91	285.07	285.82	288.25	283.61	285	285.16	285.97
Assignment	CH_x Chain	CH_x Branch	C-O	C=O or Carbonate	e- Rich C	CH_x Chain	CH_x Branch	C-O
Area (%)	28.71	57.41	10.9	2.98	1.79	30.28	60.56	7.37

Nylon 6 ,6	Before ALD				After ALD					
	1	2	3	4	1	2	3	4	5	6
BE (eV)	285.01	285.47	286.03	288.03	283.48	284.96	285.42	285.98	287.98	288.61
Assignment	$(CH_2)_x$	$CH_2C=O$	CH_2N	C=O	e- Rich C	$(CH_2)_x$	$CH_2C=O$	CH_2N	C=O	C=O or carbonate
Area (%)	57.5	11.3	17.6	13.4	8.4	60.09	5.34	17.09	3.33	5.74

CHAPTER 3

MECHANISTIC UNDERSTANDING OF DOPANT ADDITION ON ETHANE OXIDATIVE DEHYDROGENATION

3.1 Introduction

Recent work focusing on improving the activity of M1/M2 catalysts has examined the utilization of catalyst doping [14]. However, a detailed understanding of how these dopants influence the catalyst beyond simply changing its activity is lacking. Therefore, this work seeks to understand how a variety of different dopants influence the redox and structural properties of the catalyst via a variety of in-situ and ex-situ characterization methods. Catalyst activity was determined by evaluating conversion and selectivity at differential conversion, structural properties were determined via XRD and Raman spectroscopy, and redox properties of the catalyst were evaluated with TPR and in-situ Raman spectroscopy in a variety of gas environments.

Herein, a framework utilizing the previously mentioned characterization methods is utilized with a variety of different doping elements of interest in previous literature. In-situ Raman spectroscopy yielded interesting results revealing the influence of different dopants on oxygen transport and redox properties and these results were correlated with TPR and catalytic activity measurements determining that Ti plays a large role in oxygen mobility within the catalyst.

3.2 Ethane Oxidative Dehydrogenation on doped $Mo_8V_2Nb_1$

The use of differential conversion allows for the elimination of mass transfer limitations and allows examination of the primary active site of the catalyst by minimizing the activity of less selective/active sites that function primarily at high temperatures. Therefore, utilizing differential catalytic testing allows for a one-to-one comparison of the primary active site and the effect of dopants on that site, shown in Figure 3.1. Additionally,

the Weisz-Prater criterion was satisfied for the catalysts under differential conversion, where the criterion is as follows in equation 1:

$$\frac{r_A' \rho_c R_P^2}{D_e C_{AS}} \ll 1 \tag{3.1}$$

Where r_A' is the measured reaction rate, ρ_c is the pellet density, R_p is the pellet radius, D_e is the effective diffusivity, and C_{AS} is the surface concentration. D_e is given by equation 2

$$D_e = \frac{D_{C2H6-N2} \varphi_P \sigma}{\tau} \tag{3.2}$$

Where φ_p is the pellet porosity, σ is the constriction factor, τ is the tortuosity, and $D_{C2H6\text{-}N2}$ is the diffusion coefficient. A close approximation of φ_p=0.4, σ=0.8, and τ=3 was used for the catalyst system [106]. The diffusion coefficient was taken to be 1.46×10^{-6} m^2/s [107]. Under differential conditions the observed rate varied from 2.3×10^{-3} mol/kg/s to 4.7×10^{-3} mol/kg/s, ρ_c was taken to be 4.69×10^3 kg/m^3, Rp was 2.25×10^{-4} m and C_{AS} was taken to be equivalent to the bulk gas phase concentration of 14.86 mol_{C2H6}/m^3. This resulted in a range of values for the LHS of the Weisz Prater criterion that varied between 0.026 to 0.0521, which is much less than 1; therefore, the criterion is satisfied and there is no mass transfer limitation.

While nearly all catalysts display a similar product distribution, the catalysts only doped with low amounts of Pd display a much high propensity to form unselective combustion products. Interestingly, the addition of Te tempers this overoxidation, indicating an interaction between these species. This interaction can be explained by considering that perhaps Pd and Te selectively reside in the same site but doping of Te displaces Pd from these sites, influencing their chemistry and catalytic activity. This claim

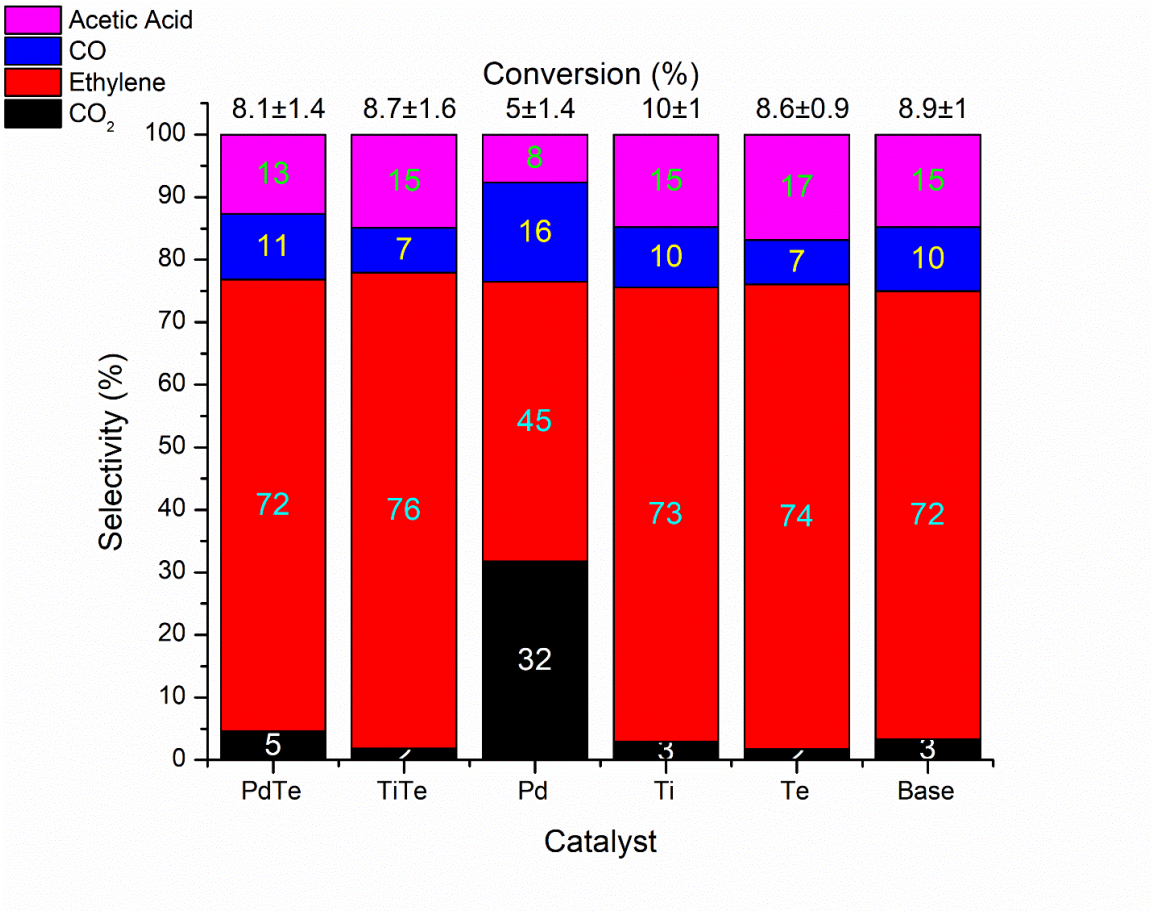

Figure 3.1. Ethane ODH product distribution at differential conversion. Reaction Conditions: Ethane: O_2: He ratio of 2:1:3, 12,000 hr^{-1}, 325 ^oC, 1 atm.

is further supported by examining the literature for ethane oxidation over supported Pd catalysts. Even with substantially higher weight loadings of Pd than those used in this study, the rate of ethane oxidation over Pd is low at approximately 325°C [108]. However, if Pd was located at the same site in the six-membered ring that Te normally occupies, it may contribute to the over-oxidation of activated ethane. Literature suggests that the V=O bond, in particular the V^{5+}=O bond [30], or M-O-V bond [30]–[32], located in the six-member ring may be responsible for the activation of ethane and additional active oxidation centers near this site contribute to over-oxidation of activated ethane [37]. Palladium

adjacent to this active site is likely to react with the activated ethane intermediate more easily than an isolated Pd site reacting with un-activated ethane. Further, based on bond valence theory, Pd^{2+} can fit within the five or six-membered rings of these catalysts [109]. However, as Te is present in such excess, it may be more likely to add to its preferential site when compared to Pd, potentially explaining differences seen with Pd and PdTe catalysts. When considering the other dopants, their activity and product distributions remain nearly identical and higher conversion conditions must be employed to discern how these dopants influence catalytic activity.

The performance of the doped MoVNb catalysts was probed under higher conversion than the previous differential test to probe the influence of dopant addition on selectivity towards ethylene, shown in Figure 3.2. Similar to the differential conversion regime, the addition of small amounts of Pd contributes to the overoxidation of ethylene to CO and CO_2 as shown in the reduced ethylene selectivity. As conversion increases with temperature, the selectivity to ethylene increases likely due to the increasing rate of ethylene activation and desorption from the surface of the catalyst reducing the relative effect channel Pd could have on activity. As previously documented in existing literature [33], [37], the addition of Te improves catalyst activity by increasing conversion and selectivity to ethylene. This effect is also seen with the PdTe catalyst as low ethylene selectivity is not observed regardless of conversion. The remaining catalysts show a similar trend concerning ethylene selectivity. Notably, the most active catalysts for ethylene formation are the Te, PdTe, and TiTe, which all show comparable ethylene yields of approximately 35%. The ethylene yield for the base, Ti, and Pd doped catalyst are 23%, 26%, and 19%; respectively. However, when examining the product selectivity to

oxygenated non-combustion products, namely acetic acid, differences can be noted with both Pd and Ti redox dopants. Furthermore, even at high conversion, the Weisz Prater criterion was satisfied, where the maximum value for the criterion in this study was 0.52, which is still below unity; therefore, there is no mass transfer limitation. However, the reaction is limited by oxygen, where oxygen consumption from combustion depletes available oxygen for olefin production. This is often mitigated by using a 3:2 ratio of ethane to oxygen instead of the stoichiometric 2:1 [110], however since this study was concerned with probing the system spectroscopically; we chose to utilize the stoichiometric value for the ethane ODH reaction of 2:1 ethane to oxygen.

The addition of Pd and Ti increases selectivity to acetic acid when compared to the base catalyst, shown in Figure 3.3, which shows no acetic acid production at low temperatures outside of differential conversion conditions shown previously. As palladium is capable of dissociating oxygen readily [111], the presence of these species on the surface or near the primary active site of the catalyst could potentially be responsible for the formation of high levels of acetic acid. Interestingly, the addition of Ti, even with the presence of Te shows high acetic acid selectivity as well. In fact, in a previous study conducted by this laboratory at a different space velocity and gas composition, the catalyst with this level of Ti and Te doping had the highest overall yield for acetic acid out of all of the catalysts [14]. This effect is not yet well understood but may relate to either more rapid oxygen diffusion throughout the catalyst, resulting in a more facile regeneration of active species for oxygen insertion on the surface, or through the incorporation of extra oxygen throughout the catalyst after exposure to heightened temperatures.

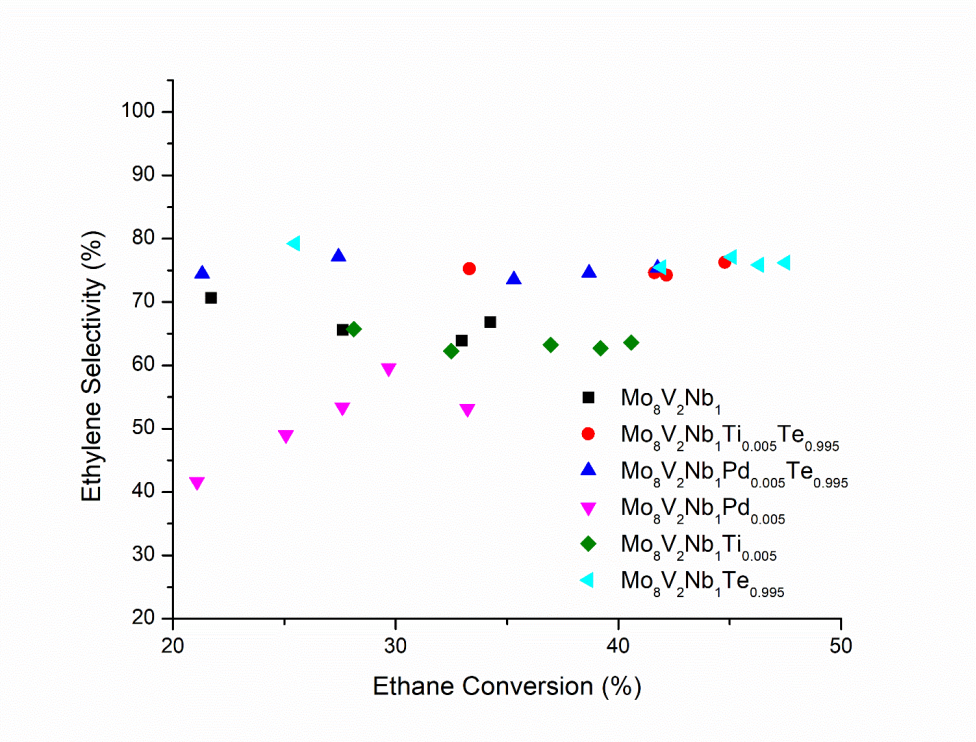

Figure 3.2. Ethylene selectivity as a function of ethane conversion.

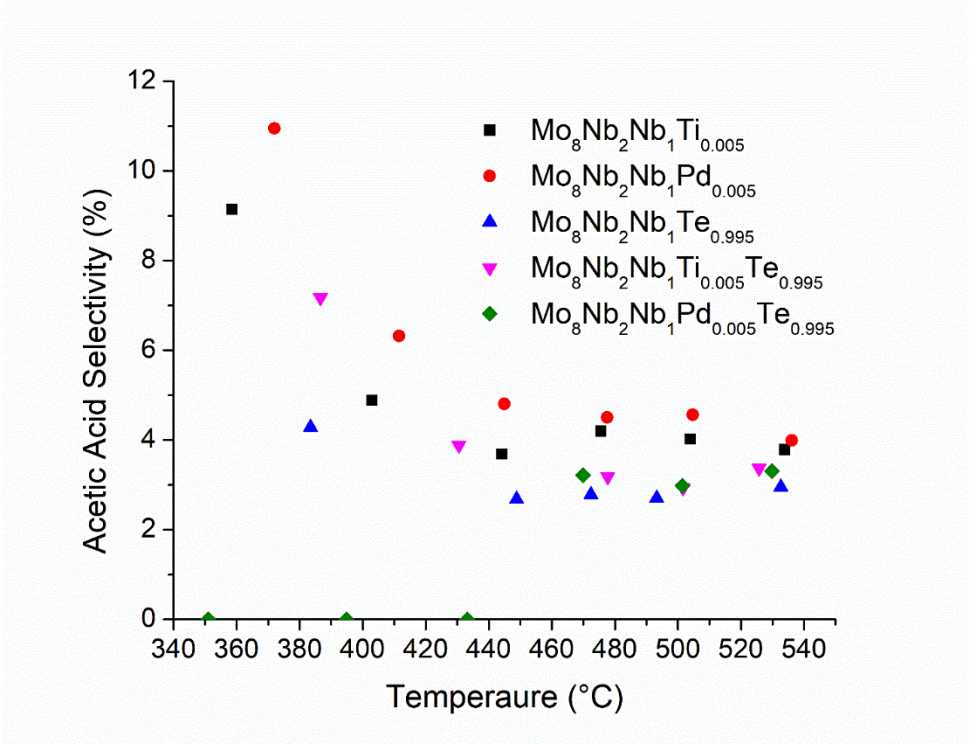

Figure 3.3. Acetic acid selectivity as a function of reaction temperature.

3.3 Reducibility of $Mo_8V_2Nb_1$ doped catalysts

Based on the reduction profiles depicted in Figure 3.4, the base catalyst had the highest onset reduction temperature of the main reduction event, similar to that seen elsewhere in literature [112], while all the dopants lowered the temperature of the main reduction event. Furthermore, there is also a drastic lowering of the reduction temperature due to the addition of Pd. Interestingly, with the addition of Te to Pd containing samples, the bulk of the reduction occurs near the main reduction event for the rest of the catalysts. This can once again be potentially attributed to Pd and Te residing in the same site in the catalysts. The six-membered channels of this catalyst have previously been shown to be an oxygen reservoir and facilitate the transfer of oxygen throughout the catalyst [113], [114]. If palladium resided in the top of these rings, hydrogen dissociated by palladium [115], [116] could find a labile supply of oxygen that would result in a significantly lowered reduction temperature as shown with the above TPR experiments. In the PdTe samples, a peak near 150°C is present, indicative of the reduction of PdO [117] in addition to a shift of the bulk reduction event to a lower temperature potentially due to hydrogen spillover from isolated Pd sites on the surface of the catalyst or in other rings providing hydrogen to labile oxygen in the six-membered ring channels. This is further supported by quantifying hydrogen uptake of the Pd and PdTe samples, hydrogen uptake for both catalysts is approximately 7.3 mmol H_2/g cat. If the addition of only Pd were contributing to excess reducibility of the catalyst, this number would be expected to deviate with the addition of Te. However, similar uptakes indicate that the addition of Pd is only altering the temperature at which reduction occurs. The addition of Ti to the catalyst causes the formation of a spike at the high-temperature end of the main reduction event for the

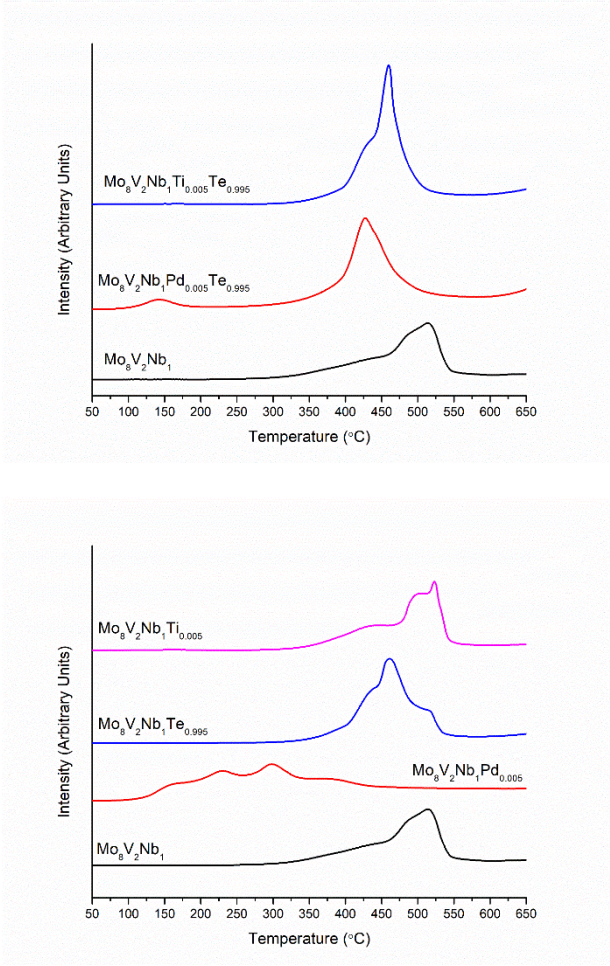

Figure 3.4. Hydrogen Temperature Programmed Reduction for catalysts with one dopant (top) and catalysts with two dopants (bottom).

catalyst. The additional peak in this region is at a similar reduction temperature to TiO_2 seen previously in literature [118], [119] and suggests that Ti is present in an oxidized state within the catalyst. This oxidized state could be due to Ti bonding with oxygen within the rings of the catalyst as anatase or rutile TiO_2 is not observed via XRD or Raman spectroscopy even at high Ti dopings corresponding to $Mo_8V_2Nb_1Ti0.5$. The addition of Te, with or without additional dopants, has the general effect of shifting the reduction event to lower temperature conclusive with its oxygen mobility effect noted previously in

literature [34]. The formation of facile transport of oxygen from the bulk of the catalyst to the surface via infinite or semi-infinite Te chains would facilitate lower temperature reduction by providing oxidizing species at the surface of the catalysts.

3.4 Crystallinity of $Mo_8V_2Nb_1$ doped catalysts

The introduction of dopants into this catalyst system can cause the formation of various species in addition to the base M1/M2 structure at high dopant concentrations; predominantly MoO_x [14] as shown in Figure 3.5. Due to the low dopant concentration of the Ti and Pd addition, the production of secondary phases of the dopant oxides was not detected via XRD. However, the addition of high concentrations of Te does cause the formation of secondary phases, namely MoO_x, potentially due to distortion of the crystal structure of the M1/M2 catalyst or by causing crystallization of amorphous portions of the catalyst.

Sharp peaks at 22° and 45° as well as a broad amorphous peak at 27° are present in all spectra and correspond to the M1 phase of the catalyst [14]. Additional secondary phases present in catalysts containing Te corresponds to MoO_3, indicating that high doping of this element contributes to substantial secondary phase formation as shown previously in the literature [8], [14]. However, this phase is generally regarded as unselective and inactive for ethane partial oxidation and should not greatly influence the activity or performance of the catalyst [5]. For both Ti and Pd-containing catalysts, there is no observed formation of independent dopant oxides, i.e. TiO_2 or PdO, which would signal the onset of phase segregation; however, for such low loading of dopant secondary phase formation is not expected. As the dopants are highly dispersed and in small quantities

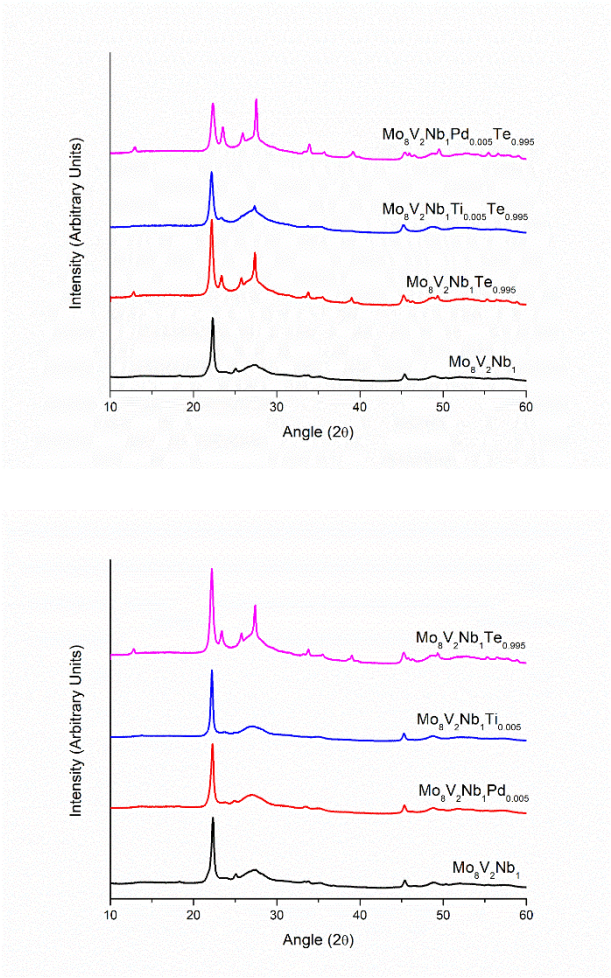

Figure 3.5. XRD of doped catalysts for catalysts containing Te (top) and for catalysts without Te (bottom).

changes to the crystalline structure via XRD are expected to mainly influence the principle phases of the M1 catalyst. Specifically, the peaks at 22^{o} and 27^{o}. where the ratio of these two can be used as an indicator of structure, which will be referred to as the Primary-Phase Intensity Ratio (PPIR) [14]. The slablike (100) diffraction of the M1 phase at 22^{o} is often an indicator of catalytic performance for M1/M2 catalysts since it indicates the preferential growth of the M1 phase, while the crystallinity referenced relative to the amorphous growth of the 27^{o} peak is indicative of the degree of ordered crystallographic growth. The PPIR

for the base $Mo_8V_2Nb_1$ formulation was found to be 3.44, consistent with our earlier work [14]. A decrease in the PPIR would suggest that the preferential crystallographic phase was suppressed while an increase suggests the promotion of crystalline growth. The PPIR for the catalysts are as follows for Te, Pd, Ti, PdTe, and TiTe: 2.7, 3.2, 4.2, 3.5, and 3.5; respectively. Upon addition of the Te, not only does the PPIR decrease but also a noticeably higher formation of secondary oxides occurs, where the formation of secondary MoO_3 phases may suppress the preferential growth of the (100) M1 structure. However, upon the addition of PdTe and TiTe, the PPIR is brought back in line with the original base catalysts formulation, despite the occurrence of secondary oxide formation evidenced by the peaks at 28°, 34°, and 39°. This suggests the addition of the redox elements is facilitating the ordered growth of the (100) M1 phase, even in the presence of Te; which by itself increases the amorphous properties of the mixed metal oxide. Tellurium also has an affinity to promote secondary MoO_3 phase formation, which may contribute to the amorphous character of the 27^o peak. Interestingly, the inclusion of only Ti seems to increase the PPIR of the base catalyst considerably, from 3.4 to 4.2; which suggest that Ti is facilitating the growth of the ordered phase, even at low metal loadings.

3.5 Vibrational Structure of $Mo_8V_2Nb_1$ doped catalysts

To determine the influence of dopant addition on the crystal structure of the catalysts, Raman spectra were obtained for each catalyst under ambient conditions, shown in Figure 3.6. Raman spectra were consistent with other literature for bulk synthesized MoVNb catalysts [120] with M-O-V peaks, where M is a metal atom (V or Mo), located at approximately 873 cm^{-1} and 932 cm^{-1}, peaks corresponding to terminal V=O, Mo=O, and Te=O are generally not observed due to the lack of surface sensitivity of Raman

spectroscopy, however, they are prominent in the case of supported versions of these catalysts [121].

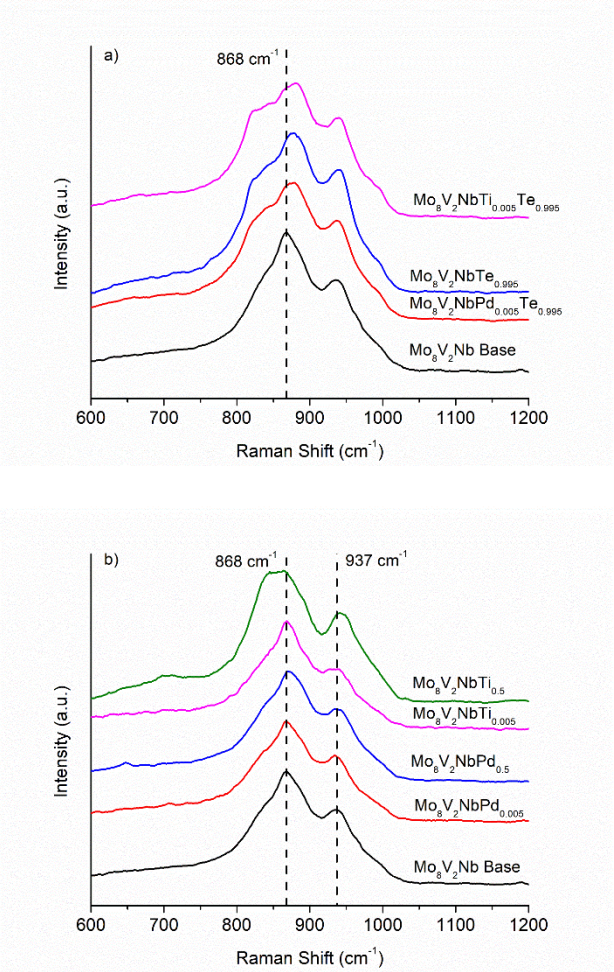

Figure 3.6. Raman spectra of doped catalysts under ambient conditions for catalysts containing Te (top) and for catalysts without Te (bottom).

In reference to the base, undoped catalyst formulation the addition of dopants causes subtle changes in the structure of the catalysts as evidenced by changes in the Raman spectra. As shown in Figure 6, the addition of Te causes a blue-shift of the main band at ~873 cm^{-1} as previously noted by Wachs [120] in this catalyst system due to Te addition and blue shifting has been noted in other catalysts systems due to induced lattice strain

[122]. In addition, the development of a shoulder peak at approximately 850 cm^{-1} and ~1000cm^{-1}, both of which correspond to the formation of MoO_3 as indicated via XRD, is observed for the Te-containing catalysts. The formation of this phase which is unselective to ethane ODH does not cause a significant decrease in reaction performance and in fact, the addition of Te increases ethylene selectivity indicating that Te may not be causing destruction of the M1 phase but instead may be inducing the crystallization of the amorphous phase surrounding the M1 phase [18]. This is also supported by previous literature which suggests that Te helps stabilize the M1 phase during synthesis [123]. Similarly to Te, the addition of high amounts of Pd ($Mo_8V_2Nb_1Pd_{0.5}$) cause a similar blue-shift of the peak at ~873 cm^{-1}, however, the shift is not as severe and the doping does not cause the formation of distinct shouldering as with the case of Te. This is potentially due to the lower loading of Pd when compared to Te. As shown previously, Te^{4+} is coordinated primarily with ring oxygen within the catalyst [33] and forms an oxygen reservoir within the six-membered ring [33], [34]. This oxygen reservoir may induce oxidation of V or Mo in the ring resulting in a strengthened M-O-V bond which corresponds to the blue shift of the band at ~868 cm^{-1} in the base catalyst. Pd may also have a similar effect, however as the blue shifting due to Pd introduction is much less than that of Te, Pd likely has a lesser contribution as it likely does not form an oxygen reservoir. Despite this, a similar effect on the spectra was seen for both dopants, potentially suggesting that Pd and Te may reside in the same site in these catalysts. In contrast, the addition of Ti, even at high loadings, does not display the same characteristic shifting as Pd or Te. While a shoulder is formed near the ~873 cm^{-1} band, it is in a different location and blue-shifting of the ~873 cm^{-1} band

does not occur. Interestingly the band near 923 cm^{-1} does display a blue shifting indicating that it may be adding to a different ring or site in the catalyst, unique to Ti.

3.6 in situ Raman Spectroscopy under inert atmosphere

To discern the effect of each gas component, *in-situ* Raman spectroscopy was performed with only inert, with only oxygen, and finally under working reaction conditions with a gas composition of 33.3% C_2H_6, 16.7% O_2, and 50% inert. The inert-only experiments were conducted to determine the effect of temperature on the catalysts as a previous study on vanadia reported peak shifting due to temperature effects [124]. Therefore, by determining shifting due to purely thermal effects, thermal shifting can be quantitatively accounted for in later analyses. Representative spectra for such an experiment are presented in Figure 3.7.

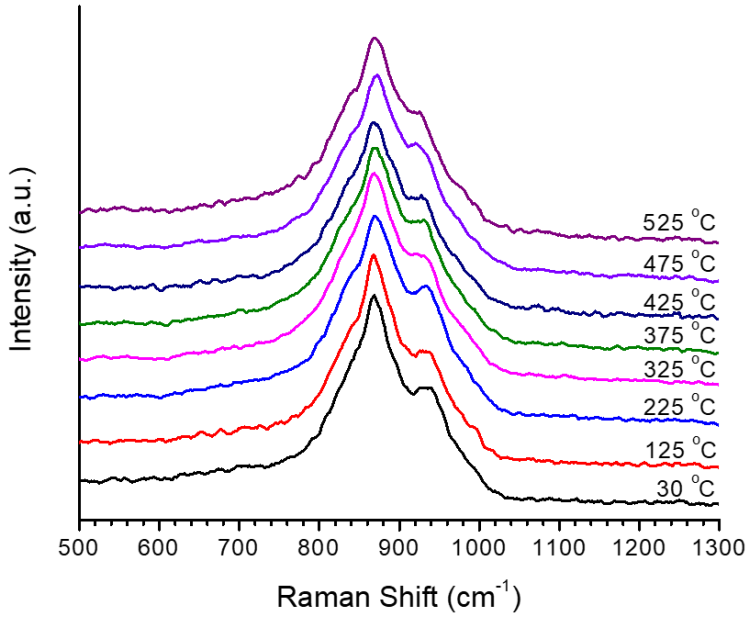

Figure 3.7. Raman spectra of $Mo_8V_2Nb_1Ti_{0.005}$ heated under an inert environment.

3.7 Ethane ODH in situ Raman Spectroscopy

Raman spectroscopy is a powerful vibrational spectroscopy technique that allows for the monitoring of changes in bond strength via the shifting of a Raman active band. Therefore, changes in the Raman shift of a vibrational mode are indicative of a change in the bond strength of that vibrational mode. When *in-situ* measurements are conducted, Raman spectroscopy allows for the determination of oxidation and reduction of catalytically relevant bands via the change in peak position (redshifting or blueshifting) as a function of temperature or gas composition which allows for the extraction of knowledge of how the catalyst behaves under actual operating conditions. From this, the effect of the addition of dopants on the behavior of the active site of the catalyst can be elucidated. The Raman active bonds for these catalysts correspond to the M-O-V vibration of the catalyst and changes in the positioning of the band corresponding to a lengthening or shortening of the constituent M-O or O-V bond. A lengthening of either of these bonds would result in a decreased Raman shift, i.e. red-shifting, while an increased Raman shift would be due to a decrease in the bond length of either bond, resulting in a blue-shift. Figure 3.8 graphically represents this with the assumption that the O-V bond is impacted by the reaction conditions.

A representative spectrum for *in-situ* Raman of $Mo_8V_2Nb_1Ti_{0.005}$ is shown in Figure 3.9. Under elevated temperatures and gas compositions, several of the catalysts exhibited bulk MoOx peaks at roughly 820 and 990 cm^{-1} [125], where the cross-sectional area of MoO_x for Raman scattering is significantly higher than the M1/M2 M-O-M bands; which has been reported for MoVTe based mixed metal oxides [125]. To quantify the peak shifting of the relevant Raman Bands attributed to the proposed active Mo-O-M (M=

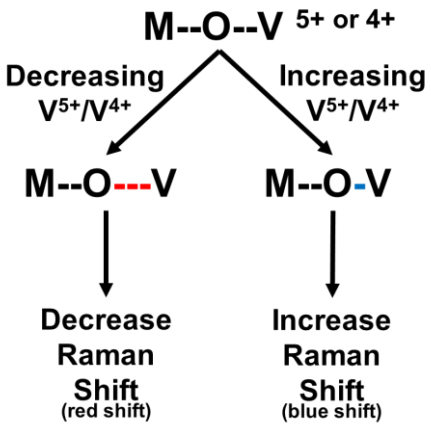

Figure 3.8. General effect of dopants on the Raman active site.

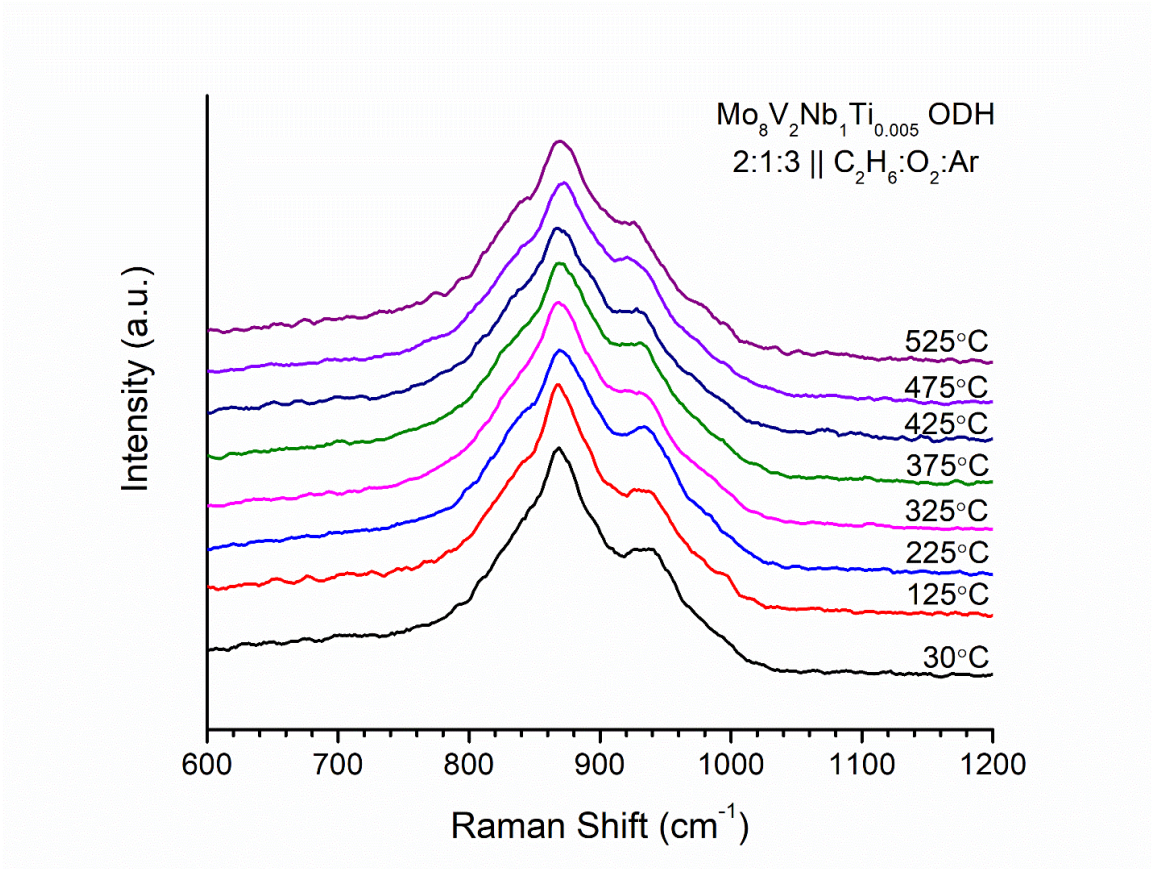

Figure 3.9 *in situ* Raman spectra of $Mo_8V_2Nb_1Ti_{0.005}$ under ethane ODH conditions.

Mo or V) vibrational modes at ~930 cm^{-1} and ~870 cm^{-1}, the spectra were fitted, where a representative spectrum fitting for the base catalysts is shown in Supplemental Figure S6 for the base $Mo_8V_2Nb_1$ catalyst under inert conditions. As the presence of MoO_x oxides cannot be ruled out the spectra were all fitted using four peaks, attributed to the two M-O-V bands located at ~873 cm^{-1} and ~932 cm^{-1}, and two bands at ~820 cm^{-1} and ~990 cm^{-1} corresponding to MoO_x. During the reaction, the band located at ~932 cm^{-1} was the most volatile band with regards to changing position while the band located at ~873 cm^{-1} was fairly constant in position. This suggests that the band at ~932 cm^{-1} may be responsible for oxygen transport within the catalyst and may correspond to an M-O-V stretch in the six-membered ring of the catalyst while the other band at ~873 cm^{-1} may be present in another ring of the catalyst or be in a portion of the ring not responsible for oxygen transport. As Raman spectroscopy cannot resolve surface species without the use of surface-enhanced techniques on bulk oxides, we cannot rule out the contributions of the terminal surface species in the reaction[126]. All shifting is calculated as the difference between the peak position at 525 °C minus the original position of the peak at 30 °C, corrected for thermal effects calculated with inert only experiments by making the same temperature correction under an inert environment. This methodology also corrects for the red or blue shifting of the band due solely to dopant incorporation potentially through structural effects and not changes induced due to the reaction environment. The summary of these results is presented in Table 3.1.

When compared to the base catalyst under reaction conditions, the addition of dopants can either increase or decrease the shift of the peak at ~940 cm^{-1} (relative to the base catalyst) indicative of a decrease in the degree of oxygen coordination to V (or the M

Table 3.1. Summary of thermally corrected *in situ* Ethane ODH Raman for $Mo_8V_2Nb_1$ Catalysts

Catalyst	Shifting of ν = 870 cm^{-1}	Shifting of ν = 940 cm^{-1}
$Mo_8V_2Nb_1$ (Base)	-3.1	-10.1
$Mo_8V_2Nb_1Te_{0.995}$	2.2	-5.2
$Mo_8V_2Nb_1Ti_{0.005}$	0.5	1.8
$Mo_8V_2Nb_1Pd_{0.005}$	-7	-9.6
$Mo_8V_2Nb_1Pd_{0.005}Te_{0.995}$	-3.9	-6.1
$Mo_8V_2Nb_1Ti_{0.005}Te_{0.995}$	5.3	-6.3

*Raman shifting calculated by correcting for thermal effect using an inert gas under identical conditions

species) or an increase in oxygen coordination. The effect of dopant addition can be broken down into two general groups, Te-containing catalysts and redox doped catalysts (Pd and Ti). For the case of Te containing catalysts, the shifting under reaction conditions is consistent across all the catalysts with a red shifting of 5-6 cm^{-1}. For MoV based oxides with the inclusion of Te, various mechanisms have been proposed for the reported increase in catalytic performance such as Te volatilization resulting in highly active O^- radicals next to the Mo-O-V active site [6], [33] the surface enrichment of Te to form distinct active sites [9], or an increase in overall oxygen mobility/formation of an oxygen reservoir due to the inclusion of Te [34]. This is consistent with our results that show the vibrational mode of all the Te-based catalysts, regardless of the secondary redox element, have a similar shifting; suggesting they all undergo a similar mechanism in the presence of Te. Furthermore, relative to the base catalysts, the Te containing catalysts have a less pronounced shifting; where the base catalysts have a 10 cm^{-1} red shift while the Te doped

samples show a *ca* 6 cm^{-1} red shift; which may be due to the effect of Te serving as a labile oxygen reservoir that stabilizes the M1/M2 structure under reaction [34].

For the Pd and Ti based catalysts, there is a shifting of the 940 cm^{-1} band of -9.6 cm^{-1} and 1.8 cm^{-1}; respectively. The blue shifting of the Ti may be due to the increase in lattice oxygen availability due to the Ti, which is consistent with the formation of an additional reduction event shown in the H_2 TPR for the MoVNbTi catalyst, suggesting the Ti is likely either inhibiting oxidation of ethane or allows for faster transport of oxygen to and from the bulk of the catalyst. The red shifting of the Pd doped catalyst is most likely due to the increased reducibility, where the 940 cm^{-1} band remains constant relative to the base MoVNb, however, the otherwise stable 870 cm^{-1} also considerably red shifts; which may be caused by the reduction of a separate site on the M1/M2 catalyst. Furthermore, as the Pd doped catalysts show the highest rate of combustion (CO_x formation) at all ethane conversion amounts we are attributing the promotion of the 870 cm^{-1} to the formation of secondary active sites which may be active for combustion as opposed to the partial oxidation towards ethylene. Additionally, Pd is well known to dissociate oxygen [111], which can result in highly active adsorbed oxygen which can promote combustion products, while ethylene formation generally occurs via a Mars-van-Krevelen mechanism which requires gas diffusion from the bulk oxide [127], [128]. However, due to the complex nature of the active site for this reaction over M1/M2 structures [129], the precise nature of the reaction mechanism over Pd doped catalysts was not explored.

A summary of the complete peak shifting for both the *in situ* Raman collected under an inert atmosphere and reaction conditions are shown in Table 3.2. Under inert conditions, the shifting of the 870 cm^{-1} bands remains relatively constant at ~1 cm^{-1} while the 940 cm^{-}

[1] remains at *ca* 8 cm^{-1}, except for the Te doped catalysts, which shows a shift of *ca* 4 cm^{-1} of the 940 cm^{-1} band. Te is known to have high oxygen mobility in the MoVNb systems, even under elevated temperatures under inert gas; which may contribute to the slight difference in the shifting of the 940 cm^{-1} band. More interestingly, the bands under reaction conditions show a clear trend that the 940 cm^{-1} is most influenced; whereas the 870 cm^{-1} band does not change relative to the inert gas measurements. We propose that the 940 cm-1 band is the catalytically relevant band, whereas the 870 cm-1 band is influenced primarily through structural effects; which justify the lack of apparent change between the inert and reaction measurements while the 940 cm-1 band shifts considerably from inert to reaction. The outlier to this is the Pd doped catalysts, which possess a large shifting of the 870 band under reaction; which may be attributed to the excess reduction of the MoVNb base, where the H_2 TPR shows that the inclusion of just Pd considerably decreases the reduction temperature of the catalyst.

Table 3.2. Summary of Raman band shifting under inert and reaction conditions for M-O-V bands

	Inert Atmosphere Shifting		Ethane ODH Shifting	
Catalyst	**ν = 870 cm^{-1}**	**ν = 940 cm^{-1}**	**ν = 870 cm^{-1}**	**ν = 940 cm^{-1}**
$Mo_8V_2Nb_1$ (Base)	0.1	-6.1	-3	-16.2
$Mo_8V_2Nb_1Te_{0.995}$	-1	-4.3	1.2	-9.5
$Mo_8V_2Nb_1Ti_{0.005}$	-0.9	-8.6	-1.4	-6.8
$Mo_8V_2Nb_1Pd_{0.005}$	-0.3	-9.6	-6.7	-15.6
$Mo_8V_2Nb_1Pd_{0.005}Te_{0.995}$	3.1	-8.6	-0.8	-14.7
$Mo_8V_2Nb_1Ti_{0.005}Te_{0.995}$	-7.2	-8.4	-1.9	-14.7

3.8 in situ Raman Spectroscopy under pure oxygen

Further evidence for this role comes from examining the catalyst under oxidizing conditions. For the base catalyst, Ti-doped catalyst, and Pd doped catalyst discussed

previously, the catalyst can be exposed to pure oxygen at 525°C and cooled down to room temperature without the development of any secondary phases. However, when the doping of Ti is increased, a secondary phase, MoO_x, is formed as shown in Figure 3.10. The same effect is not observed for an identical increase in Pd doping, further supporting the oxidizing effect of Ti addition.

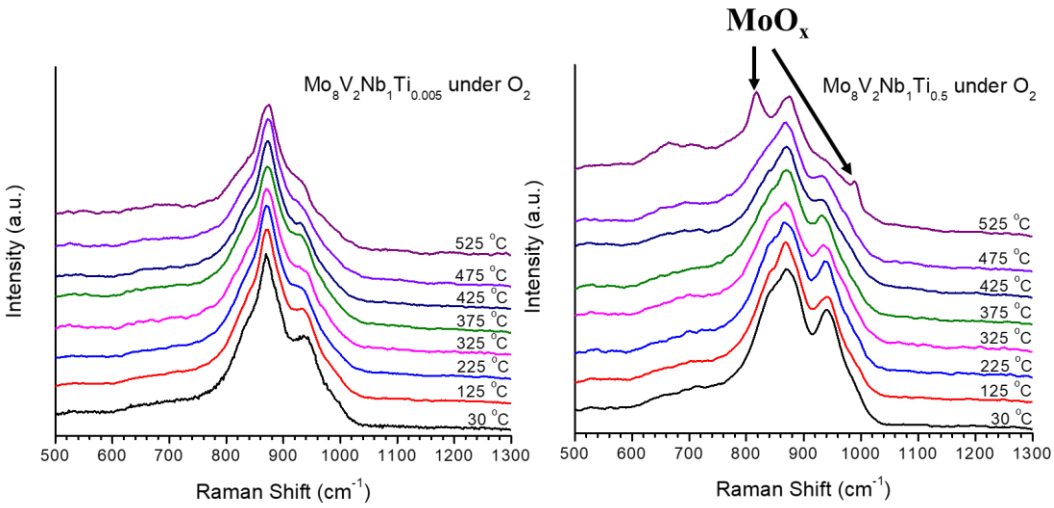

Figure 3.10. Raman spectra of $Mo_8V_2Nb_1Ti_X$ under a pure oxygen environment.

3.9 Structure/Activity Relationship of doped $Mo_8V_2Nb_1$ catalysts

By combining evidence obtained through each of the techniques discussed previously (TPR, *in-situ*, and *ex-situ* Raman Spectroscopy) the role of select dopants and how they impact the complex chemistry of these catalysts can be better understood. The incorporation of Pd within the catalyst increases the reducibility of the catalyst by likely occupying a site adjacent to one of the ethane activation centers of the catalyst. This proximity would allow active dissociated oxygen species access to react with the activated ethane, resulting in excess non-selective over oxidation of ethane to CO_2 which was seen

exclusively for the Pd only catalyst. As this proposed site is the same as the known site for Te, the incorporation of both these dopants simultaneously results in the displacement of Pd as Te is added in significantly higher quantities and could potentially have a higher affinity for this site. The addition of Ti and Te influences the degree of oxygen coordination or oxygen mobility of one of the active species within the catalyst (M-O-V) and influences the product distribution of the reaction to favor more selective oxygenated compounds, namely acetic acid. Further evidence for this is provided by examining *in-situ* Raman spectroscopy of catalysts with high Ti dopings, as these catalysts exhibit over-oxidation of the catalyst to form MoO_x at high temperatures under oxygen.

3.10 Conclusions

In this study, the doping of $Mo_8V_2Nb_1$ catalysts with redox (Pd and Ti) and acid (Te) elements was investigated to gain a deeper understanding of how these dopants influence the complex chemistry of these catalysts. The addition of Pd contributes to the enhanced reducibility of the catalyst, potentially through being located in the six membered-ring of the catalyst adjacent to the active site for ethane activation. This proximity to the active site allows it to interact with activated ethane as well as sit at the top of a channel of labile oxygen. However, Te resides in this site and may displace Pd causing it to potentially reside in another ring or on the surface of the catalyst. Although out of the scope of this study, detailed electron microscopy could shed further light on the location of Pd in the catalyst. The addition of Ti increases the coordination (with oxygen) of one of the species in the M-O-V band as evidenced by *in-situ* Raman spectroscopy. This extra oxygen may be responsible for the enhanced selectivity to oxygenated species, namely acetic acid, seen for Ti-containing catalysts seen in this study. As noted elsewhere

in the literature, this effect is similar to that of Te, as Te can function as an oxygen reservoir and increase oxygen mobility throughout the catalyst. The experimental methodologies utilized in this work could be extended to other dopant materials to gain a more fundamental understanding of how they influence catalytic performance as well.

CHAPTER 4

CO OXIDATION ON STAINLESS STEEL MESH

4.1 Introduction

Previous literature has examined the use of washcoat free stainless steel and aluminum monolithic catalysts. However, essentially no work has been done to understand the influence of preparation conditions on the activity of the produced catalysts and to fundamentally understand changes to the catalyst and monolith. Therefore, this work seeks to develop these relationships and optimize catalyst performance using a Taguchi Design of Experiments. This was accomplished by varying applied voltage, acid weight percentage in the electrolyte solution, and acid identity while examining catalytic activity, precious metal uptake, mass loss from anodization, applied current, and analysis of the electrolyte solution.

Herein, this work demonstrates that these synthesis parameters greatly modulate activity with acid identity playing the largest role in catalyst activity. The optimal acid electrolyte consisted of citric acid in water and outperformed stronger and weaker acids. While increasing acid strength resulted in higher applied current which has a somewhat positive correlation with increased catalyst activity, citric acid was also found to influence mass loss/oxidation and precious metal uptake which had more pronounced effects on activity. Additionally, the optimal catalyst was found to activate over time, and utilizing optimized synthesis conditions resulted in a 5.5 times increase in activity when compared to an unoxidized reference catalyst. This type of catalyst could potentially be utilized in applications with a high vibrational load where washcoats can be unsuitable.

4.2 Variation of Synthesis Parameters

To determine the effect of acid identity/strength, voltage, and weight loading on catalytic activity, an L9 Taguchi design of experiments (DOE) was implemented with the

experimental test points shown in Figure 2.4 and listed in Table 4.1 along with the corresponding initial and final currents as well as mass loss due to anodization.

Table 4.1. Current dependence on anodic treatment parameters.

Sample ID	Acid	Weight Percent Acid (%)	Voltage (V)	Initial Current (A)	Final Current (A)	CO Conversion at 600°C (%)	Anodization Mass Loss (%)
A5	Acetic Acid	5	3	0.007	0.006	10.5	0.16
A10	Acetic Acid	10	5	0.026	0.029	19.7	0.17
A15	Acetic Acid	15	7	0.050	0.053	23.1	0.16
C5	Citric Acid	5	7	0.124	0.135	77.8	0.13
C10	Citric Acid	10	3	0.016	0.019	59.2	0.05
C15	Citric Acid	15	5	0.068	0.082	61.8	0.12
P5	Phosphoric Acid	5	5	0.351	0.459	47.5	1.8
P10	Phosphoric Acid	10	7	0.961	1.08	41.8	1.9
P15	Phosphoric Acid	15	3	0.161	0.192	39.8	2.1

For most catalysts, the activity initially lights off at approximately 250°C with a general increase in activity up to 400°C and then a decrease in activity with increasing temperature up to 600°C, as shown in Figure 4.1. However, acetic acid-treated catalysts have inferior low-temperature activity and light off at 300°C. For acetic acid (pKa_1=4.75) treated catalysts (Figure 2a), the untreated baseline case catalyst slightly outperforms the anodized catalysts at temperatures below 400°C. At 550°C and 600°C, catalysts A10 and A15 outperform the untreated catalyst. However, the untreated catalyst lights off at 50°C before all of the acetic acid-treated catalysts. For citric acid (pKa_1=3.13) treated catalysts (Figure 2b), all catalysts outperform the base catalyst regardless of temperature, indicating

that the treatment procedure enhances activity, especially at higher temperatures. Phosphoric acid (pKa_1=2.16) treated catalysts (Figure 2c) have roughly similar activity to the base catalyst at temperatures less than 400°C, but this activity increases with increasing temperature, and all treated catalysts outperform the base catalyst at temperatures over 500°C.

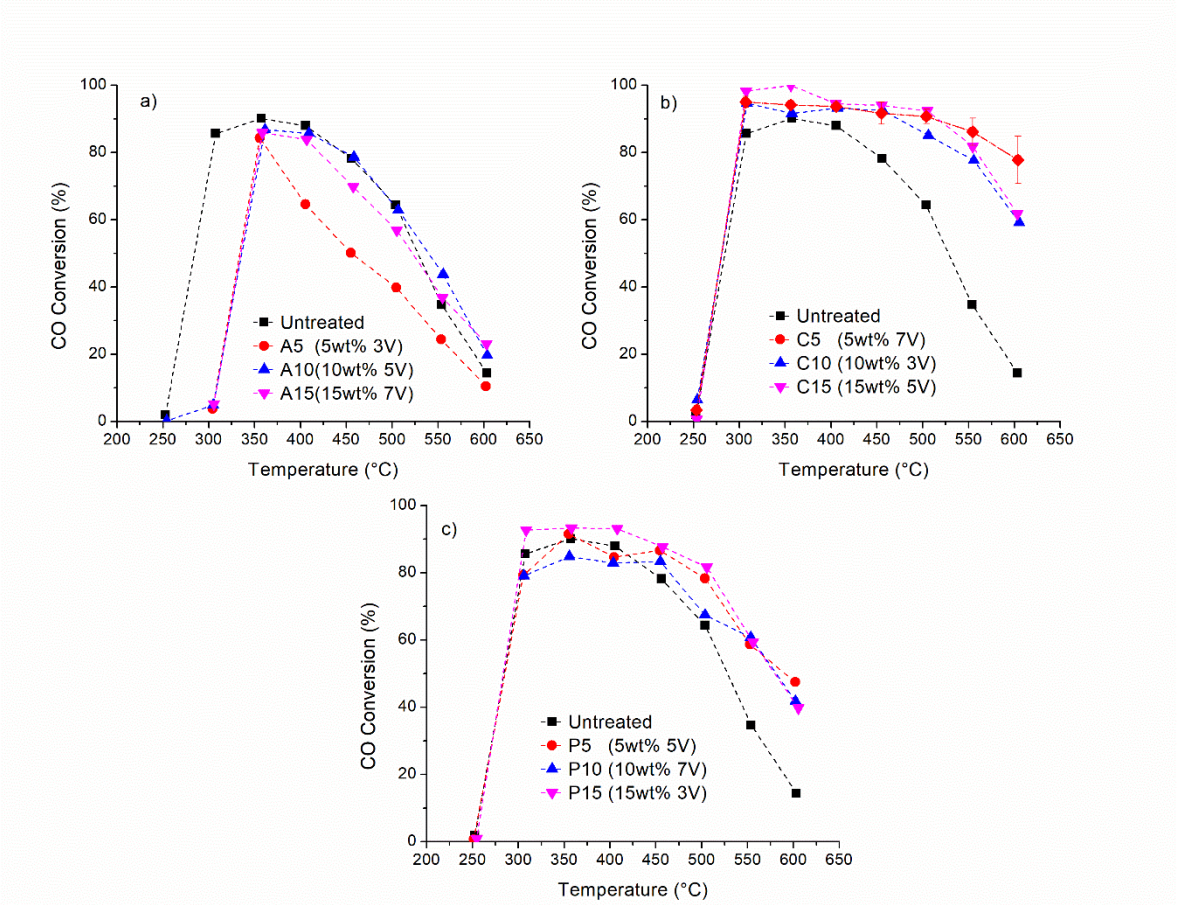

Figure 4.1. a) Acetic acid b) Citric acid and c) Phosphoric acid catalytic activity as a function of treatment condition.

The decrease in activity as a function of temperature indicates that either sintering or reversible deactivation by steam likely occurs. As the catalyst is calcined at 800°C, well above the maximum evaluated reaction temperature, purely thermal sintering is likely not entirely responsible for the observed loss of activity. By evaluating the activity of a spent

catalyst under the same reaction conditions as a fresh catalyst, some light can be shed on the mechanism of activity loss. As seen in Figure 4.2, during the second sequential experiment with the same mesh piece, the activity is significantly reduced at all tested points, indicating that irreversible deactivation is occurring. This deactivation can be explained by considering steam enhanced sintering, in which surface hydroxyl groups regulate the degree to which precious metal species can sinter [130]. As stainless steel is hydrophilic [131], the surface can be populated with water, which could form OH groups on the surface of the metal species and induce steam-enhanced sintering. Platinum [132], [133] and palladium [71], [130], [134], [135] particles have been documented to sinter more rapidly in the presence of steam when compared to dry conditions, consistent with these experimental observations. This also illustrates that much work remains to be done in regards to improving the sintering resistance of these materials and techniques such as adding Ce or other materials known for trapping mobile precious metals may prove effective [136], [137].

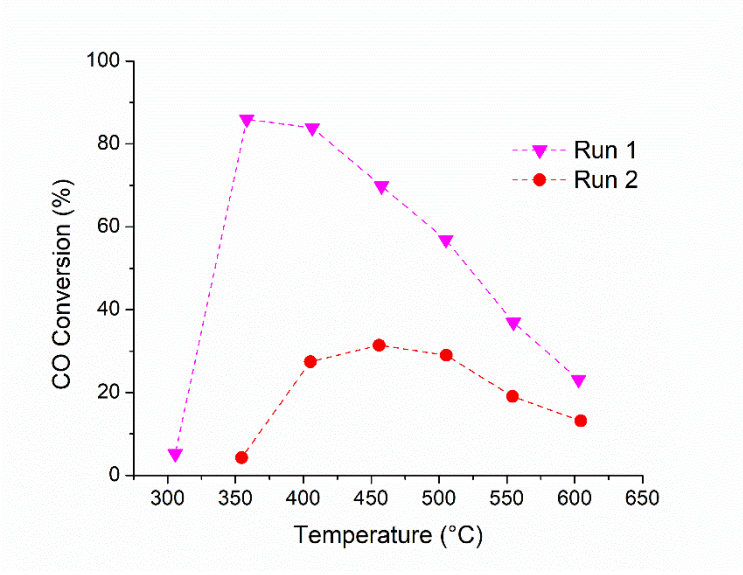

Figure 4.2. Deactivation of catalyst A15 (acetic acid-treated catalyst at 7V and 15 wt%).

As mentioned previously, actual combustion exhaust would contain additional species, namely NO_x, CO_2, and unburnt hydrocarbons, that would diminish the activity of the catalyst. The addition of 0.1% propylene as a model unburnt hydrocarbon and 14% CO_2 delayed light off by 50-100°C and suppressed activity at all temperature points for catalyst C15, except for at 600°C where the activity with and without propylene and CO_2 began to converge as shown in Figure 4.3. Therefore, at high temperatures, the effect of hydrocarbon inhibition on the catalyst is minimal.

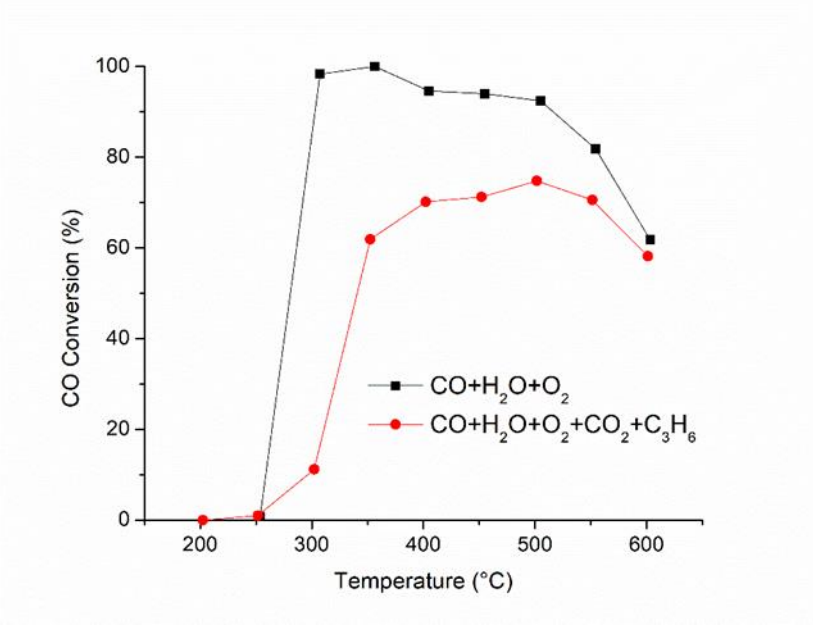

Figure 4.3. Activity of catalyst C15 with varying gas composition, black) simplified conditions with 3.5% CO, 13.5% H_2O, 4.5% O_2, balance Ar and red) expanded conditions with the addition of 14% CO_2 and 0.1% propylene.

To determine the influence of each of the synthesis parameters on the performance of the produced catalyst, the main effects plot is generated. The proportionality of the response of each parameter is indicated by the slope of the line, where a higher absolute value for the slope indicates a stronger interaction and dependence on the synthesis

parameter. As shown in Figure 4.4a), most of the difference in catalyst activity can be directly attributed to the identity or acidity (pKa_1) of the electrolyte solution. Previous work done with alumina has shown that acid identity can greatly influence surface morphology [138]–[140], partially explaining the large differences in catalytic activity shown in this work. Also, voltage and acid weight loading have lesser influence, with both effects being statistically insignificant ($p>0.1$). In light of the insignificance of both of these parameters, the optimum condition was selected from the most active catalyst (at 600°C) in the experimental data set, namely catalyst C5 (mesh treated with 5 wt% citric acid-treated at 7V).

Though the anodization voltage might have a statistically insignificant effect on the overall CO conversion, it can influence the structure of the catalyst as increasing the cell voltage increases the anodization current. The anodization current is a direct measure of the amount of the stainless-steel substrate is removed during pre-treatment, which controls the surface area and roughness. Interestingly, citric acid, with relatively medium acidity, performed the best, suggesting that increased treatment intensity does not necessarily directly correlate with increased activity. Previous literature examining volatile organic compound oxidation over similar catalysts showed that weaker acids could have lower light-off temperatures and increased activity compared to strong acids such as sulfuric acid [68]. Therefore, a contour plot of voltage vs. acid pKa_1 at constant acid weight loading (5 %) was constructed, Figure 4.4b). The contour plot showed that the peak activity was achieved for citric acid-treated catalysts at the highest voltages, which agrees with the main effects plot in Figure 4.4a).

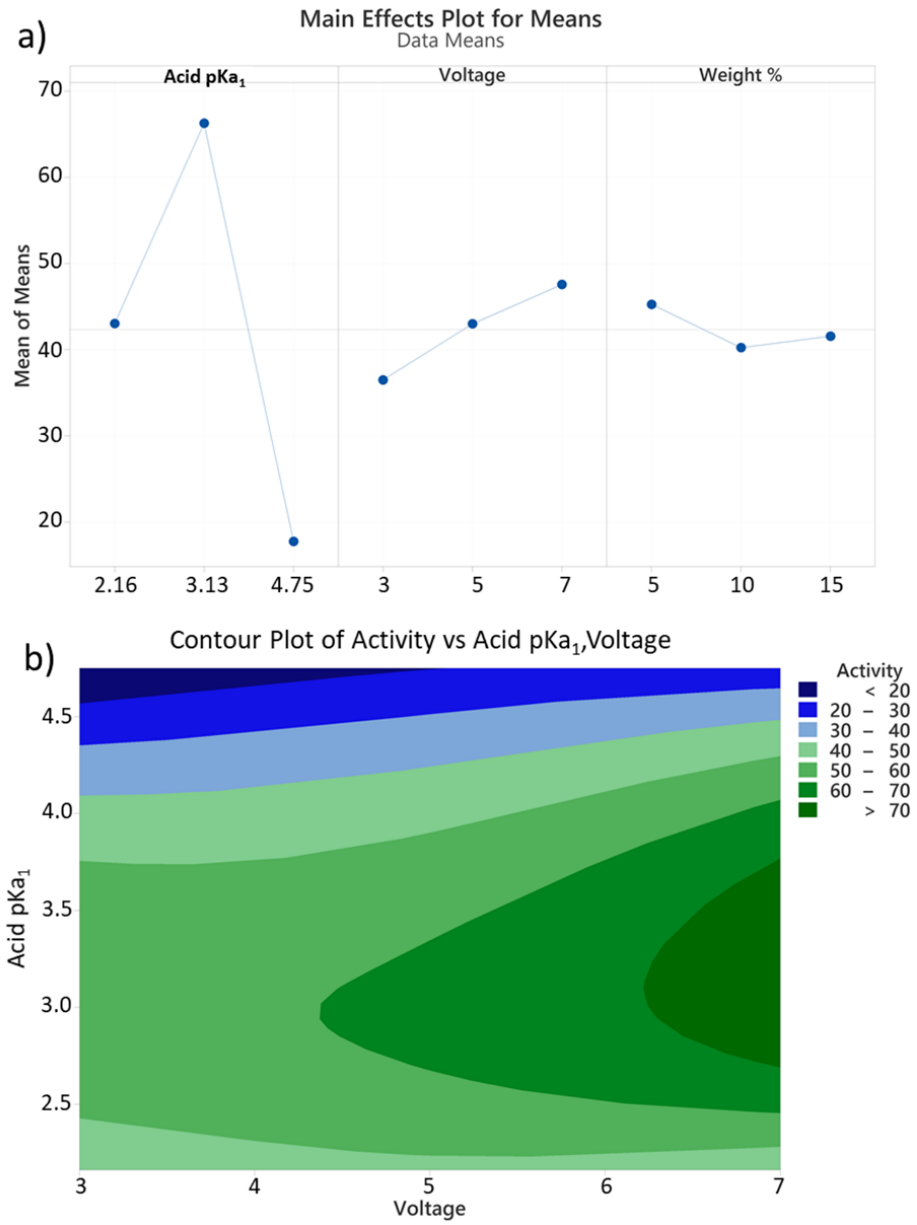

Figure 4.4. a) Main effects plot for CO oxidation over anodically oxidized stainless steel with Pt/Pd loading and b) Catalytic activity as a function of applied voltage and dissociation constant of the first acidic proton of the acidic electrolyte with constant weight percent acid (5 wt%) at 600°C.

As mentioned previously, increasing voltage, acid strength, and weight loading cause a corresponding increase in anodic oxidation current responses. Therefore, examining the activity of the produced catalyst as a function of treatment initial current

response of each catalyst support can provide additional information and insights regarding current as a dependent synthesis parameter and provide a unifying synthesis variable allowing all data points to be combined on one plot. When the catalytic activity is plotted against the initial anodization current, activity initially increases with an eventual tapering off at high currents observed with phosphoric acid, as shown in Figure 4.5. In general, an increase in current causes an increase in surface roughness and surface area [74], which has been previously shown to help inhibit the sintering of Pd nanoparticles [75]. Considering this, the effect of increasing anodic oxidation current can potentially explain the increase in activity at high temperatures relative to the untreated catalyst. As previously shown with anodized alumina catalysts, as anodization time increases, surface roughness initially rapidly increases but eventually tapers off and does not change with increased treatment time [74]. This trend is similar to the general trend seen in this study, with increased current increasing activity likely due partially to sintering inhibition or increased dispersion. While the citric acid-treated catalysts appear to follow the same trend, with an increase in activity with increasing current, the citric acid-treated catalysts have substantially higher activity than catalysts treated with other acids at either higher or lower current. A summary of the initial and final anodization currents is tabulated as a function of experimental parameters in Table 1, with an increase in anodization current from the beginning to the end of the experiment, as previously seen for stainless steel [141].

One advantage of anodic oxidation is the increase in the surface roughness and corresponding increase in surface area, which can improve the potential loading of catalyst on the stainless steel support as determined by ICP-OES. As shown in Figure 4.6a), palladium uptake was relatively constant once above the mesh treated with acetic acid at

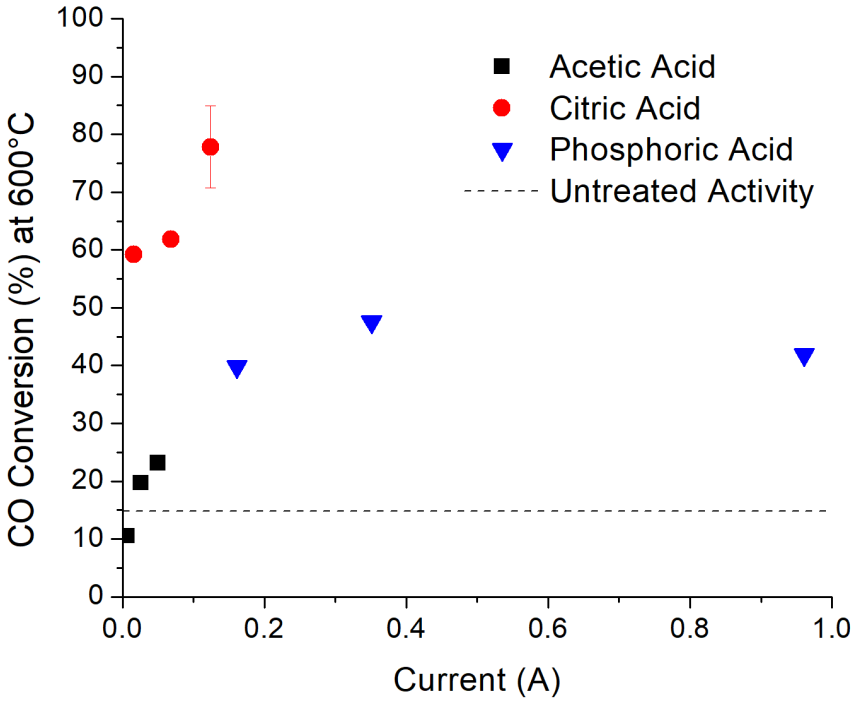

Figure 4.5. Catalytic activity as a function of initial current response during anodic oxidation where the dotted line indicates a non-anodically oxidized mesh-based catalyst.

the lowest current and was substantially higher than that of an untreated metal mesh. Similar to the palladium uptake, all anodically treated meshes had significantly higher platinum uptake than the untreated mesh as shown in Figure 4.6b). Conversely, the uptake of platinum is highly dependent on the applied current and electrolyte identity. Additionally, the increase in platinum uptake is mirrored by the increase in activity seen with the citric acid-treated catalysts.

However, the variation in platinum uptake from the anodized mesh with the lowest and highest metal uptake is less than 20%, and the fairly small increase in platinum uptake or total metal uptake, shown in Figure 6c) may not fully explain the increase of activity.

The impact of the ratio of platinum to palladium is well understood for CO oxidation and has been shown to reach maximum activity for catalysts with a 1:1 platinum to palladium ratio [142], [143] or becomes more active and stable with increasing platinum content [45]. This result is consistent with the experimentally determined platinum to palladium ratio for each of the catalysts shown in Figure 6d). In addition to increasing activity, alloyed platinum-palladium bimetallic catalysts have been previously shown to display increased sinter resistance [134], [135] and resistance to steam poisoning by decreasing the concentration of surface hydroxyl species that are less active or inactive [134]. This corresponds well to the lesser degree of activity decrease observed with the citric acid-treated stainless steel mesh catalysts relative to phosphoric, or acetic acid-treated catalysts.

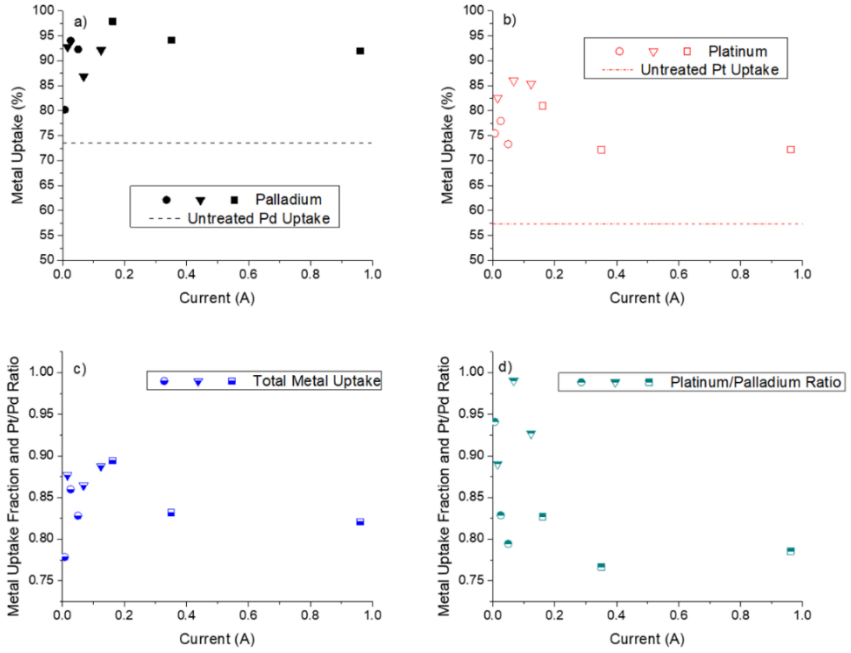

Figure 4.6. a) Variation in palladium uptake, b) platinum uptake, c) total precious metal uptake, and d) platinum to palladium ratio as a function of anodization initial current for acetic acid-treated meshes (circles), citric acid-treated meshes (triangles), phosphoric acid-treated meshes (squares).

In general, the most active catalysts had corresponding high metal uptakes and platinum to palladium ratios. However, as acetic acid-treated catalysts generally had higher platinum to palladium ratios and similar total metal uptake rates but lower catalytic activity than phosphoric acid-treated metal mesh monoliths, it illustrates that other factors can have a profound effect on catalytic performance. This result may be partially attributed to increased surface roughness and, therefore, the surface area of the produced mesh pieces [74] as well as potential changes in surface structuring due to the use of different acids. As shown in Figure 4.7, changes in surface structure are observed due to variations in the anodic treatment. Each image in Figure 7 shows the sample treated with the highest current for each of the acid electrolytes with Figure 7a) showing an unoxidized wire mesh.

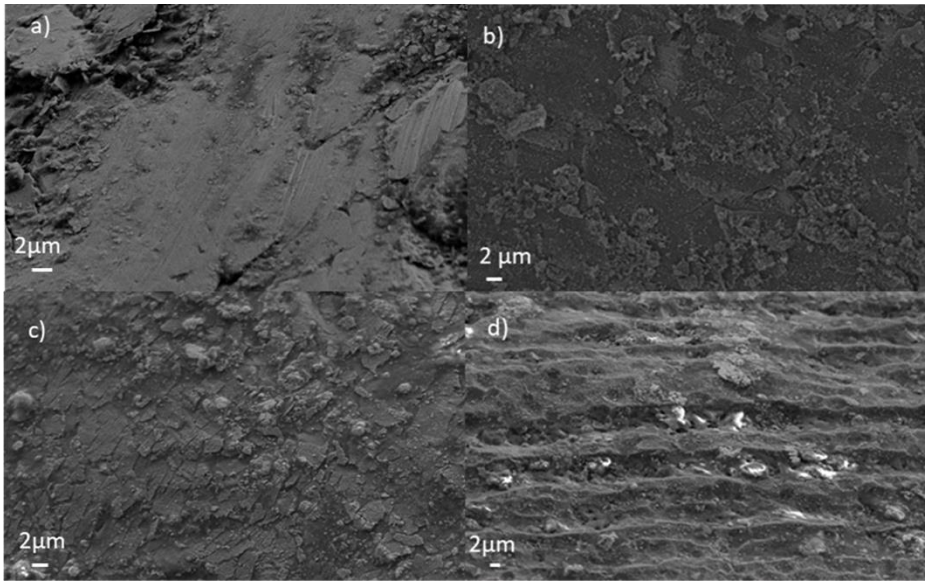

Figure 4.7. SEM images of a) an unoxidized wire mesh and catalysts b) A15 c) C5 and d) P10.

These changes can be most readily observed when comparing Figures 4.7b-c) to Figure 4.7d), which corresponds to meshes treated with acetic and citric acid, respectively, when compared to mesh treated with phosphoric acid. Phosphoric acid-treated samples

display micron-sized surface channels and pores, not seen for meshes treated with acetic or citric acid.

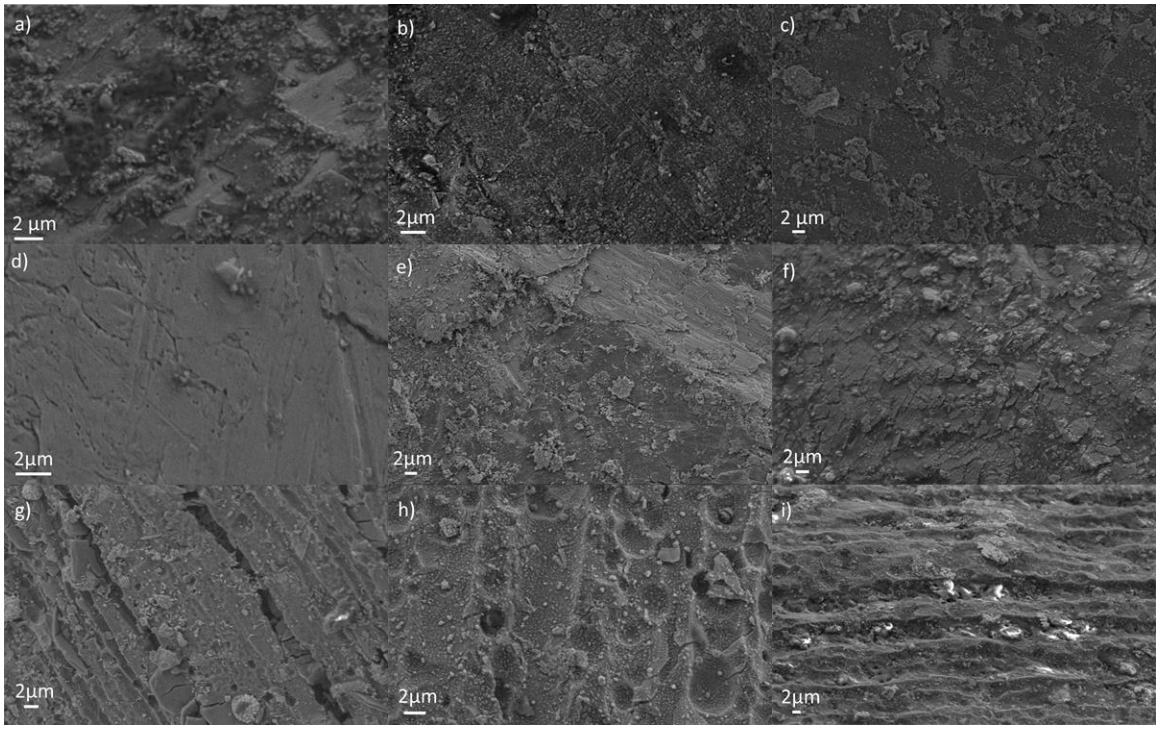

Figure 4.8. Scanning Electron Microscopy (SEM) images of metal mesh surfaces after anodic oxidation and catalyst impregnation a) A5, b) A10, c) A15, d) C10, e) C15, f) C5, g) P15, h) P5, i) P10 (in order of increasing current during anodic treatment).

Similarly, changes seen with acetic and citric acid-treated catalysts shown in Figure 4.8 a-c) and d-f) are less pronounced than those treated with phosphoric acid shown in Figure 4.8 g-i) in line with Figure 4.7, but as anodization current increases, the presence of the darker overlayer decreases and surface structuring begins to develop with a noticeable "cracked mud" like texture observed in Figure 4.7c) followed by micron-sized channels in Figure 4.7d) when compared to non-anodized and calcined meshes shown in Figure 4.9a-b). These observations suggest that while increasing surface roughness may play a role in describing the differences seen between meshes treated with acetic and phosphoric acid,

another factor is responsible for the increase in activity observed for citric acid-treated mesh-based catalysts.

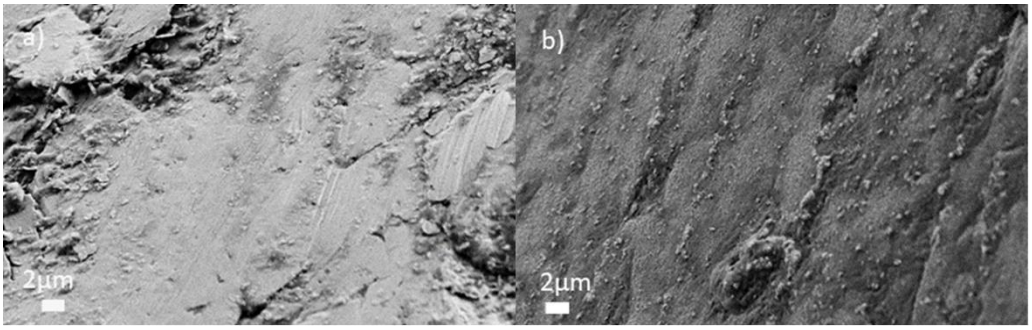

Figure 4.9. Scanning Electron Microscopy (SEM) images of metal mesh surfaces without anodic oxidation or catalyst impregnation order a) fresh mesh, b) calcined mesh.

The mass loss of each of the metal monoliths is influenced by the anodic treatment conditions shown in Table 4.1. When comparing acetic and citric acid-treated monoliths, citric acid monoliths had less mass loss despite being treated under more severe conditions with a higher applied current than the acetic acid-treated meshes. In contrast, phosphoric acid-treated monoliths show a constant high mass loss regardless of current, as shown in Figure 4.10a). In general, there are two competing paths in which the surface changes during anodic oxidation, depending on the applied voltage and a variety of other factors [63]. The first path is surface roughening via a dissolution process that results in the removal of material, as seen with the phosphoric acid-treated catalysts in Figure 4.7d). In contrast, the second pathway is surface metal oxide growth [63], [144]. To compare the relative amount of each process, mass loss per applied amp can be plotted against the initial current response, as shown in Figure 4.10b), allowing for a more direct comparison between samples with anodic treatment conditions as it normalizes the mass loss to a per amp basis. Citric acid-treated catalysts are characterized by low mass loss both on an

absolute basis and a per amp basis, indicating that the second route is likely more prevalent relative to the other electrolytes, resulting in the formation of a thicker oxide layer. This effect has been previously shown to be essential for producing a more effective catalyst for aluminum/alumina-based catalysts [63]. Therefore, more extensive oxide growth may also contribute to the better performance of citric acid-treated monoliths relative to the other examined acids.

In addition to morphological changes, the treatment procedures also induce chemical changes at the surface of the mesh. As shown in Figure 4.10c), as the initial current increases, the relative amounts of iron and chromium present in the electrolyte, and therefore the quantities of iron and chromium removed from the surface of the mesh change. At low current conditions with acetic acid, the ratio of iron/chromium removed from the mesh is low, indicating a more selective depletion of chromium from the surface. This result may explain partially why A5 (mesh treated with acetic acid at 5 wt% and 3V) was less active than the untreated base catalyst and displayed delayed light off even though it had higher uptake of both platinum and palladium. The promotional effects of chromium relative to that of iron have been previously documented for Pd-based methane oxidation catalysts [145]. In this study, the addition of chromium to the catalyst increased the methane conversion to a higher degree than iron added at an identical loading. Overall, the increase in the iron/chromium ratio, and therefore an increase in the amount of iron removed from the mesh relative to chromium, is directly mirrored by the increase in catalytic activity at 600°C except for the activity spike seen for citric acid-treated catalysts. Additionally, previous combustion literature has shown significantly different activity for precious metals supported on different metal oxide supports [146], [147]. This mirroring

would suggest that the chemical environment of the surface of the mesh has a substantial role in the efficacy of the final catalyst. The change in surface oxide composition may also partially explain the differences in precious metal uptake, in particular for platinum, which was highly dependent on the anodic treatment conditions.

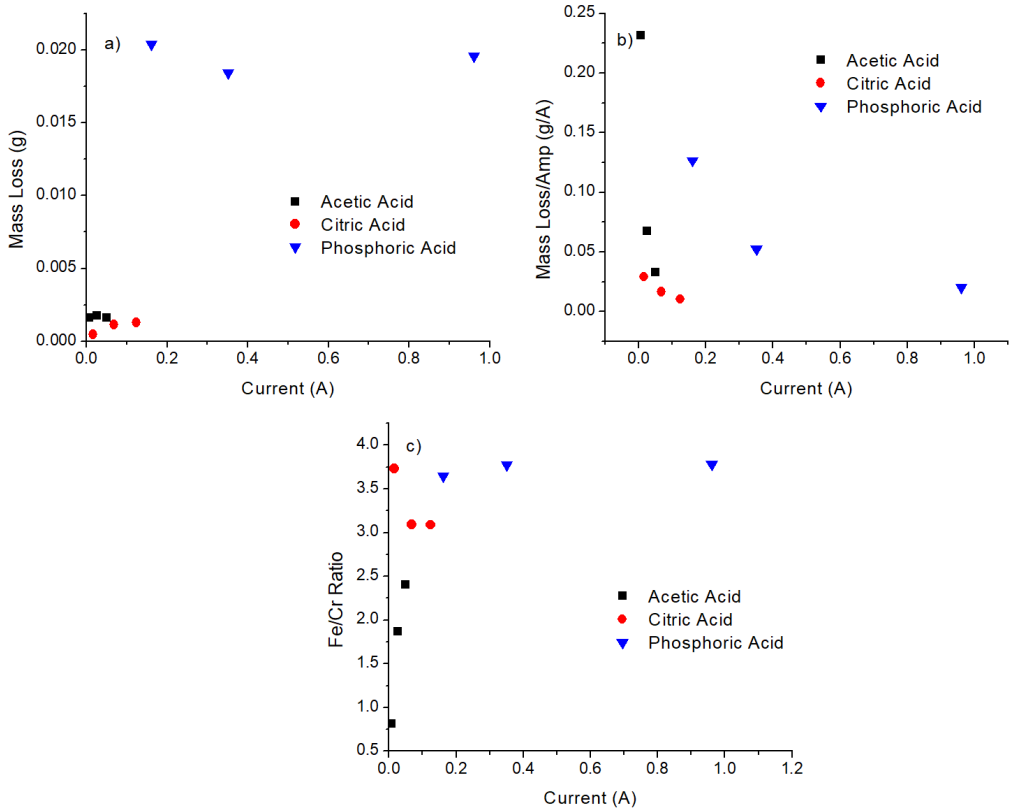

Figure 4.10. a) Mass loss, b) Normalized mass loss, and c) Ratio of Iron/Chromium in the electrolyte as a function of initial current response.

4.3 Time on Stream Study

To evaluate the catalyst's longevity, the catalyst was left on stream for 100 hours. As seen in Figure 4.11, there is a rapid initial decrease in activity with a gradual increase in activity with subsequent time on stream after reaching minimum activity.

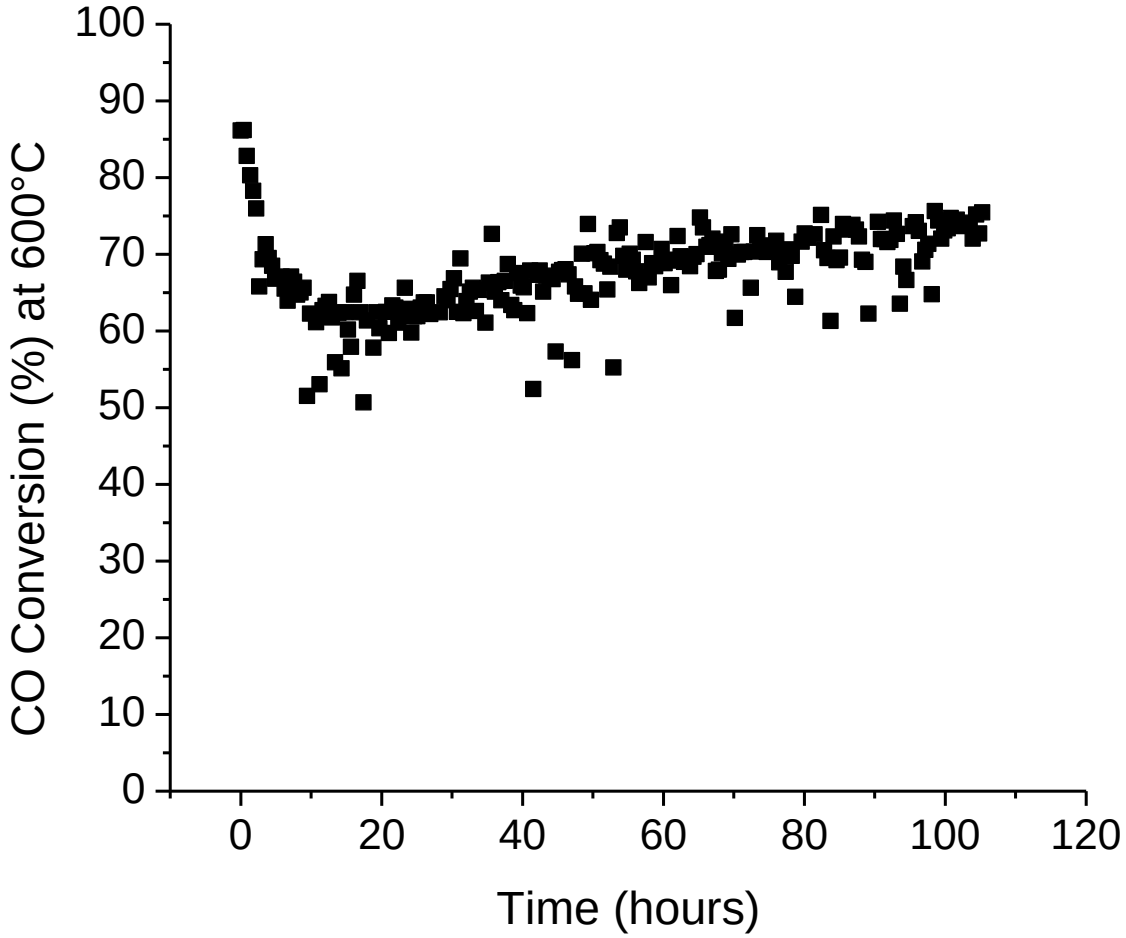

Figure 4.11. Time on stream study for catalyst C5 (mesh treated with 5 wt% citric acid at 7V).

While the rapid initial decrease in activity is likely due to sintering as discussed previously [134], [135], the subsequent increase in activity could be caused by a variety of phenomena, which is further complicated by the presence of a variety of different surface metal species present on a highly alloyed material such as stainless steel. Ferritic stainless steels with high alloying of chromium are known to form larger clusters of chromium during aging at temperatures at and below 600°C [148], which may increase activity either by creating platinum/palladium metal centers on these clusters and improving activity or conversely by depleting chromium from the support near the platinum/palladium clusters. Additionally, platinum and palladium may initially be dispersed in a sub-optimal manner.

However, they may redisperse over time to form sites with increased activity [149], similar to catalysts prepared by Jones et al. [136] or by a restructuring of the bimetallic cluster which has been previously documented for platinum palladium bimetallic catalysts for methane combustion [134]. Previous literature has also reported increased activity with time on stream for palladium catalysts, although this effect is dependent on the nature of the oxide support [147]. Additionally, examining the metal content of the electrolyte after anodic oxidation reinforces this hypothesis as the amount of chromium removed from the mesh, relative to that of iron, can be correlated with the catalytic activity of the produced mesh.

4.4 Influence of Different Stainless Steel Monoliths

A variety of different grades of stainless steel were anodically oxidized and impregnated utilizing the optimized electrolyte and voltage determined previously in this work to determine the influence of the underlying stainless steel. As shown in Table 4.2, the elemental composition of each of the four grades of stainless steel (410,310,430, and 316) varies widely.

Table 4.2. Content of varying grades of stainless steel.

Element	410	310	430	316
C	< 0.15%	< 0.25%	< 0.12%	< 0.03%
Cr	11.5-13.5 %	24-26 %	16-18 %	16-18 %
Ni	>0.75%	19-22%	<0.75%	10-14%
Mn	<1.0%	<2.0%	<1.0%	<2.0%
Si	<1.0%	<1.5%	<1.0%	<1.0%
P	<0.04%	<0.045%	<0.04%	<0.045%
S	<0.03%	<0.03%	<0.03%	<0.03%
Mo	0.0%	0.0%	0.0%	2-3%

*Iron content of the steel is not listed explicitly but composes the balance of the steel content

Correspondingly, the activity of catalysts produced with each of these different grades of steel also greatly varies as shown in Figure 4.12. In general, higher amounts of metallic alloying elements (Cr, Ni, Mo) result in poorer performing catalysts after anodic oxidation and sonication. However, the exact reason is not exactly clear. As documented previously, these catalysts can activate with time on stream aging and one potential reason for this is the clustering of Cr on the catalyst. Therefore, it is not unreasonable that the changing chemical environment of the surface with different steel alloys can modulate the activity of the produced catalysts. However, it is impossible to say exactly what is causing these changes as the varying alloys of steel also influence the synthesis of the catalyst before precious metals are added. Since alloying elements are added for enhanced corrosion protection, higher alloyed steels will not anodically oxidize at the same rate as less alloyed steel. Therefore, higher alloyed steels were less harshly treated which as demonstrated in this work would also cause an expected decrease in activity. However, what can be said definitively is that changing the composition of the steel can have a great influence on the activity of the produced catalyst, with the lowest alloyed steel examined here not deactivating at all at 600°C indicating superior performance to the CRAL 20-5 steel previously used in this work. It should also be noted here that no catalyst reaches 100% as can be seen with the CRAL 20-5 steel and this is due to the choice in stainless steel wire selected for these experiments. To keep all as many variables as constant as possible when changing the grade of stainless steel, identical diameter wires were used to avoid changing the surface area to volume ratio of the monolith. However, wire of the same diameter as the previously utilized CRAL 20-5 was not available for all grades of steel and therefore larger diameter wire was purchased. Unfortunately, this made packing the reactor

tube much more difficult and some slip of CO was expected. However, since the wire diameter remained consistent between each of the steels used here, relative comparisons can still be drawn.

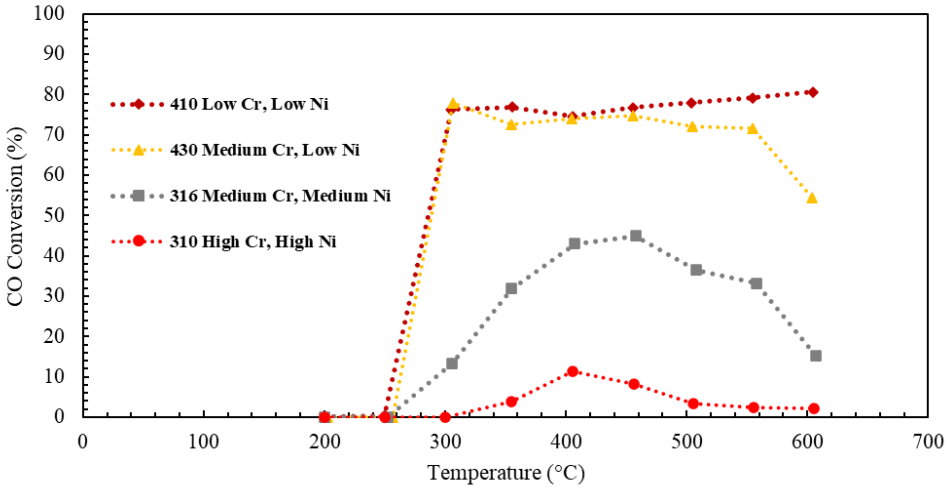

Figure 4.12. Activity of catalysts synthesized from varying grades of stainless steel.

Additionally, other synthesis parameters were investigated including sonication time and anodic oxidation time with a 316 stainless steel monolith. This grade of steel was selected particularly because of its low activity and the increase in activity would be easy to observe when compared to a better performing alloy. With constant anodization time, an increase in sonication time resulted in increased activity of the produced catalysts as shown in Figure 4.13. While metal uptakes were not recorded for these experiments, previous experiments in this work have shown that with other stainless steel monoliths, metal uptake was near complete at 3 hours, so while some incremental increase in metal uptake may occur when sonicated for 5 hours, it is also likely that sonication causes a more effective catalyst via changing active species cluster size and structuring as previously documented in the literature [150].

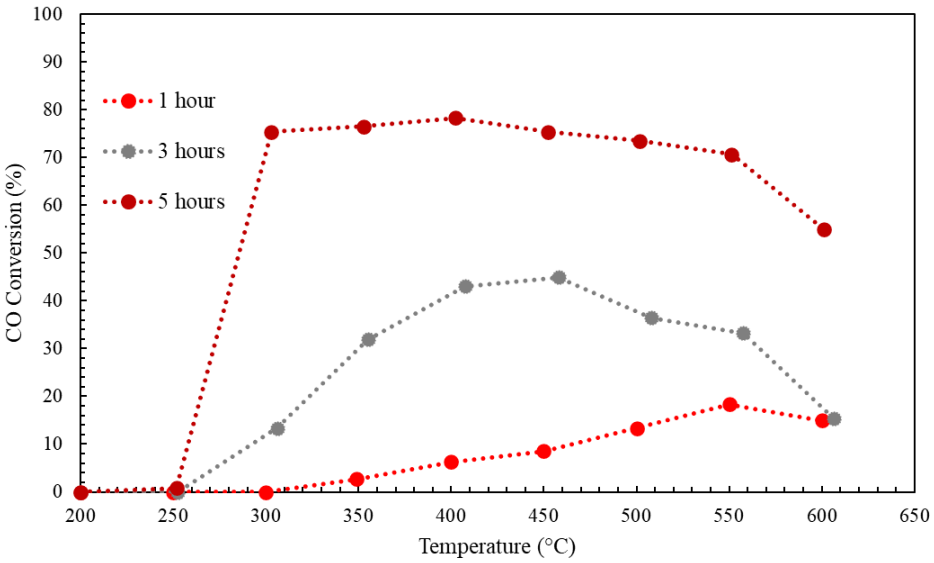

Figure 4.13. Influence of sonication time on catalyst activity.

Finally, high-temperature catalyst performance increased with anodization time as shown in Figure 4.14, corresponding with previous results from this work in which a more severe anodization process (i.e. higher current) generally resulted in higher catalyst activity due to increased surface structuring if the effect of electrolyte identity is not considered. Interestingly, catalysts anodized for 50 minutes performed worse than those anodized for 30 minutes. One potential explanation for this is considering the changing composition of material removed from the surface of the mesh as a function of process severity as shown in Figure 4.10c where anodization current increases the Fe/Cr in the electrolyte is changed as the alloying element rich surface is removed and nears the bulk composition of the mesh. This change can alter the chemical environment around the metal clusters as well as their uptake which can modulate their activity and how the catalyst behaves at varying temperatures. However, detailed experiments analyzing precious metal uptake or the identity of metal in the electrolyte were not conducted here and would be important for a thorough understanding of these phenomena.

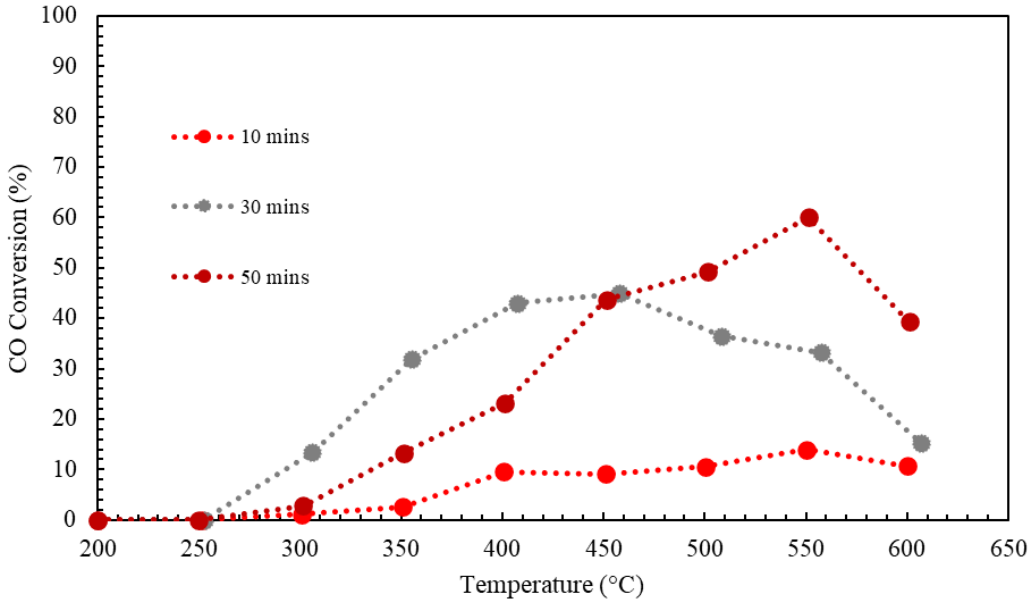

Figure 4.14. Influence of anodization time on catalyst activity

4.5 Conclusions

This work demonstrates that anodically oxidized stainless steel has the potential to be utilized as an effective washcoat free catalyst support for CO oxidation at high temperatures with quantities of steam relevant to combustion exhaust. However, significantly more optimization and experimentation would be required to commercially utilize such a methodology and to prevent sintering and deactivation. However, these types of catalysts may have a role in applications with high vibrational or mechanical load or where their ability to be shaped and differences in properties of a metallic monolith compared to a ceramic one (such as increased heat transfer) would be advantageous.

Acetic acid proved to be a relatively ineffective electrolyte with the low current acetic acid-treated support displaying inferior activity compared to an untreated stainless

steel mesh catalyst. However, phosphoric acid and citric acid-treated catalysts had significantly higher activity than the untreated and acetic acid-treated stainless steel monolith, likely due to increased surface roughness and the corresponding decrease in sintering rate caused by high-temperature steam. Interestingly, the medium strength citric acid had higher activity than the more acidic phosphoric acid. Upon examination of precious metal uptake, it was determined that citric acid-treated catalysts generally had higher precious metal loadings due to increased platinum uptake and, therefore, higher platinum to palladium ratios. Stainless steel monoliths treated with citric acid, also had significantly less mass loss both on an absolute and per amp basis than acetic acid and phosphoric acid-treated meshes, likely corresponding to more preferential surface oxide growth compared to dissolution. Further, changing the anodic treatment conditions modified the surface chemistry of the mesh pieces by changing the amount of Fe or Cr removed from the mesh during anodization. Therefore, the higher activity of the citric acid-treated catalysts is mainly attributed to increased precious metal uptake at optimum platinum to palladium ratio, preferential oxide growth relative to that observed with the other electrolytes, and changes in surface chemistry of the stainless steel mesh. Decreases in activity seen at high temperatures (above 400°C) were determined to be due to steam-enhanced sintering. However, the best performing catalyst showed stability during a time on stream study with some of the initial activity loss recovered over time, potentially due to previously documented chromium agglomeration on the surface of the stainless steel support which can potentially influence the support metal interactions between the steel surface and the platinum and palladium clusters as noted in previous literature. Further experimentation is required to determine how these catalysts would behave under realistic

operating conditions, namely via the addition of NO, CO_2, and unburnt hydrocarbons as well as a one-to-one comparison with a washcoated catalyst.

CHAPTER 5

MAGNETICALLY SEPARABLE CATALYTIC BIOMASS TORREFACTION

5.1 Introduction

The utilization of waste biomass could prove to be useful bridge technology as the transition to renewable energy (solar, wind, etc.) occurs over the next few decades. During this time, current commercial coal power plants could burn waste biomass allowing current infrastructure to generate electricity with less heavy metal emissions and non-fossil fuels. However, current power plants require pulverization of fed biomass which proves troublesome for raw biomass which jams these pulverizers. Torrefaction can treat biomass and produce grindable material which could potentially be utilized in current coal power plants without significant modification. However, this process is energy-intensive and produces significant amounts of CO which causes air quality issues. Therefore, this work seeks to use coal combustion flue gas as an energy source and low oxygen stream for torrefaction along with a novel magnetically separable catalyst developed in this work to improve process economics and CO emissions respectively.

Herein, this work demonstrates that the use of the magnetically separable catalyst developed in this work can remove up to 95% of the CO produced during torrefaction although the efficiency of this removal is dependent on the amount of oxygen in the simulated flue gas. Additionally, the increase in the heating value of the torrefied biomass allows it to be co-fired in a conventional coal power plant at a 30-40% replacement rate without any capital changes to the power plant unit. Additionally, interactions between bio-oil produced in the process, O_2, and H_2O were identified that contribute to H_2 production and CO removal.

5.2 Catalyst Development

The biomass torrefaction catalysts utilized in this work have been synthesized via two distinct methods, that is wet impregnation and co-precipitation. Apart from their activity differences, each synthesis technique has different physical properties that influence how the final catalyst pellet/shape can be formed. Producing the catalysts via the wet impregnation methodology yields a paste-like consistency that can be physically shaped into not only pellets but can be formed around an SSWM monolith of any shape, which may prove to be useful for certain applications. While the co-precipitation synthesis produces a similar paste-like consistency, the paste does not retain its shape after calcination either due to the decomposition of Cu, Zn, as well as Al carbonates in contrast to wet impregnation in which the alumina is present in its final oxidized form from the beginning, or due to the low alumina content of these catalysts since alumina can be utilized as a binding agent [151]. Therefore, the most reliable way to create a solid pellet for the co-precipitated catalyst sample is to press the powder into a pellet with an SSWM core via the usage of a hydraulic press.

As detailed previously, these catalysts can be produced via two distinct pathways depending on the desired properties of the final catalyst. Apart from just differences in the ability to shape the catalysts, there are also differences in the activity of the catalysts. The catalysts produced via wet-impregnation have low activity, although the addition of zinc to the catalysts helps to increase their activity, especially at higher temperatures, as shown in Figure 5.1.

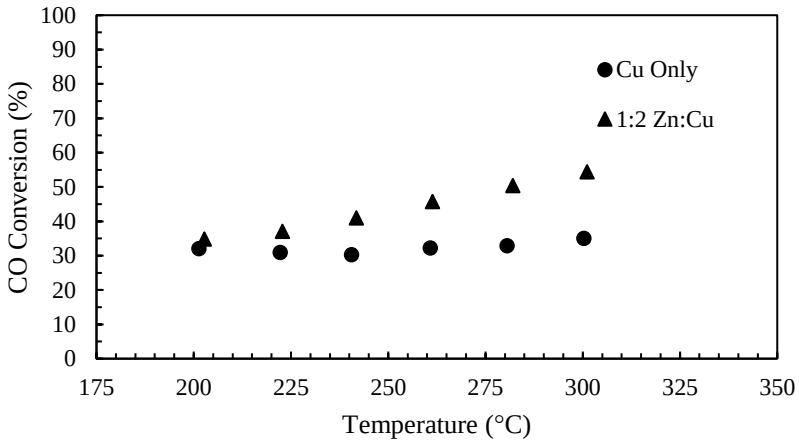

Figure 5.1. Comparison between Cu and Cu/Zn wet-impregnation catalysts.

In contrast, co-precipitation catalysts have higher activity at all temperatures when compared to wet-impregnation catalysts as shown in Figure 5.2. Even when normalizing the catalysts on a space velocity basis, co-precipitated catalysts outperform those produced via wet-impregnation. As co-precipitated catalysts contain 80 wt% active materials (26.7% Zn and 53.3% Cu) and wet-impregnated catalysts contain 20 wt% active materials (6.7% Zn and 13.3% Cu), 500 mg of wet-impregnated catalyst would have the same active metal normalized space velocity as 125 mg of co-precipitated catalyst. As 100 mg of co-precipitated catalyst can out-perform 500 mg of wet-impregnated catalyst, this catalyst is more efficient on a per gram of active metal basis and was therefore selected as the optimum synthesis route.

Based on these results, co-precipitation was selected as the synthesis methodology, as it is more efficient on a per mass basis and therefore more cost-effective. This methodology is also easier to scale on a laboratory basis due to only the need for a larger pump, mixer, and vessel as opposed to requiring a larger heater necessary for solvent evaporation for wet impregnation. Additionally, it should be noted that additional

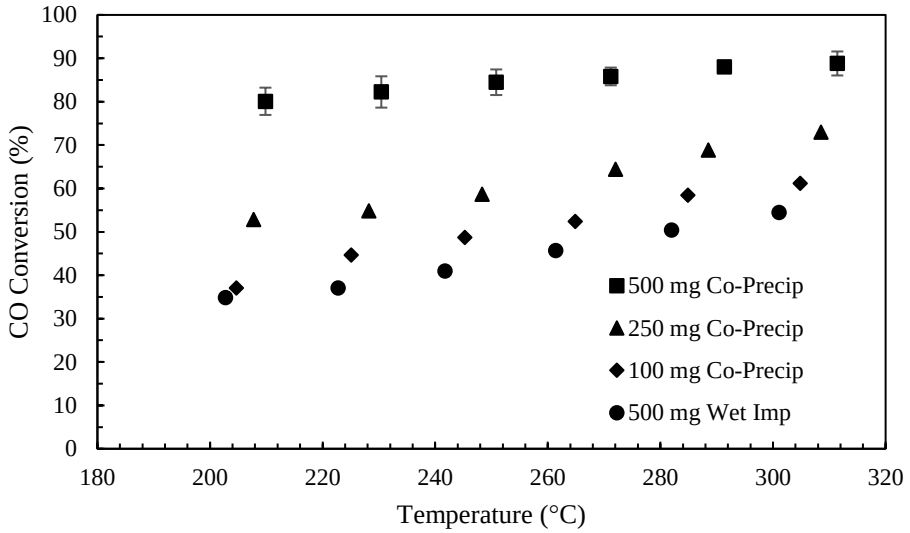

Figure 5.2. Comparison between wet-impregnation and co-precipitation catalysts.

experiments were conducted to determine the influence of co-precipitation temperature as well as gas blanket composition and it was determined that the difference in catalyst activity when co-precipitated at room temperature and 80°C, as well as the difference in activity when using a nitrogen blanket vs static air in the co-precipitation vessel was within experimental error. Therefore, all further experimentation utilizes catalysts co-precipitated at room temperature and without any inert blanketing (exposed to air). As utilizing heating an inert gas blanketing adds additional cost without any increase in activity, these additional expenses are unjustified and therefore not needed.

To further determine optimal synthesis conditions, a Plackett-Burman design of experiments was utilized. This particular design of experiments allows for the screening of a large number of different factors with a low number of experiments and was well suited for determining the effect of a variety of different synthesis factors, specifically calcination temperature, Cu:Zn ratio, stirring rate, aging time, and synthesis volume. A complete

summary of the experimental parameters of the design of experiments can be found below in Table 5.1.

Table 5.1. Experimental Parameters for Plackett Burman Design on Experiments.

Experimental Number	Cu:Zn Ratio (weight)	Stir Rate (rpm)	Volume (mL)	Calcination Temperature (°C)	Aging Time (h)
1	1	180	75	450	2
2	1	180	125	350	5
3	2	250	125	350	2
4	2	180	125	450	5
5	2	250	75	350	2
6	2	180	75	350	5
7	1	180	125	350	2
8	2	250	125	450	5
9	1	250	125	450	2
10	2	180	75	450	2
11	1	250	75	450	5
12	1	250	75	350	5

Utilizing these experimental parameters and comparing the activity of the catalysts to a commercial standard (Hi-Fuel R120) benchmark at temperatures from 200°C and 300°C. In general, the best-performing catalysts synthesized here were comparable or outperformed the Hi-Fuel standard while the worst performing catalysts significantly underperformed relative to the benchmark, especially at lower temperatures. A summary of the activity data at all examined temperatures is shown below in Table 5.2.

Since this synthesis methodology can produce catalysts with activity comparable to a commercial benchmark, however an understanding of how each synthesis variable influences the activity of the produced catalyst is also required to not only improve activity but also reduce synthesis cost. For example, if aging time or solution volume only has a

Table 5.2. Catalyst conversion for DOE catalysts at selected temperatures.

Experiment Number	Conversion at 200°C (%)	Conversion at 220°C (%)	Conversion at 240°C (%)	Conversion at 260°C (%)	Conversion at 280°C (%)	Conversion at 300°C (%)
1	35.5	61.2	66.6	79.2	83.5	86.1
2	55.8	59.7	69.2	72.2	79.2	87.3
3	61.1	67.8	71.9	73.2	75.3	79.1
4	61.0	64.7	79.7	82.9	90.1	89.0
5	51.3	62.7	67.9	68.6	78.4	79.9
6	62.8	65.9	71.6	75.3	80.5	81.4
7	55.8	68.3	74.9	78.6	83.5	87.6
8	57.6	68.7	67.3	72.4	75.9	83.8
9	65.7	77.2	85.2	86.2	88.4	90.8
10	55.0	69.2	78.7	81.6	87.9	88.0
11	65.6	76.1	80.5	86.8	88.4	90.0
12	49.7	58.6	65.0	74.2	74.8	76.6
Hi Fuel R120	69.7	73.5	76.8	80.5	85.7	90.4

negligible influence on the activity of the catalyst it may be more advantageous to choose a shorter aging time or to reduce solution volume to save costs if only an incremental increase in activity accompanies the additional cost. A summary of the influence of each of the synthesis parameters at varying temperatures is shown in Figure 5.3. It should also be noted here that allowing the catalyst to dry fully before calcining results in a superior catalyst than calcining while the catalyst powder is wet.

As shown in Table 5.2, the differences in activity between the catalysts decrease as a function of temperature and the convergence in catalyst performance makes concluding how various synthesis parameters influence performance more difficult. Therefore, to draw statistically significant conclusions and to make the process more robust over a wider range of temperatures, statistical analysis of the data set was done at 260°C, 280°C, and 300°C. At 300°C no single factor is significant ($p<0.05$) and no conclusions can be drawn about

Term	Contrast		Lenth t-Ratio	Individual p-Value
Calcination Temperature	3.91667		4.58	0.0073*
Cu:Zn Ratio	-1.93333		-2.26	0.0458*
Stir Rate	-0.70000		-0.82	0.3759
Aging Time	-0.30000		-0.35	0.7561
Volume	-0.01667		-0.02	0.9852

Term	Contrast		Lenth t-Ratio	Individual p-Value
Calcination Temperature	3.55000		3.19	0.0212*
Stir Rate	-1.96667		-1.77	0.0919
Cu:Zn Ratio	-0.80000		-0.72	0.4433
Aging Time	-0.68333		-0.61	0.5894
Volume	-0.08333		-0.07	0.9477

Term	Contrast		Lenth t-Ratio	Individual p-Value
Calcination Temperature	2.98333		1.57	0.1244
Stir Rate	-1.60000		-0.84	0.3664
Cu:Zn Ratio	-1.43333		-0.76	0.4181
Volume	1.30000		0.68	0.4651
Aging Time	-0.28333		-0.15	0.8932

Figure 5.3. Statistical analysis of DOE synthesis parameters at 260°C (top), 280°C (middle), and 300°C (bottom).

the effect of synthesis parameters on the catalyst at this temperature. However, at 280°C and 260°C calcination temperature becomes a statistically significant synthesis variable and at 260°C Cu:Zn ratio also becomes statistically significant. For these variables, a high calcination temperature, and low Cu:Zn ratio is optimal and a catalyst in the DOE with these factors had the highest activity at 300°C.

In addition to a low Cu:Zn ratio improving the activity of the catalyst, the presence of additional Zn also enhances the sulfur resistance of the catalyst as Zn will poison with sulfur before Cu, forming a sacrificial portion of the catalyst [152]. Additionally, the knowledge that the other synthesis variables are not statistically significant also allows cost-saving measures to be made regarding catalyst synthesis. As stir rate, solution volume, and aging time do not statistically influence catalyst activity, larger-scale catalyst

production could be accomplished with less powerful stirrers, lower solution volumes, and shorter aging times or without aging. Therefore, this knowledge can save on capital costs, waste treatment, and increase catalyst production throughput respectively.

It should also be noted that the catalyst is also active when oxygen is added to the simulated gas feed. As shown in Figure 5.4, the presence of oxygen suppresses activity at low temperatures but is more active at high temperatures. However, the water gas shift reaction no longer occurs, and instead, CO oxidation by O_2 occurs as no H_2 production is observed.

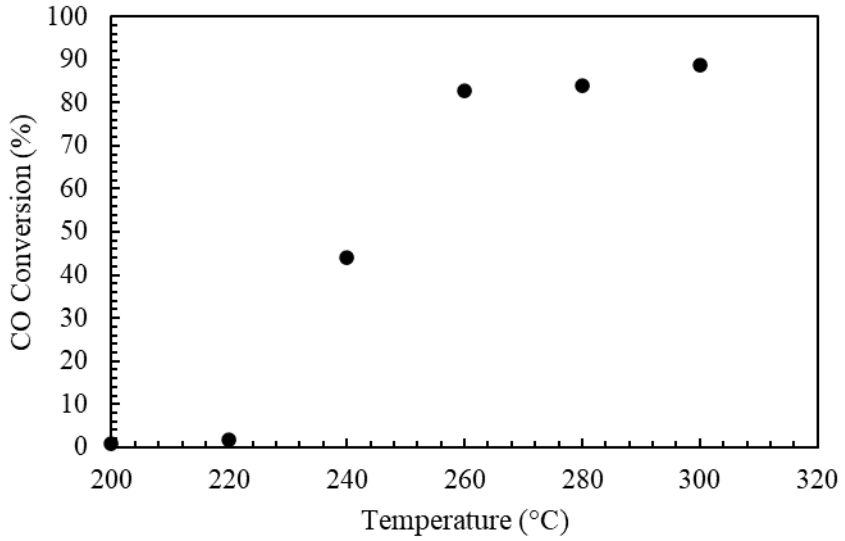

Figure 5.4. Activity of the optimized catalyst when O_2 is present

Catalysts prepared both by wet-impregnation and co-precipitation initially consisted of copper oxide and zinc oxide and after exposure to CO, H_2O, and O_2, these phases remained present with XRD of freshly prepared catalysts shown in Figure 5.5 where the weight loading refers to the weight loading of total active metal (copper and zinc) at the ratio that was previously optimized.

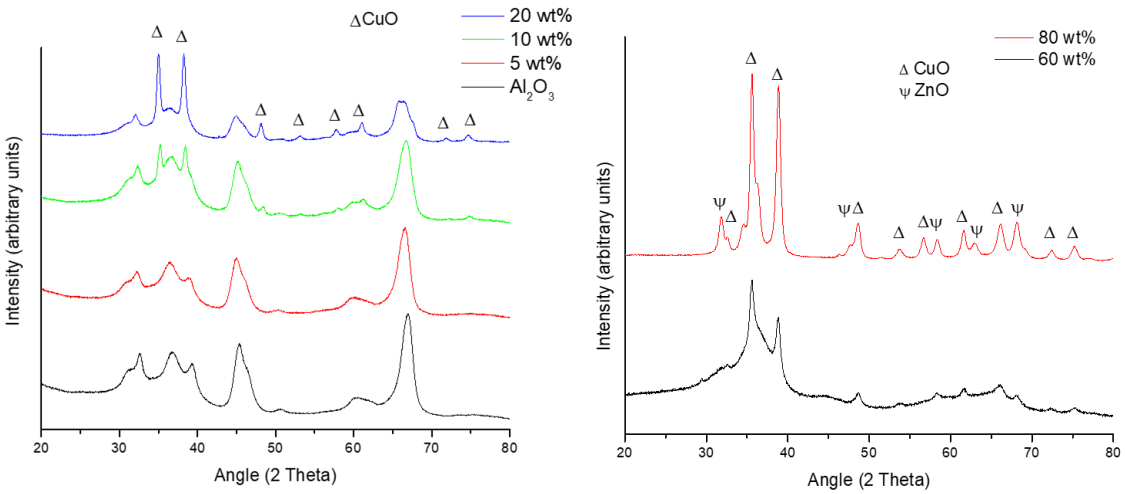

Figure 5.5. XRD patterns of freshly prepared (left) wet impregnated and (right) co-precipitated water gas shift catalysts at varying loadings of active metals.

However, when exposed to CO and H_2O only, copper oxide was reduced to copper metal as shown in Figure 5.6 for both wet-impregnated and co-precipitated catalysts. Therefore, under these conditions, water is not a strong enough oxidant to fully oxidize the catalyst to oxide, and oxygen is required. This also confirms that when oxygen is present, the catalyst remains in the oxide form while when oxygen is not present the catalyst is present as a metal.

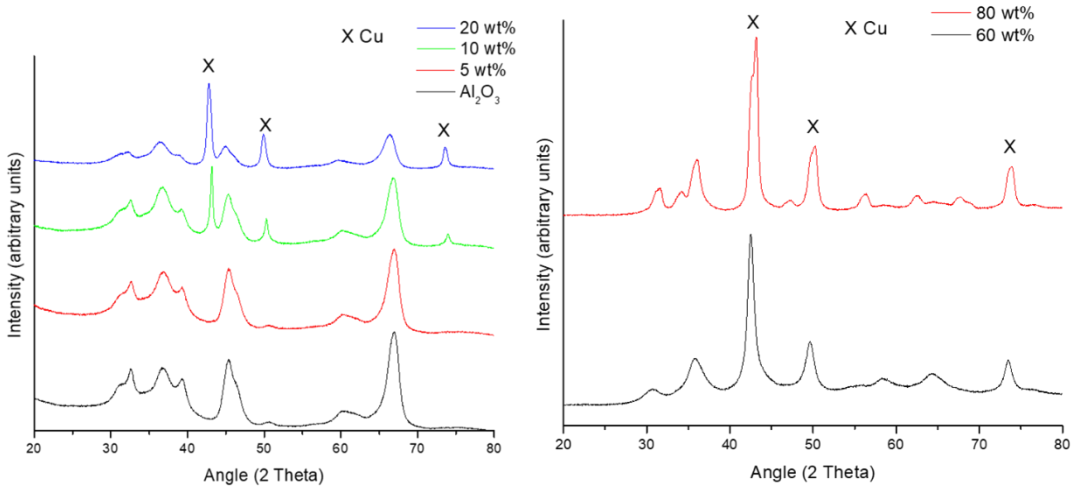

Figure 5.6. XRD patterns (left) wet impregnated and (right) co-precipitated water gas shift catalysts at varying loadings of active metals after reaction without oxygen.

In addition to varying the chemical composition of the catalyst, additional design choices must be made due to the methodology in which the catalyst is used. To maintain contact of the biomass and catalyst, the two are physically mixed and are required to be separated before utilization of the biomass as a lack of separation results in contamination of the biomass feedstock with metals as well as higher catalysts costs required to make up for the lack of catalyst recycling in the process without proper separation. For this reason, the catalyst was pelletized via one of two methods. First, catalysts synthesized via wet impregnation can be dried almost to completion (before calcination) until resembling a play-doh like consistency and then physically shaped to the desired form. However, this requires careful control of the drying procedure to avoid drying out before shaping, intensive physical processing, lower catalyst activity, and a practical limit of active metal loading to around 20-30%. However, one advantage to this process is the ability to shape the catalyst into essentially whatever shape is required and may have some use in specialty applications but for this work, the advantage is significantly outweighed by the disadvantages and is not considered for the rest of the work. Attempting to use co-precipitated catalyst powder in the same manner as described above results in pellets that crumble upon slight touch. In contrast, calcining and fully drying the powders and pelletizing using a hydraulic press produces pellets with good mechanical properties regardless of how the catalyst powder was synthesized. However, these pellets are extremely difficult to separate from torrefied biomass pellets as they are approximately the same color and are both pelletized as shown in Figure 5.7 where biomass pellets are mixed with catalyst pellets. There are differences in pellet density that could be exploited the enable separation but an incomplete separation of the pellet from the biomass would likely

be a major problem when utilizing this method, therefore an additional method is required that can rapidly separate the pellets from the biomass in a cost-effective manner.

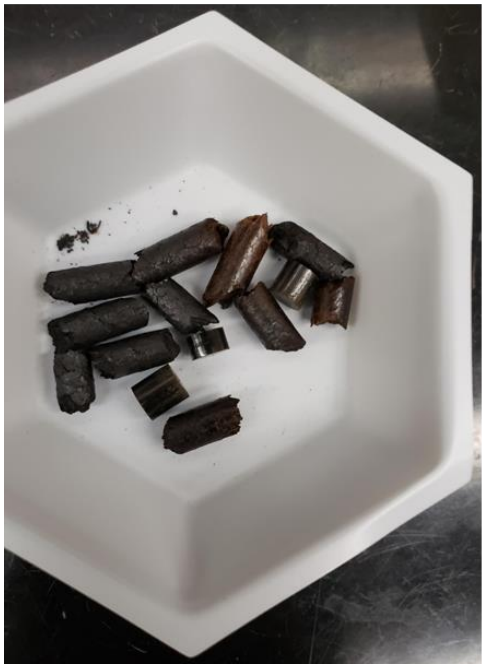

Figure 5.7. A mixture of biomass and catalyst pellets.

One methodology to accomplish rapid, accurate separation of the two pellets is to utilize magnetic separation. However, zinc, aluminum, and copper are not magnetic enough to separate from the torrefied biomass and an additional magnetic component is required to be added to the pellets. Additional metals could be precipitated along with the copper, zinc, and aluminum to serve as the magnetic component, but extensive testing would be required to optimize the required loading of this component while maintaining the catalytic activity of the pellet. Therefore, a magnetic core or sheath was embedded into the pellets during pelletization in the form of stainless-steel wire mesh. This can either be done via embedded into the core of the pellet or as a sheath around the pellet and has the advantage of physically stabilizing the pellet in addition to making the pellets magnetic. To

investigate the increase in physical stability, the pellets were tumbled for specified periods and the mass remaining in the solid pellet was recorded as shown in Figure 5.8.

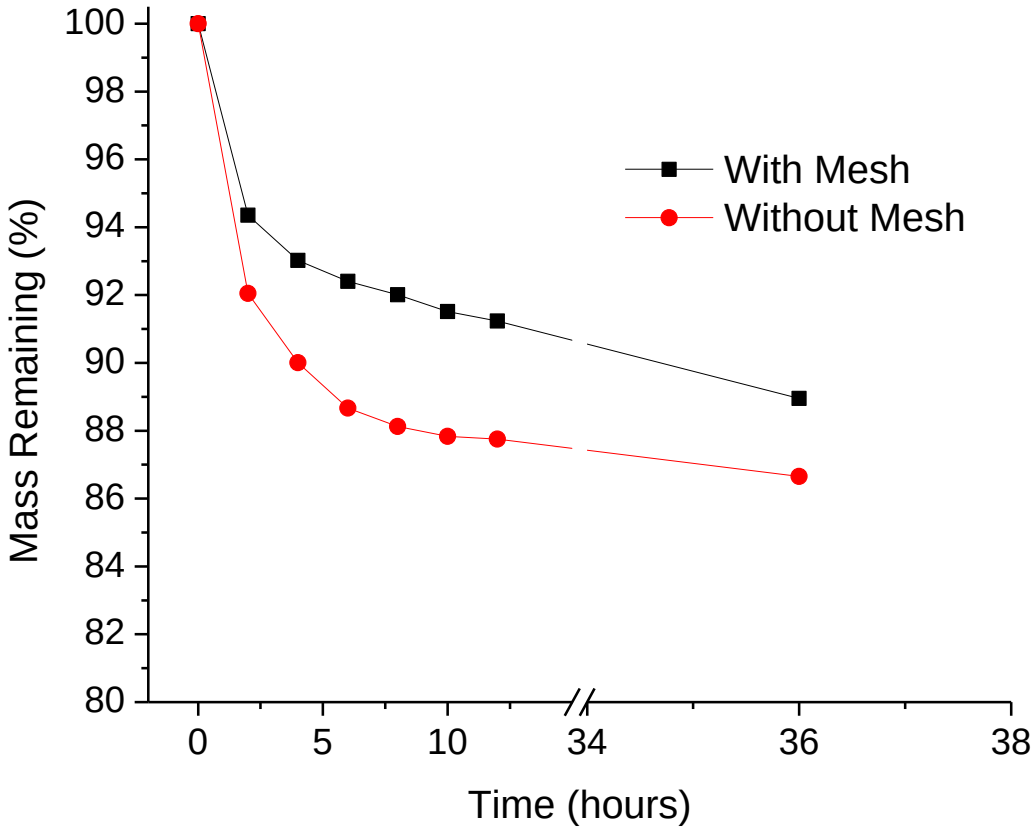

Figure 5.8. Differences in mechanical stability for mesh reinforced and mesh-free catalyst pellets.

As shown above, the addition of mesh to the pellets helps prevent mass loss from the pellet at all time points and is particularly beneficial initially. Therefore, in addition to allowing magnetic separation of biomass and catalyst, the addition of the stainless steel also enhances the mechanical properties of the biomass pellets. To further examine this, images of mesh-free and mesh-containing catalyst pellets are shown in Figure 5.9, with mesh-free catalyst pellets exhibiting significantly more pronounced rounding and physical damage during the testing process when compared to the mesh-containing catalyst.

To demonstrate the ability of the mesh containing catalyst pellets to be readily separated from torrefied biomass, a simple laboratory magnetic stir bar was utilized to retrieve the catalyst pellets from a mixture of catalyst pellets and torrified biomass as shown in Figure 5.10.

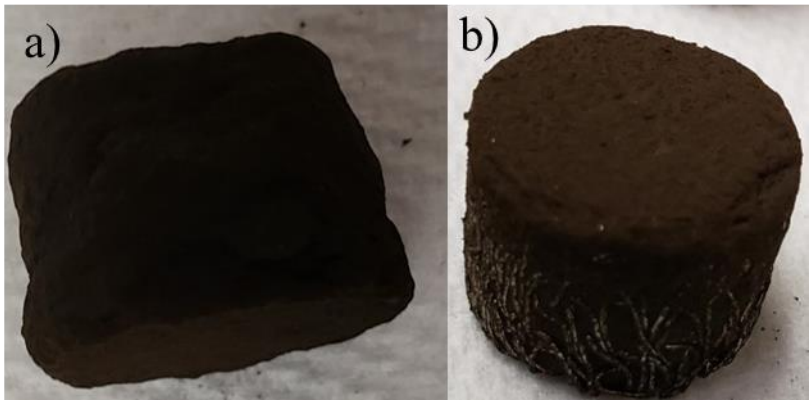

Figure 5.9. Catalyst pellets after mechanical testing a) with and b) without the use of stainless steel mesh.

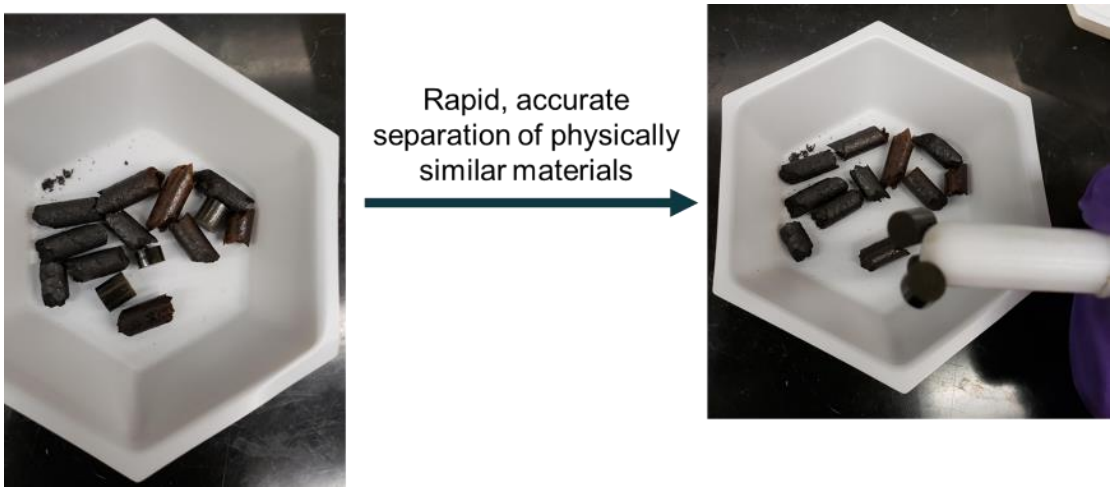

Figure 5.10. Separation of biomass and catalyst pellets using magnetic separation.

5.3 Biomass Torrefaction

While a variety of different biomass feedstocks can be utilized, the main feedstock utilized in this work is forestry and logging residue as this is the most relevant feedstock for South Carolina and much of the southeast due to the thriving wood and paper industry in the region [153]. Therefore, we selected woody residue biomass produced from Enviva located in Greenwood, SC as representative biomass for the region that would enable a more seamless transition from laboratory testing scale to a potentially scaled-up production facility if that route was pursued in the future. However, before investigating the effect of the catalyst on biomass torrefaction, a thorough understanding of the torrefaction process influences the biomass is required. Therefore, catalyst-free torrefaction experiments were carried out to gain this understanding. To determine the influence of torrefaction temperature and time (both measures of torrefaction severity) on product yields these factors were varied at constant oxygen concentration (2%). A summary of these results is shown in Figure 5.11 where increasing torrefaction severity results in a lower solid yield and an increase in liquid and gas yield.

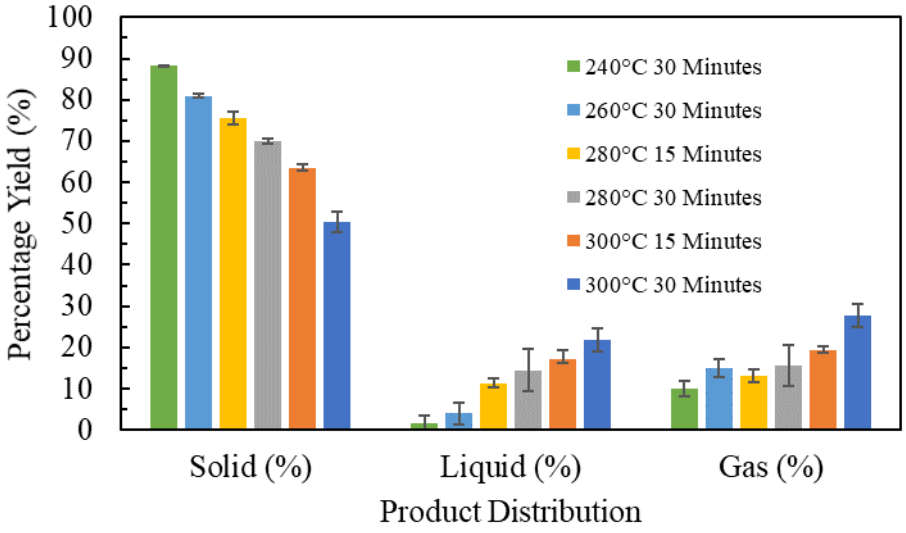

Figure 5.11. Torrefaction yields as a function of temperature and torrefaction time with 2% oxygen in the simulated flue gas.

Each increase in torrefaction temperature or time of yield reduces the yield of solid biochar by a fairly constant amount (around 5-10% per each 20°C increase) except for the increase from 280 to 300 °C which resulted in a large decrease in solid yield from ~70% to ~50%. In addition, a decrease in solid yield is accompanied by an increase in liquid or gas yield with both yields increasing fairly monotonically with increasing treatment severity. Photographs of torrefied biomass at various times and temperatures compared to raw biomass pellets are presented in Figure 5.12.

Figure 5.12. Photographs of torrefied and raw biomass.

Additionally, increasing the severity of torrefaction also increases the HHV of the fuel with a summary of this increase shown in Table 5.3.

Table 5.3. HHV of torrefied biomass

Units	Raw Biomass	**260°C**	**280°C**	**300°C**
MJ/kg	18.9	20.1	21.2	22.7

Due to the quantities of biomass produced within the reactor system at UofSC, some types of analysis are not feasible to be conducted and therefore larger sample sizes are required. To accomplish this, biomass was torrefied within the flue gas system of Santee Cooper's Cross Generating station at 300°C with nominally ~2% O_2. In addition to allowing larger amounts of biomass to be tested simultaneously, this also has the advantage of being tested under actual, non-simulated test conditions which gives a more realistic measure of torrefaction efficacy. As shown in Table 5.4, the properties of the biomass change drastically after torrefaction.

Table 5.4. Properties of woody biomass before and after torrefaction at Cross Generating Station.

Analysis	Units	Raw Biomass	**Biomass w catalyst**
Calorific Value (ar)	BTU/lb	7855	11037
Calorific Value (dry)	BTU/lb	8439	11465
Calorific Value (maf)	BTU/lb	8515	11662
Total Moisture	%	6.93	3.73
Ash (ar)	%	0.83	1.63
Ash (dry)	%	0.89	1.7
Sulfur (ar)	%	0.02	0.07
Sulfur (dry)	%	0.02	0.07
Carbon (ar)	%	47.58	65.69
Carbon (dry)	%	51.01	68.23
Hydrogen (ar)	%	5.78	4.62
Hydrogen (dry)	%	6.21	4.8
Nitrogen (ar)	%	0.15	0.19
Nitrogen (dry)	%	0.16	0.2
Volatile Matter (ar)	%	80.15	49.55
Volatile Matter (dry)	%	86.12	51.47
Fixed Carbon (ar)	%	12.09	45.08
Fixed Carbon (dry)	%	13	46.83
Oxygen (ar)	%	38.82	24.06
Oxygen (dry)	%	41.71	24.99
H:C Ratio (ar)		1.46	0.84
H:C ratio (dry)		1.46	0.84
O:C Ratio (ar)		0.61	0.27
O:C Ratio (dry)		0.61	0.27

After torrefaction, the dry heating value increases from 8439 BTU/lb to 11465 BTU/lb. At this heating value, torrefied biomass is capable of replacing 30-40% of coal at a conventional coal-burning power plant such as Cross Generating Station with no structural or capital adjustments required at the plant. Although not qualitatively measured here, after torrefaction the biomass is capable of being crushed using the coal pulverizers currently utilized at the plant. Conventional biomass has been previously run through these pulverizers, however, this quickly resulted in the jamming and gumming up of these grinders resulting in costly downtime and interruption in power generation which has implications at the state and regional level. Additionally, the moisture content is nearly halved resulting in superior storage properties as high moisture contents enable microbial growth which results in loss of biomass and the potential for fires due to heat generation. Additionally, as most power plants have non-condensing boilers and heat recovery systems, the vaporization of water results in a loss of potentially harvestable heat decreasing the efficiency of the power generating station. The increase in sulfur content can be due to a decrease in mass due to loss of volatile biomass species with the retention of natural sulfur, resulting in a concentration of natural sulfur. However, because the sulfur concentration more than triples and under these conditions, the biomass does not reduce in mass to a third of its original mass (based on experiments conducted in our laboratory at similar conditions), sulfur must also be added to the biomass. Since sulfur is a well-known component of coal flue gas, the source of this sulfur is likely uptake from the flue gas the biomass is treated with. A decrease in hydrogen content and increase in carbon content is expected due to the loss of water and other volatile species during bio-char formation and is observed here and graphically shown on the Van-Krevelen diagram shown below in

Figure 5.13 with the red star representing fresh biomass and the red pentagon representing biomass torrefied at Cross Generating Station. As shown, the torrefaction process changes the chemical composition of the raw biomass enough to shift the biomass to be more like a medium to high-grade lignite coal. While this is still a low-rank coal, this is a significant improvement in the quality of the biomass.

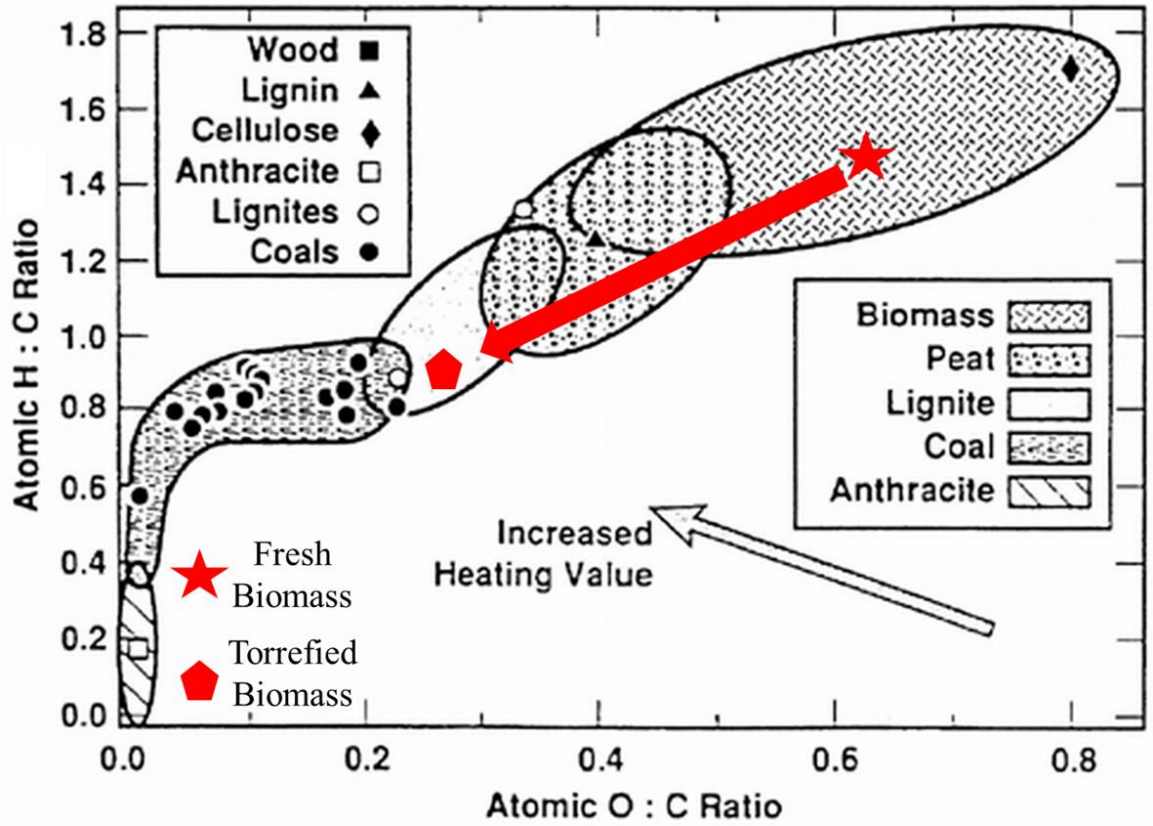

Figure 5.13. Van Krevelen Diagram of Fresh and Torrified Biomass modified from [154].

As the oxygen concentration in the flue gas is not constant with coal boiler load and increases and the load on the boiler is decreased, it is also important to gain an understanding of how changes to the oxygen concentration in the flue gas influences torrefaction performance as shown in Figure 5.14.

The largest difference in product yield occurs when comparing oxygen-free simulated flue gas with oxygen-containing flue gas. For oxygen-free torrefaction, a solid yield of ~70% is observed while the inclusion of only 2% oxygen results in a solid recovery of only about 50%. However, increasing oxygen concentration beyond the point does not continue to have a similar trend. Even with 11% oxygen, an over fivefold increase in oxygen concentration, the solid yield only decreases to ~35%. Therefore, increasing

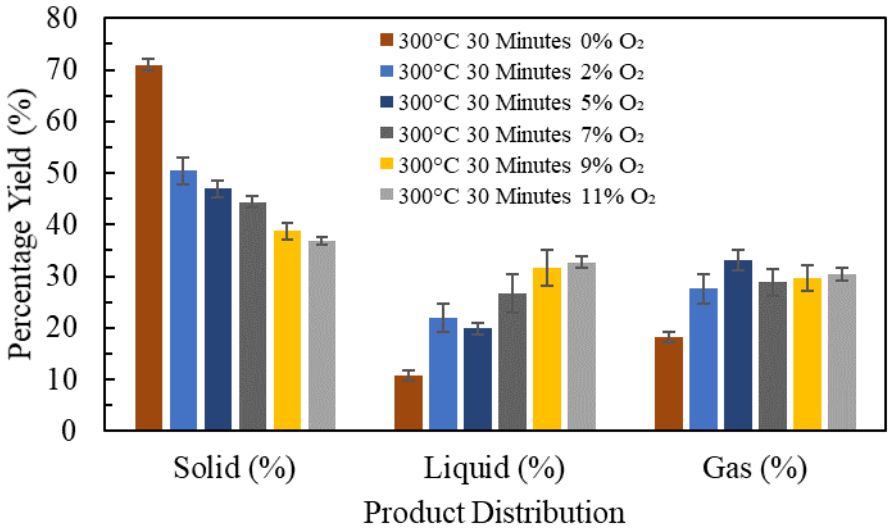

Figure 5.14. Torrefaction yields as a function of torrefaction time and simulated flue gas oxygen concentration.

oxygen does play a role in torrefaction severity, but the largest amount of change occurs upon the initial introduction of oxygen. In general, liquid yields increase with increasing oxygen content but gas yields are essentially within experimental error for oxygen contents at and above 2%. As liquid yields increase with essentially constant gas yield, increasing oxygen content either increases the production of bio-oils or causes increased production of water. As the ratio of H:C is decreased during torrefaction and continues decreasing with increasing torrefaction severity, increased water production would be consistent with this

change in the H:C ratio and would explain the increase in liquid yield as a function of increased oxygen concentration.

5.4 Analysis of Torrefaction Gas Exhaust With and Without Catalysts

With a basic understanding of how temperature, residence time, and oxygen concentration influence torrefaction yields, further experimentation can be done to analyze how these factors influence torrefaction at a more fundamental level. To accomplish this, mass spectrometry of the torrefaction effluent gases was accomplished utilizing a homemade vacuum chamber with an adjustable leak valve to admit controllable amounts of analyte gas continuously. Due to the size of the torrefaction reactor, it takes time to fully flush the gas contents of the reactor system out and replace it with fresh gas flowing into the system or record changes happening within the system. Therefore, it is also important to have an idea of how long it takes before a change within the system can be recorded analytically. To better understand this, a mixture of nitrogen, hydrogen, oxygen, and carbon dioxide was flown through the reactor at a total flow rate of 250 mL/min without the presence of biomass until an analytical steady-state was reached. After reaching steady-state, all gases except nitrogen were shut off between 1.5 and 2.5 minutes on stream (hydrogen was shut off first and then carbon dioxide and oxygen). Within around 30 seconds to a minute after shutting off the gas flow, the concentration of each non-nitrogen gas begins to quickly drop in concentration and within an additional minute or two, the non-nitrogen gases are no longer detected by the mass spectrometer as shown in Figure 5.15. For gases at lower concentrations (hydrogen and oxygen), the time required to no longer be detected is lower (nearly half) than that of carbon dioxide suggesting that this difference is likely due to differences in the time required to clear the reactor system of the

previously utilized gas as opposed to delays within the analytical system which should be less sensitive to concentration due to the differential pumping utilized here.

The shapes shown here are also important to understand when considering the analytical results presented later in this chapter. As the biomass is admitted into the system at room temperature, two delays occur when analyzing the torrefaction off-gas. The first is

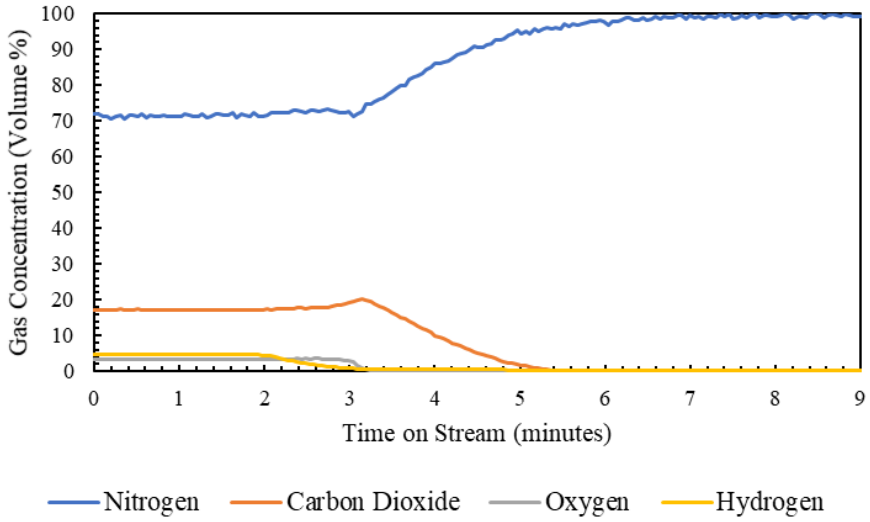

Figure 5.15. Result of a complete gas change over in the torrefaction reactor system.

the previously discussed delay is caused by gas mixing and the second is due to transient temperature in the biomass. After admitting into the reactor there is generally a 3-4 minute delay until the simulated flue gas changes in composition and it takes an additional 5-7 minutes before the amount of carbon dioxide and carbon monoxide is observed to experimentally peak. Therefore, there is a distinct period where the biomass heats up without significant off-gassing and an additional period of a few minutes in which the biomass continues to warm before reaching peak emission. After peaking, the effluent begins to approach the initial inlet gas composition but remains offset due to prolonged torrefaction of the biomass. During this period, carbon dioxide and carbon monoxide

concentration remain elevated, and oxygen remains lower corresponding to the production of CO_2 further nitrogen concentration is slightly decreased due to dilution with additional gas species produced during torrefaction. When 2% O_2 is used, all of the fed oxygen can be consumed at high catalyst loadings. In contrast, only a portion of the fed oxygen is consumed at higher oxygen concentrations. However, at least 2% oxygen is consumed in all experiments containing oxygen. An example analysis of the torrefaction gas effluent is shown in Figure 5.16. All gas concentrations are read from the main left axis except for nitrogen (black trace) which is read from the right secondary axis. It should also be noted here that a bump and change in gas composition occurs within the first few minutes of torrefaction and is a result of changing the gas flow from the bypass channel to the experimental channel which results in nitrogen or air present in the reactor due to sample loading that is flushed out when the experiment begins.

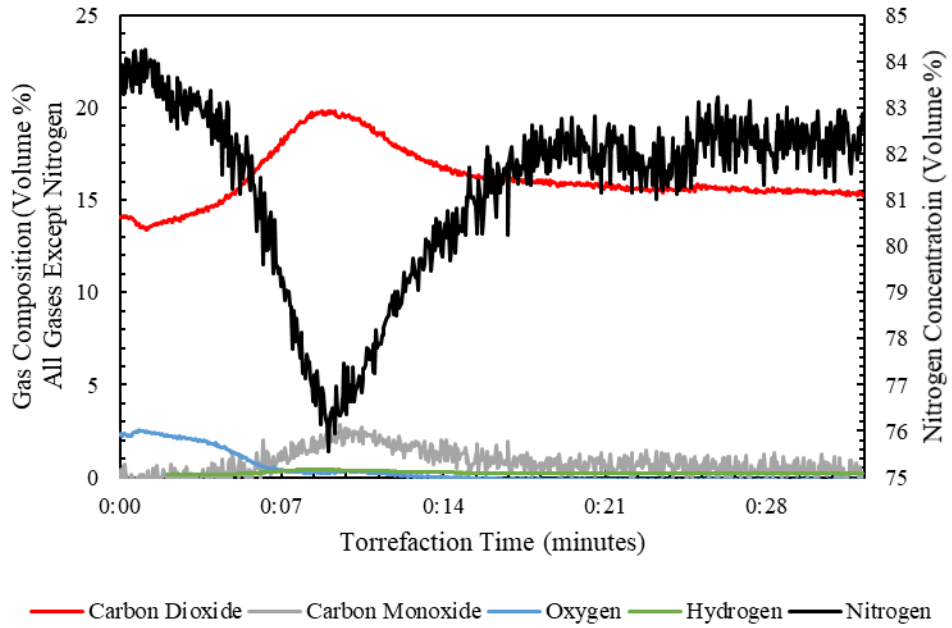

Figure 5.16. Example analysis of torrefaction gas effluent.

With an understanding of the transient behavior of the torrefaction process utilized in this work, the effect of the previously mentioned torrefaction parameters can be further and more fundamentally examined by examining the effluent of the torrefaction process.

In general, torrefaction without the presence of a catalyst resulted in the formation of 3-4% CO at peak emission levels, this number had some variance due to slight changes in heating rate due to positioning of the biomass in the reactor which influenced how rapidly the emissions peaked after introduction into the reactor, therefore comparisons between CO emissions from various experiments were made between total amounts of CO production by integrating the area under the concentration vs. time curve and comparing these integrated values. In addition, the mass spectrometer was calibrated at the start of each day to prevent drift. Additionally, each day a complete set of experiments were done to prevent day-to-day drift influencing results. For example, on a typical day, four experiments were done (no catalyst, 1g catalyst, 0.5 g catalyst, 0.25 g catalyst) at a particular temperature and oxygen concentration.

Optimal CO removal was found utilizing 2% O_2 at high catalyst loadings (1 g catalyst with 4 grams of biomass) with a decrease in peak CO emissions, window in which CO was produced, and the virtual elimination of tailing behavior where low levels of CO continued to be produced after peak emission as shown in Figure 5.17 where integrated CO emissions were reduced by approximately 95%.

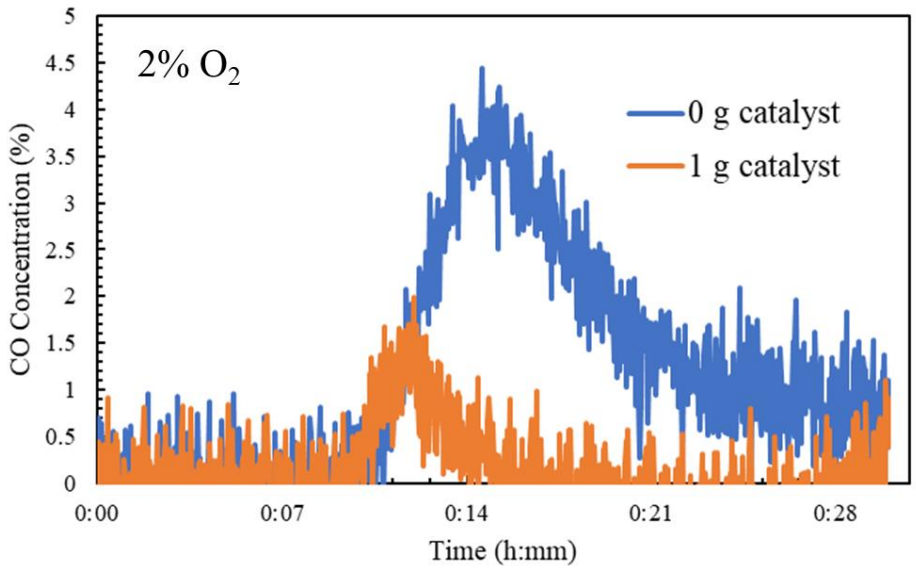

Figure 5.17. Change in CO emissions as a function of catalyst loading at 2% O_2.

At the same oxygen concentration, as the catalyst loading decreased, CO removal efficiency also decreased as shown in Figure 5.18. However, this result was not unexpected as less catalyst is present to carry out the reaction and as the catalyst is physically mixed with the biomass, more slip of CO can occur as this is not a conventional packed bed reactor. Additionally of note, the high degree of error shown here is due to the inhomogeneity of mixing the catalyst with the biomass and slight variances within loading the biomass and positioning the biomass into the reactor system. This inhomogeneity is of greater importance at lower weight loadings where one catalyst pellet is mixed with biomass and settles within the reactor system in-homogenously from experiment to experiment.

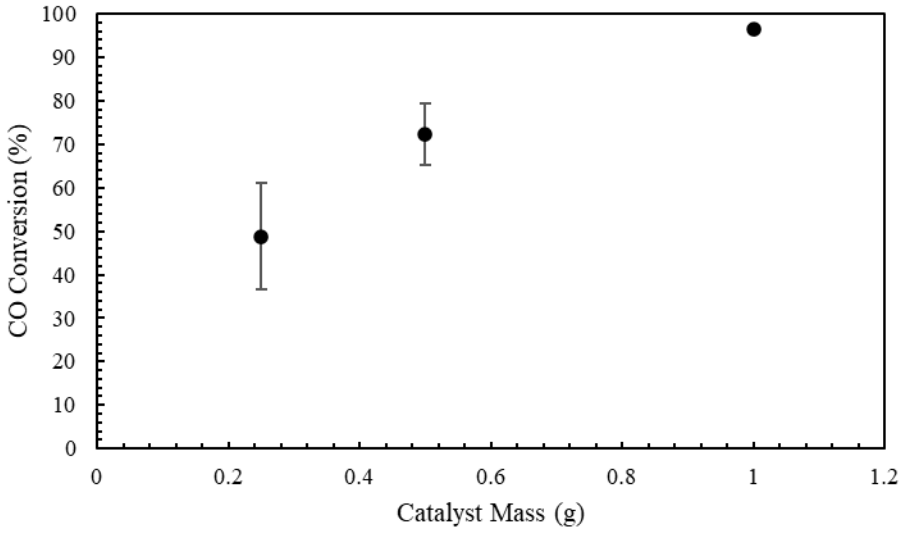

Figure 5.18. Conversion of CO produced via biomass torrefaction as a function of catalyst loading.

Under these conditions, almost all of the fed oxygen is consumed by the biomass as shown in Figure 5.19, where even without the presence of a catalyst around 75% of the fed oxygen is consumed within the process after 20 minutes. With the addition of catalyst, additional oxygen is consumed, and additional oxygen consumption occurs with increased catalyst loading, however, 0.5 g and 0.25 g catalyst data points are similar. The addition of catalyst also causes a steeper drop in oxygen concentration (and at earlier times) indicating that the catalyst consumes oxygen both during initial heating and after peak gas emission from the biomass.

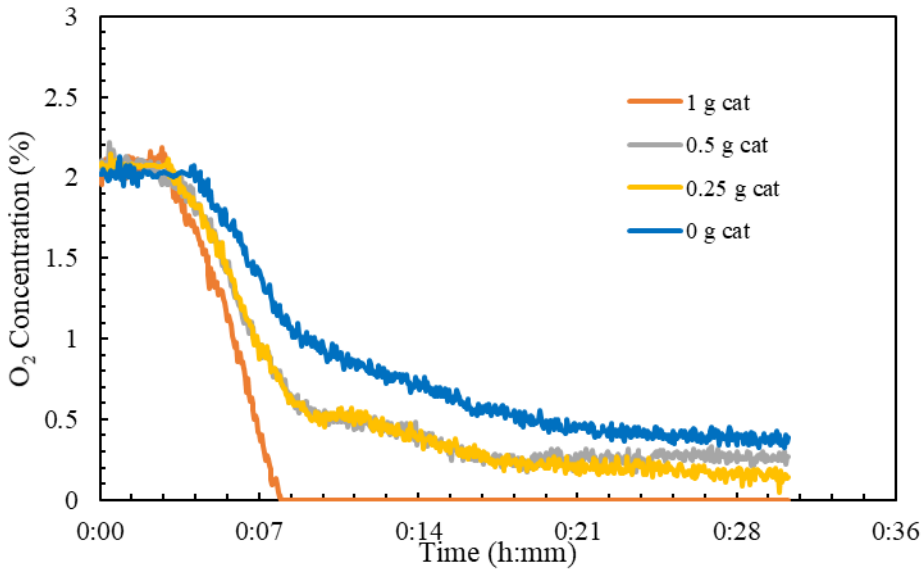

Figure 5.19. Oxygen concentration in torrefaction effluent gas as a function of catalyst loading at 2% oxygen.

These results are interesting because as shown in Figure 5.20, the concentration of hydrogen produced within the process increases with increasing catalyst loading and this increase in hydrogen production corresponds with an increase in oxygen consumption as shown in Figure 5.19. Without the presence of a catalyst, essentially no hydrogen is produced ruling out the biomass by itself producing high levels of hydrogen. As shown in simplified reactions where known concentrations of gas were utilized without biomass, no hydrogen was produced when oxygen was utilized indicating that oxygen suppressed the formation of hydrogen.

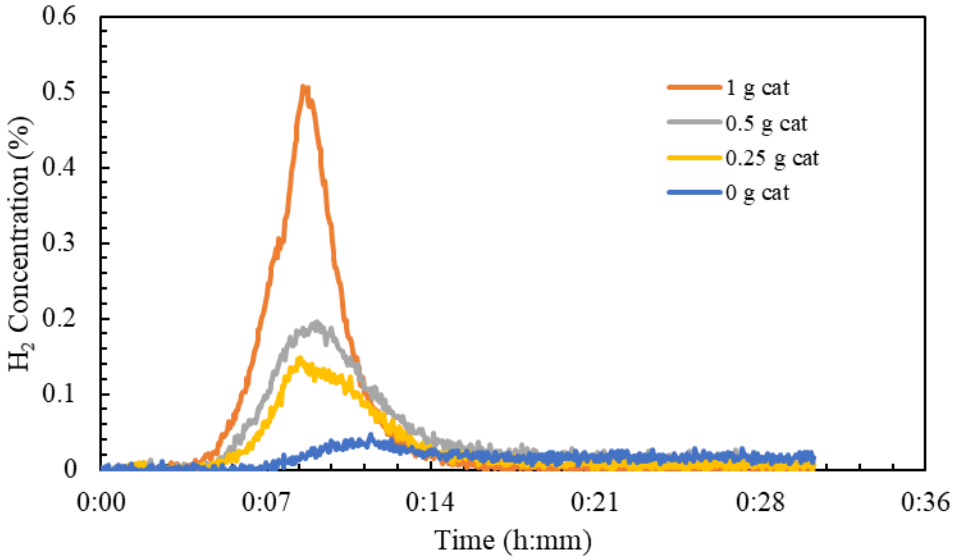

Figure 5.20. Hydrogen concentration in torrefaction effluent gas as a function of catalyst loading at 2% oxygen.

This is not unexpected as metallic copper is responsible for the water gas shift reaction [155] and with the presence of oxygen, copper oxide forms as shown in previous XRD results. This can be seen experimentally as catalysts under water gas shift reaction conditions had an orange/copper appearance indicating metallic copper while catalysts exposed to oxygen in the feed gas remained black corresponding to metal oxide, this is further confirmed via XRD analysis mentioned previously. Additionally, the addition of oxygen suppressed the activity of the catalyst in these simplified experiments at low temperatures further indicating the removal of active metallic copper. However, as shown in experiments where biomass is present, catalysts consume oxygen with increasing oxygen consumption with increasing catalyst loading and this corresponds to increasing hydrogen production. One possible explanation for this is the interaction between the catalyst and bio-oils produced during torrefaction. Further evidence for this interaction is provided in Figure 5.21 where at 2% oxygen, increasing catalyst loading causes darkening

of the produced bio-oil. In general, the darkening of organics is a good indicator for oxygenation or degradation [156] suggesting that the catalyst is interacting with the bio-oil in some way.

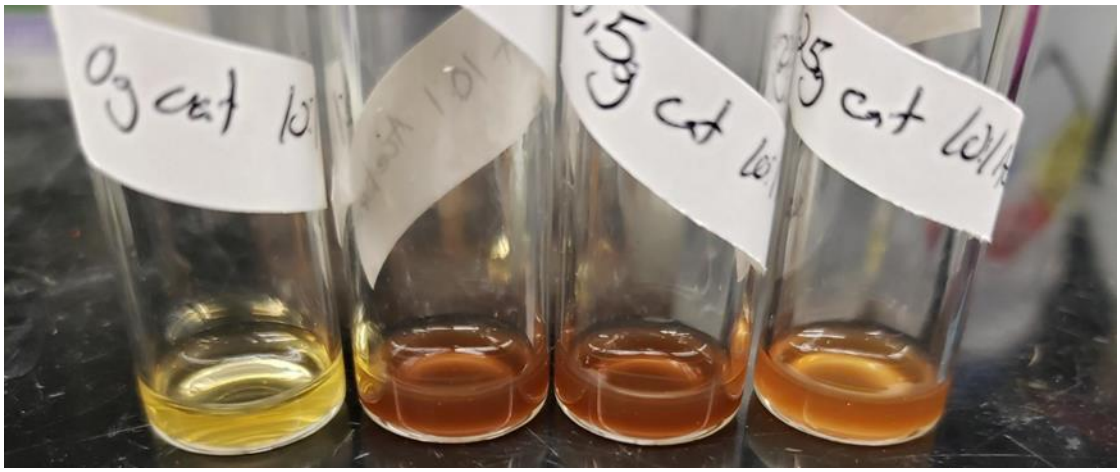

Figure 5.21. Coloration of bio-oil produced during torrefaction as a function of catalyst loading (0g, 1g, 0.5g, and 0.25g catalyst from left to right).

In addition to bio-oil darkening, indications of interactions between the catalyst and torrefaction process can be seen by examining CO_2 concentration as a function of catalyst loading as shown in Figure 5.22. Increasing catalyst loading causes an increase in CO_2 levels in effluent gas again corresponding with hydrogen production, CO reduction, bio-oil darkening, and oxygen consumption. Interestingly, the increase in CO_2 production does not correspond 1:1 with the increase in oxygen consumption as the 0.5-1% difference in oxygen consumption when comparing 0 g catalyst and 1 g catalyst does not correspond to the approximately 10% difference in peak CO_2 emissions. Additionally, it is highly unlikely that solid-solid reactions are occurring with the biomass and catalyst causing direct oxidation of biomass and therefore a gas-phase species or bio-oil must be oxidized to cause this increase in CO_2 production. As bio-oil is known to have highly oxygenated components [157], oxidation of bio-oil would produce more CO_2 per C atom than in longer

chain hydrocarbons within the biomass itself. Additionally, the use of H_2O as an oxidant would also provide a pool of oxygen to produce CO_2 that O_2 itself could not provide. Although it is difficult to determine exactly what reactions are occurring on the surface without extensive experimentation (even for simple reactions), the presence of a complex mixture of bio-oils makes an exact determination essentially impossible. However, a simplified set of reactions that are known to occur with these chemistries can provide a guide for examining phenomena observed here. Tri-reforming, water gas shift, and CO oxidation reactions utilize hydrocarbons, CO, O_2, H_2O, and H_2 and provide a useful pool of reactions to consider where CH_4 serves as a general organic compound that would be present in bio-oil.

$$CH_4 + CO_2 \rightarrow 2CO + 2H_2 \quad (5.1)$$

$$CH_4 + H_2O \rightarrow CO + 3H_2 \quad (5.2)$$

$$CH_4 + \tfrac{1}{2}O_2 \rightarrow CO + 2H_2 \quad (5.3)$$

$$CH_4 + 2O_2 \rightarrow CO_2 + 2H_2O \quad (5.4)$$

$$CO + H_2O \rightarrow CO_2 + H_2 \quad (5.5)$$

$$CO + \tfrac{1}{2}O_2 \rightarrow CO_2 \quad (5.6)$$

While oxygen consumption is not proportional to CO_2 production, H_2 production trends closely mirror the increase in CO_2 formation suggesting the occurrence of reaction 5.5 which produces CO_2 and H_2. Therefore, this increase in both gas species may be due to the water-gas reaction occurring on the catalyst with organic species from bio-oil (represented by CH_4 in the above reactions) initially adsorbed on the surface reacting that

may occupy reactive sites being removed by oxygen exposure (Reaction 5.1) allowing CO to react with water from the reactor feed or organic combustion (Reaction 5.4). These organic species may not be able to be oxidized by the water fed in the process as O_2 is a stronger oxidant which would indicate that some amount of oxygen may be necessary for "cleaning" the surface of the catalyst and water gas shift reaction to occur and H_2 to be produced. However, as shown in the previous activity data with simplified gas feed without the presence of biomass, water can be activated and utilized in the reaction at lower temperatures when only CO and H_2O are present, and it takes higher temperatures to activate O_2. This is readily demonstrated, as oxidation with O_2 only becomes significant at temperatures above 240 °C. While the trends in CO_2 and H_2 production are similar, the amount of H_2 formation also cannot explain CO_2 production from CO oxidation by itself as only ~0.5% H_2 is produced at most. However, as an oxidation catalyst is present much of the H_2 produced may be oxidized either by O_2 or used to re-reduce the catalyst to enable the water gas shift reaction to occur. After peak emission, CO_2 concentrations settle to approximately 14% which does correspond well to the oxygen consumption indicating at the point, most of this oxygen consumption is via the biomass itself. Also as shown previously, increasing oxygen concentration causes increased mass loss of solid biomass, likely due to oxidation and corresponding CO_2 production.

Further confirmation of the role of oxygen can be seen when oxygen is not included as a feed to the torrefaction process. Without oxygen, CO conversion decreases significantly, and interestingly, conversion decreases with increasing catalyst loading as shown in Figure 5.23. Interestingly, for 0.25 g catalyst loading, CO conversion with and

without oxygen is similar, however, at other loadings, 2% oxygen is superior when compared with oxygen-free torrefaction.

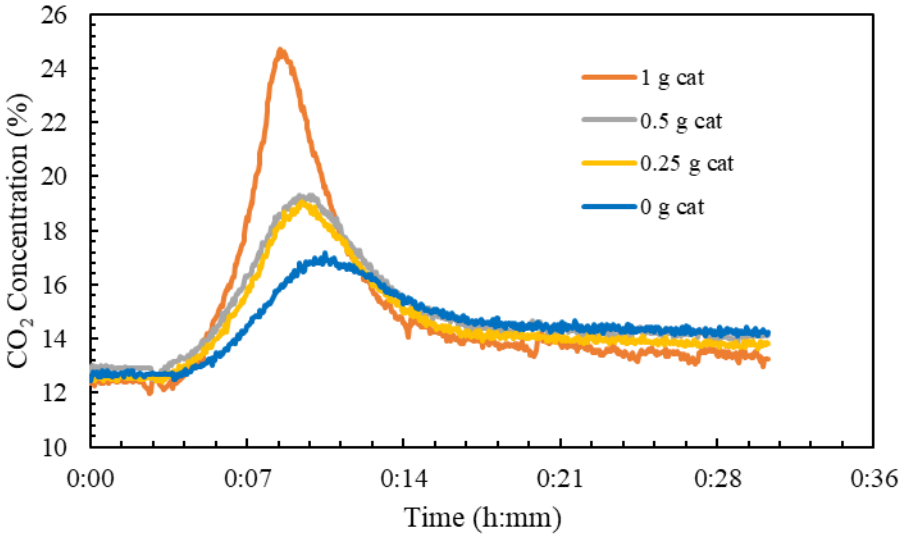

Figure 5.22. CO_2 concentration in torrefaction effluent gas as a function of catalyst loading at 2% oxygen.

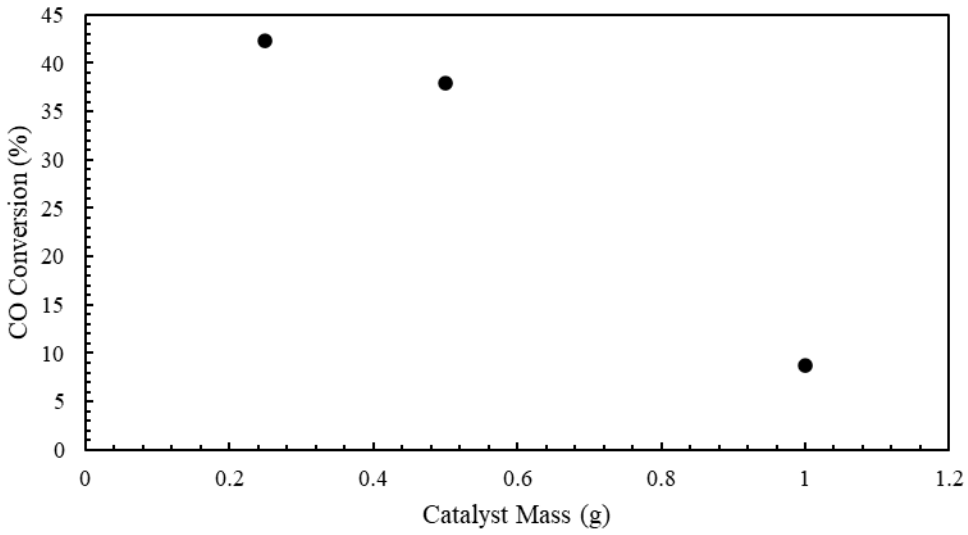

Figure 5.23. Conversion of CO produced via biomass torrefaction as a function of catalyst loading without oxygen.

Both with and without 2% O_2, similar amounts of H_2 are produced with the presence of a catalyst. This suggests that while the removal of O_2 can promote the water-gas shift reaction via prevention of oxidation of the catalyst, the presence of small amounts of oxygen is also beneficial and can promote H_2 production in other ways.

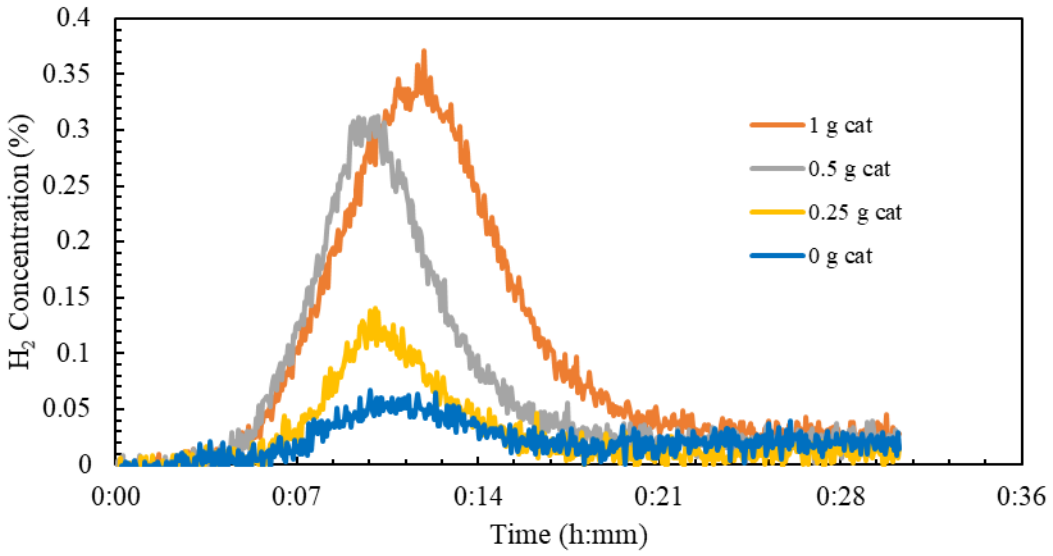

Figure 5.24. Hydrogen concentration in torrefaction effluent gas as a function of catalyst loading without oxygen.

The largest change when comparing oxygen-containing and oxygen-free torrefaction is the amount of CO_2 produced. As shown in Figure 5.25 with no oxygen in the torrefaction feed, similar amounts of CO_2 are produced with and without the presence of 0.25 g of catalyst, but excess CO_2 is produced with 0.5 g and 1 g of catalyst suggesting that to some extent, water or a species produced during torrefaction can serve as an oxidant although this oxidant is not as strong as oxygen. Additionally, bio-oil color changes are still observed with increasing catalyst loading even without the presence of O_2, suggesting that if oxidation is responsible for the color change, then it can still occur without O_2 which

would mean another oxidizing species, such as H_2O would need to be responsible for this change.

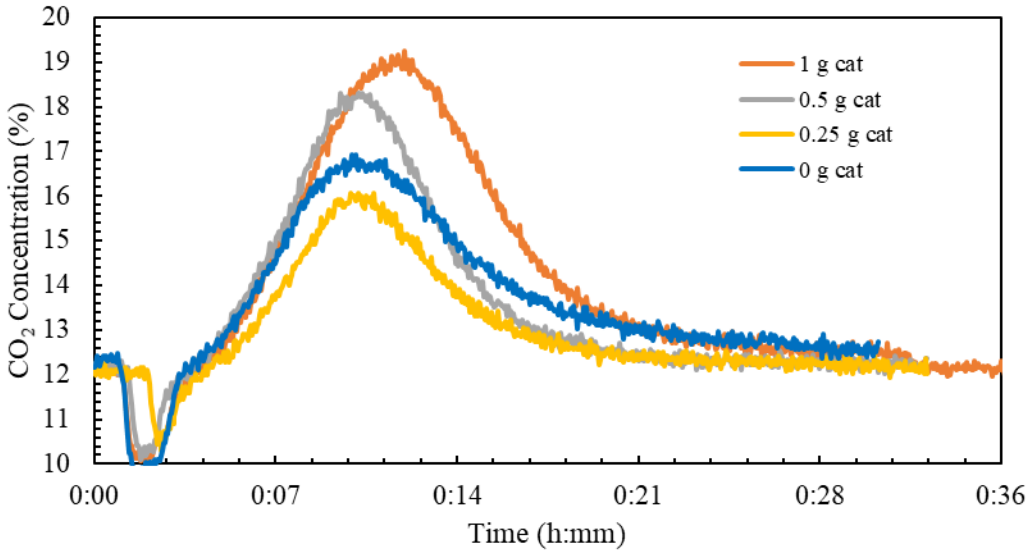

Figure 5.25. CO_2 concentration in torrefaction effluent gas as a function of catalyst loading without oxygen.

Interestingly, removal of oxygen is not beneficial for CO removal as shown in Figure 5.26, where at high catalyst loading, less than 20% of the CO produced during torrefaction is removed by the catalyst and with 0.25 g of catalyst "negative" conversion is shown indicating that more CO was produced than without the presence of the catalyst although based on the size of the error bars shown with 2% O_2 in the feed, this is within error of no change in CO concentration happening at all.

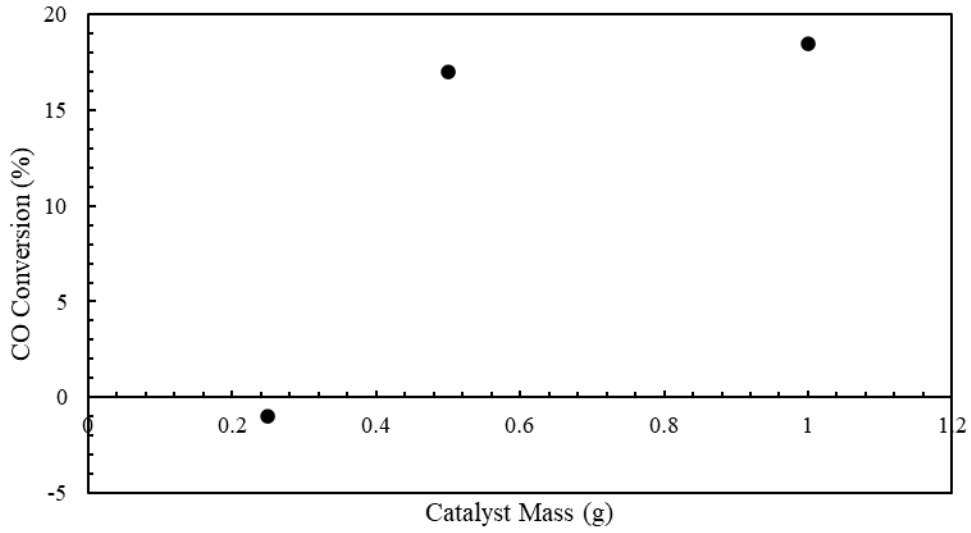

Figure 5.26. Conversion of CO produced via biomass torrefaction as a function of catalyst loading without oxygen.

It is rather unexpected that additional H_2 is produced with the addition of more O_2, in fact at all catalyst loadings, significantly more H_2 is produced with 5% O_2 when compared with 0% or 2% O_2. Additionally, of note is the shouldering behavior of the H_2 production curve with 1 g of catalyst on the left side of the curve before maximum production shown in Figure 5.27. Some shouldering behavior also appears to be occurring for 0.5 g of catalyst. For all other experiments, with lesser amounts of catalyst or lesser amounts of oxygen, curves were smooth and did not exhibit shouldering.

Also of interest is the O_2 consumption of torrefaction at higher levels of fed O_2. As shown in Figure 5.28, with 5% O_2 in the torrefaction feed, catalyst-free torrefaction consumes more O_2 than when 2% O_2 is fed which also corresponds well with the higher amount of solid mass loss presented previously with increasing oxygen concentration. With the presence of a catalyst, more oxygen is consumed at all catalyst loadings when compared to catalyst-free experiments or at lower oxygen concentrations. However, of particular

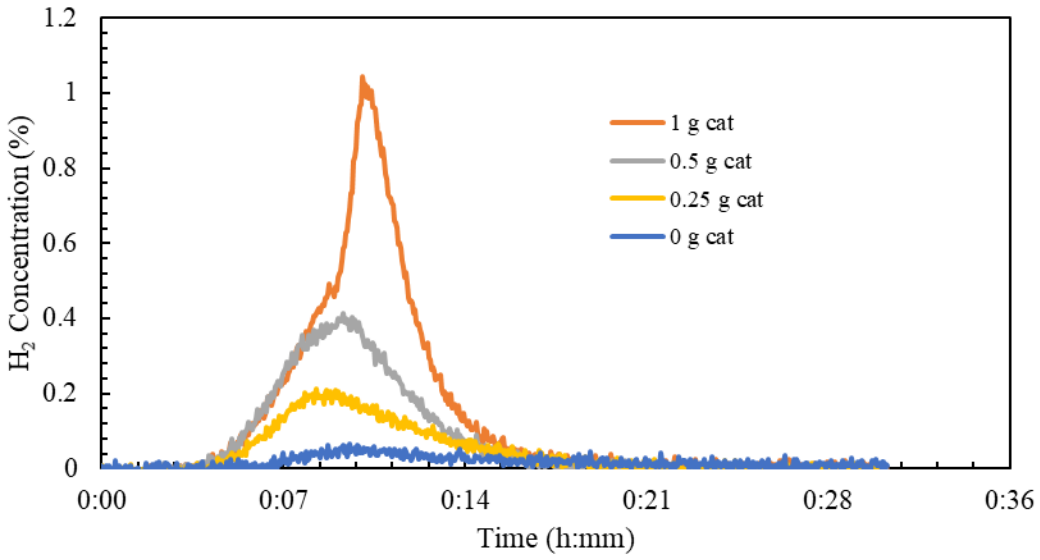

Figure 5.27. Hydrogen concentration in torrefaction effluent gas as a function of catalyst loading with 5% O_2.

interest the shapes of the curves with 1 g or 0.5 g of catalyst in comparison to no catalyst or 0.25 g of catalyst. For the latter set of experiments, the oxygen concentration curve is very similar to what has been presented before and the curve is very smooth and gradual. However, for the two higher catalyst loadings, the curve is no longer as smooth and has multiple inverted peaks indicating multiple oxygen consumption "events" occurring. Interestingly, these oxygen consumption "events" correspond well with the shouldering in the hydrogen production curve.

As shown in Figure 5.29, the minimum oxygen concentration at approximately 10 minutes corresponds well with the peak in hydrogen production for 1 g of catalyst. Additionally, with 0.5 g of catalyst, similar behavior is noted although it is not as prevalent. Therefore, there appears to be a counter-intuitive relationship between oxygen consumption and hydrogen production. The increasing amount of hydrogen production with increasing oxygen concentration is interesting especially again considering that in a

model reaction with CO, O_2, and H_2O, the presence of only 2% O_2 was capable of completely suppressing H_2 formation.

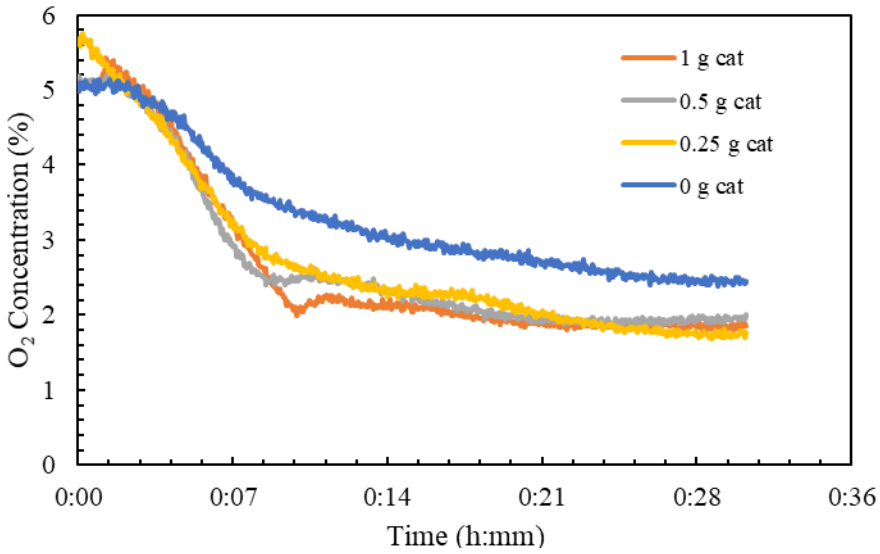

Figure 5.28. Oxygen concentration in torrefaction effluent gas as a function of catalyst loading at 5% oxygen.

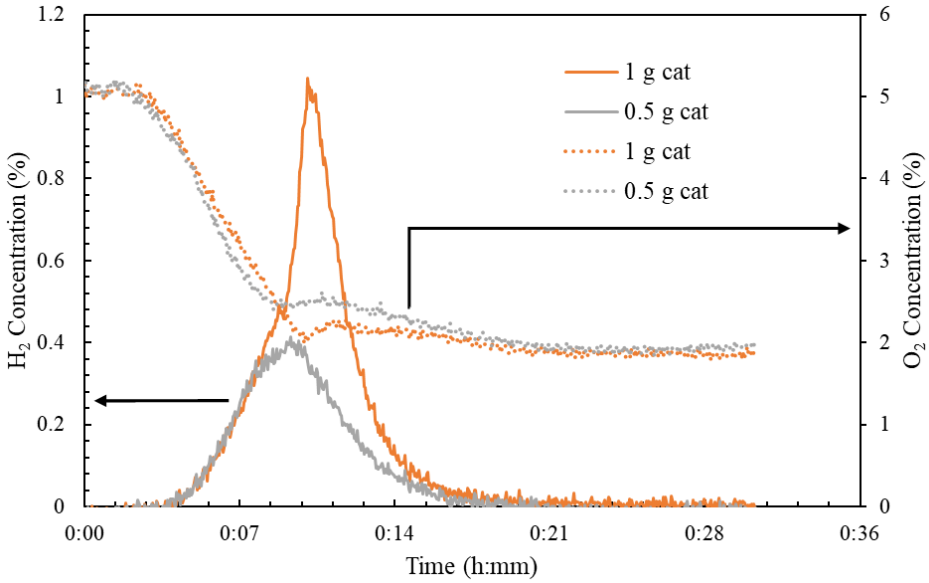

Figure 5.29. Correlation between hydrogen production and oxygen consumption for torrefaction at 5% O_2.

Finally, the higher amounts of oxygen consumption resulted in enhanced CO_2 production again with the steady-state amount of CO_2 production after ~15 minutes shown in Figure 5.30 corresponding well with the amount of oxygen consumption after ~15 minutes and again explains the enhanced mass loss at elevated oxygen concentrations.

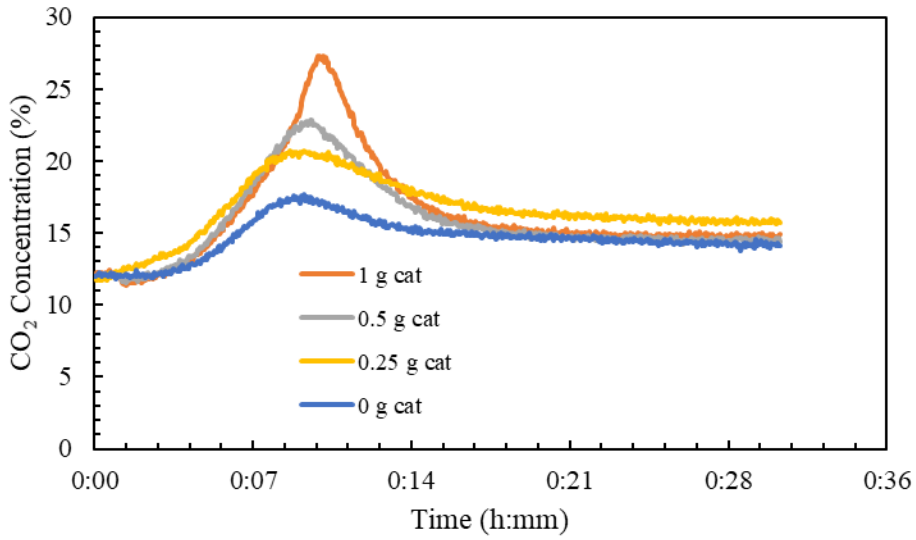

Figure 5.30. CO_2 concentration in torrefaction effluent gas as a function of catalyst loading at 5% O_2.

Although higher oxygen concentrations were tested, 5% O_2 displayed the highest amount of hydrogen production. Therefore, to understand the relationship between oxidizing species and hydrogen production, water was removed from the reactor feed. However, it is essentially impossible to eliminate the presence of water under these reaction conditions as water is produced during torrefaction in addition to the water artificially fed to simulate combustion exhaust. However, the elimination of a large source of water for the reaction could provide additional information about hydrogen production in this system. As shown in Figure 5.31, hydrogen production was severely reduced

(approximately 5 times less) without the presence of additionally fed water indicating that the presence of water is important for hydrogen production.

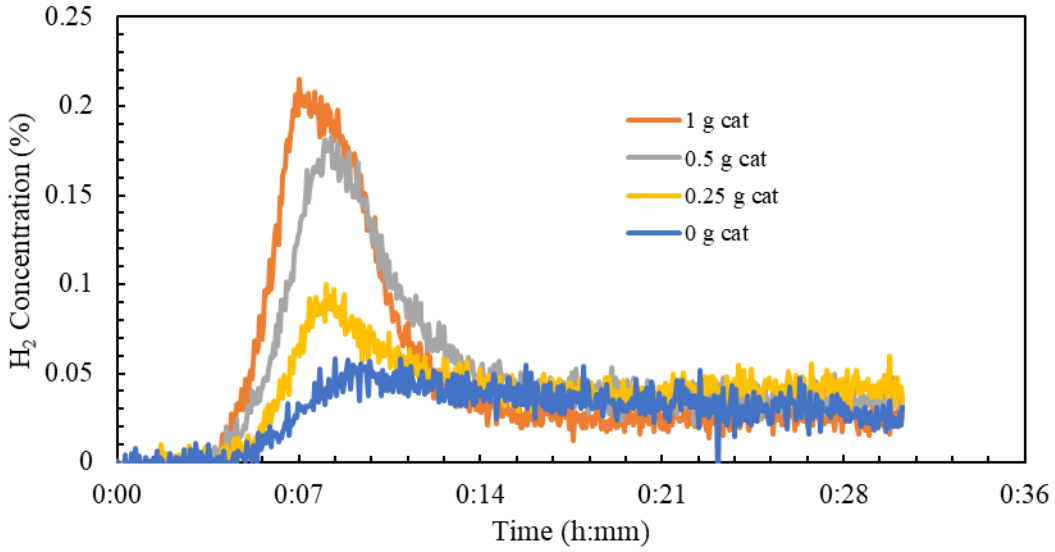

Figure 5.31. Hydrogen concentration in torrefaction effluent gas as a function of catalyst loading with 5% O_2 without water.

Further, without the presence of additionally fed water, oxygen consumption was suppressed as shown in Figure 5.32, and the multiple consumption events mentioned previously are not seen here indicating a cooperative effect of water and oxygen together not seen when only species is present (excluding water unavoidably produced via torrefaction).

Correspondingly, the production of CO_2 is also reduced without the presence of water as shown in Figure 5.33, again corroborating the influence of oxygen and water functioning together on the catalyst to produce hydrogen. Interestingly, more CO_2 is produced when water is present, and oxygen is removed than for the opposite case. Additionally, more H_2 is produced when water is fed without oxygen than when oxygen is

fed without water further supporting water being a more readily usable oxidant as previously suggested.

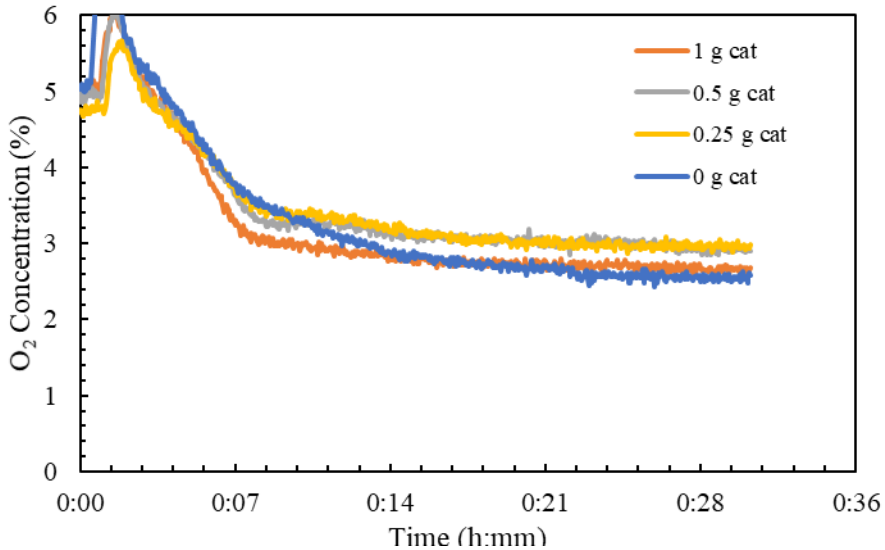

Figure 5.32. Oxygen concentration in torrefaction effluent gas as a function of catalyst loading at 5% oxygen without water.

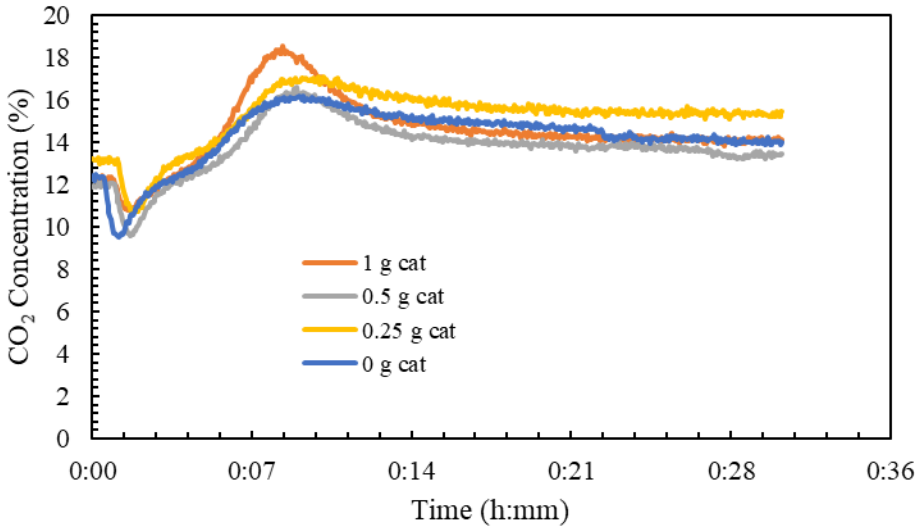

Figure 5.33. CO_2 concentration in torrefaction effluent gas as a function of catalyst loading at 5% O_2 without water.

To verify that further increases to oxygen concentration did not increase CO elimination or H_2 production, 7% O2 was utilized and as shown in Figure 5.34 which provides a summary of the CO removal efficacy of all oxygen concentrations and catalyst loadings. With 7% O_2, the removal efficiency is negative indicating production of additional CO with the presence of a catalyst at high oxygen levels, likely via combustion of bio-oils or other volatile components. Further increasing fed oxygen concentration to 9% or 11% results in the formation of additional CO as seen with 7% O_2 shown here. Therefore, control of oxygen concentration is very important for regulating CO emissions from this process.

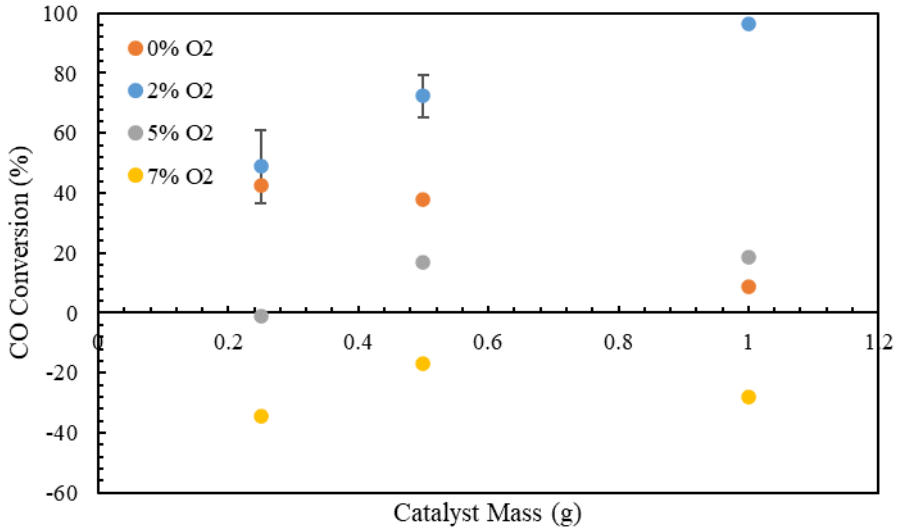

Figure 5.34. Effect of oxygen concentration and catalyst loading on removal efficiency of CO from torrefaction.

Similar to when 5% O_2 is used, without the presence of a catalyst, the biomass by itself consumes around 2% O_2 at a steady state as shown in Figure 5.35. With the presence of a catalyst, once again additional oxygen is consumed but the multiple oxygen

consumption “events” are much more prominently seen with high catalyst loadings when compared to 5% O_2 experiments.

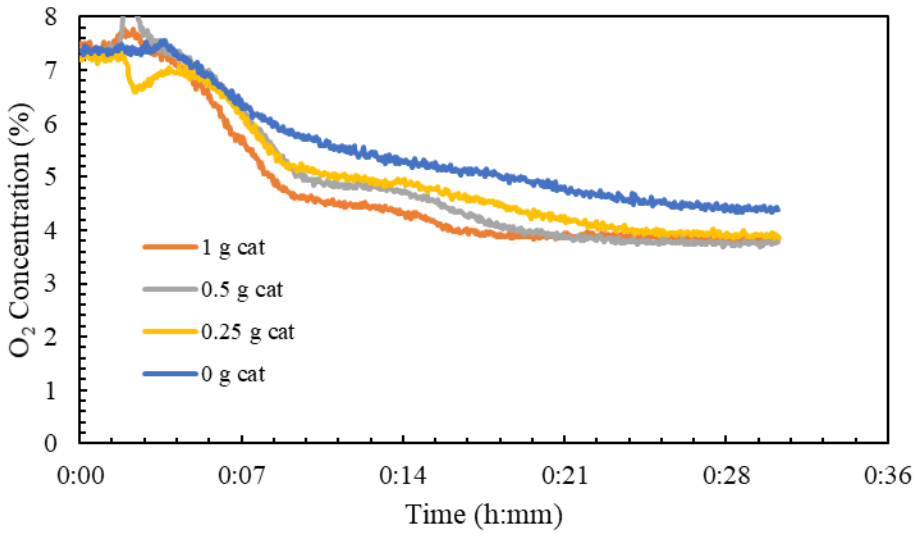

Figure 5.35. Oxygen concentration in torrefaction effluent gas as a function of catalyst loading at 7% O_2.

Correspondingly, the shouldering behavior for hydrogen production becomes much more pronounced and two distinct peak maxima are present at high catalyst loading with 7% O_2 as shown in Figure 5.36. As this trend is consistent both within experiments with 7% O_2 and 5% O_2, this once again corroborates that interaction between oxygen consumption and hydrogen production exists. This could be the result of two different types of events occurring with the two different oxidants present (water and O_2).

When examining CO_2 production at 7% O_2, without the presence of a catalyst, CO_2 production is nearly identical experiments with 2% and 5% O_2 (with and without water) indicating that oxygen interacts similarly with biomass regardless of oxygen concentration within this range and that water does not play a role in CO_2 production with biomass without the presence of a catalyst as shown in Figure 5.37. Therefore, any changes in CO_2

production with changing oxygen or water concentration are due solely to the presence of the catalyst and interactions between these species, the catalyst, and torrefaction products.

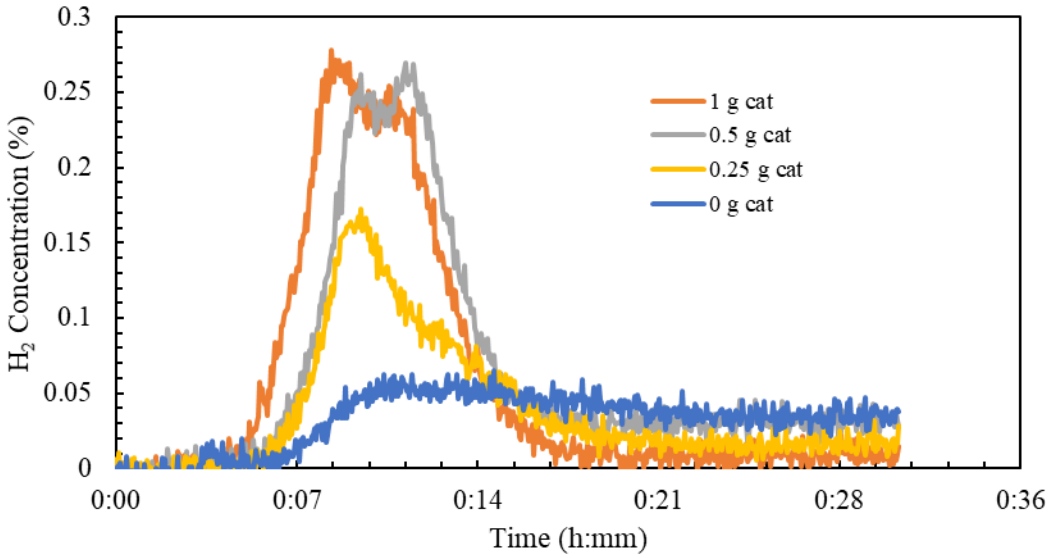

Figure 5.36. Hydrogen concentration in torrefaction effluent gas as a function of catalyst loading with 7% O_2.

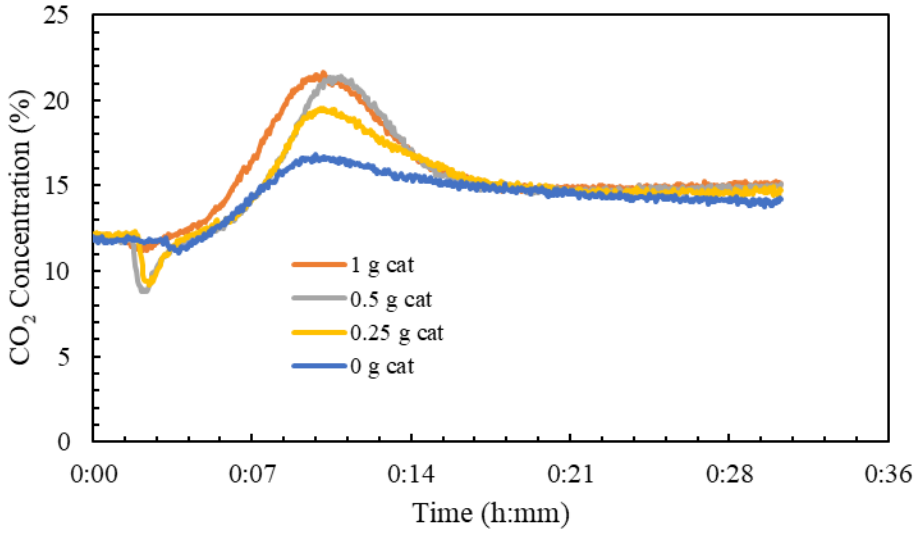

Figure 5.37. CO_2 concentration in torrefaction effluent gas as a function of catalyst loading at 7% O_2.

To determine more information about the interaction of bio-oil and catalyst, an experiment was devised to eliminate the presence of biomass from the experiment to determine what role bio-oil plays by itself. To do this, previously collected bio-oil was pumped into the reactor system without the presence of biomass to establish the role of bio-oil by itself. Before injecting bio-oil, the catalyst was exposed to oxygen and water and eventually CO to verify previous fixed bed results that resulted in no production of H_2 under these conditions. As shown in Figure 5.38, O_2 concentration and CO_2 concentrations start at approximately 5% and 12% respectively corresponding to baseline simulated flue gas. Shortly after, 3.5% CO is added to the gas mixture and passed over the catalyst. This addition causes an increase in CO_2 concentration as well as a corresponding decrease in O_2 with no unreacted CO present in the effluent due to CO oxidation via oxygen. This corresponds well with previous experiments examining the reactivity of the catalyst with and without the presence of oxygen as no hydrogen is produced indicating that the water gas shift reaction is not occurring here. After approximately 20 minutes, a low flow of bio-oil (1.9 mL/hr) was added to the reactor system and left on stream for approximately 40 minutes with no appreciable change to the effluent gas except for a slight change in CO_2 production and O_2 consumption. However, no CO or H_2 is detected in the effluent gas in these conditions indicating that the catalyst is still oxidizing CO via O_2. Interestingly, when the amount of bio-oil is increased to 9.3 mL/hr, activity more like that observed during torrefaction is observed. Namely, there is an increase in O_2 consumption, and this consumption is coupled with an increase in CO_2 production as well as H_2 production. Additionally, this is also accompanied by an increase in CO indicating that the catalyst is either no longer as efficiently oxidizing fed CO or additional CO is produced by the catalyst

via contact with bio-oil. However, as shown previously, during torrefaction with 5% O_2, CO removal efficiency is significantly reduced than when compared to 2% O_2. Interestingly, while CO_2 production begins to taper off and O_2 consumption either remains constant or begins to decrease soon after bio-oil is fed to the process, H_2 production increases as a function of time on stream potentially indicating that the mechanisms for this production increase as a function of time. As seen with simplified experiments without biomass or bio-oil, H_2 production is accompanied by an in-situ reduction of the catalyst under operating conditions as evidenced by XRD when O_2 is not fed to the process.

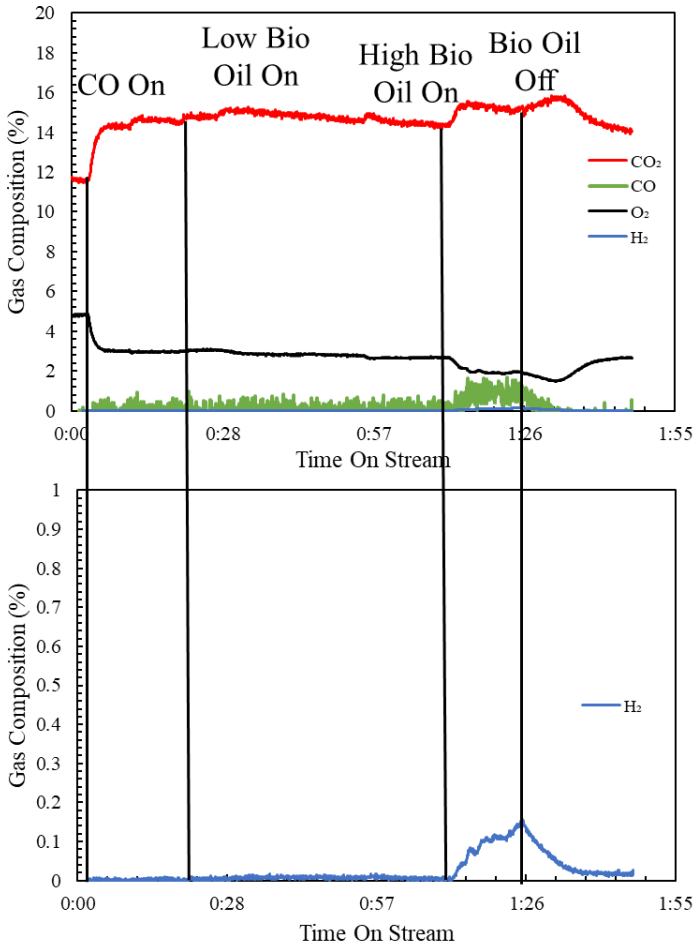

Figure 5.38. Gas-phase analysis of feeding bio-oil to a catalyst without the presence of biomass.

Potentially, over time the catalyst begins to be reduced and becomes active for H_2 production which explains the increase in production over time. After shutting off bio-oil to the process, H_2 production immediately drops again indicating that bio-oil is responsible for H_2 production. Further, CO_2 concentration again increases suggesting that without the presence of bio-oil the catalyst can reversibly change under operating conditions potentially due to changing oxidation states. Removal of bio-oil from the process is accompanied by an increase in O_2 consumption, and CO_2 production, however as no hydrocarbons are fed to the process during this time this carbon is likely deposited on the catalyst during operation and the removal of bio-oil from the process allows re-oxidation of the catalyst and coke burn off which causes a transient increase in O_2 consumption, and CO_2 production before beginning to return to a gas composition associated with CO oxidation via O_2 as seen before the addition of bio-oil. Time on stream reactor results in which the gas environment was switched from O_2 containing to O_2 free conditions (as shown in Figure 5.39) also corroborates that the catalyst can readily switch from reduced to oxidized by the addition of O_2 as an oxidizing species so it is plausible that the addition of a reducing species (bio-oil) can cause a similar but opposite change.

The high and low amounts of bio-oils were calculated considering the period in which bio-oil is produced during the torrefaction process and therefore what the catalyst is exposed to in-situ. For a 30-minute torrefaction experiment with 5% O_2, approximately 1 g of bio-oil is produced from 4 g of biomass, corresponding to approximately 2g/hr of bio-oil production. However, examining the effluent of the torrefaction process means that this previously calculated number is somewhat misleading. As shown, bio-oil is responsible for H_2 production and substantial amounts of H_2 are only produced during an approximately

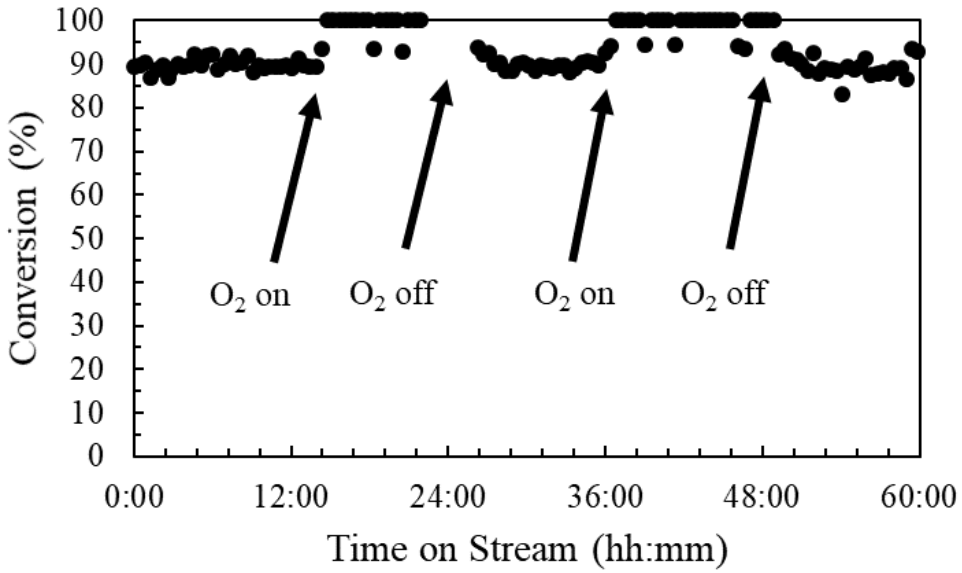

Figure 5.39. Time on stream activity of 500 mg catalyst with switching on and off of O_2 indicating the ability of the catalyst to readily change oxidation state via changing activity.

7-minute window even under the best conditions corresponding to around 9g/hr of bio-oil exposure in-situ during actual torrefaction. Therefore, these two flow rates were used to examine both tailing behavior at low bio-oil production levels as well as peak production.

Experimentally, it is difficult and time-consuming to carry out experiments looking at the influence of bio-oil by itself as the system produces 1g of bio-oil per 30-minute experiment, and pumping bio-oil at approximately 9 mL/hr requires 4.5 hours of torrefaction experiments to be conducted to pump bio-oil directly for 1 hour. This renders it difficult to carry out multiple experiments with bio-oil and significantly increases the costs and time required for this experimentation. Therefore, to reduce this time, synthetic bio-oil was blended to serve as a stand-in mixture to expedite testing. As presented later in this work, bio-oil was characterized by GC-MS and a blend of components was utilized

that served as analogs for the main functionality of the bio-oil. The composition of the synthetic oil is presented below in Table 5.5.

Table 5.5. Composition of Synthetic Bio-Oil.

Functional Group Identified in Bio-Oil	Area Percent from GC-MS	Analogue Molecule Utilized	Volume Percent of Analogue (vol %)
Organic Acid	35%	Acetic Acid	35%
Ketone	25%	Acetone	25%
Furan/Furfural Derivatives	15%	Tetrahydrofuran	7.5%
		Furfural	7.5%
Aldehydes	8%	Butyraldehyde	8%
Phenols	5%	Phenol	5%
Aromatics	2%	Xylene	2%
Non-Aromatic Rings	10%	Cyclohexane	10%

The synthetic bio-oil was then fed to the torrefaction reactor without biomass and only catalyst present as previously done with previously produced bio-oil. Similar to the torrefaction produced bio-oil, the addition of bio-oil along with water and O_2 results in the formation of additional CO_2 and H_2 while consuming O_2. However, under these conditions, the synthetic bio-oil better replicates observations seen during torrefaction experiments. Specifically, CO_2 concentrations observed with the utilization of synthetic bio-oil better mirror observations during actual torrefaction experiments at 5% O_2 as shown in Figure 5.40.

The use of synthetic bio-oil also allows for longer experiments to be conducted and longer-term phenomena to be observed. Immediately after the injection of bio-oil, CO_2 concentration spikes and is accompanied by an increase in O_2 consumption, but H_2 production only slowly begins to increase. After the immediate spike in CO_2 concentration, the concentration of CO_2 begins to decrease while the production of H_2 begins to increase as a function of time for nearly a half-hour. As previously noted with torrefaction experiments, the production of CO_2 and consumption O_2, as well as the production of H_2

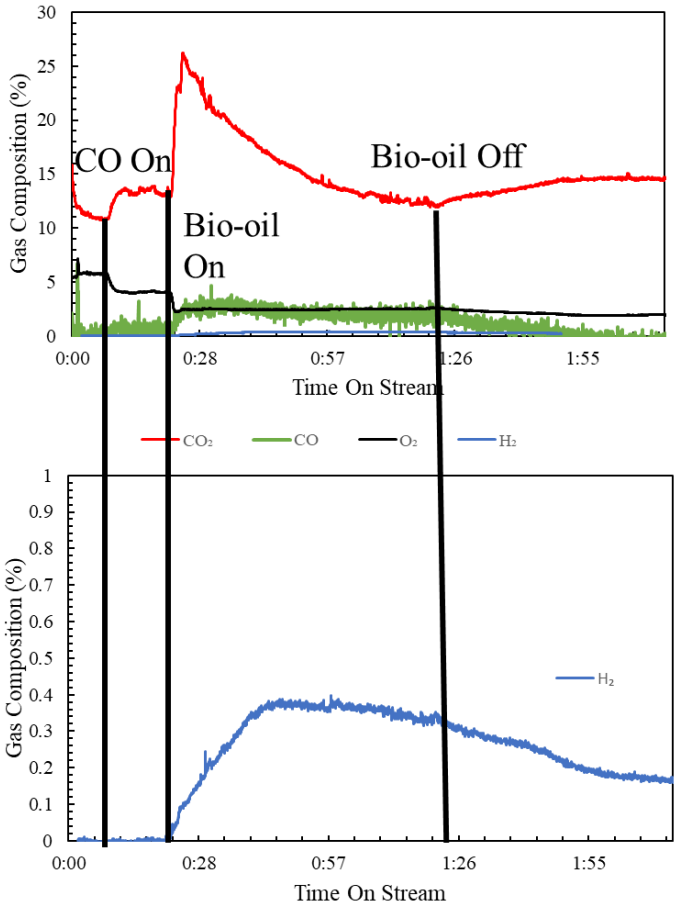

Figure 5.40. Effluent analysis of synthetic bio-oil injection.

appear to be correlated. Although as seen with bio-oil injection experiments, on a longer time scale, significantly more information can be gained about this interaction. First, under these conditions, O_2 consumption appears to be essentially constant regardless of the time on stream after the initial injection of bio-oil. Secondly, H_2 production increases as the production of CO_2 decreases, indicating that distinct mechanisms for the production of each of these species may exist. Additionally, the presence of CO after injection of bio-oil also suggests that the mechanism for CO removal (CO oxidation via O_2 before bio-oil injection) is either prevented from occurring or additional CO is produced by the catalyst. However, the decrease in CO and the corresponding increase in H_2 production as a function

of increasing time may suggest that the former is happening, and the activity of the catalyst is changing as a function of time. To understand these phenomena, catalysts were removed from the reactor at two distinct time points, namely during the period in which the catalyst continues to produce more H_2 as a function of time on stream and after peak emission has occurred (specifically at the end of the experiment shown in Figure 5.40). After cooling and removal from the reactor, the catalysts were characterized by XRD. As shown in Figure 5.41, the catalyst becomes more and more reduced as a function of time after exposure to bio-oil in the reactor. Before testing, the catalyst is present entirely as an oxide as shown earlier in this chapter while Cu metal begins to form as a function of time on stream. This is interesting as there is still oxygen remaining in the torrefaction gas indicating that the catalyst is being reduced even under the presence of oxygen. This change in oxidation states can result in a change in the reactivity of the catalyst. As mentioned previously, CuO is active for CO oxidation to CO_2 via O_2 which does not produce H_2. Additionally, this phase is also responsible for the oxidation of hydrocarbons [158], therefore it is not surprising initial CO_2 production is high with the CuO phase that is initially present. However, over time, CuO is reduced to Cu which can produce H_2 via the water gas shift reaction. Therefore, the change in catalyst activity as a function of time is due to the change in catalyst oxidation state which modulates which mechanism for CO/hydrocarbon oxidation occurs on the catalyst. The catalyst removed mid-experiment (Figure 5.41a) smelled distinctly of bio-oil while the catalyst removed at the end of the experiment (Figure 5.41b) did not. However, as shown in Figure 5.40, the catalyst removed at the end of the process was exposed to oxygen without bio-oil after bio-oil injection was stopped and it remains in the Cu state, indicating that O_2 was being utilized to remove organics from the

surface as indicated by the lack of smell as well as the increase in CO_2 concentration even after the hydrocarbon source (bio-oil) was removed. Further, a build-up of organics on the surface also helps explain why the production of H_2 began to slightly decrease as a function of time after reaching peak production, likely due to the blockage of active sites. Finally, as shown in Figure 5.38, when the bio-oil injection is interrupted while the reduction of the catalyst is occurring, H_2 production immediately stops. Conversely, when the catalyst becomes fully reduced and H_2 production peaks, the catalyst is still capable of producing H_2 even without the presence of fed bio-oil. Therefore, the reduced catalyst can either produce H_2 via the water gas shift reaction or through decomposition of the organics present on the surface of the catalyst. After the removal of bio-oil from the process, the CO concentration begins to decrease, and CO_2 concentration begins to increase along with a decrease in H_2 concentration. The increase in CO_2 can either be correlated with oxidation of CO or removal of organics from the surface.

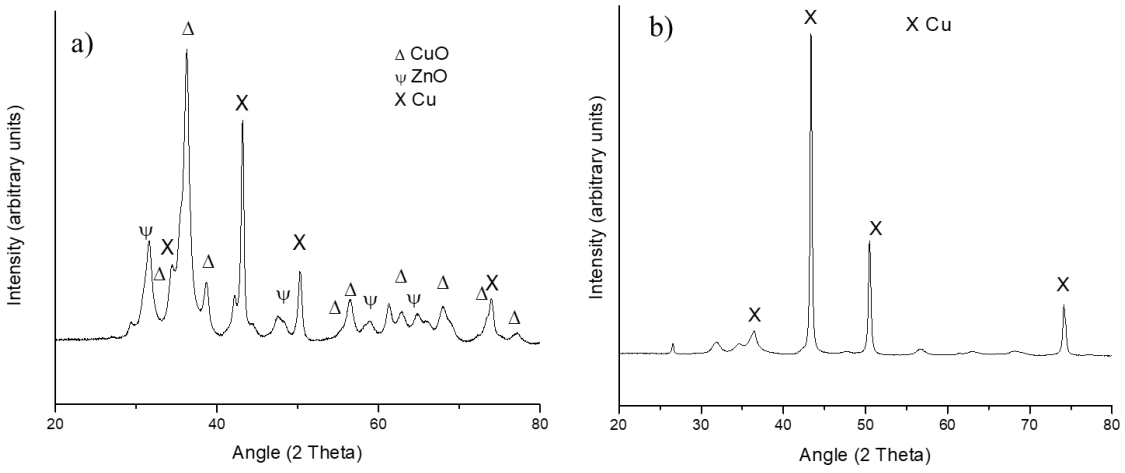

Figure 5.41. XRD patterns of catalysts removed a) while the H_2 productivity of the catalyst increases and b) at the end of the experiment.

By varying the gas composition fed to the torrefaction process, a wealth of information can be gleaned. First, without the presence of a catalyst, the biomass itself is

relatively insensitive to oxygen concentration from 2-7% with consumption of 1-2% at steady state after peak emission. Additionally, CO_2 production at steady state mirrors this decrease in oxygen concentration indicating that after peak emission, oxygen is consumed by the biomass to produce CO_2. Further, peak CO_2 production levels are similar for all catalyst-free experiments. The presence or lack of additionally fed water (simulating flue gas) does not influence this behavior without the presence of a catalyst. Additionally, essentially no H_2 is produced regardless of oxygen or water content without the presence of a catalyst.

In contrast, the presence of a catalyst brings about several changes to the torrefaction system. First, the presence of a catalyst with oxygen results in H_2 production with increasing catalyst loading generally increasing H_2 production. Additionally, peak H_2 production was observed with 5% O_2 with less H_2 produced with less oxygen or at higher oxygen concentrations. However, simplified experiments where only CO, H_2O, and O_2 were utilized with the catalyst indicate the presence of oxygen prevents the water gas shift reaction from occurring and eliminates the formation of H_2 that is seen when only CO and H_2O are used. Therefore, the formation of H_2 with the presence of O_2 is rather interesting, and the trend of increasing H_2 production when increasing O_2 concentration from 0% to 5% is unexpected.

Additionally, with the presence of a catalyst, O_2 consumption increases, and CO_2 production also increases. However, the increase in CO_2 production does not correspond well with the increase in O_2 consumption. For example, when 2% O_2 is fed to the torrefaction process, only an additional 1% is consumed with the highest catalyst loading while CO_2 production increases by 10% at peak emission. Therefore, something other than

carbon from biomass or CO being oxidized is responsible for the increase in CO_2 that is observed at steady state. As the increase in hydrogen production corresponds well with the increase in CO_2 production, the two responses are likely correlated. When additional water is no longer fed to the process at the same O_2 concentration, H_2 production, CO_2 production, and O_2 consumption are suppressed, suggesting that not only are these three factors correlated but that a synergistic reaction between oxygen and water occurs to produce CO_2 and H_2 with the presence of a catalyst. Additionally, darkening of the bio-oil fraction has been documented with increasing catalyst loading which can be characteristic of increasing levels of bio-oil oxidation with increasing catalyst loading [156]. Therefore, a possible explanation for this phenomenon is the interaction of bio-oil with water and oxygen on the catalyst to produce H_2 and CO_2 while consuming O_2. The exact mechanism of this is not well understood, but bio-oil components on the surface of the catalyst could be oxidized by O_2 producing H_2 and CO_2 with water also serving as a secondary oxidant. Additionally, as shown via XRD, the presence of bio-oil causes an *in-situ* reduction of the catalyst from CuO to Cu which is likely responsible for the production of H_2, although additional experiments are required to establish the mechanism for H_2 production.

Additionally, at high oxygen concentrations and high catalysts loadings, multiple oxygen consumption and hydrogen production events occur at corresponding times indicating that these two events are correlated with one another. This further demonstrates that counter-intuitively the presence of oxygen is crucial for high levels of hydrogen production. When oxygen is not fed to the process, hydrogen production is suppressed relative to 2% or 5% O_2 and CO removal efficiencies are low indicating that water and O_2

are both crucial to have present together for optimal performance of the catalyst to remove CO and produce H_2.

As mentioned previously, the coloration of bio-oils changes with catalyst loading suggesting oxidation of the bio-oil occurring with increasing catalyst loading. To determine this change quantitatively, bio-oil samples were analyzed via GC-MS to determine changes in chemical composition induced by the presence of the catalyst. The bio-oil mixture is composed of a very large number of different compounds and to determine changes in bio-oil composition the 40 most abundant species were used for quantification. As shown in Figure 5.42, when each of the 40 most abundant species is categorized by functional groups, changes to bio-oil composition are essentially within error. Therefore, GC-MS is not capable of detecting changes in bio-oil oxidation, oxidation occurs with a minority component neglected via this analysis, or another portion of the bio-oil is responsible for the color change observed in the bio-oil [156].

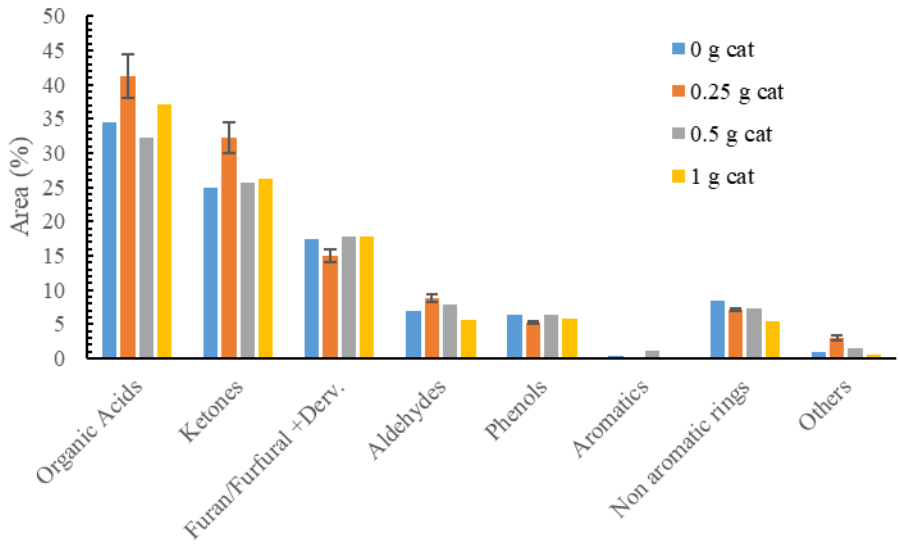

Figure 5.42. Bio-oil composition at varying catalyst loadings.

Additionally, NMR was utilized to analyze bio-oils because GC-MS separates mixtures and detects different molecules as they exit the GC column and poor separation can result in peaks eluting before or with the solvent, lack of elution for larger molecules, or poor separation of peaks rendering it difficult to determine changes based on function group if only small changes are occurring. Therefore, NMR which requires no separation during sample preparation and analysis and discriminates based on the functional group may allow detection of small changes that would be difficult to observe in GC-MS. Collected NMR data is shown in Figure 5.43 for 0g, 0.5g, and 1g catalyst.

Some small changes occur when comparing bio-oil produced with torrefaction with and without the presence of a catalyst, particularly at approximately 6.5 ppm where new features begin to form with the presence of a catalyst as well as a reduction in intensity at approximately 2.8 ppm with the presence of a catalyst. The increase in intensity at 6.5 ppm could correspond to aromatic hydrogen, aromatic alcohol, or amide groups of which the latter two would be indicative of oxidation. The peak at ~2.8 ppm could correspond to an amine, ketone, or a C-H group attached to an aromatic ring. Therefore, if this change is correlated it is most likely a change from an aromatic alkyl group to aromatic alcohol or an amine to an amide, both of which would be indicative of oxidation. However, the likelihood of either of these changes occurring is questionable. At a more bulk level, only small changes in each of the labeled regions are observed via the addition of catalyst as shown in Figure 5.44.

The only quantifiable changes occurring at a bulk level are a decrease in intensity in NMR region 2 and a corresponding increase in the intensity of NMR region 7. Region 2 corresponds to a wide variety of compounds ranging from amines, alcohols, ketones,

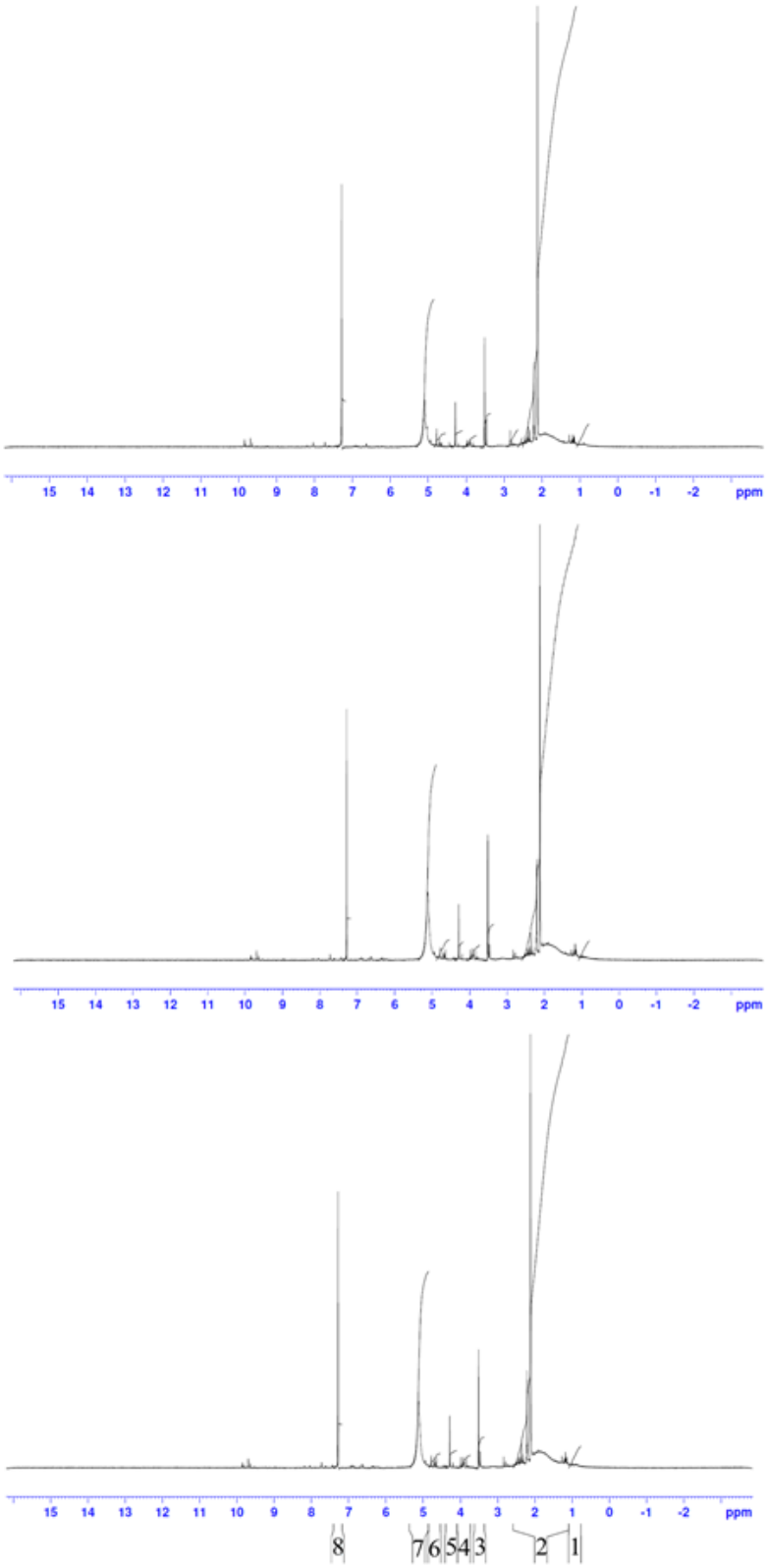

Figure 5.43. NMR spectra of bio-oil from torrefaction with 0 g cat, 0.5 g cat, and 1 g cat (from top to bottom) with regions labeled on the bottom panel.

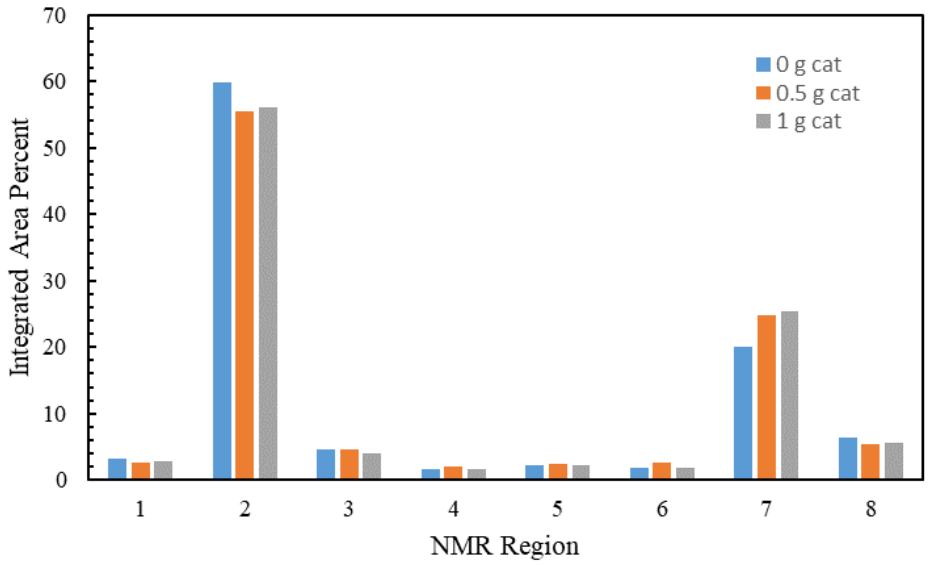

Figure 5.44. Bulk quantification of NMR regions of bio-oil produced with and without catalyst during torrefaction.

alkynes, and alkanes while region 7 corresponds mainly to amides, aromatic alcohols, and alkenes. Therefore, this change could also correspond to the conversion of amines to amides however the likelihood of this conversion remains questionable. However, conversion of alkyl to alkene groups would explain this change as well as provide a source for produced hydrogen as seen in this study as well as correspond well with previous observations of darkening of bio-oil components [156]. A full summary of each of the selected NMR regions and the type of functional groups that they correspond to is found in Table 5.6. Additionally, the uniformity of region 3 (residual ^{1}H from the $CDCl_3$ solvent) from experiment to experiment indicates similar amounts of bio-oils and water are present regardless of catalyst content as the percentage of region 3 is proportional to other regions for each experiment.

Table 5.6. Identification of NMR regions for bio-oil quantification

Region	Approximate Chemical Shift (ppm)	Possible functional groups
1	0.9-1.1	Alkyl, amine, alcohol
2	1.1-2.5	Alkyl, aromatic alkyl, alcohol, alkyne, ketone
3	3.4-3.7	Alcohol, halides, **solvent**
4	3.7-4.2	Alcohol, halides, alkene
5	4.2-4.5	Alcohol, halides, alkene
6	4.6-4.8	Alcohol, alkene
7	4.8-5.4	Alcohol, alkene, amide
8	7.2-7.4	Aromatic, amide

5.5 Impact of Pollutant Species From Power Plant Flue Gas

To understand how additional flue gas components (S, As, etc) influence the activity of the catalyst, catalyst pellets were exposed to flue gas at Cross Generating station for 15 and 30 minutes to determine how the exposure changed the activity of the catalysts. As shown in Figure 5.45, the exposure to flue gas significantly altered the activity of the catalysts with only 60 minutes of exposure reducing the activity of the catalyst to below 50% relative to a fresh catalyst without flue gas exposure under WGS conditions.

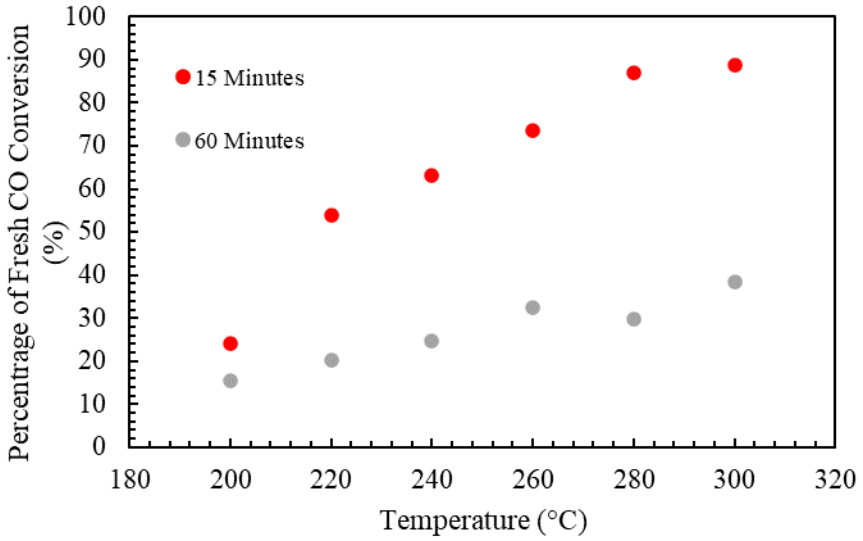

Figure 5.45 Effect of power plant flue gas exposure on catalyst performance for water gas shift reaction.

However, when oxygen is present in the feed gas, deactivation does not begin to be prevalent at high temperatures until 60 minutes of exposure as shown in Figure 5.46. However, as mentioned previously, this reaction does not produce hydrogen and instead occurs via oxidation by O_2. However, as this work has shown, even with O_2 present when the catalyst is added to the torrefaction system, hydrogen is produced. Therefore, further testing with the deactivated catalyst within the laboratory scale torrefaction reactor as well as testing the catalyst under conditions in which these deactivating species are present would be required.

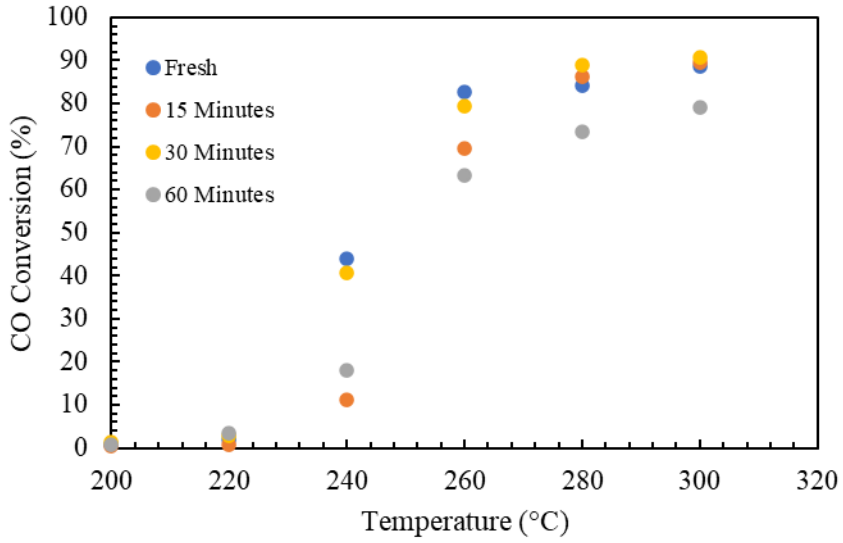

Figure 5.46. Activity of power plant flue gas exposed catalysts as a function of temperature with steam, CO, and O_2.

As shown in Figure 5.47, the content of heavy metals increases after exposure to power plant flue gas. In general, the content increases with increasing exposure time, however, due to the low content of heavy metals the experimental error is quite high. Regardless, exposure to coal flue gas does increase the heavy metal content of the catalysts providing a potential route in which poisoning and activity loss can occur.

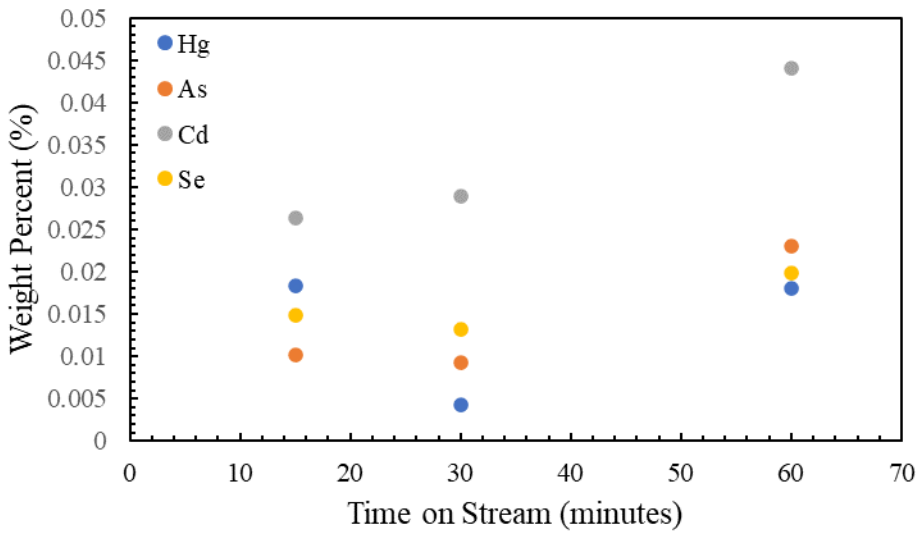

Figure 5.47. Heavy metal content of catalysts after exposure to coal flue gas at varying times.

To address the issue of sulfur poisoning, catalysts with previously documented sulfur resistance [152], [159], [160] were synthesized and tested both in the torrefaction reactor and utilizing model water gas shift reactions and also with the addition of oxygen. Under water-gas shift conditions, each of these catalysts exhibits negligible activity regardless of temperature. With the addition of oxygen, the activity of each of the catalysts greatly increases as shown in Figure 5.48.

While these catalysts are capable of oxidizing CO via O_2, these catalysts are not capable of significant water gas shift activity. This is not surprising considering that these catalysts have been previously utilized for soot oxidation and other total oxidation applications [161]. While this means these catalysts are more than capable of oxidizing CO, they are also unfortunately capable of oxidizing other organic compounds during torrefaction, likely the bio-oils produced during the reaction. This oxidation results in the

formation of more CO with the presence of these catalysts than when no catalysts are present.

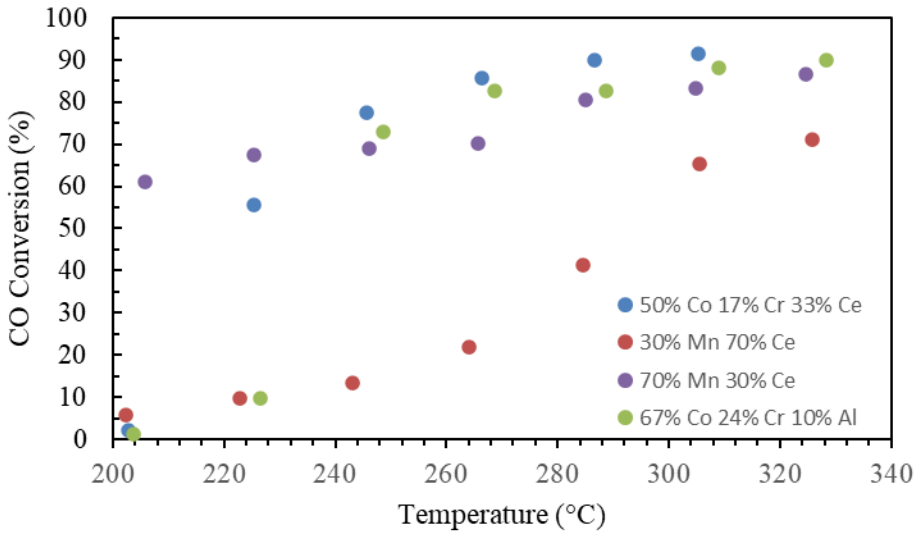

Figure 5.48. Activity of mixed metal oxide biomass torrefaction catalysts.

as shown in Figure 5.49. Therefore, the use of these catalysts is not recommended unless oxidation of bio-oils is desired and the concentration of CO in the effluent stream is not of concern. As one of the focuses of this project was to remove CO from the exhaust stream, these catalysts were not further utilized as they result in the formation of additional CO.

Finally, in addition to serving as a potential fuel source for coal power plants, torrefied biomass can also be used as a structural reinforcement agent in polymers. The physical properties of the produced polymer heavily depend on the synthesis parameters with the biggest change occurring with the addition of a plasticizing agent. Without the presence of a plasticizing agent, a hard but brittle polymer is formed and with the presence of plasticizer, flexible rubbery material is produced similar to athletic track material made of recycled shoe soles. However, some plasticizers did not produce materials with good physical properties, particularly polymeric plasticizers. The best performance of the

flexible polymers was obtained when using glycerin as the plasticizer and an image of a polymer sample utilizing glycerin as the plasticizer is shown in Figure 5.50.

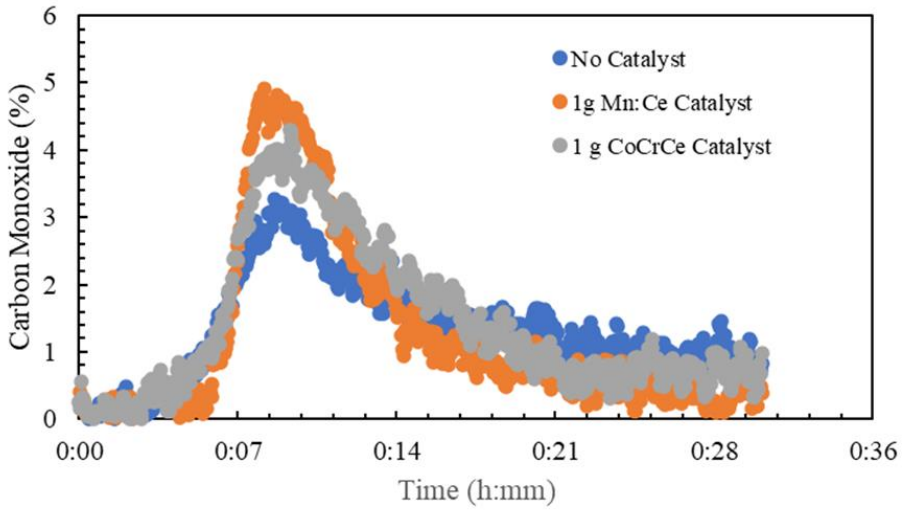

Figure 5.49. Activity of other mixed metal oxide catalysts as biomass torrefaction catalysts.

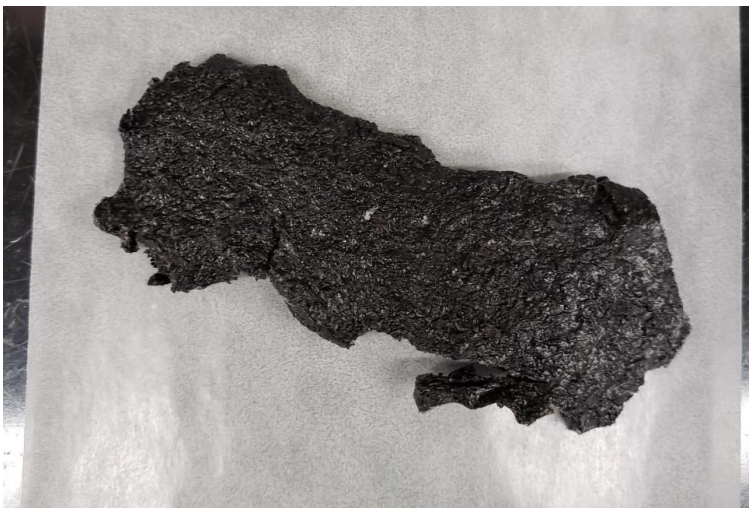

Figure 5.50. Image of a polymer reinforced with torrefied biomass.

5.6 Conclusions

As demonstrated in this work, torrefied biomass can be utilized as a partial replacement for coal in conventional power plants with no large capital changes in processing equipment and can serve as a promising bridge fuel utilizing current infrastructure while capacity for other renewable energy sources is brought online. Further, it was demonstrated that the utilization of a novel, magnetically separable Cu/Zn catalyst could be utilized to reduce CO emissions by up to 95% while producing value-added hydrogen. However, this was highly dependent on oxygen concentration in the simulated flue gas with optimal CO removal occurring at 2% O_2 and optimal H_2 production occurring at 5% O_2. Interestingly, the catalyst is capable of producing H_2 in an oxygenated environment during torrefaction as, without biomass, no H_2 production occurred. This interaction happens due to the interaction of bio-oil with the catalyst as the color of the bio-oil is changed as a function of catalyst loading indicating that it is interacting with the catalyst. Additionally, a relationship between the presence of water, O_2 consumption, CO_2 production, and H_2 production was observed indicating that there is likely interaction with the catalyst, bio-oil, water, and O_2 to produce CO_2 and H_2. Additionally as shown via bio-oil injection experiments, the presence of bio-oil reduces the catalyst during torrefaction and changes the catalyst from CuO to Cu which modulates its activity and reactivity under operating conditions.

Further, the torrefaction process is capable of successfully being run with O_2 concentrations up to 11% for 30 minutes without the biomass catching fire, however, based on catalyst performance it is more optimal to operate the process at roughly 2-5% depending on the desired tradeoff between CO removal and H_2 production. The utilization

of a magnetically separable catalyst also allows for rapid separation of the catalyst and torrefied biomass for catalyst recycling within the process. As an added benefit, the presence of the mesh structurally reinforces the catalyst pellets increasing their resistance to abrasion by tumbling.

Scaled testing using biomass pellets within the flue gas at Cross Generating Station, an online coal-burning power plant increased the heating value of the biomass from 7855 BTU/lb to 11037 BTU/lb which can correspond to a co-firing rate of 30-40% indicating that this process has the potential to displace a large amount of coal consumption within the state of South Carolina while utilizing waste biomass. Additionally, the torrefied biomass can also be utilized as a structurally reinforcing agent in polymers.

CHAPTER 6

ATOMIC LAYER DEPOSITION

6.1 Introduction

The goal of this work is to test the performance of a home-built ALD reactor located at BASF in Ludwigshafen, Germany, and to verify the performance of the system when using a well-characterized model process, namely the TMA/water process. To understand that the system is functioning as intended, three different methodologies were utilized to determine the thickness of films deposited during the ALD process. After verification of performance, the ALD system is capable of being utilized with novel processes with the confidence that the system is functioning properly. Qualitative film thicknesses were determined via the thickogram methodology from XPS, and qualitatively utilizing TOF-SIMS coupled with profilometry as well as ellipsometry. It was desired to verify that both qualitative methods resulted in similar values that match with literature and that the thickogram method can be utilized to rapidly diagnose if the process displays linear growth per cycle. Finally, extension to different chemistries and the utilization of more novel substrates such as polymers and biological materials was conducted.

Herein, it is demonstrated that the experimental system functions ideally with the TMA/water process and that the thickogram method successfully predicts linear growth per cycle independent of the number of cycles. Further, results from TOF-SIMS coupled with profilometry and ellipsometry are essentially within error of one another and are both able to quantitatively determine film thickness. Additionally, these values are in excellent agreement with literature values. However, extension to $TiCl_4$/water proved to be problematic and changes to experimental parameters need to be manipulated to transition to linear growth. Finally, when utilizing polymer substrates, the growth of Al_2O_3 with the TMA/water process was dependent on the presence of reactive surface functionality of the polymer. Additionally, when film growth occurred, chemical changes to the surface of the

polymer were able to be detected. Therefore, the system could also be capable of determining the degradation of biological materials during film deposition which would be crucial when beginning work on these materials.

6.2 TMA/Water Process

As mentioned previously, the thickogram method is a useful tool to examine and verify the linearity of ALD growth for films less than approximately 10 nm thick. Film thicknesses estimated via the thickogram method for the TMA/water process are shown below in Figure 6.1. An example of how Cu and Al overlap in the Al 2p region with Cu 3p was deconvoluted is shown in Figure S9 for the Cu substrate.

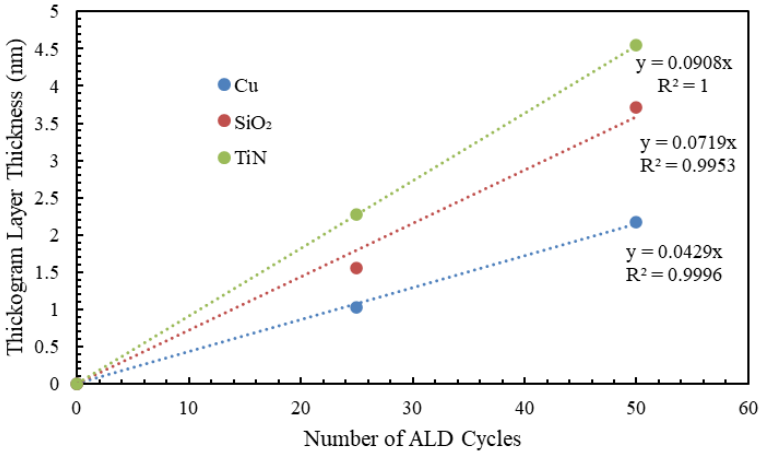

Figure 6.1. Film thickness estimation from the TMA/water process as a function of number of ALD cycles on various substrates.

As shown, a linear fit of 25 and 50 growth cycles forced through (0,0) displays excellent linearity for all substrates, but the slopes and therefore the corresponding growth per cycle varies significantly between each of the substrates, and the estimated growth per cycle does not correspond with literature values for this process. However, as the density of the deposited film is not known, inaccuracies in the absolute value of the growth per

cycle are to be expected and only the linearity of the growth is of interest from this method. Additionally, no underlying substrate was observed via XPS for 100 or 200 cycles and therefore this method is not capable of estimating film thicknesses for these samples. To determine the actual film thickness, TOF-SIMS combined with profilometry was utilized and the results of this technique are shown below in Figure 6.2.

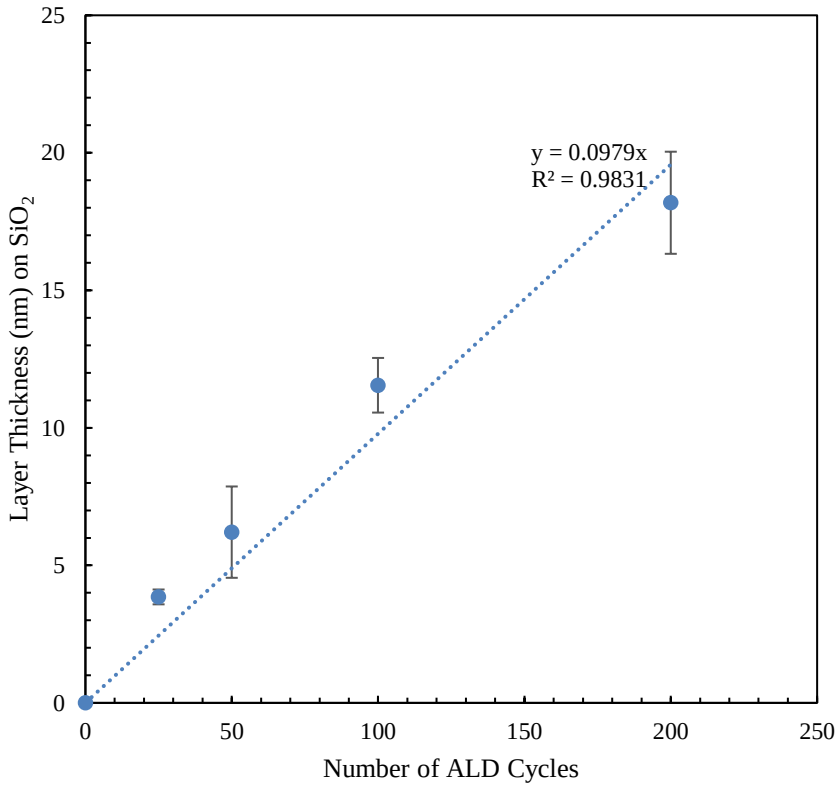

Figure 6.2. Film thickness for the TMA/water process as a function of number of ALD cycles on SiO_2 as determined by TOF-SIMS and profilometry.

The growth per cycle (0.098 nm/cycle) determined by this method shows excellent agreement with literature growth per cycle of ~0.1 nm/cycle [1] with a reasonable correlation coefficient. Therefore, this method also corroborates the linear results obtained via the thickogram method. In addition to the full data set on the SiO_2 substrate, the same TOF-SIMS and profilometry analysis was conducted on the 200 cycle samples with the

TMA/water process on Cu and TiN and forced through (0,0) to approximate the growth rate and is shown below in Table 6.1.

In addition to TOF-SIMS/profilometry, ellipsometry also provides a quick way to quantitively measure film thicknesses, assuming that an appropriate model has been built for the underlying substrate. For well-defined samples or samples in which the composition and chemical makeup of the substrate is well defined and well modeled this provides a reliable and rapid method to measure film thicknesses. To test the applicability of this technique and determine how well the results match with TOF-SIMS coupled with profilometry, the layer thickness determined by both methods is plotted in Figure 6.3a. Examination of this plot shows the excellent agreement between these two techniques, in this case, all data points are essentially within the measurement error of the profilometer when utilizing multiple sputtered craters. Additionally, a parity plot confirming the agreement between the two techniques is shown in Figure 6.3b. The dotted line in this plot indicates a perfect correlation between the two measurement techniques, and all points are within error of this line, indicating the excellent correlation and applicability of both techniques to measure film thicknesses for this process. Therefore, it may be desired to utilize ellipsometry when the underlying substrate is well defined and utilize TOF-SIMS coupled with profilometry as a verification method or for samples that were poorly modeled or not well-defined substrates. In this way, rapid and inexpensive quantification of film thickness can be made without requiring large amounts of time with TOF-SIMS. Ellipsometer data was obtained for all coated samples, however, for Cu and TiN substrates, detailed information about the construction of the substrate was not provided by the manufacturer (adhesion layer identity and thickness, as well as the thickness of the Cu and

TiN layers) which makes accurate quantification of deposited film thicknesses difficult. However, when this information is provided, these film thicknesses can be readily determined.

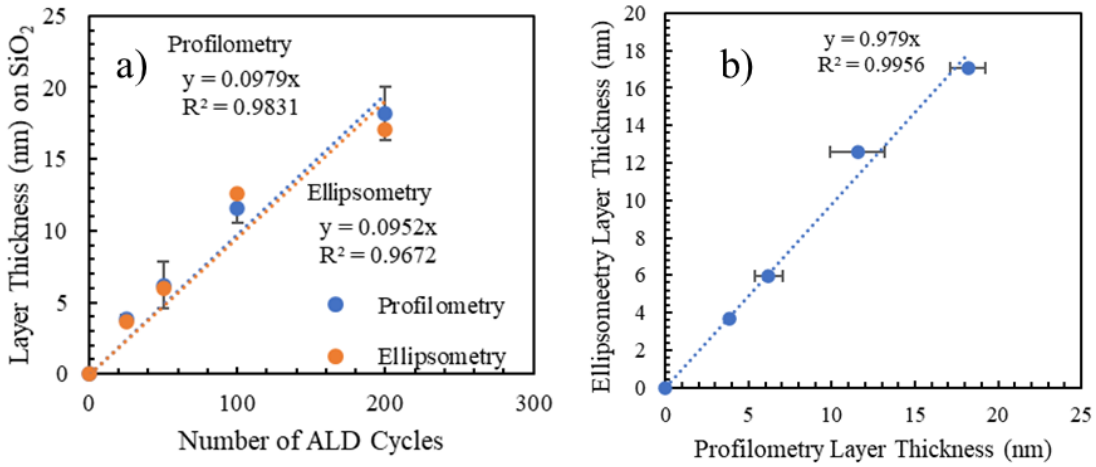

Figure 6.3. a) Film thickness for the TMA/water process as a function of number of ALD cycles on SiO_2 as determined by TOF-SIMS and profilometry compared to ellipsometry and b) parity plot comparing thicknesses determined by the two methodologies.

Table 6.1. Growth per cycle for the TMA/Water process determined via different methods.

Substrate	TOF-SIMS/Profilometry GPC (Å)	Ellipsometry GPC (Å)	Literature GPC (Å)
SiO_2	0.98	0.95	1 [1]
Cu	1.29*	-	1.25 [5]
TiN	1.06*	-	1 [6]

*indicates that only the 200 cycle sample was utilized to determine this value

6.3 $TiCl_4$/Water Process

In addition to the TMA/water process, $TiCl_4$/water was also utilized to verify the performance of a second chemistry with the reactor system. Due to the deposition of TiO_2 on the TiN wafters, proper deconvolution was crucial to determine the thickness of the TiO_2 layer. The results of these experiments are presented below in Figure 6.4. An example

of how various Ti species were quantified to determine TiO_2 and TiN content is shown in Figure S10.

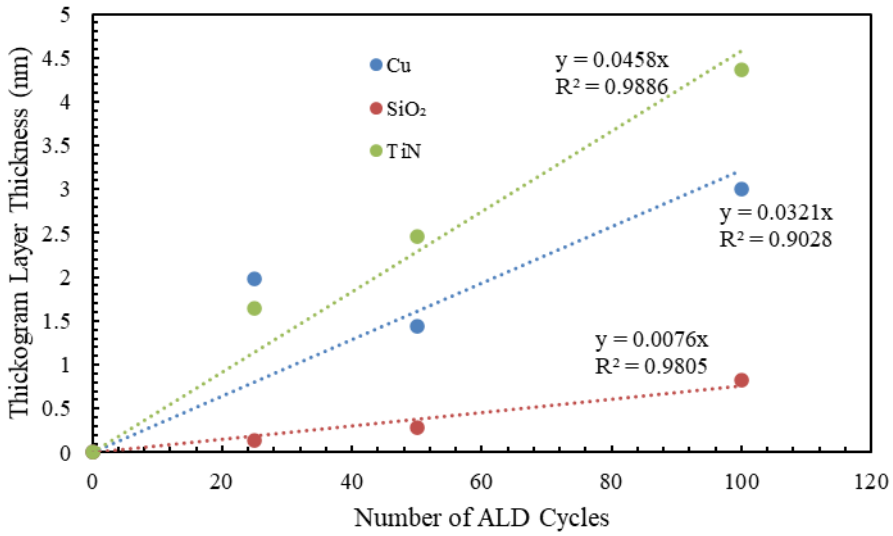

Figure 6.4. Film thickness estimation for $TiCl_4$/water process on various substrates utilizing the thickogram method.

Unlike the TMA/water process, this chemistry displays some non-ideal behavior for all substrates. For example, the TiN substrate appears to exhibit substrate enhanced growth with a higher growth rate per cycle initially which lowers are more cycles are completed. Interestingly, for the Cu substrate, more Ti is observed in XPS with 25 cycles than with 50 cycles. While substrate enhanced growth, similar to that seen with TiN, could be expected, the presence of more Ti with fewer cycles is unexpected and needs further work. However, previous literature also shows substrate inhibition for TiO_2 deposition on Cu [7]. Both the 25 and 50 cycle experiments were repeated on different days and resulted in similar spectra and growth trends using the thickogram method as shown below in Figure 6.5. By conducting TOF-SIMS sputtering combined with profilometry or by ellipsometry with a properly defined model, it could be more definitively determined if this is an issue

with the thickogram methodology or is characteristic of the substrate. Previous literature has shown that TiO_2 film growth on Cu is often characterized by island growth and high surface roughness which may pose issues for analysis via the thickogram method which assumes a homogenous film [7, 4]. Additionally, changing film densities (which are assumed constant here) can greatly influence the predicted thickness. In all cases, the fit of the linear regression as well as the estimated growth per cycle are similar with original and repeated data sets indicating good reproducibility from experiment to experiment.

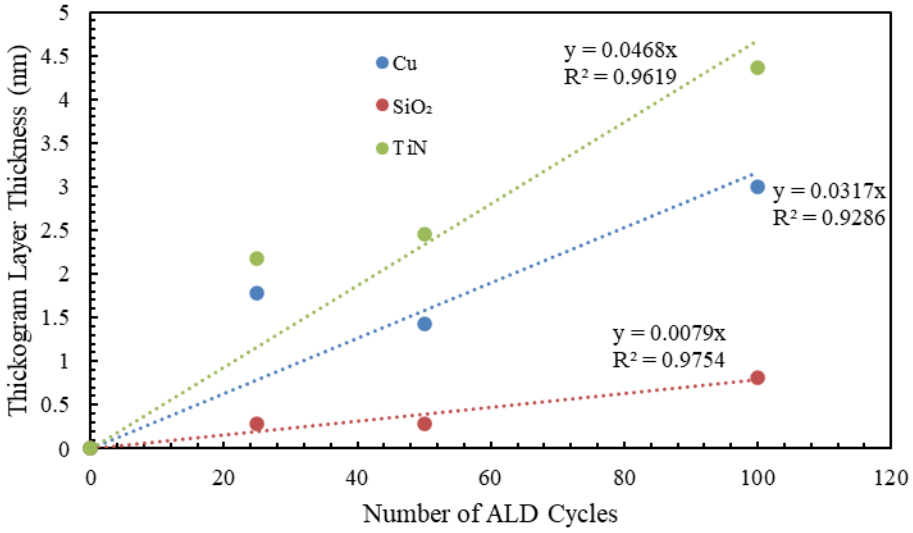

Figure 6.5. Film thickness estimation for $TiCl_4$/Water process on various substrates utilizing the thickogram method utilizing a second set of experimental points for 25 and 50 cycle experiments.

While the linear regression forced through (0,0) is reasonable for the SiO_2 substrate, a better (and more realistic) fit can be obtained by removing the constraint of a (0,0) intercept as shown in Figure 8 below. The negative intercept indicates substrate inhibited growth or the presence of a nucleation period on the SiO_2 substrate and results from ellipsometry (utilizing the same substrate model as with TMA/water experiments) also confirm this non-ideality as a negative intercept is fit, once again suggesting an effect from

the substrate inhibiting initial film growth as shown in Figure 6.6. However, some previous literature has documented substrate enhanced growth for this process [8]. However, the effect of this is highly dependent on the chemical nature of the SiO_2 surface, and analysis of the surface of the substrate used here relative to that of the literature study would provide more information on this phenomenon.

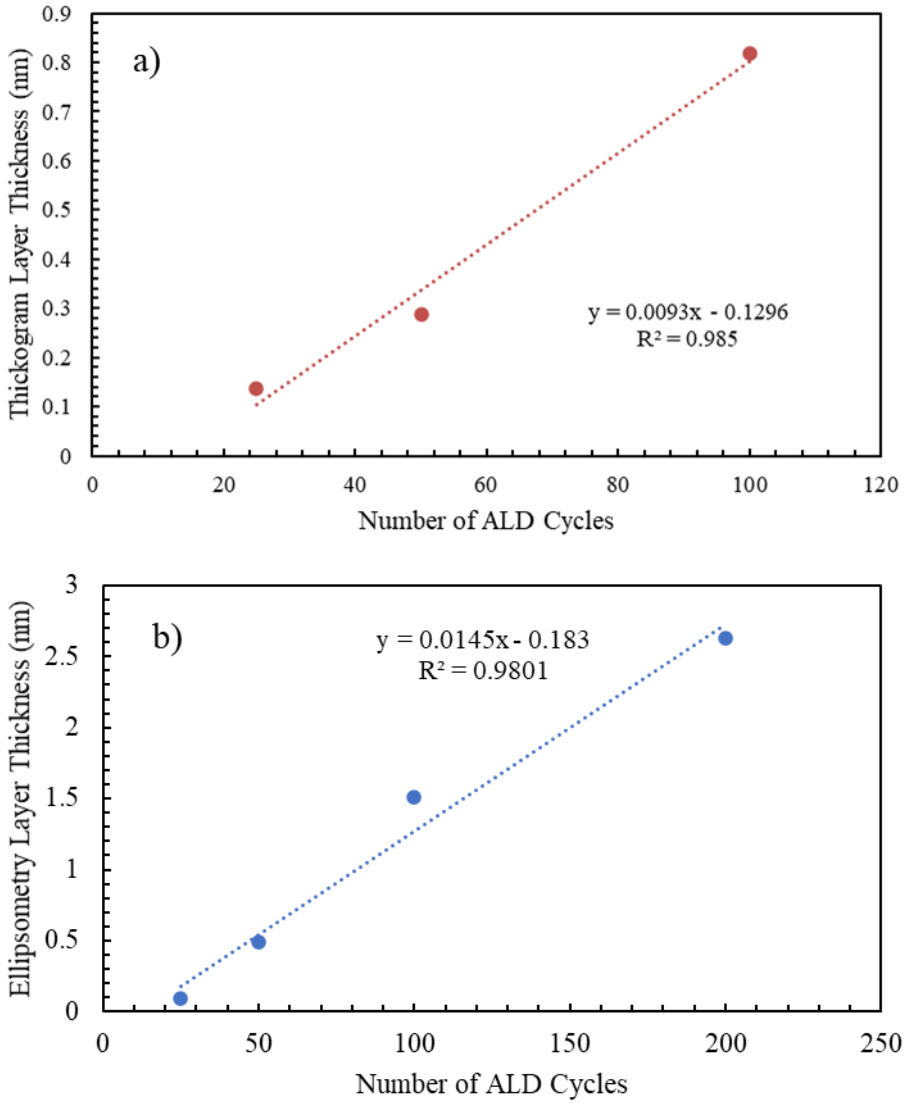

Figure 6.6. Film thicknesses for $TiCl_4$/Water process on SiO_2 a) utilizing the thickogram method and b) ellipsometry.

6.4 Film Quality

Film quality has been partially investigated by examining the concentration of impurity species as determined by XPS. For the TMA/water process, the initial experimental data point (100 cycles) displayed contamination by Cl and Ge, residual species from a previous chemistry investigated in the ALD reactor system. Subsequent experiments do not show any Ge contamination although residual Cl was detected, and after switching to the $TiCl_4$/water process, no Ge or Al contamination was detected. In addition to the presence of residual species from previously examined chemistries, the presence of undesired species present in the metal precursors can degrade the performance of the deposited film (C for the TMA/water process and Cl for the $TiCl_4$/water process). As shown in Figure 6.7, Ge contamination is only observed for the 100 cycle experiment for all substrates, which was the first experiment conducted at the beginning of this work, with all subsequent experiments showing no Ge contamination. In general, Cl contamination was below 1 atom percent and was lowest for 200 cycle experiments or decreased with an increasing number of cycles. Similarly, C contamination generally decreased with an increasing number of cycles. Therefore, it is probable that most of the carbon inclusion is not from unfavorable degradation of the precursor throughout the entire film but unfavorable degradation at the initial stages of film growth or is present on the wafer before film growth. Although wafers were cleaned and degreased ultrasonically before film deposition, wafers were exposed to the atmosphere between sonication and deposition causing adventitious carbon deposition which would be further and further covered with increasing numbers of cycles and cause attenuation of the C signal through the deposited film overlayer. Additionally, this level of carbon contamination is consistent

with previous literature. Previous work utilizing XPS depth profiling via sputtering for Al_2O_3 deposited by the TMA/water process on Cu substrates has shown approximately 25% C with no sputtering (comparable to 25 cycles data presented here with ~22% C as the literature sample was exposed to air before moving to the XPS and much of the contamination here is likely adventitious carbon as discussed previously) which decreases down to approximately 5% once within the film (comparable to 100 or 200 cycle data presented here as no underlying substrate signal was observed) where this work also shows approximately 5-7% C [9]. The carbon contamination within the film is due to the incomplete reaction of TMA with water and is consistent with the previously mentioned study from the literature indicating that the extent of incomplete reaction is also consistent with previous work and the film qualities are comparable.

In addition to examining film contamination, examining the stoichiometry of the deposited film can also provide information about film growth. While there may be some initial effects due to the nature of the underlying substrate, a sufficiently thick film should be relatively insensitive to the substrate and should exhibit consistent composition across multiple substrates. Figure 6.8 presents the composition of Al and O of the films on various substrates as a function of the number of TMA/water ALD cycles. During initial film growth (25 and 50 cycles) the composition changes as the underlying substrate signal are present, for example, high O concentration is present for SiO_2, which contains significant O in the underlying substrate. However, for 100 and 200 cycle samples, no underlying substrate is detected and only Al_2O_3 film is observable. As the composition is independent of cycle number (at and above 100 cycles) and substrate, the film quality is high as it is

essentially identical for all substrates and is not influenced by the underlying substrate or any other experimental parameters.

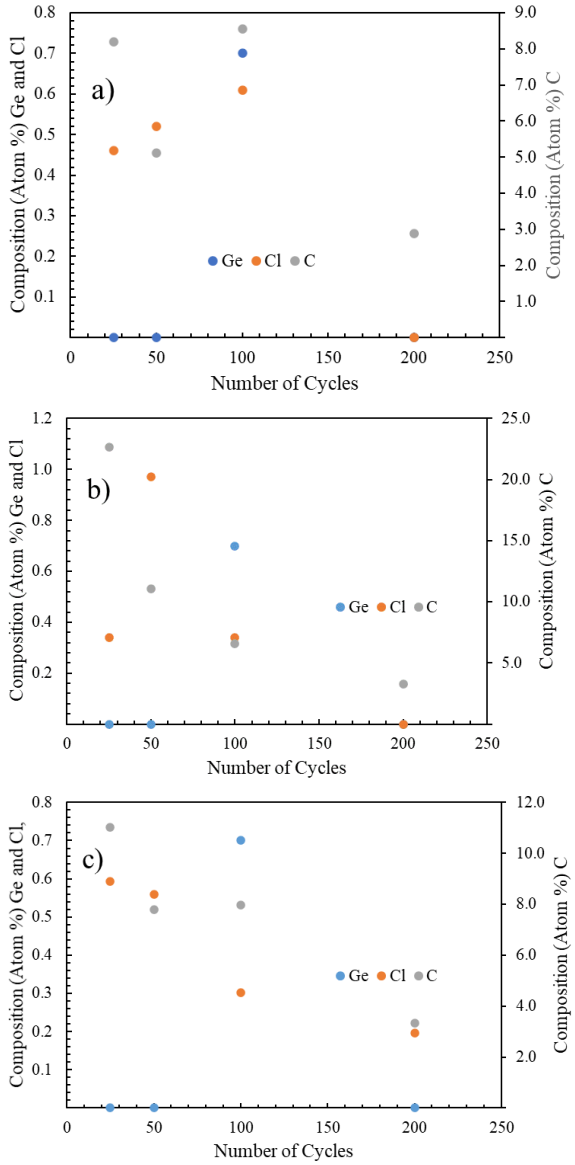

Figure 6.7. Quantification of film contamination for the TMA/Water process for a)SiO_2, b) Cu, and c)TiN substrates.

As shown in Figure 6.9, there is a lack of trend regarding C and Cl contamination for the $TiCl_4$/water process. In general, a maximum in film contamination is observed with intermediate numbers of cycles (50 or 100) and a minimum in contamination is observed for low and high numbers of cycles (25 and 200 respectively). The reason for this is unclear,

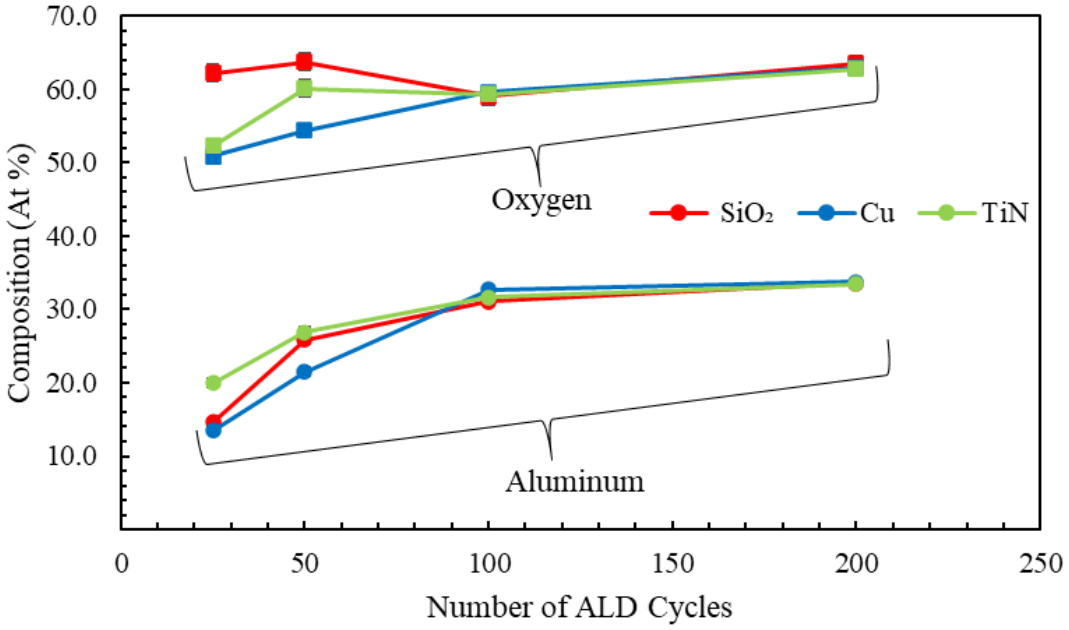

Figure 6.8. Quantification of Al and O atom percent deposited on a) SiO_2, b) Cu, and c)TiN substrates as a function of the number of ALD cycles.

especially as for the $TiCl_4$/water process no additional carbon atoms are present in either precursor. Therefore, increasing, or constant carbon contamination with increasing film thickness must be due to additional contamination with the system from previous precursors (TMA) or back-streamed mechanical roughing pump oil. Interestingly, no Al contamination was noted in the TiO_2 films, and therefore residual TMA in the system is may not be responsible for this contamination, although Cl contamination has been noted without Ge or Ti inclusion in other films deposited in this work.

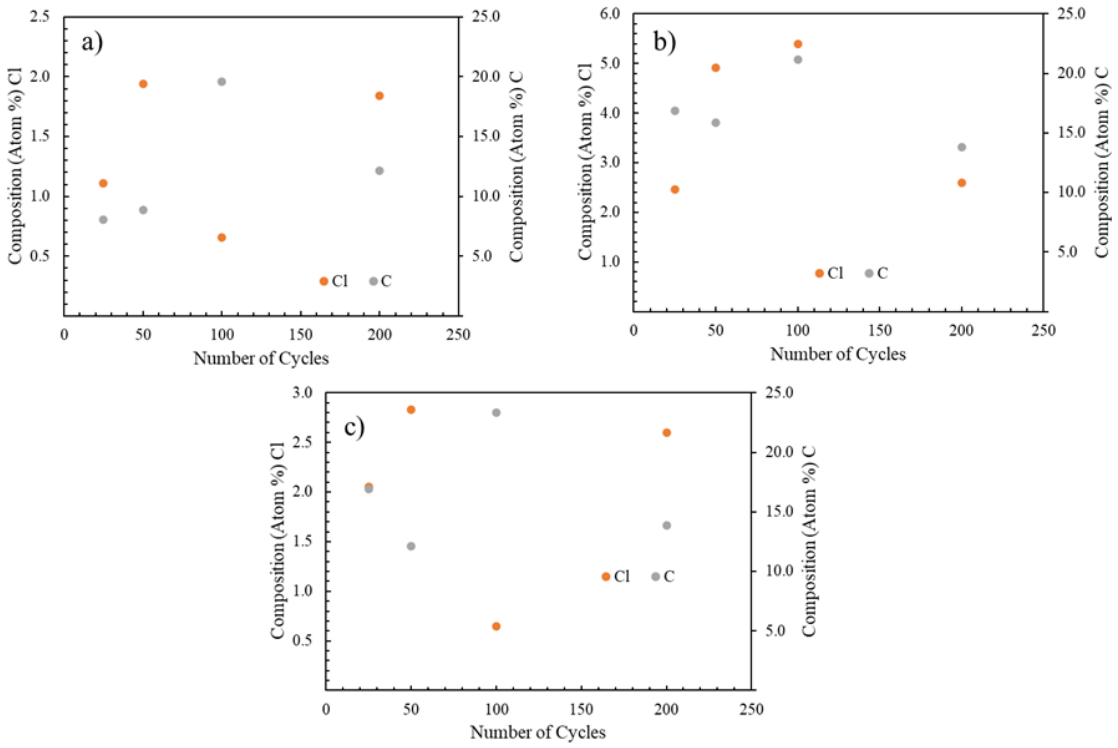

Figure 6.9. Quantification of film contamination for the $TiCl_4$/Water process for a) SiO_2, b) Cu, and c)TiN substrates.

6.5 Film Deposition on Soft Materials – Polymers

Ideal film growth via ALD requires certain properties from the underlying substrate and deviations from ideal ALD growth often occurs during initial growth where substrate properties play a large role in growth mechanisms. One such required property is the presence of reactive surface speciation (often -OH groups for metals and metal oxides), and while some polymers have such functionality, many commonly utilized polymers (low-density polyethylene (LDPE), polypropylene (PP), etc.) do not. Therefore, there is an initial induction period, referred to as the nucleation period, in which precursor materials are strongly adsorbed onto the polymers themselves to create reactive sites instead of solely reacting with surface functionality. In general, this period is often around 10-20 ALD cycles and it is desired to understand how the surface chemistry of non-functionalized

polymers are impacted by this nucleation period via XPS analysis. Once these types of interactions are well understood on this system and changes can be quantified or qualified then further experiments can be possible on more complex soft materials such as enzymes or other biological substrates. To this end, three polymers, LDPE, PP, and polyamide (Nylon 6,6) were coated with low numbers of cycles of Al_2O_3, via the TMA/water process which this work has previously shown to work reliably with a variety of substrates and for a range of thicknesses. The process could also be extended to the $TiCl_4$/water process, however, this process has not behaved as ideally as TMA/water and therefore would be more complicated to use for initial testing. The polymer selection also allows for a direct comparison of polymers with potentially reactive O and N functionality (Nylon 6,6) and those with no added functionality (LDPE and PP).

A complete comparison of C XPS spectra before and after coating with the TMA/water is shown in Table S1 and C spectra before and after coating are shown in Figures 6.10a and 6.10b respectively. Each of the polymers displays a different response to the ALD process with Nylon 6,6 developing a substantial Al_2O_3 layer, while PP has a less Al and LDPE does not develop a detectable amount of Al after 25 deposition cycles as shown in Figure 6.11. This is not surprising considering the structure of these polymers. As mentioned previously, the presence of reactive surface functionality is crucial for the initial stages of ALD deposition before a full monolayer of the film is deposited. Since Nylon 6,6 has oxygen and nitrogen-containing surface functionality it follows that these species can be active in initial film growth. While both PP and LDPE both only contain C-C and C-H bonds, PP contains a surface with repeating C-H and C-(CH_3) functionality that could present a more favorable surface for nucleation than LDPE which only presents

homogenous C-(CH_3) bonding. Interestingly, incorporation of Cl into the polymer and film is only observed in cases in which a film is deposited as LDPE exhibits no detectable Cl after 25 ALD cycles. Therefore, it is plausible that Cl incorporation occurs not on the polymer but instead on reactive surface functionality introduced during the ALD cycle by either reacting with exposed Al or OH groups for example, and this incorporation does not occur directly on the polymer itself. Examination of Cl detailed XPS spectra in Figure 12c shows that Cl is present as a metal chloride, confirming that Cl incorporation occurs due to the presence of Al and explains why a lack of Cl is observed with LDPE [10] where no Al deposition is observed.

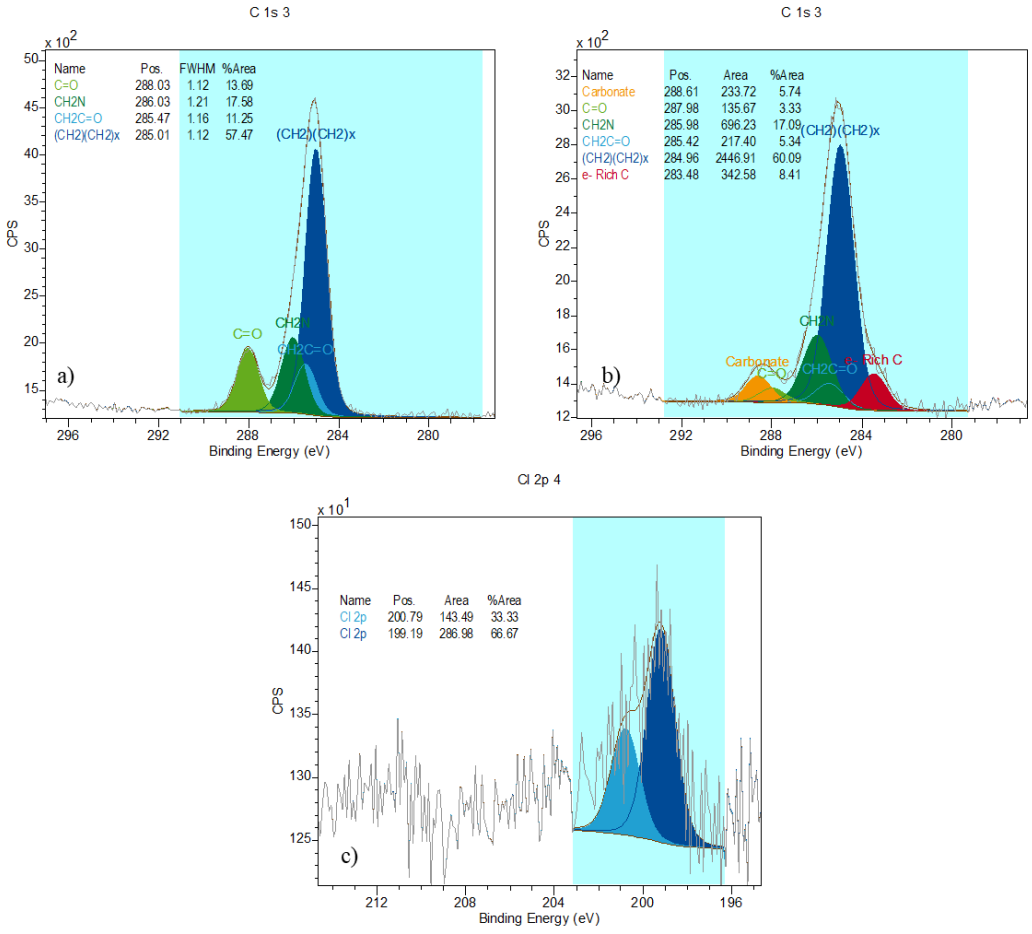

Figure 6.10. XPS of Nylon 6,6 a) C spectra before ALD, b) C spectra after ALD, and c) Cl spectra after ALD.

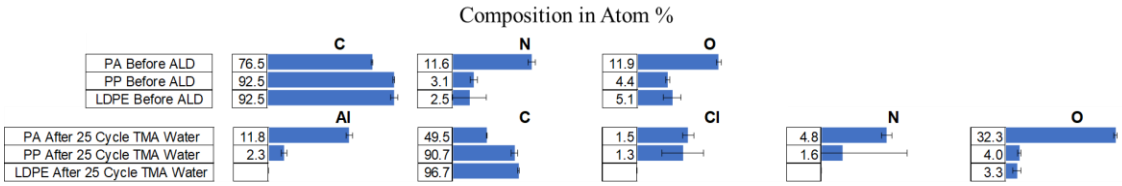

Figure 6.11. Composition of the film in atom percent for various polymer samples before and after 25 TMA/Water ALD cycles.

The role of surface functionality is also supported by observing detailed XPS spectra for C. As shown in Table S1, LDPE has essentially no change to surface chemistry. PP has slight changes via the introduction of a low binding energy peak, likely corresponding to species present on the surface from the decomposition of TMA during film growth. As this is a low binding energy peak it is more electron-rich than the C-C bond and is likely tied to C-Al bonding or other electron-rich species formed during the interaction of the polymer with TMA. In addition, the amount of native oxygen functionality at the surface is reduced (C=O) as these species likely contributed to initial film growth. As shown in the before and after C XPS for Nylon 6,6, the amount of C=O functionality decreased and was replaced by carbonate species, likely due to reaction between these sites and TMA and water. Finally, for Nylon 6,6 a larger amount of the low binding energy species (at approximately the same binding energy as the new species observed for PP) is detected, supporting it being a partial decomposition product as its higher concentration corresponds to the thicker Al_2O_3 film deposited on Nylon 6,6 and is roughly independent of the polymer identity. In addition, a high binding energy component is also observed, potentially corresponding to a carbonate species present from a reaction with TMA and O functionality of the polymer or potentially with the N functionality. An examination of both the N and O detailed XPS for Nylon 6,6 shown in Figure 6.12 displays

the formation of new species after the ALD process. Both a higher and lower binding energy N species form and two new species are present in the O spectra. Changes to the O spectra correspond to an oxide of aluminum and a higher binding energy component corresponding to a carbonate. For N, the presence of a lower binding energy component helps confirm that the N functionality is an important reactive surface species as this component would be similar to that previously discussed for C, where the reactive N is bound to an electron-rich species such as Al. Additionally the ratio of C/N changes from 6.6 before coating to 10.3 after coating indicating a depletion in N content. However, some of this change is likely due to the incorporation of additional C from TMA, however, this cannot explain all the differences. A similar trend is also observed for PP and LDPE where the N content is reduced for PP and all N content is removed for LDPE. This would suggest that N species are potentially forming a volatile species during ALD deposition or nucleation that causes them to enter the gas phase and would explain the reduction in N content. Utilization of a mass spectrometer during processing would allow for this to be verified experimentally. The higher binding energy N component also likely corresponds to an N component that has been modified during the ALD process like the development of a more oxygenated component seen with the carbonate formed in the C spectra. The presence of aluminum oxide in the O spectra also confirms that the TMA/water process can deposit a metal oxide on a polymer substrate under these conditions.

Due to the formation of new species for polymers that were effectively coated during the ALD process, it is desired to verify that the treatment procedure did not induce unfavorable degradation in the underlying polymer. One rapid way to accomplish this is to visually inspect the polymer and check for discoloration, cracking, or cloudiness. As shown

in Figure 6.13, except for a slight change in polymer translucency for Nylon 6,6 all coated samples are indistinguishable from their uncoated reference samples.

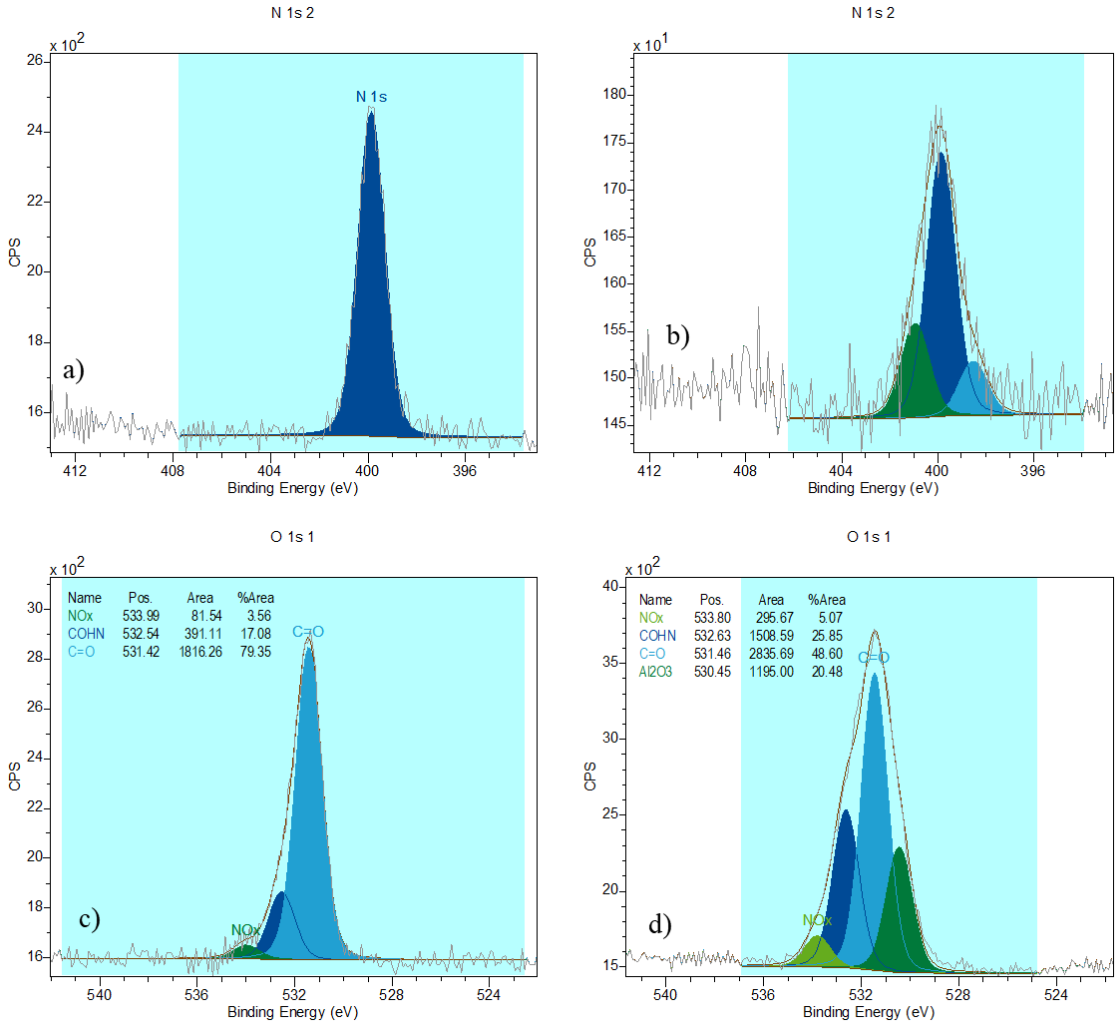

Figure 6.12. XPS of Nylon 6,6 a) N spectra before ALD, b) N spectra after ALD, b) O spectra before ALD, and d) O spectra after ALD.

Coating a polymer with Al_2O_3 provides a useful barrier layer that can improve the stability of the underlying polymer in performance applications. One such application is providing a barrier against oxygen incorporation and substrate oxidation and subsequent degradation at elevated temperatures. To test the oxidation resistance of coated Nylon 6,6,

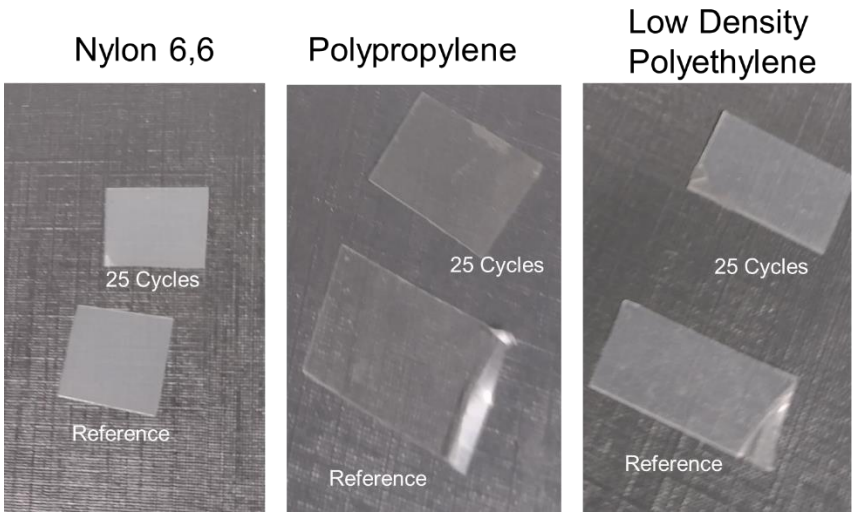

Figure 6.13. Photographs of various untreated reference polymers and polymers coated with 25 ALD cycles of the TMA/Water process.

a sample coated with 25 TMA/water cycles and an untreated reference sample was placed in an oven with static air at 200°C for 24 hours. It is expected that darkening and degradation of the polymer will occur under these conditions, therefore any reduction in this darkening for the ALD coated polymer would indicate enhanced performance and oxidation resistance. Unfortunately, as shown in Figure 6.14, the treated polymer did not display any enhanced oxidation resistance relative to an untreated reference polymer. One likely reason for a lack of change in stability is that the deposited layer of Al_2O_3 is very thin. If it is assumed that no nucleation period exists for Nylon 6,6 and that ideal ALD growth occurs according to the growth rates established in this work for the wafer-based substrates, then the Al_2O_3 layer is only about 2-2.5 nm thick and is likely less accounting for a potential nucleation period. For reference, the native oxide layer on aluminum is generally around 4 nm thick (although can be up to around 6 nm) [11] and protective barrier coatings can typically have thicknesses up to 100 nm. Therefore, it is not unexpected that the thin coating used in this experiment did not produce any observable difference in

oxidation resistance performance. As the thickness of the native oxide is representative of how far oxygen can readily diffuse through the oxide, this layer thickness is insufficient, especially considering that diffusion rates increase with temperature and that native oxide layers increase with increasing time and temperature [12].

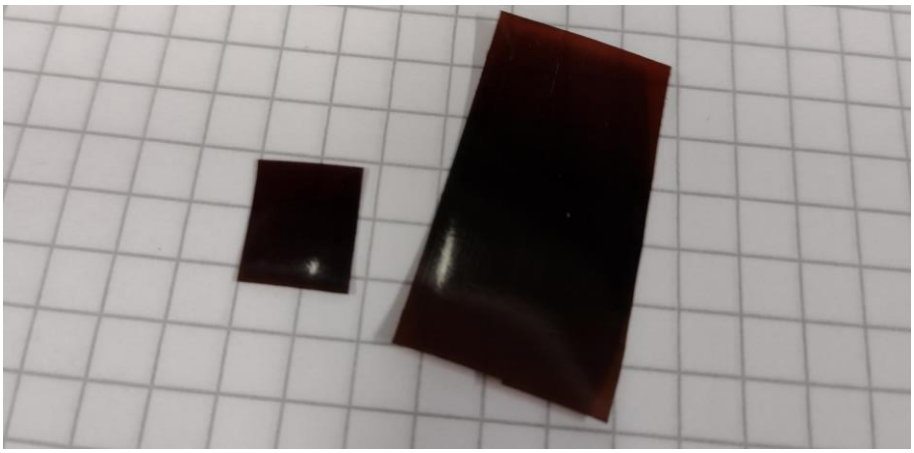

Figure 6.14. Photograph of 25 TMA/Water Cycle coated Nylon 6,6 (left) and untreated reference Nylon 6,6 (right) after exposed to static air in an oven for 24 hours.

As shown in Figure 6.15, SEM shows the untreated reference Nylon 6,6 (16,5a) and Nylon 6,6 with 25 TMA/water cycles look roughly the same at a scale of hundreds of microns and that the treatment procedure did not induce any additional cracking or damage to the underlying polymer. After heat treatment at 200°C for 24 hours, some additional cracking of the reference polymer is observed as seen in Figure 6.15c, where larger cracking begins to develop. This is also observed for Nylon 6,6 coated with 25 TMA/water cycles and then heat-treated as shown in Figure 6.15d. The ALD process neither causes additional cracking nor prevents cracking of the underlying polymer. This also implies that cracking of the deposited Al_2O_3 layer does not occur at least at these scales. As the polymer sample is insulating and was not sputtered coated with a conductive overlayer, such as

gold, significant artifacts are introduced due to the charging of the sample under the electron beam. Further magnification resulted in damaging the material due to beginning to burn holes it in so images were not possible at further magnification.

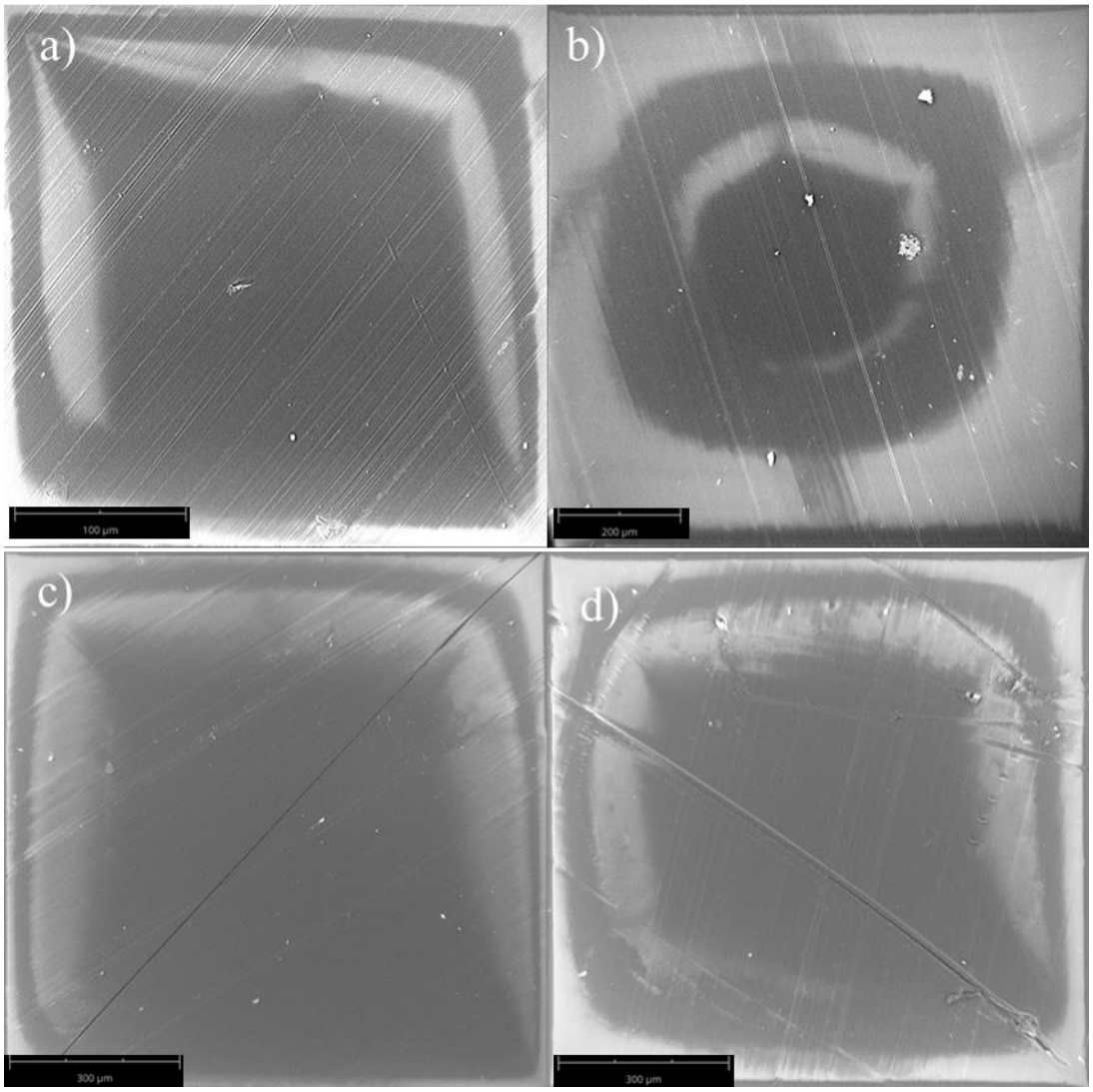

Figure 6.15. SEM Images of a)untreated reference Nylon 6,6 b) Nylon 6,6 with 25 TMA/Water cycles c)untreated reference Nylon 6,6 after 24 hours at 200°C and d) b) Nylon 6,6 with 25 TMA/Water cycles after 24 hours at 200°C.

6.6 Conclusions

This work demonstrates the home-built ALD system at BASF in Ludwigshafen, Germany functions well when utilizing a well-defined chemistry, namely the TMA/water

process. Additionally, excelled agreement between absolute values of film thickness and growth per cycle determined by ellipsometry and TOF-SIMS coupled with profilometry was observed indicating that both analytical systems are capable of reliably determining film thickness and could be utilized independently under these conditions. Additionally, these values were in excellent agreement with literature values. Further, the thickogram method was successfully utilized to qualitatively determine that growth per cycle measurements were linear. However, extension to the $TiCl_4$/water process displayed a lack of linearity and exhibited lower growth per cycle values than previous literature.

When the TMA/water process was utilized to coat polymer samples, the degree of coating was dependent on the presence of reactive surface functionalities. LDPE and PP showed no and minimal Al_2O_3 growth respectively as these polymers lack reactive O or N surface functionality. However, Nylon 6,6 which contains this functionality displayed significant Al_2O_3 growth, and changes to the N and O functionality were observed in XPS indicating that these species are responsible for the growth here while LDPE and PP were still within their nucleation periods. The coated Nylon 6,6 was tested as a boundary layer for prevention of oxidative damage to the polymer, however, due to only the low number of cycles, the coat was not thick enough to prevent diffusion of oxygen and was damaged to essentially the same extent as an uncoated polymer sample.

CHAPTER 7

FUTURE WORK AND CONCLUSIONS

7.1 Ethane Partial Oxidation

This work demonstrated how dopants influence the properties of the M1/M2 catalyst using in-situ and ex-situ characterization techniques. Utilizing TPR, it was suggested that Pd resides within one of the rings of the catalyst which has previously been documented to be an "oxygen highway" for the catalyst. The presence of an element capable of dissociating hydrogen on this oxygen highway can explain the interesting low-temperature TPR behavior of this catalyst although further work needs to be conducted to verify the position of Pd within the catalyst.

Further, utilizing in-situ Raman under reaction conditions, inert gas, and oxygen it was determined that the presence of Ti influences the oxygen mobility and incorporation within the catalyst and was correlated with the increased acetic acid production (a more oxygenated product) observed catalytically. Additionally, at high temperatures under oxygen, MoO_x was documented to form which did not form with Pd doped catalysts or with undoped catalysts further supporting that Ti influences oxygen incorporation within the catalyst. To further confirm this, the use of temperature-programmed isotopic oxygen exchange can be utilized. In this experiment, $^{18}O_2$ flows over the catalyst in a tube furnace and the ratio of $^{16}O_2$, $^{18}O_2$, and $^{16}O\ ^{18}O$ are determined to determine how the presence of dopants and temperature influence how easily oxygen can exchange and be transported within the catalyst. Further, this experimental framework can be extended to examine other dopants utilized in this catalyst system.

7.2 CO Oxidation over Stainless Steel Mesh

Due to the nature of stainless steel monoliths, thorough characterization of the produced catalysts supported on stainless steel mesh can prove to be difficult. For example,

due to the lack of porosity of the steel, quantifying surface area via conventional techniques such as N_2 physisorption is difficult. Alternative techniques such as profilometry (either via contact or optical method) [162] can quantify surface roughness before and after anodic treatment to provide an indirect measure of surface area. However, the diameter of the mesh (~0.2 mm) also poses issues due to equipment limitations and minimum sample sizes. One methodology to bypass these issues is to make and catalytically test mesh-based catalysts but also simultaneously synthesize samples under identical conditions using a plate of the same grade of stainless steel. These plate samples can be analyzed via profilometry to provide information about the relative surface roughness of the produced mesh catalysts. This can be accomplished by utilizing grades of stainless steel that are commercially available both in wire and sheet form. Unfortunately, the grade of stainless steel utilized in the bulk of the study presented earlier is almost entirely utilized for resistive heating elements and is only available in wire form and is extremely difficult to find a supplier for sheets of CRAL 20-5 without minimum order sizes that are not accessible for small scale academic testing.

One additional change induced by anodic oxidation that was not extensively examined in this study is the incorporation of the electrolyte anion into the surface of the stainless steel mesh. This has been previously documented for anodically oxidized aluminum and other metals [163], [164] as well as stainless steels [165]. Therefore, changing the electrolyte during anodic oxidation changes the composition of the stainless steel surface. As the catalyst is impregnated with precious metal salts with positive metal cations, the addition of electrolyte anions to the surface of the steel can modulate how the precious metal uptake occurs due to favorable interactions between the metal cations in

solution and the anions present at the surface of the mesh. In addition, this may explain the differences observed in the uptake of platinum and palladium during catalyst impregnation. The metal precursor utilized for palladium doping results in the formation of palladium containing polyatomic ion with an overall -2 charge meaning that it would have unfavorable interactions with any electrolyte incorporated into the steel surface and may explain why differences were not seen in precious metal uptake except concerning an unoxidized or weakly treated mesh which can be explained by examining changes in surface roughness or surface area. In contrast, the platinum precursor produces a +4 metal-containing polyatomic ion in the solution that would be capable of having favorable interactions with any surface incorporated electrolyte. This is a plausible reason why the uptake of platinum was strongly modulated by treatment conditions and primarily described by differences in the electrolyte composition. The catalysts with the highest activity and the highest platinum uptakes were those treated by citric acid. As explained previously, this is rather unexpected as these catalysts do not have a higher surface area than phosphoric acid-treated meshes. However, citrate is known to be a strong chelating agent [166] and this property is a likely reason for the enhanced uptake and activity due to citrate incorporation of the mesh and production of a more suitable substrate for metal deposition. In addition, work utilizing a variety of different precious metal precursors with different valences would elucidate this phenomenon more thoroughly, for example using a positive ion palladium source and a negative ion platinum source and examining the differences in precious metal uptake as done in this work. Therefore, quantifying the amount and oxidation state of electrolyte anion incorporated into the stainless steel could provide important information regarding how anodic treatment influences metal uptake.

The usage of additional electrolytes with different types of anions (both organic and inorganic) would also determine how the incorporation of different anions influences the activity of the produced catalyst. These experiments can be carried out via either X-Ray Photoelectron Spectroscopy or Auger Electron Spectroscopy, although Auger Electron Spectroscopy is more commonly used for the examination of oxide layer thickness and contamination studies [167], [168] at least partly due to enhanced surface sensitivity and enhanced ease in determining differences in oxidation state (depending on the metal system examined).

The majority of the catalysts tested in this study were capable of reaching at or near 90% conversion at intermediate temperatures (250-450°C), although significant irreversible deactivation occurred after exposure to simplified simulated combustion exhaust at 600°C. However, the use of anodic oxidation is capable of preventing this deactivation by multiple possible pathways, with the optimal anodic synthesis parameters creating a catalyst with 8 times the activity of an untreated catalyst at 600°C. However, deactivation still occurs to an appreciable extent over even a short time. Therefore, additional methodologies to improve the sintering resistance of these catalysts would be a viable path forward to improving the efficacy of these catalysts. One way to accomplish this would be to add material, such as ceria, capable of atom trapping mobile previous metals present during sintering. Either the use of a metallic mesh containing ceria or impregnating a ceria-free monolith with ceria could be two viable synthetic routes for this.

An increase in hydrothermal stability would also allow for more extensive testing under severe operating conditions. This could be accomplished by either aging or testing at temperatures above 600°C or on an extended time scale (much greater than 100 hours).

In addition, the use of a comprehensive simulated combustion exhaust, or actual combustion exhaust, would provide more understanding of how these catalysts perform under actual operating conditions.

Additionally, a variety of different synthesis parameters can be adjusted in an attempt to improve performance. First, the order of impregnation of precious metals could be changed from a simultaneous impregnation to a sequential one with experiments on utilizing either precious metal first. As mentioned previously, the inclusion of anions into the surface oxide layer also presents a unique opportunity during catalyst synthesis. As the change of these anion groups can be adjusted as a function of pH during precious metal impregnation, commonly utilized during strong electrostatic adsorption synthesis, more favorable dispersion or bimetallic interactions between platinum and palladium may be able to be controlled. Careful control and use of alternating positively and negatively charged metal precursors would also be a viable route towards controlling bimetallic interactions in the produced catalyst.

Interestingly, an increase in activity with time on stream was observed for the optimal catalyst after an initial decrease due to sintering. It was hypothesized that clustering of Cr on the surface of the catalyst could modulate the activity and such clustering has been previously observed for similar grades of stainless steel. SEM with EDX mapping both before and after time on stream testing would reveal the presence or lack thereof of these clusters and determine their proximity to active precious metal sites.

Finally, more thorough studies could be conducted to further understand the nature of the precious metals on the surface of the stainless steel mesh. Common methodologies

such as TEM and H_2 or CO chemisorption present issues as the thickness of the steel monolith prevents the use of TEM and the variety of transition metals present in stainless steel are also capable of adsorbing H_2 or CO. A potential way around this would be to control the temperature that the experiments are conducted at to minimize adsorption of probe molecules on species present naturally in the steel and examine only added precious metal species, but methodology validation would need to be conducted as CRAL 20-5 wire contains Fe, Cr, Y, among other metals that can pose analytical issues with characterization.

7.3 Catalytic Biomass Torrefaction

As shown in this work, power plant flue gas can successfully be utilized to torrefy biomass that can be utilized as a coal replacement at up to a 40% co-firing rate. Additionally, a magnetically separable catalyst was developed that can remove up to 95% of the CO produced during the process, although this is highly dependent on the oxygen concentration in the flue gas. Finally, the dependence on oxygen concentration and the ability of the catalyst to produce H_2 under oxidizing conditions was investigated via bio-oil injection experiments which determined that the catalyst changes oxidation states under reaction conditions due to the presence of bio-oil.

To definitively determine how catalysts, behave during torrefaction, and the nature of the species present on the surface of the catalysts under operating conditions, detailed spectroscopic experiments are required. However, these experiments present several technical issues due to the nature of the torrefaction process. The bio-oils produced during torrefaction tend to form films on tubing and eventually cause plugs in analytical lines on

experimental setups. One spectroscopic technique to accomplish this would be FT-IR, however, the experimental cell used either in a transmission or DRIFTS mode would suffer from the formation of bio-oil films on the cell windows causing both attenuation of the signal but also irreversible damage. Therefore, these experiments are practically infeasible without a custom-designed cell that is capable of being fully cleaned either between scans or after each experiment. As a synthetic bio-oil was created that accurately replicates the results seen during torrefaction, it may be possible to conduct these experiments utilizing a synthetic bio-oil. However, film formation still appears to be an issue even with the synthetic bio-oil meaning that these experiments would still present equipment issues.

As the synthetic bio-oil is an acceptable analog for actual bio-oil injected into the process without biomass in addition to simulating actual torrefaction experiments it would additionally be interesting to determine which components are responsible for changes to the catalyst during torrefaction that results in the formation of H_2. As the composition of the bio-oil is known, single functional groups can be removed from the mixture and tested to determine if a specific component or mixture of components is responsible. This would also potentially enable FT-IR experiments if problematic components of the bio-oil could be eliminated with no change to the performance of the catalyst under simulated operating conditions.

Additionally, it would be interesting to determine the composition of the biochar after torrefaction as a function of treatment conditions as well as the heating value for each of these samples. Quantification of grinding energy as a function of treatment conditions would also guide the minimum temperature and oxygen concentration required to satisfy

industrial requirements for processability to not jam power plant pulverizers as previously discussed [45], [106] in a quantitative as opposed to qualitative manner.

7.4 Atomic Layer Deposition

The results of this work demonstrate that the reactor system used for these experiments can produce reliable and accurate data with well-studied ALD processes. Therefore, this system can also be utilized with new chemistries and processes, and this constitutes the main body of future work to be done with this system. Planned work on this system includes depositing Co-based films, although this would require a modification of the system to accommodate a higher wattage heater capable of supplying sufficient energy for this reaction. Additionally, an extension of this system to new materials systems such as polymers and enzymes instead of well-defined wafers provides an interesting route forward. Finally, deposition of multilayer materials (e.g. alternating layers of TiO_2 and Al_2O_3) would be possible by adding an additional valve system and slightly modifying the python code automating the process. This would also require optimizing the $TiCl_4$/water process to coat material in a more ALD-like manner. As the film growth rate is significantly lower than literature values, increasing the dosage pressure or dosage time would be a good first step to addressing this issue and determining why issues were observed in this work. For future chemistries, it would also be important to check the dependence of dosing pressure and time to verify that saturated ALD growth is occurring.

Additionally, the use of soft materials, such as polymers, and biological materials, such as enzymes as substrates also provide an interesting direction for future work. ALD processes are generally carried out on substrates with reactive surface functionality such as -OH groups on metal oxides and many polymers and other soft materials do not have such

functionality. Therefore, a nucleation period (~10-20 cycles) is often observed before regular ALD growth is observed on these materials and it is interesting to determine what happens to the surface of these materials during this period. Preliminary work examining 3 different polymers has shown that changes to the surface of the polymers can occur, depending on the nature of the polymer itself. However, because for Nylon 6,6, a detectable Al_2O_3 layer was deposited it is more difficult to determine in relative changes in speciation are due to attenuation or changes in surface chemistry. Therefore, half-cycle resolved experiments may be able to provide more information about nucleation and initial surface chemistry change, especially for Nylon 6,6. Additionally, further oxidative stability testing could be conducted with Nylon 6,6 utilizing a thicker Al_2O_3 coating that could enable superior performance testing characteristics.

REFERENCES

[1] M. Alifanti, G. Bueno, V. I. Parvulescu, V. I. Parvulescu, and V. Cortés Corberán, "Oxidation of ethane on high specific surface SmCoO3 and PrCoO3 perovskites," *Catal. Today*, vol. 143, no. 3–4, pp. 309–314, May 2009.

[2] P. M. Frederik and D. H. W. Hubert, "Cryoelectron Microscopy of Liposomes," *Methods Enzymol.*, vol. 391, pp. 431–448, Jan. 2005.

[3] T. Ren, M. Patel, and K. Blok, "Olefins from conventional and heavy feedstocks: Energy use in steam cracking and alternative processes," *Energy*, vol. 31, no. 4, pp. 425–451, Mar. 2006.

[4] E. M. Thorsteinson, T. P. Wilson, F. G. Young, and P. H. Kasai, "The oxidative dehydrogenation of ethane over catalysts containing mixed oxides of molybdenum and vanadium," *J. Catal.*, vol. 52, no. 1, pp. 116–132, Mar. 1978.

[5] K. Ruth, R. Burch, and R. Kieffer, "Mo – V – Nb Oxide Catalysts for the Partial Oxidation of Ethane II . Chemical and Catalytic Properties and Structure Function Relationships," *J. Catal.*, vol. 175, pp. 27–39, 1998.

[6] J. S. Valente *et al.*, "Chemical, structural, and morphological changes of a MoVTeNb catalyst during oxidative dehydrogenation of ethane," *ACS Catal.*, vol. 4, no. 5, pp. 1292–1301, May 2014.

[7] C. A. Gärtner, A. C. van Veen, J. A. Lercher, A. C. van Veen, and J. A. Lercher, "Oxidative dehydrogenation of ethane: common principles and mechanistic aspects," *ChemCatChem*, vol. 5, no. 11, pp. 3196–3217, Nov. 2013.

[8] B. Deniau, J. M. M. Millet, S. Loridant, N. Christin, and J. L. Dubois, “Effect of several cationic substitutions in the M1 active phase of the MoVTeNbO catalysts used for the oxidation of propane to acrylic acid,” *J. Catal.*, vol. 260, no. 1, pp. 30–36, Nov. 2008.

[9] E. V. Ishchenko, T. Y. Kardash, R. V. Gulyaev, A. V. Ishchenko, V. I. Sobolev, and V. M. Bondareva, “Effect of K and Bi doping on the M1 phase in MoVTeNbO catalysts for ethane oxidative conversion to ethylene,” *Appl. Catal. A Gen.*, vol. 514, pp. 1–13, Mar. 2016.

[10] E. V. Ishchenko *et al.*, “Effect of Bi on catalytic performance and stability of MoVTeNbO catalysts in oxidative dehydrogenation of ethane,” *Appl. Catal. A Gen.*, vol. 534, pp. 58–69, Mar. 2017.

[11] X. Li and E. Iglesia, “Support and promoter effects in the selective oxidation of ethane to acetic acid catalyzed by Mo-V-Nb oxides,” *Appl. Catal. A Gen.*, vol. 334, no. 1–2, pp. 339–347, 2008.

[12] Y. S. Yun *et al.*, “Promoting effect of cerium on MoVTeNb mixed oxide catalyst for oxidative dehydrogenation of ethane to ethylene,” *Appl. Catal. B Environ.*, vol. 237, pp. 554–562, Dec. 2018.

[13] J. . Oliver, J. . López Nieto, P. Botella, and A. Mifsud, “The effect of pH on structural and catalytic properties of MoVTeNbO catalysts,” *Appl. Catal. A Gen.*, vol. 257, no. 1, pp. 67–76, Jan. 2004.

[14] J. D. Jimenez *et al.*, “Statistically Guided Synthesis of MoV-Based Mixed-Oxide Catalysts for Ethane Partial Oxidation,” *Catalysts*, vol. 8, no. 9, p. 370, Sep. 2018.

[15] M. A. Bañares, “Supported metal oxide and other catalysts for ethane conversion: a review,” *Catal. Today*, vol. 51, no. 2, pp. 319–348, Jun. 1999.

[16] N. Haddad, E. Bordes-Richard, and A. Barama, “MoOx-based catalysts for the oxidative dehydrogenation (ODH) of ethane to ethylene: Influence of vanadium and phosphorus on physicochemical and catalytic properties,” *Catal. Today*, vol. 142, no. 3–4, pp. 215–219, Apr. 2009.

[17] R. K. Grasselli *et al.*, “Active centers in Mo-V-Nb-Te-Ox (amm)oxidation catalysts,” *Catal. Today*, vol. 91–92, pp. 251–258, Jul. 2004.

[18] T. Vogt, D. A. Blom, L. Jones, and D. J. Buttrey, “ADF-STEM Imaging of Nascent Phases and Extended Disorder Within the Mo–V–Nb–Te–O Catalyst System,” *Top. Catal.*, vol. 59, no. 17–18, pp. 1489–1495, 2016.

[19] M. Sadakane *et al.*, “Synthesis of orthorhombic Mo-V-Sb oxide species by assembly of pentagonal Mo6O21polyoxometalate building blocks,” *Angew. Chemie - Int. Ed.*, vol. 48, no. 21, pp. 3782–3786, 2009.

[20] D. A. Blom, T. Vogt, L. F. Allard, and D. J. Buttrey, “Observation of Sublattice Disordering of the Catalytic Sites in a Complex Mo-V-Nb-Te-O Oxidation Catalyst Using High Temperature STEM Imaging,” *Top. Catal.*, vol. 57, no. 14–16, pp. 1138–1144, 2014.

[21] W. D. Pyrz, D. A. Blom, T. Vogt, and D. J. Buttrey, “Direct imaging of the MoVTeNbO M1 phase using an aberration-corrected high-resolution scanning transmission electron microscope,” *Angew. Chemie - Int. Ed.*, vol. 47, no. 15, pp. 2788–2791, 2008.

[22] D. A. Blom and T. Vogt, “Multi-slice frozen phonon simulations of high-angle annular dark field scanning transmission electron microscopy images of the structurally and compositionally complex Mo–V–Nb–Te oxide catalyst,” *Adv. Struct. Chem. Imaging*, vol. 4, no. 1, p. 9, 2018.

[23] Q. He, J. Woo, A. Belianinov, V. V. Guliants, and A. Y. Borisevich, “Better catalysts through microscopy: Mesoscale M1/M2 intergrowth in molybdenum-vanadium based complex oxide catalysts for propane ammoxidation,” *ACS Nano*, vol. 9, no. 4, pp. 3470–3478, 2015.

[24] Y. V. Kolen’ko *et al.*, “Unusual Phase Evolution in MoVTeNb Oxide Catalysts Prepared by a Novel Acrylamide-Gelation Route,” *ChemCatChem*, vol. 4, no. 4, pp. 495–503, Apr. 2012.

[25] D. Melzer *et al.*, “Design and synthesis of highly active MoVTeNb-oxides for ethane oxidative dehydrogenation,” *Nat. Commun.*, vol. 10, no. 1, pp. 1–9, 2019.

[26] “Process for producing ethylene via oxidative dehydrogenation (odh) of ethane,” Apr. 2009.

[27] B. Chu, L. Truter, T. A. Nijhuis, and Y. Cheng, “Performance of phase-pure M1 MoVNbTeOx catalysts by hydrothermal synthesis with different post-treatments for the oxidative dehydrogenation of ethane,” *Appl. Catal. A Gen.*, vol. 498, pp. 99–106, Jun. 2015.

[28] T. T. Nguyen, M. Aouine, and J. M. M. Millet, “Optimizing the efficiency of MoVTeNbO catalysts for ethane oxidative dehydrogenation to ethylene,” *Catal. Commun.*, vol. 21, pp. 22–26, May 2012.

[29] J. S. Valente, R. Quintana-Solórzano, H. Armendáriz-Herrera, G. Barragán-Rodríguez, and J. M. López-Nieto, “Kinetic Study of Oxidative Dehydrogenation of Ethane over MoVTeNb Mixed-Oxide Catalyst,” *Ind. Eng. Chem. Res.*, vol. 53, no. 5, pp. 1775–1786, Feb. 2014.

[30] P. DeSanto *et al.*, “Structural aspects of the M 1 and M 2 phases in MoVNbTeO propane ammoxidation catalysts,” *Z. Krist.*, vol. 219, pp. 152–165, 2004.

[31] P. DeSanto *et al.*, “Structural characterization of the orthorhombic phase M1 in MoVNbTeO propane ammoxidation catalyst,” *Top. Catal.*, vol. 23, no. 1–4, pp. 23–38, 2003.

[32] L. Annamalai, Y. Liu, S. Ezenwa, Y. Dang, S. L. Suib, and P. Deshlahra, “Influence of Tight Confinement on Selective Oxidative Dehydrogenation of Ethane on MoVTeNb Mixed Oxides,” *ACS Catal.*, vol. 8, no. 8, pp. 7051–7067, Aug. 2018.

[33] Y. Zhu *et al.*, “Formation of Oxygen Radical Sites on MoVNbTeOx by Cooperative Electron Redistribution,” *J. Am. Chem. Soc.*, vol. 139, no. 36, pp. 12342–12345, 2017.

[34] M. Aouine, T. Epicier, and J. M. M. Millet, “In Situ Environmental STEM Study of the MoVTe Oxide M1 Phase Catalysts for Ethane Oxidative Dehydrogenation,” *ACS Catal.*, vol. 6, no. 7, pp. 4775–4781, 2016.

[35] P. Concepción, P. Botella, and J. M. L. Nieto, “Catalytic and FT-IR study on the reaction pathway for oxidation of propane and propylene on V- or Mo–V-based catalysts,” *Appl. Catal. A Gen.*, vol. 278, no. 1, pp. 45–56, Dec. 2004.

[36] M. H. Castaño, R. Molina, S. Moreno, M. H. Castaño, R. Molina, and S. Moreno, "Oxygen storage capacity and oxygen mobility of Co-Mn-Mg-Al mixed oxides and their relation in the VOC oxidation reaction," *Catalysts*, vol. 5, no. 2, pp. 905–925, May 2015.

[37] R. K. Grasselli *et al.*, "Multifunctionality of Active Centers in (Amm)oxidation Catalysts: From Bi–Mo–Ox to Mo–V–Nb–(Te, Sb)–Ox," *Top. Catal.*, vol. 23, no. 1/4, pp. 5–22, 2003.

[38] European Union, *REGULATION (EC) No 715/2007 OF THE EUROPEAN PARLIAMENT AND OF THE COUNCIL*. 2007.

[39] M. Khosravi, A. Abedi, R. E. Hayes, W. S. Epling, and M. Votsmeier, "Kinetic modelling of Pt and Pt:Pd diesel oxidation catalysts," *Appl. Catal. B Environ.*, vol. 154–155, pp. 16–26, Jul. 2014.

[40] S. Salomons *et al.*, "On the use of mechanistic CO oxidation models with a platinum monolith catalyst," *Appl. Catal. B Environ.*, vol. 70, no. 1–4, pp. 305–313, Jan. 2007.

[41] Z. Hu, C. Z. Wan, Y. K. Lui, J. Dettling, and J. J. Steger, "Design of a novel Pd three-way catalyst: Integration of catalytic functions in three dimensions," *Catal. Today*, vol. 30, no. 1–3, pp. 83–89, Jun. 1996.

[42] A. P. Wong, E. A. Kyriakidou, T. J. Toops, and J. R. Regalbuto, "The catalytic behavior of precisely synthesized Pt–Pd bimetallic catalysts for use as diesel oxidation catalysts," *Catal. Today*, vol. 267, pp. 145–156, Jun. 2016.

[43] J. M. Herreros, S. S. Gill, I. Lefort, A. Tsolakis, P. Millington, and E. Moss, "Enhancing the low temperature oxidation performance over a Pt and a Pt–Pd diesel oxidation catalyst," *Appl. Catal. B Environ.*, vol. 147, pp. 835–841, Apr. 2014.

[44] M. Kärkkäinen *et al.*, "Deactivation of Diesel Oxidation Catalysts by Sulphur in Laboratory and Engine-Bench Scale Aging," *Top. Catal.*, vol. 56, no. 9, pp. 672–678, 2013.

[45] C. H. Kim, M. Schmid, S. J. Schmieg, J. Tan, and W. Li, "The Effect of Pt-Pd Ratio on Oxidation Catalysts Under Simulated Diesel Exhaust," in *SAE 2011 World Congress & Exhibition*, 2011.

[46] D. Wu and H. Zhang, "Mechanical Stability of Monolithic Catalysts: Scattering of Washcoat Adhesion and Failure Mechanism of Active Material," *Ind. Eng. Chem. Res.*, vol. 52, no. 41, pp. 14713–14721, Oct. 2013.

[47] D. L. Trimm, "Materials selection and design of high temperature catalytic combustion units," *Catal. Today*, vol. 26, no. 3, pp. 231–238, 1995.

[48] J. I. Balakrishnan, G.; Thirumurugesan, R.; Mohandas, E.; Sastikumar, D.; Kuppusami, P.; Song, "Phase Transition and Thermal Expansion Studies of Alumina Thin Films Prepared by Reactive Pulsed Laser Deposition Title," *J. Nanosci. Nanotechnol.*, vol. 14, no. 10, pp. 7728–7733, 2014.

[49] M. S. Elmaghraby, A. I. M. Ismail, and Z. L. Belal, "Thermal Expansion, Physico-Mechanical Properties and Microstructure of Cordierite Synthesized from Different Starting Materials," *Interceram - Int. Ceram. Rev.*, vol. 64, no. 4, pp. 209–213, 2015.

[50] M. Adamowska and P. Da Costa, “Structured Pd/γ-Al_2O_3 Prepared by Washcoated Deposition on a Ceramic Honeycomb for Compressed Natural Gas Applications,” *J. Nanoparticles*, vol. 2015, p. 601941, 2015.

[51] P. Jiang, G. Lu, Y. Guo, Y. Guo, S. Zhang, and X. Wang, “Preparation and properties of a γ-Al2O3 washcoat deposited on a ceramic honeycomb,” *Surf. Coatings Technol.*, vol. 190, no. 2–3, pp. 314–320, Jan. 2005.

[52] C. Agrafiotis and A. Tsetsekou, “The effect of powder characteristics on washcoat quality. Part I: Alumina washcoats,” *J. Eur. Ceram. Soc.*, vol. 20, no. 7, pp. 815–824, Jun. 2000.

[53] F. M. Z. Zotin, O. da F. M. Gomes, C. H. de Oliveira, A. A. Neto, and M. J. B. Cardoso, “Automotive catalyst deactivation: Case studies,” *Catal. Today*, vol. 107, pp. 157–167, 2005.

[54] D. Wu, Y. Zhang, and Y. Li, “Mechanical stability of monolithic catalysts: Improving washcoat adhesion by FeCrAl alloy substrate treatment,” *J. Ind. Eng. Chem.*, vol. 56, pp. 175–184, 2017.

[55] G. Qi, Y. Zhang, A. Chen, and Y. Yu, “Potassium-Activated Wire Mesh: A Stable Monolithic Catalyst for Diesel Soot Combustion,” *Chem. Eng. Technol.*, vol. 40, no. 1, pp. 50–55, 2017.

[56] D. Wu, S. Kong, H. Zhang, and Y. Li, “Mechanical stability of monolithic catalysts: Factors affecting washcoat adhesion and cohesion during preparation,” *AIChE J.*, vol. 60, no. 8, pp. 2765–2773, 2014.

[57] M. L. Godoy, E. D. Banús, O. Sanz, M. Montes, E. Miró, and V. G. Milt, “Stacked wire mesh monoliths for the simultaneous abatement of VOCs and diesel soot,” *Catalysts*, vol. 8, no. 1, p. 16, 2018.

[58] A. Lotfollahzade Moghaddam, T. Hamzehlouyan, V. Hosseini, and A. Mayer, “Beneficial Role of Oxygen in CO and Propylene Oxidation over a Pt–Pd-Based Wiremesh Catalyst as a Retrofit Emission Control Device for Four-Stroke Gasoline Spark-Ignited Motorcycles,” *Energy & Fuels*, 2021.

[59] Y. Matatov-Meytal and M. Sheintuch, “Catalytic fibers and cloths,” *Appl. Catal. A Gen.*, vol. 231, no. 1–2, pp. 1–16, 2002.

[60] K.-S. Chung, Z. Jiang, B.-S. Gill, and J.-S. Chung, “Oxidative decomposition of o-dichlorobenzene over V2O5/TiO2 catalyst washcoated onto wire-mesh honeycombs,” *Appl. Catal. A Gen.*, vol. 237, no. 1–2, pp. 81–89, 2002.

[61] M. L. Godoy, E. D. Banús, E. E. Miró, and V. G. Milt, “Single and double bed stacked wire mesh cartridges for the catalytic treatment of diesel exhausts,” *J. Environ. Chem. Eng.*, vol. 7, no. 5, p. 103290, 2019.

[62] L. Chen *et al.*, “Effect of calcination temperature on structural properties and catalytic soot combustion activity of MnOx/wire-mesh monoliths,” *Appl. Surf. Sci.*, vol. 467, pp. 1088–1103, 2019.

[63] J. C. Ganley, K. L. Riechmann, E. G. Seebauer, and R. I. Masel, “Porous anodic alumina optimized as a catalyst support for microreactors,” *J. Catal.*, vol. 227, no. 1, pp. 26–32, Oct. 2004.

[64] C. Song, M. Chen, C. Ma, and X. Zheng, “Pd-Mn/Stainless Steel Wire Mesh Catalyst for Catalytic Oxidation of Toluene, Acetone and Ethyl Acetate,” *Chinese J. Chem.*, vol. 27, no. 10, pp. 1903–1906, Oct. 2009.

[65] M. Chen, Y. Ma, G. Li, and X. Zheng, “Support effect, thermal stability, and structure feature of toluene combustion catalyst,” *Catal. Commun.*, vol. 9, no. 6, pp. 990–994, Mar. 2008.

[66] L. Zhou, Y. Guo, M. Yagi, … M. S. journal of, and undefined 2009, “Investigation of a novel porous anodic alumina plate for methane steam reforming: hydrothermal stability, electrical heating possibility and reforming reactivity,” *Elsevier*.

[67] Z. Rui, C. Chen, Y. Lu, and H. Ji, “Anodic Alumina Supported Pt Catalyst for Total Oxidation of Trace Toluene,” *Chinese J. Chem. Eng.*, vol. 22, no. 8, pp. 882–887, Aug. 2014.

[68] T. Zhang, M. Chen, Y. Gao, and X. Zheng, “Preparation process and characterization of new Pt/stainless steel wire mesh catalyst designed for volatile organic compounds elimination,” *J. Cent. South Univ.*, vol. 19, no. 2, pp. 319–323, Feb. 2012.

[69] S. . Tikhov *et al.*, “Honeycomb catalysts for clean-up of diesel exhausts based upon the anodic-spark oxidized aluminum foil,” *Catal. Today*, vol. 53, no. 4, pp. 639–646, Nov. 1999.

[70] E. M. Holmgreen, M. M. Yung, and U. S. Ozkan, “Dual-catalyst aftertreatment of lean-burn natural gas engine exhaust,” *Appl. Catal. B Environ.*, vol. 74, no. 1–2, pp. 73–82, Jun. 2007.

[71] R. Gholami, M. Alyani, and K. J. Smith, “Deactivation of Pd catalysts by water during low temperature methane oxidation relevant to natural gas vehicle converters,” *Catalysts*, vol. 5, no. 2, pp. 561–594, 2015.

[72] S. Mahboob, M. Haghighi, F. R.-U. sonochemistry, and undefined 2017, “Sonochemically preparation and characterization of bimetallic Ni-Co/Al2O3-ZrO2 nanocatalyst: effects of ultrasound irradiation time and power on catalytic,” *Elsevier*.

[73] W. M. Haynes, Ed., *CRC handbook of chemistry and physics*, 94th Editi. CRC press, 2014.

[74] G. Patermarakis and C. Pavlidou, “Catalysis over Porous Anodic Alumina Catalysts,” *J. Catal.*, vol. 147, no. 1, pp. 140–155, May 1994.

[75] A. Binder, M. Seipenbusch, and G. Kasper, “Sintering of Pd Catalyst Particles on SiO2−TiO2 Carrier Particles of Different Mixing Ratios,” *J. Phys. Chem. C*, vol. 114, no. 17, pp. 7816–7821, Apr. 2010.

[76] M. Anik and K. Osseo-Asare, “Effect of pH on the Anodic Behavior of Tungsten,” *J. Electrochem. Soc.*, vol. 149, no. 6, pp. B224–B233, 2002.

[77] B. G. Santos, J. J. Noël, and D. W. Shoesmith, “The effect of pH on the anodic dissolution of SIMFUEL (UO2),” *J. Electroanal. Chem.*, vol. 586, no. 1, pp. 1–11, Jan. 2006.

[78] H. Takahashi, K. Fujimoto, and M. Nagayama, “Effect of pH on the distribution of anions in anodic oxide films formed on aluminum in phosphate solutions,” *J. Electrochem. Soc.*, vol. 135, no. 6, p. 1349, 1988.

[79] C. Kozlowski and P. M. A. Sherwood, “X-ray photoelectron-spectroscopic studies of carbon-fibre surfaces. Part 5.—The effect of pH on surface oxidation,” *J. Chem. Soc. Faraday Trans. 1 Phys. Chem. Condens. Phases*, vol. 81, no. 11, pp. 2745–2756, 1985.

[80] O. Jessensky, F. Müller, and U. Gösele, “Self-organized formation of hexagonal pore arrays in anodic alumina,” *Appl. Phys. Lett.*, vol. 72, no. 10, pp. 1173–1175, Mar. 1998.

[81] N.-Q. Zhao, X.-X. Jiang, C.-S. Shi, J.-J. Li, Z.-G. Zhao, and X.-W. Du, “Effects of anodizing conditions on anodic alumina structure,” *J. Mater. Sci.*, vol. 42, no. 11, pp. 3878–3882, 2007.

[82] S. E. Voltz, C. R. Morgan, D. Liederman, and S. M. Jacob, “Kinetic study of carbon monoxide and propylene oxidation on platinum catalysts,” *Ind. Eng. Chem. Prod. Res. Dev.*, vol. 12, no. 4, pp. 294–301, 1973.

[83] US Energy Information Administratoin, “Record U.S. electricity generation in 2018 driven by record residential, commercial sales - Today in Energy - U.S. Energy Information Administration (EIA),” *Today in Energy*, 2019. [Online]. Available: https://www.eia.gov/todayinenergy/detail.php?id=38572. [Accessed: 30-Oct-2019].

[84] H. Friedli, H. Lötscher, H. Oeschger, U. Siegenthaler, and B. Stauffer, “Ice core record of the 13C/12C ratio of atmospheric CO2 in the past two centuries,” *Nature*, vol. 324, no. 6094, pp. 237–238, Nov. 1986.

[85] G. Hartfield, J. Blunden, and D. S. Arndt, “State of the Climate in 2018,” *Bull. Am. Meteorol. Soc.*, vol. 99, no. 8, p. Si-S310, Aug. 2018.

[86] G. Zanchi, N. Pena, and N. Bird, “Is woody bioenergy carbon neutral? A comparative assessment of emissions from consumption of woody bioenergy and fossil fuel,” *Gcb Bioenergy*, vol. 4, no. 6, pp. 761–772, 2012.

[87] N. Ungureanu, V. Vladut, G. Voicu, M.-N. Dinca, and B.-S. Zabava, “Influence of biomass moisture content on pellet properties–review,” *Eng. Rural Dev.*, vol. 17, pp. 1876–1883, 2018.

[88] L. Wang *et al.*, “Effect of Torrefaction on Properties of Pellets Produced from Woody Biomass,” *Energy & Fuels*, vol. 34, no. 12, pp. 15343–15354, Dec. 2020.

[89] M. Rudolfsson, W. Stelte, and T. A. Lestander, “Process optimization of combined biomass torrefaction and pelletization for fuel pellet production – A parametric study,” *Appl. Energy*, vol. 140, pp. 378–384, 2015.

[90] D. R. Nhuchhen, P. Basu, and B. Acharya, “A comprehensive review on biomass torrefaction,” *Int. J. Renew. Energy Biofuels*, vol. 2014, pp. 1–56, 2014.

[91] W.-T. Tsai *et al.*, “Conversion of water caltrop husk into torrefied biomass by torrefaction,” *Energy*, vol. 195, p. 116967, 2020.

[92] Y. Niu *et al.*, “Biomass torrefaction: properties, applications, challenges, and economy,” *Renew. Sustain. Energy Rev.*, vol. 115, p. 109395, 2019.

[93] B. Batidzirai, A. P. R. Mignot, W. B. Schakel, H. M. Junginger, and A. P. C. Faaij, “Biomass torrefaction technology: Techno-economic status and future prospects,” *Energy*, vol. 62, pp. 196–214, Dec. 2013.

[94] M. Phanphanich and S. Mani, “Impact of torrefaction on the grindability and fuel characteristics of forest biomass,” *Bioresour. Technol.*, vol. 102, no. 2, pp. 1246–1253, Jan. 2011.

[95] T. Onsree *et al.*, “Torrefaction of pelletized corn residues with wet flue gas,” *Bioresour. Technol.*, vol. 285, p. 121330, Aug. 2019.

[96] J. P. Breen and R. Burch, “A review of the effect of the addition of hydrogen in the selective catalytic reduction of NO x with hydrocarbons on silver catalysts,” *Top. Catal.*, vol. 39, no. 1–2, pp. 53–58, Sep. 2006.

[97] H. Hamada and M. Haneda, “A review of selective catalytic reduction of nitrogen oxides with hydrogen and carbon monoxide,” *Appl. Catal. A Gen.*, vol. 421–422, pp. 1–13, Apr. 2012.

[98] S. C. Paik and J. S. Chung, “Selective catalytic reduction of sulfur dioxide with hydrogen to elemental sulfur over Co-Mo/Al2O3,” *Appl. Catal. B Environ.*, vol. 5, no. 3, pp. 233–243, Feb. 1995.

[99] R. K. Grasselli, C. G. Lugmair, and A. F. Volpe, “Towards an understanding of the reaction pathways in propane ammoxidation based on the distribution of elements at the active centers of the M1 phase of the MoV (Nb, Ta) TeO system,” *Top. Catal.*, vol. 54, no. 10, pp. 595–604, 2011.

[100] M. Roussel, M. Bouchard, K. Karim, S. Al-Sayari, and E. Bordes-Richard, “MoVO-based catalysts for the oxidation of ethane to ethylene and acetic acid: Influence of niobium and/or palladium on physicochemical and catalytic properties,” *Appl. Catal. A Gen.*, vol. 308, pp. 62–74, Jul. 2006.

[101] B. MacQueen, E. Barrow, G. Rivera Castro, Y. Pagan-Torres, A. Heyden, and J. Lauterbach, “Optimum Reaction Conditions for 1, 4-Anhydroerythritol and Xylitol Hydrodeoxygenation over a ReO x–Pd/CeO2 Catalyst via Design of Experiments,” *Ind. Eng. Chem. Res.*, vol. 58, no. 20, pp. 8681–8689, 2019.

[102] J. F. Saldarriaga, R. Aguado, A. Pablos, M. Amutio, M. Olazar, and J. Bilbao, "Fast characterization of biomass fuels by thermogravimetric analysis (TGA)," *Fuel*, vol. 140, pp. 744–751, 2015.

[103] J. Parikh, S. A. Channiwala, and G. K. Ghosal, "A correlation for calculating HHV from proximate analysis of solid fuels," *Fuel*, vol. 84, no. 5, pp. 487–494, 2005.

[104] M. Davies, "High resolution XPS of organic polymers: The Scienta ESCA300 database: G. Beamson and D. Briggs John Wiley, Chichester, UK 1992." Elsevier, 1994.

[105] M. Peng, L. Li, J. Xiong, K. Hua, S. Wang, and T. Shao, "Study on surface properties of polyamide 66 using atmospheric glow-like discharge plasma treatment," *Coatings*, vol. 7, no. 8, p. 123, 2017.

[106] V. Prasad, A. M. Karim, A. Arya, and D. G. Vlachos, "Assessment of Overall Rate Expressions and Multiscale, Microkinetic Model Uniqueness via Experimental Data Injection: Ammonia Decomposition on Ru/γ-Al2O3 for Hydrogen Production," *Ind. Eng. Chem. Res.*, vol. 48, no. 11, pp. 5255–5265, Jun. 2009.

[107] D. T. PRITCHARD and J. A. CURRIE, "Diffusion of coefficients of carbon dioxide, nitrous oxide, ethylene and ethane in air and their measurement," *J. Soil Sci.*, vol. 33, no. 2, pp. 175–184, Jun. 1982.

[108] Y. Xin, H. Wang, and C. K. Law, "Kinetics of catalytic oxidation of methane, ethane and propane over palladium oxide," *Combust. Flame*, vol. 161, no. 4, pp. 1048–1054, Apr. 2014.

[109] M. Roussel, S. Barama, A. Löfberg, S. Al-Sayari, K. Karim, and E. Bordes-Richard, “MoV-based catalysts in ethane oxidation to acetic acid: Influence of additives on redox chemistry,” *Catal. Today*, vol. 141, no. 3–4, pp. 288–293, Mar. 2009.

[110] P. Botella, E. García-González, A. Dejoz, J. . López Nieto, M. . Vázquez, and J. González-Calbet, “Selective oxidative dehydrogenation of ethane on MoVTeNbO mixed metal oxide catalysts,” *J. Catal.*, vol. 225, no. 2, pp. 428–438, Jul. 2004.

[111] D. Söderberg and I. Lundström, “Competition between hydrogen and oxygen dissociation on palladium surfaces at atmospheric pressures,” *Solid State Commun.*, vol. 45, no. 5, pp. 431–434, Feb. 1983.

[112] P. Botella, A. Dejoz, M. C. Abello, M. I. Vázquez, L. Arrúa, and J. M. López Nieto, “Selective oxidation of ethane: Developing an orthorhombic phase in Mo–V–X (X = Nb, Sb, Te) mixed oxides,” *Catal. Today*, vol. 142, no. 3–4, pp. 272–277, Apr. 2009.

[113] J. M. M. Millet, “Mechanism of first hydrogen abstraction from light alkanes on oxide catalysts,” *Top. Catal.*, vol. 38, no. 1–3, pp. 83–92, Jul. 2006.

[114] O. V. Safonova, A. Benoit Deniau, and J.-M. M. Millet*, “Mechanism of the Oxidation−Reduction of the MoVSbNbO Catalyst: In Operando X-ray Absorption Spectroscopy and Electrical Conductivity Measurements,” *J. Phys. Chem. B*, vol. 110, no. 47, pp. 23962–23967, 2006.

[115] M. Pozzo and D. Alfè, “Hydrogen dissociation and diffusion on transition metal (= Ti, Zr, V, Fe, Ru, Co, Rh, Ni, Pd, Cu, Ag)-doped Mg(0001) surfaces,” *Int. J. Hydrogen Energy*, vol. 34, no. 4, pp. 1922–1930, Feb. 2009.

[116] H. L. Tierney, A. E. Baber, J. R. Kitchin, and E. C. H. Sykes, “Hydrogen Dissociation and Spillover on Individual Isolated Palladium Atoms,” *Phys. Rev. Lett.*, vol. 103, no. 24, p. 246102, Dec. 2009.

[117] R. Gopinath, N. Lingaiah, B. Sreedhar, I. Suryanarayana, P. S. Sai Prasad, and A. Obuchi, “Highly stable Pd/CeO2 catalyst for hydrodechlorination of chlorobenzene,” *Appl. Catal. B Environ.*, 2003.

[118] J. Li *et al.*, “Effect of TiO_2 crystal structure on the catalytic performance of Co_3O_4 /TiO_2 catalyst for low-temperature CO oxidation,” *Catal. Sci. Technol.*, vol. 4, no. 5, pp. 1268–1275, Apr. 2014.

[119] M. Kamitsou, G. D. Panagiotou, K. S. Triantafyllidis, K. Bourikas, A. Lycourghiotis, and C. Kordulis, “Transformation of α-limonene into p-cymene over oxide catalysts: A green chemistry approach,” *Appl. Catal. A Gen.*, vol. 474, pp. 224–229, Mar. 2014.

[120] Z. Zhao, X. Gao, I. E. Wachs, Zhen Zhao, and Xingtao Gao, and I. E. Wachs*, “Comparative Study of Bulk and Supported V−Mo−Te−Nb−O Mixed Metal Oxide Catalysts for Oxidative Dehydrogenation of Propane to Propylene,” *J. Phys. Chem. B*, vol. 107, no. 26, pp. 6333–6342, 2003.

[121] J. Moncada, W. R. Adams, R. Thakur, M. Julin, and C. A. Carrero, “Developing a Raman Spectrokinetic Approach To Gain Insights into the Structure–Reactivity Relationship of Supported Metal Oxide Catalysts,” *ACS Catal.*, vol. 8, no. 10, pp. 8976–8986, Oct. 2018.

[122] C. Schilling, A. Hofmann, C. Hess, and M. V. Ganduglia-Pirovano, “Raman Spectra of Polycrystalline CeO_2 : A Density Functional Theory Study,” *J. Phys. Chem. C*, vol. 121, no. 38, pp. 20834–20849, Sep. 2017.

[123] P. Korovchenko, N. R. Shiju, A. K. Dozier, U. M. Graham, M. O. Guerrero-Pérez, and V. V. Guliants, “M1 to M2 Phase Transformation and Phase Cooperation in Bulk Mixed Metal Mo–V–M–O (M=Te, Nb) Catalysts for Selective Ammoxidation of Propane,” *Top. Catal.*, vol. 50, no. 1–4, pp. 43–51, Nov. 2008.

[124] Shuibo Xie, A. Enrique Iglesia, and A. T. Bell, “Effects of Temperature on the Raman Spectra and Dispersed Oxides,” 2001.

[125] I. E. Wachs, J.-M. Jehng, and W. Ueda, “Determination of the Chemical Nature of Active Surface Sites Present on Bulk Mixed Metal Oxide Catalysts,” *J. Phys. Chem. B*, vol. 109, no. 6, pp. 2275–2284, Feb. 2005.

[126] K. Amakawa *et al.*, “Multifunctionality of Crystalline MoV(TeNb) M1 Oxide Catalysts in Selective Oxidation of Propane and Benzyl Alcohol,” *ACS Catal.*, vol. 3, no. 6, pp. 1103–1113, Jun. 2013.

[127] J. B. Wagner *et al.*, “Surface texturing of Mo–V–Te–Nb–O x selective oxidation catalysts,” *Top. Catal.*, vol. 38, no. 1–3, pp. 51–58, 2006.

[128] P. Mars and D. W. van Krevelen, “Oxidations carried out by means of vanadium oxide catalysts,” *Chem. Eng. Sci.*, vol. 3, pp. 41–59, Jan. 1954.

[129] D. Melzer *et al.*, “Atomic-scale determination of active facets on the MoVTeNb oxide M1 phase and their intrinsic catalytic activity for ethane oxidative dehydrogenation,” *Angew. Chemie Int. Ed.*, vol. 55, no. 31, pp. 8873–8877, 2016.

[130] A. Setiawan *et al.*, “Towards understanding the improved stability of palladium supported on TS-1 for catalytic combustion,” *Phys. Chem. Chem. Phys.*, vol. 18, no. 15, pp. 10528–10537, Apr. 2016.

[131] C.-V. Ngo and D.-M. Chun, “Fast wettability transition from hydrophilic to superhydrophobic laser-textured stainless steel surfaces under low-temperature annealing,” *Appl. Surf. Sci.*, vol. 409, pp. 232–240, Jul. 2017.

[132] J. Barbier and D. Duprez, “Steam effects in three-way catalysis,” *Appl. Catal. B Environ.*, vol. 4, no. 2–3, pp. 105–140, Sep. 1994.

[133] A. Samavati, M. Fattahi, and F. Khorasheh, “Modeling of Pt-Sn/γ-Al2O3 deactivation in propane dehydrogenation with oxygenated additives,” *Korean J. Chem. Eng.*, vol. 30, no. 1, pp. 55–61, 2013.

[134] K. Persson, L. D. Pfefferle, W. Schwartz, A. Ersson, and S. G. Järås, “Stability of palladium-based catalysts during catalytic combustion of methane: The influence of water,” *Appl. Catal. B Environ.*, vol. 74, no. 3–4, pp. 242–250, Jul. 2007.

[135] R. Strobel, J.-D. Grunwaldt, A. Camenzind, S. E. Pratsinis, and A. Baiker, “Flame-made Alumina Supported Pd–Pt Nanoparticles: StructuralProperties and Catalytic Behavior in Methane Combustion,” *Catal. Letters*, vol. 104, no. 1, pp. 9–16, 2005.

[136] J. Jones *et al.*, “Thermally stable single-atom platinum-on-ceria catalysts via atom trapping,” *Science (80-.).*, vol. 353, no. 6295, pp. 150–154, 2016.

[137] Y.-Q. Su, J.-X. Liu, I. A. W. Filot, and E. J. M. Hensen, “Theoretical study of ripening mechanisms of Pd clusters on ceria,” *Chem. Mater.*, vol. 29, no. 21, pp. 9456–9462, 2017.

[138] A. Belwalkar, E. Grasing, W. Van Geertruyden, Z. Huang, and W. Z. Misiolek, "Effect of processing parameters on pore structure and thickness of anodic aluminum oxide (AAO) tubular membranes," *J. Memb. Sci.*, vol. 319, no. 1–2, pp. 192–198, Jul. 2008.

[139] Y. Sui and J. M. Saniger, "Characterization of anodic porous alumina by AFM," *Mater. Lett.*, vol. 48, no. 3–4, pp. 127–136, Apr. 2001.

[140] G. Patermarakis and K. Masavetas, "Aluminium anodising in oxalate and sulphate solutions. Comparison of chronopotentiometric and overall kinetic response of growth mechanism of porous anodic films," *J. Electroanal. Chem.*, vol. 588, no. 2, pp. 179–189, Mar. 2006.

[141] M. Stemp, S. Mischler, and D. Landolt, "The effect of contact configuration on the tribocorrosion of stainless steel in reciprocating sliding under potentiostatic control," *Corros. Sci.*, vol. 45, no. 3, pp. 625–640, Mar. 2003.

[142] S. Kaya and D. Üner, "CO oxidation over mono and bi-metallic sequentially impregnated Pd-Pt catalysts," *Turkish J. Chem.*, vol. 32, no. 5, pp. 645–652, 2008.

[143] M. J. Hazlett, M. Moses-Debusk, J. E. Parks, L. F. Allard, and W. S. Epling, "Kinetic and mechanistic study of bimetallic Pt-Pd/Al2O3 catalysts for CO and C3H6 oxidation," *Appl. Catal. B Environ.*, vol. 202, pp. 404–417, Mar. 2017.

[144] I. Z. Ismagilov *et al.*, "Optimization of anodic oxidation and Cu–Cr oxide catalyst preparation on structured aluminum plates processed by electro discharge machining," *Catal. Today*, vol. 105, no. 3–4, pp. 516–528, Aug. 2005.

[145] B. Yue, R. Zhou, Y. Wang, and X. Zheng, “Influence of transition metals (Cr, Mn, Fe, Co and Ni) on the methane combustion over Pd/Ce–Zr/Al2O3 catalyst,” *Appl. Surf. Sci.*, vol. 252, no. 16, pp. 5820–5828, 2006.

[146] K. Okumura, H. Tanaka, and M. Niwa, “Influence of acid–base property of support on the toluene combustion activity of palladium,” *Catal. Letters*, vol. 58, no. 1, pp. 43–45, 1999.

[147] K. Muto, N. Katada, and M. Niwa, “Complete oxidation of methane on supported palladium catalyst: Support effect,” *Appl. Catal. A Gen.*, vol. 134, no. 2, pp. 203–215, 1996.

[148] J. Ejenstam, M. Thuvander, P. Olsson, F. Rave, and P. Szakalos, “Microstructural stability of Fe–Cr–Al alloys at 450–550° C,” *J. Nucl. Mater.*, vol. 457, pp. 291–297, 2015.

[149] B. Qiao *et al.*, “Single-atom catalysis of CO oxidation using Pt1/FeOx,” *Nat. Chem.*, vol. 3, no. 8, pp. 634–641, 2011.

[150] A. Tiple, P. S. Sinhmar, and P. R. Gogate, “Improved direct synthesis of TiO2 catalyst using sonication and its application for the desulfurization of thiophene,” *Ultrason. Sonochem.*, vol. 73, p. 105547, 2021.

[151] D. Y. M. S. Devyatkov, N.V. Kuzichkin, “On comprehensive understanding of catalyst shaping by extrusion,” *Chim. Oggi- Chem. Today*, vol. 33, no. 6, pp. 57–64, 2015.

[152] A. M. Beale *et al.*, “Chemical imaging of the sulfur-induced deactivation of Cu/ZnO catalyst bodies,” *J. Catal.*, vol. 314, pp. 94–100, 2014.

[153] S. C. F. Commission, “Final report to the South Carolina Forestry Commission on potential for biomass energy development in South Carolina,” *South Carolina State Doc. Depos.*, 2005.

[154] J. Koppejan and S. Van Loo, *The handbook of biomass combustion and co-firing*. Routledge, 2012.

[155] A. A. Gokhale, J. A. Dumesic, and M. Mavrikakis, “On the Mechanism of Low-Temperature Water Gas Shift Reaction on Copper,” *J. Am. Chem. Soc.*, vol. 130, no. 4, pp. 1402–1414, Jan. 2008.

[156] K. J. B. T.-S. S. Zeitsch, Ed., “8. The discoloration of furfural,” in *the chemistry and technology of furfural and its many by-products*, vol. 13, Elsevier, 2000, pp. 28–33.

[157] S. Ren *et al.*, “The effects of torrefaction on compositions of bio-oil and syngas from biomass pyrolysis by microwave heating,” *Bioresour. Technol.*, vol. 135, pp. 659–664, 2013.

[158] K. C. Stein, J. J. Feenan, G. P. Thompson, J. F. Shultz, L. J. E. Hofer, and R. B. Anderson, “The oxidation of hydrocarbons on simple oxide catalysts,” *J. Air Pollut. Control Assoc.*, vol. 10, no. 4, pp. 275–281, 1960.

[159] K. Polychronopoulou, C. M Kalamaras, and A. M Efstathiou, “Ceria-based materials for hydrogen production via hydrocarbon steam reforming and water-gas shift reactions,” *Recent Patents Mater. Sci.*, vol. 4, no. 2, pp. 122–145, 2011.

[160] J. R. Mellor, R. G. Copperthwaite, and N. J. Coville, “The selective influence of sulfur on the performance of novel cobalt-based water-gas shift catalysts,” *Appl. Catal. A Gen.*, vol. 164, no. 1–2, pp. 69–79, 1997.

[161] Z. Yang, L. Luo, L. Tang, Z. Zhou, Z. Zhou, and Y. Li, “Trimesic acid assisted synthesis of cerium-manganese oxide for catalytic diesel soot elimination: Enhancement of thermal aging resistibility,” *Fuel*, vol. 278, p. 118369, 2020.

[162] L. Tonietto, L. Gonzaga, M. R. Veronez, C. de S. Kazmierczak, D. C. M. Arnold, and C. A. da Costa, “New Method for Evaluating Surface Roughness Parameters Acquired by Laser Scanning,” *Sci. Rep.*, vol. 9, no. 1, p. 15038, 2019.

[163] Ö. Ö. Çapraz, Q. van Overmeere, P. Shrotriya, and K. R. Hebert, “Stress induced by electrolyte anion incorporation in porous anodic aluminum oxide,” *Electrochim. Acta*, vol. 238, pp. 368–374, 2017.

[164] K. Shimizu *et al.*, “Anomalously low levels of anion incorporation into anodic oxide films on tungsten,” *Corros. Sci.*, vol. 40, no. 7, pp. 1229–1238, 1998.

[165] M. A. Ameer, A. M. Fekry, and F. E.-T. Heakal, “Electrochemical behaviour of passive films on molybdenum-containing austenitic stainless steels in aqueous solutions,” *Electrochim. Acta*, vol. 50, no. 1, pp. 43–49, 2004.

[166] P. Sivagurunathan and S. R. Gibin, “Preparation and characterization of nickel ferrite nano particles by co-precipitation method with citrate as chelating agent,” *J. Mater. Sci. Mater. Electron.*, vol. 27, no. 3, pp. 2601–2607, 2016.

[167] H. Ajo, D. Blankenship, and E. Clark, “Analysis of passivated A-286 stainless steel surfaces for mass spectrometer inlet systems by Auger electron and X-ray photoelectron spectroscopy and scanning electron microscopy,” *Metallogr. Microstruct. Anal.*, vol. 3, no. 4, pp. 263–271, 2014.

[168] M. Bizjak, A. Zalar, P. Panjan, B. Zorko, and B. Praček, “Characterization of iron oxide layers using Auger electron spectroscopy,” *Appl. Surf. Sci.*, vol. 253, no. 8, pp. 3977–3981, 2007.

APPENDIX A

PERMISSION TO REPRINT

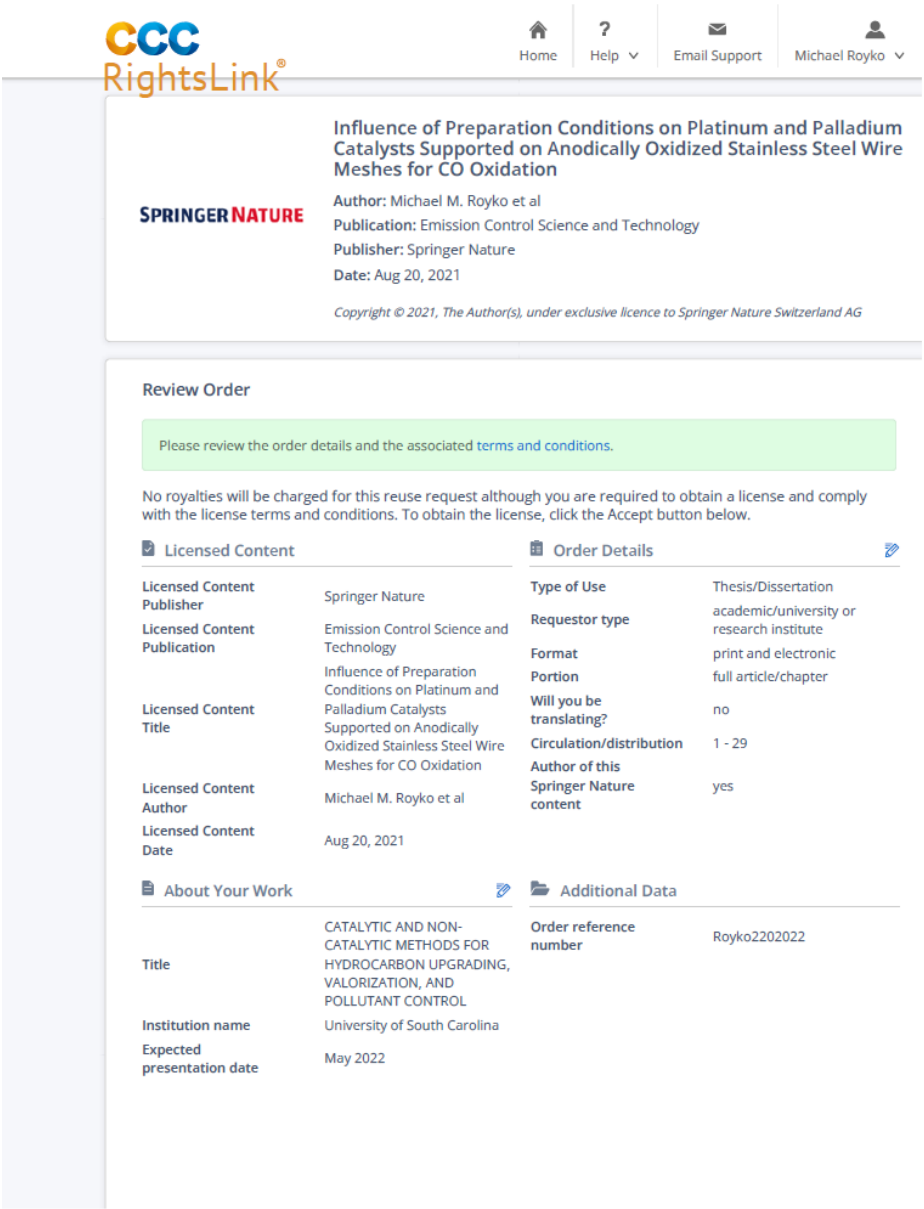

CCC RightsLink

Home | Help | Email Support | Michael Royko

SPRINGER NATURE

Influence of Preparation Conditions on Platinum and Palladium Catalysts Supported on Anodically Oxidized Stainless Steel Wire Meshes for CO Oxidation

Author: Michael M. Royko et al
Publication: Emission Control Science and Technology
Publisher: Springer Nature
Date: Aug 20, 2021

Copyright © 2021, The Author(s), under exclusive licence to Springer Nature Switzerland AG

Review Order

Please review the order details and the associated terms and conditions.

No royalties will be charged for this reuse request although you are required to obtain a license and comply with the license terms and conditions. To obtain the license, click the Accept button below.

Licensed Content

Licensed Content Publisher	Springer Nature
Licensed Content Publication	Emission Control Science and Technology
Licensed Content Title	Influence of Preparation Conditions on Platinum and Palladium Catalysts Supported on Anodically Oxidized Stainless Steel Wire Meshes for CO Oxidation
Licensed Content Author	Michael M. Royko et al
Licensed Content Date	Aug 20, 2021

Order Details

Type of Use	Thesis/Dissertation
Requestor type	academic/university or research institute
Format	print and electronic
Portion	full article/chapter
Will you be translating?	no
Circulation/distribution	1 - 29
Author of this Springer Nature content	yes

About Your Work

Title	CATALYTIC AND NON-CATALYTIC METHODS FOR HYDROCARBON UPGRADING, VALORIZATION, AND POLLUTANT CONTROL
Institution name	University of South Carolina
Expected presentation date	May 2022

Additional Data

Order reference number	Royko2202022

Chemistry Division

Brookhaven National Laboratory

Building 555
P.O. Box 5000
Upton, NY 11973-5000
Phone 516.491.1731
Jjimenez1@bnl.gov

managed by Brookhaven Science Associates
for the U.S. Department of Energy

www.bnl.gov

March 15th, 2022

Michael Royko
PhD Candidate
University of South Carolina
541 Main St.
Columbia, SC 29208

Dear Mr. Royko:

As the copyright holder for the work published in the doctoral thesis titled “Influence of Coordination Environment on Catalyst Structure and Function for CO_2 Hydrogenation and Ethane Partial Oxidation” I hereby grant you the right to reproduce in part the material herein for the preparation of your doctoral thesis.

Regards,

Juan D. Jimenez

Dr. Juan D Jimenez
Goldhaber Fellow
Brookhaven National Laboratory, Chemistry Division
Mobile. 516.491.1731
Email. Jjimenez1@bnl.gov